



HAL
open science

Laser-pyrolysed ZnFe₂O₄ anode for lithium-ion batteries : understanding of the lithium storage mechanisms

Samantha Bourrioux

► To cite this version:

Samantha Bourrioux. Laser-pyrolysed ZnFe₂O₄ anode for lithium-ion batteries : understanding of the lithium storage mechanisms. Chemical and Process Engineering. Université Grenoble Alpes; NTU Centre for contemporary art (Singapour), 2018. English. NNT : 2018GREAI014 . tel-01818046

HAL Id: tel-01818046

<https://theses.hal.science/tel-01818046>

Submitted on 18 Jun 2018

HAL is a multi-disciplinary open access archive for the deposit and dissemination of scientific research documents, whether they are published or not. The documents may come from teaching and research institutions in France or abroad, or from public or private research centers.

L'archive ouverte pluridisciplinaire **HAL**, est destinée au dépôt et à la diffusion de documents scientifiques de niveau recherche, publiés ou non, émanant des établissements d'enseignement et de recherche français ou étrangers, des laboratoires publics ou privés.

THÈSE

Pour obtenir le grade de

DOCTEUR DE LA COMMUNAUTE UNIVERSITE GRENOBLE ALPES

Spécialité : **Matériaux, Mécanique, Génie Civil, Electrochimie**

Arrêté ministériel : 25 mai 2016

Présentée par

Rémi BLANCHARD

Thèse dirigée par **Marian CHATENET, Professeur, Grenoble-
INP**, et
codirigée par **Arnaud MANTOUX, Maitre de Conférence,
Université Grenoble-Alpes**

préparée au sein du **Laboratoire d'Electrochimie et de
Physicochimie des Matériaux et des Interfaces-LEPMI**
dans **l'École Doctorale Ingénierie-Matériaux, Mécanique,
Energétique Environnement procédés Production**

Redox shuttles and Positive Electrode Protection for Li-O₂ systems

Thèse soutenue publiquement le **15 décembre 2017**,
devant le jury composé de :

Monsieur Daniel BELLET

Professeur des Universités, Grenoble INP, Président

Monsieur Sanjeev MUKERJEE

Professeur, Northeastern University, Rapporteur

Monsieur Mikhael BECHELANY

Chargé de Recherche, CNRS, Rapporteur

Monsieur Marian CHATENET

Professeur des Universités, Grenoble-INP, Directeur de thèse

Monsieur Arnaud MANTOUX

Maitre de Conférences, Université Grenoble-Alpes, Co-Directeur de
thèse

Monsieur Marc ZIMMERMAN

Ingénieur, HUTCHINSON SA, Examineur



Seul l'impossible mérite réflexion

Dezso Kosztolanyi / Les aventures de Kornel Esti

Acknowledgments

Three years. It is a lot, and in many ways, it is not enough. Thanks to this wonderful experience, my personality and vision of the world and of science changed drastically. Some aspects still appear painful, with a lot of sweat, nerve crisis because of experiment failure, and sometime, this immeasurable joy when finally, the attended result is observed, for the first time.

I would never trade this experience for anything, blood and tears, laugh and excitements, late nights at the lab, and late nights at the pub...And finally, I could not have met more wonderful persons that I had the chance to work with and made this thesis possible. For this reason, it feels necessary to acknowledge them, in proper ways.

Firstly, my two advisors, Marian CHATENET and Arnaud MANTOUX. Both Wonderful scientists and persons. They had this incredible patience, and were always willing to help me, which enabled me to seize my subject, and sense the important conclusions and directions for my work. They were also highly comprehensive, always helping me and comforting me during the harsh emotional time. For this reason I really want to thanks them for their support and their humanity.

Secondly, without the staff members of LEPMI, SIMAP and CMTC, nothing could have been done. For this reason, I really would like to thanks Claire and Yasmine of the LEPMI administrative service, for their reactivity and help, organizing conferences booking, but also filling all those purchase orders (I was a compulsive buyer). Also without their willing to form me on the Atomic Layer Deposition, a whole part of my thesis will have not been possible. For this reason, I am really grateful for Alex Crisci and Roman Reboud, thanks for your help and patience. I must also stress how I was annoying to Alex, as I wanted to do Raman, Ellipsometry, but also Vanadium deposition, on the "nano" reactor, and he was willing to help me doing those manipulations, even though he was grudgingly doing it (Joke).I would also like to thank very much Rachel Martin, which enabled me to do a lot of SEM and X-EDS analysis, late in my thesis and was always willing to help me, with the smile. For your kindness and help, thank you. Also the XPS analysis would have not been possible without Gregory Berthomé of SIMAP, thank you for your help and your patience, for explaining this powerful technique to me.

Thirdly, I would like to thanks all my PhD students colleagues, along with the other researchers of the EIP team that I had the chance to work with, with always a lot of laughs and good moments at the Lunch time at the lab, but also during all those parties organized with the entire team, which really demonstrated how we were united. Vincent, for his Jokes and weird stories that were allowing me to fully disconnect during the lunch time, Céline and Raphael, also for their kindness and friendship and all the three of you, for supporting me during the harsh time. I would also like to thank Marc, for being my mentor at the beginning of my PhD, giving me the chance to not waste any time for the seizing of the experimental apparatus. Tristan, Matthieu (Deplagne), Fanny, Clémence, Marion, Fabien, Guillaume for their friendship, and for their patience (for my jokes that can be a little bit clumsy sometimes).

To the end, I would like to thank my girlfriend, Orane, which supported me the whole time, enabled me to regain confidence when needed (but also kept my feet firmly to the ground, when I was dreaming of solving the energy crisis by myself), but also my beloved family, which supported me and make this experience possible.

Merci à tous!

Table of Contents

Chapter I: Non aqueous Li-O₂ batteries	1
I. Green pathways toward energy Storing	3
a. Actual Energy Sources	3
b. Replacement solutions for the electrical power grid	6
c. Toward high energy systems for gasoline replacement in Mobile application.....	11
II. The Li-O₂ systems	15
a. Discovery of Li-oxygen batteries	15
b. ORR and OER mechanisms in aprotic medium.....	20
c. Effect of water.....	29
d. Issues of Li-O ₂ cathodes and improvement paths	31
Conclusion	36
References	37
Chapter II : Experimental section	43
I. Electrochemistry	44
a. Washing of the glassware	44
b. Chemicals	44
c. Three-electrodes setup.....	45
d. Differential Electrochemical Mass Spectrometry	45
e. Full cell experiment	46
f. Electrochemical testing	47
II. Characterization techniques	47
a. Differential Electrochemical Mass Spectrometry	47
b. Raman Spectroscopy	52
c. Field-Emission Gun-Scanning Electron Microscopy (FEG-SEM).....	53
d. X-Ray Energy Dispersive Spectrometer (X-EDS)	54
e. UV-Visible Spectrophotometry	54
f. X-ray Photoelectron Spectroscopy (XPS)	55
g. Ellipsometry.....	57
h. X-ray Diffraction	58
References	59

Chapter III: High Surface Area Carbon-based Materials for High Energy Li-O₂ cathodes: Advantages and Drawbacks	61
I. Materials	62
a. Morphologies	62
b. Surface areas	64
c. Raman Spectroscopy	65
II. Electrochemical properties	67
a. Half Cells	67
b. Full cells	69
c. DEMS	78
d. Comparative Raman	83
Conclusion	88
References	90

Chapter IV: Redox Shuttles: necessary additives for OER enhancement in Li-O₂ batteries	93
I. Redox shuttle screening for Li-O₂ cathodes	94
a. Redox Shuttles: the ideal behavior	94
b. Unfruitful selection of potential redox mediators	102
c. Useful compounds to be used as redox shuttles in Li-O ₂ batteries	110
II. OER enhancement mechanisms of Co(II)-Po and Co-salen - How the Co salen is beneficial for both the OER and ORR	128
a. Enhancement pathway of the OER for Co(II)-Po and Co-Salen	128
b. ORR Homogeneous catalysis of Co-Salen	133
Conclusions:	138
References	140

Chapter V: Carbon protection by Atomic Layer Deposition of Nb₂O₅.....	144
I. Atomic Layer Deposition: Principles	145
II. Deposits of Nb₂O₅ on Silicon: a model study	149
a. Surface morphology of Nb _x O _y deposits	150
b. Composition of the deposits for the two recipes (Thermal ALD and PEALD)	156
III. Cathode elaboration with Nb₂O₅ deposits	171
a. Composition of the deposit, non-uniformities of the deposits	172
b. Protected Li-O ₂ positive electrodes behavior	178
Conclusion.....	191
References	192
Chapter VI: Perspectives for a stable Li-O₂ positive electrode, with high recharge ability.....	197
I. Replacement of Nb₂O₅ by V₂O₅	198
a. Morphology/ thickness.....	199
b. Composition	200
c. Electrochemical behavior	202
II. Toward the use of Co-salen in a Li-O₂ full cell	205
a. Scheme of a solution	205
b. SEI-pre-forming experience	208
c. A protected Li-O ₂ full cell with Co-salen	212
Conclusion.....	216
References.....	217
General Conclusions.....	221
Annexes.....	225
Conferences & Publications.....	230

List of Figures

Figure I. 1: Energy produced from various sources worldwide, presented as published by the International Energy Agency [4], reproduced with their permission.....	4
Figure I. 2: Power risks, presented as published by the New Scientist[7], reproduced with their permission.....	6
Figure I. 3: Scheme of the discharge of a Li-S, battery as published in Fotouhi et al paper, reproduced from [17], with permission from the Renewable and Sustainable Energy Reviews.....	13
Figure I. 4 : Design of the Li-O ₂ cell, operated by Molten Salts, as published in Semkov and Sammells paper, reproduced from [1], with permission from the Electrochemical Society.....	16
Figure I. 5 : Galvanostatic cycling of the cell at 20 mA cm ⁻² , as published in Semkov and Sammells paper, reproduced from [19], with permission from the Electrochemical Society.....	16
Figure I. 6 : Design of the Li-O ₂ cell, presented as published by Abraham and Jiang, reproduced from [1], with permission from the Electrochemical Society.....	17
Figure I. 7 : Discharge curve of the LI/PAN Li-O ₂ cell at 0.1 mA cm ⁻² , presented as published by Abraham and Jiang, reproduced from [1], with permission from the Electrochemical Society.....	18
Figure I. 8 : Discharge curve of the LI/PAN Li-O ₂ cell at 0.1 mA cm ⁻² , with a graphite cathode, presented as published by Abraham and Jiang, reproduced from [1], with permission from the Electrochemical Society.....	18
Figure I. 9 : Raman Spectra of a discharge Li-O ₂ battery cathode. Presented as published by Abraham and Jiang, reproduced from [1], with permission from the Electrochemical Society.....	19
Figure I. 10 : Ragone diagram of some secondary batteries, fuel cells and ICE, presented as published by Padbury et and Zhang, reproduced from [22], with permission from the Journal of Power Sources.....	20
Figure I. 11 : ORR scheme in aprotic medium, in presence of Li+.....	21
Figure I. 12 : Oxygen purged 0.1 M LiPF ₆ MeCN on GC at various scan rates, presented as published by Laoire et al , reproduced from [24] with permission from ACS.....	23
Figure I. 13 : 0.1 M LiPF ₆ DMSO at room temperature, on GC at 100 mV/s with various reverse potentials, presented as published, reproduced from [33], with permission from ACS.....	24
Figure I. 14 : Plot of the half wave potential of ORR (TBAClO ₄) versus the Donor Number of the solvent. Data used in Table1.....	27
Figure I. 15 : Plot of half peak potential vs. MCB value, with pyridine. Data extracted from [42, 43]	28
Figure I. 16 : Plot of half peak potential vs. MCB value, without pyridine. Data extracted from [42, 43]	29
Figure I. 17 : Nucleophilic attack of superoxide on an alkyl carbonate molecule : a possible pathway (scheme extracted from [61], reproduced with permission from Elsevier.....	32
Figure II. 1: Scheme of the DEMS spectro-electrochemical cell.....	46
Figure II. 2 : Mass spectrum of Di-oxygen.....	49
Figure II. 3 : mass spectrum of Carbon Dioxide.....	49
Figure II. 4: mass spectrum of dimethyl sulfoxide.....	50
Figure II. 5 : mass spectrum of sulfur dioxide.....	50
Figure II. 6 : mass spectrum methane.....	51

Figure II. 7: Differential Electrochemical Mass spectrometry experiment, from the Open circuit voltage to -1.5 V vs. Ref. primary Y-axis: Ion current of gases detected at the SEM; Secondary Y-axis: Electrochemical current. Scan rate of the LSV: 2 mV s ⁻¹	51
Figure II. 8: Differential Electrochemical Mass spectrometry experiment, from the Open circuit voltage to 1 V vs. Ref. primary Y-axis: Ion current of gases detected at the SEM; Secondary Y-axis: Electrochemical current. Scan rate of the LSV: 2mV s ⁻¹	52
Figure III. 9: Scanning Electron Micrographs, taken at an accelerating voltage of 3 kV (Panex, MOF and Phen-MOF), or of 15 kV (Basolite) with a 500 X (Panex 30, Basolite and MOF) or 200 X (Phen-MOF) magnification. A-Panex 30 carbon Fibers.B- Basolite ZIF-8. C- MOF. D-Phen-MOF.....	63
Figure III. 10: Scanning Electron Microscopy Pictures, taken at 3 kV, with a 10 kX magnification. A-Panex 30 carbon Fibers. B- Basolite ZIF-8. C- MOF. D-Phen-MOF.....	64
Figure III. 11: Raman spectra of the pristine materials, conducted with a LASER beam of 514 nm in the D and G bands region (from 1200 to 1800 cm ⁻¹).....	65
Figure III. 12: Voltamperogram obtained for the three catalyst materials in an O ₂ -purged 0.2 M LiClO ₄ electrolyte. The voltamperogram of the bare Panex 30 substrate is also given for comparison. Scan rate at 5 mV s ⁻¹ , KF below 100 ppm before the start of the experiment.....	68
Figure III. 13: Full cell configuration; discharge at -50 μA, charge at 50 μA; cutoff voltage: 4.2 V, maintained for 20 hours, for I _{charge} > 5 μA. One shall note that these very time-consuming experiments were not reproduced in multiple replicates.....	70
Figure III. 14: SEM micrograph of the surface of a Panex 30 cathode surface at an accelerating voltage of 3.00 kV, magnification 20 kX. A- pristine. B-Discharged.....	72
Figure III. 15: XEDS spectra of A-Pristine Panex 30. B- Discharged Panex 30 cathode.....	73
Figure III. 16: SEM micrographs of the surface of a Basolite cathode surface at an accelerating voltage of 3.0 kV, magnification 20 kX .A- pristine. B-Discharged.....	73
Figure III. 17 : XEDS spectra of A-Pristine Basolite. B- Discharged Basolite cathode.....	74
Figure III. 18: SEM micrographs of the surface of a MOF cathode surface obtained at an acceleration voltage of 3.0 kV, and a magnification of 10 kX. A- pristine. B-Discharged.....	75
Figure III. 19: XEDS spectra of A-Pristine MOF. B- Discharged MOF cathode.....	76
Figure III. 20: SEM micrograph of the surface of a Phen-MOF cathode surface, obtained at an accelerating voltage of 3.0 kV and a magnification of 10 kX. A- pristine. B-Discharged.....	77
Figure III. 21: XEDS spectra of A-Pristine Phen-MOF. B- Discharged Phen-MOF cathode.....	77
Figure III. 22: O ₂ ion current (primary Y-axis) and faradic current (secondary Y-axis) monitored during the voltamperogram at 5 mV s ⁻¹ , in O ₂ -saturated 0.2 M LiClO ₄ DMSO electrolyte. A-Panex 30. B-Basolite. C-MOF. D-Phen-MOF.....	79

Figure III. 23: CO ₂ ion current (primary Y-axis) and faradic current (secondary Y-axis) monitored during the first voltamperogram at 5 mV.s ⁻¹ , in O ₂ -saturated 0.2 M LiClO ₄ DMSO electrolyte. A-Panex 30. B-Basolite. C-MOF. D-Phen-MOF.....	80
Figure III. 24: CO ₂ ion current (primary Y-axis) and faradic current (secondary Y-axis) monitored during the first voltamperogram at 5 mV.s ⁻¹ , in Ar-saturated 0.2 M LiClO ₄ DMSO electrolyte. A-Panex 30. B-Basolite. C-MOF. D-Phen-MOF.....	81
Figure III. 25: CO ₂ ion current (primary Y-axis) and faradic current (secondary Y-axis) monitored during the first voltamperogram at 5 mV.s ⁻¹ , upper reverse potential at 0.7 V vs. Ref, in O ₂ -saturated 0.2 M LiClO ₄ DMSO electrolyte. A-Panex 30. B-Basolite. C-MOF. D-Phen-MOF.....	82
Figure III. 26: Raman spectroscopy, with a laser beam of 514 nm, for a Panex 30 cathode -Pristine (black); -Discharged (red).....	83
Figure III. 27: Raman spectroscopy, with a laser beam of 514 nm, for a Basolite cathode -Pristine (black); -Discharged (red).....	84
Figure III. 28: Raman spectroscopy, with a laser beam of 514 nm, for a MOF cathode -Pristine (black); -Discharged (red).....	84
Figure III. 29: Raman spectroscopy, with a laser beam of 514 nm, for a PhenMOF cathode -Pristine (black); -Discharged (red).....	85
Figure IV. 1: Proposed scheme for the (electrochemical) OER process in the absence of a redox shuttle.....	95
Figure IV. 2: Proposed scheme for the OER process in presence of a soluble redox shuttle to chemically assist the recharge of Li ₂ O ₂	97
Figure IV. 3: Scheme of the potential scale of the ORR/OER processes, comprising a well-chosen redox shuttle.....	98
Figure IV. 4: Cyclic voltamperogram of a glassy-carbon electrode in O ₂ -purged (5.1 grade), 0.2 M LiClO ₄ DMSO electrolyte. Scan rate 5mV.s ⁻¹ . Reference : Ag/AgNO ₃ (2 mM in 0.2 M LiClO ₄ DMSO). Added is a simulated cyclic voltamperogram of a useful redox mediator to assist the recharge of Li ₂ O ₂	98
Figure IV. 5: Scheme of the parasitic reactivity of lithium with dissolved oxygen, in a Li-O ₂ battery with an oxygen-saturated electrolyte.....	100
Figure IV. 6: Undesired mechanism of the reaction between the redox and the negative (lithium) electrode.....	101
Figure IV. 7: Oxidoreduction activity of potassium ferrocyanide in 0.2 M TBAClO ₄ DMSO, 100 mV.s ⁻¹	103
Figure IV. 8: Voltamperogram obtained for a glassy-carbon electrode in an Ar-purged electrolyte composed of 5.5 mM TetraFluoroBenzoquinone in 0.2 M TBAClO ₄ in acetonitrile, at 100 mV.s ⁻¹ . The plot puts into evidence the self-poisoning of the electrode.....	105
Figure IV. 9: Voltamperogram obtained for a glassy-carbon electrode in an O ₂ -purged electrolyte composed of 5.5 mM TetraFluoroBenzoquinone in 0.2 M TBAClO ₄ in acetonitrile, at 100 mV.s ⁻¹	106
Figure IV. 10: Voltamperogram obtained for a glassy-carbon electrode in an O ₂ -purged electrolyte composed of 3 mM TetraChloroBenzoquinone in 0.2 M TBAClO ₄ DMSO, 100 mV.s ⁻¹ . Evidence of Strong Reactivity with ORR product.....	107
Figure IV. 11 : Voltamperogram obtained for a glassy-carbon electrode in an Ar -purged electrolyte composed of 3 mM TetraChloroBenzoquinone in 0.2M TBAClO ₄ DMSO, purged at 100 mV.s ⁻¹ . No self-poisoning is observed.....	108
Figure IV. 12: Voltamperogram obtained for a glassy-carbon electrode in an O ₂ -purged electrolyte with the chromium difluoride ink in 0.2 M TBAClO ₄ DMSO at 100 mV.s ⁻¹	109

Figure IV. 13 : Chemical Structure of Co(II)-Po and Co-Salen.....	111
Figure IV. 14: Voltamperogram obtained for a glassy-carbon electrode in an O ₂ -purged electrolyte of 0.2 M LiClO ₄ DMSO, in presence of either Co(II)-Po (red dashed line) or Co-salen (blue short dashed line), or without additives (plain line) 5 mV.s ⁻¹ , Karl-Fisher titration of water traces below 100 ppm.....	112
Figure IV. 15: Voltamperogram obtained for a glassy-carbon electrode in an O ₂ -purged electrolyte. Regeneration experiment conducted in 0.2 M LiClO ₄ without additives, 5 mV.s ⁻¹ , KF below 100 ppm.....	113
Figure IV. 16: UV-Visible spectra of A-Co(II)-Po and B-Co-salen in the presence/absence of O ₂	114
Figure IV. 17: Voltamperogram obtained for a glassy-carbon electrode in an O ₂ -purged electrolyte. Regeneration experiment conducted in 0.2 M LiClO ₄ containing < 2 mM Co(II)-Po, 5 mV.s ⁻¹ , KF below 100 ppm.....	116
Figure IV. 18: iR-corrected voltamperogram obtained for a glassy-carbon electrode in an Ar-purged electrolyte comprising less than 2 mM of Co(II)-Po in 0.2 M LiClO ₄ in DMSO. The scan rates varies from 5 to 100 mV.s ⁻¹	117
Figure IV. 19: Linear Scan Voltammeteries, in 0.2 M LiClO ₄ DMSO, 0.265 mM Co(II)-Po, at 5 mV.s ⁻¹ . Ar-purged medium. A-From OCV to -1.5 V vs. Ref. B-From OCV to 0.4 V vs. Ref.....	118
Figure IV. 20: Levich plot for A- Reduction of Co(II)-Po to Co(I)-Po . B- Oxidation of Co(II)-Po to Co(III)-Po.....	119
Figure IV. 21: Linear Scan Voltammeteries, in 0.2 M LiClO ₄ DMSO, 0.265 mM Co(II)-Po, at 5 mV.s ⁻¹ Ar (black) and O ₂ (green) purged media. A-From OCV to -1.5 V vs. Ref. B-From OCV to 0.4 V vs. Ref.....	120
Figure IV. 22: Voltamperogram obtained for a glassy-carbon electrode in an O ₂ -purged electrolyte. Regeneration experiment conducted in 0.2 M LiClO ₄ containing 2.8 mM Co-Salen, 5 mV.s ⁻¹ , KF below 100 ppm.....	122
Figure IV. 23: iR-corrected voltamperogram obtained for a glassy-carbon electrode in an Ar-purged electrolyte comprising 3.8 mM of Co-salen, in 0.2 M TBAClO ₄ in DMSO. The scan rates varies from 20 to 200 mV.s ⁻¹	123
Figure IV. 24: iR-corrected voltamperogram obtained for a glassy-carbon electrode in an Ar-purged electrolyte comprising 3.8 mM of Co-salen, in either 0.2 M TBAClO ₄ (Black) or 0.2 M LiTF (Red) in DMSO, 100 mV.s ⁻¹	124
Figure IV. 25: Linear Scan Voltammeteries, 5 mV.s ⁻¹ in 0.2 M LiClO ₄ DMSO, 0.74 mM of Co-Salen, at 5 mV.s ⁻¹ . Ar-purged medium. A-From OCV to -1.5 V vs. Ref. B-From OCV to 0.4 V vs. Ref.....	125
Figure IV. 26: Levich plot for A- Reduction of Co(II)-Salen to Co(I)-Salen . B- Oxidation of Co(II)-Salen to Co(III)-Salen....	125
Figure IV. 27: Linear Scan Voltammeteries, 5 mV.s ⁻¹ in 0.2 M LiClO ₄ DMSO, 0.74 mM Co-Salen, at 5 mV.s ⁻¹ . Ar (black) and O ₂ (green) purged media. A-From OCV to -1.5 V vs. Ref. B-From OCV to 0.4 V (or 0.7 V) vs. Ref.....	127
Figure IV. 28: O ₂ ion current (primary Y-axis) and potential (secondary Y-axis) monitored during the ORR chronoamperometry experiment for A-Without additives. B-With Co(II)-Po. C-With Co-Salen, in 0.2 M LiClO ₄ DMSO.....	129
Figure IV. 29: O ₂ ion current (primary Y-axis) and potential (secondary Y-axis) monitored during the OER regeneration experiment at 5 mV.s ⁻¹ . For A-Without additives. B-With Co(II)-Po. C-With Co-Salen, in 0.2 M LiClO ₄ DMSO. KF below 350 ppm.....	131
Figure IV. 30: Initial voltamperogram of the glassy-carbon electrode in 0.2 M LiClO ₄ DMSO O ₂ -purge, v = 5 mV.s ⁻¹ . Solid line: no additives; red short Dashed line: Co(II)-Po-; dot-dashed line blue line: Co-salen,. KF titrations below 100 ppm.....	133
Figure IV. 31: O ₂ ion current (primary Y-axis) and electrochemical current (secondary Y-axis) monitored during DEMS Linear Scan Voltammeteries experiments 2 mV.s ⁻¹ , in 0.2 M LiClO ₄ DMSO. Electrolyte with Co-salen: 2.1 mM. A- ORR LSV recording from OCV to -1,5V vs. Ref. B-OER LSV from OCV (10 minutes after ORR LSV), to 0.7V vs. Ref. Karl Fisher at the beginning of the experiment: 80 ppm; at the end: 300 ppm.....	135
Figure IV. 32: CO ₂ ion current (primary Y-axis) and electrochemical current (secondary Y-axis) monitored during DEMS Linear Scan Voltammeteries experiments, 2 mV.s ⁻¹ in 0.2 M LiClO ₄ DMSO. Electrolyte with Co-salen: 2.1 mM. A- ORR LSV recording from OCV to -1.5 V vs. Ref. B-OER LSV from OCV (10 minutes after ORR LSV), to 0.7 V vs. Ref. Karl Fisher at the beginning of the experiment: 80 ppm; at the end: 300 ppm.....	137
Figure V. 1 : ALD cycle scheme for two precursors for a oxide formation recipe, reproduced from[2], with permission from Les techniques de l'Ingénieur.....	146
Figure V. 2 : Determination of the ALD window: Dependence of the GPC on the Temperature.....	147

<i>Figure V. 3 : Ligands available for metallic cation precursors, reproduced from, with permission from [7] Les techniques de l'Ingénieur.....</i>	148
<i>Figure V. 4 : Impact of the pulse time and Purge time of the Reactants on the Growth rate of an ALD deposit, reproduced from [7], with permission from Les Techniques de l'Ingénieur.....</i>	149
<i>Figure V. 5 : Chemical structure of the Niobium Precursor (TBTDEN).....</i>	150
<i>Figure V. 6 : SEM pictures taken with a tension of 3kV, at either a magnification of 20.00 kX (A,C,E) or 50.00 kX (B,D,F). Images of pristine Silicon (A & B), PEALD at 225°C and 2000 cycles (C &D), ALD thermal at 375 °C, 5000 cycles.....</i>	151
<i>Figure V. 7 : SEM Thicknesses determination, Tension 3kV, magnification 100.00 kX. PEALD at 225°C, 2000 cycles, picture without cursors (A), with (C). Thermal ALD at 375 °C, 5000 cycles, Picture without cursors (B), With (D).....</i>	153
<i>Figure V. 8 : ALD window determination for the PEALD (black) and the thermal ALD (red).....</i>	155
<i>Figure V. 9 : X-EDS of the samples for the PEALD recipe, conducted at 8, 00 kV.....</i>	156
<i>Figure V. 10 : X-EDS of the samples for the thermal ALD recipe, conducted at 8,00 kV.....</i>	157
<i>Figure V. 11 : XRD pattern of Thermal ALD recipe and PEALD, measured by ϑ, 2ϑ, with a K alpha 1 copper X-Ray source.....</i>	158
<i>Figure V. 12: XPS surface analysis of PEALD sample at 200°C, 5000 cycles. -A-Survey-B- C 1S -C- Nb3d5/2 and 3d3/2 -D- O1S -E- N1S.....</i>	159
<i>Figure V. 13 : XPS surface analysis of Thermal ALD sample at 400°C, 5000 cycles. -A-Survey-B- C 1S -C- Nb3d5/2 and 3d3/2 -D- O1S -E- N1S.....</i>	161
<i>Figure V. 14 : XPS surface analysis of Thermal ALD sample at 375°C, 5000 cycles. -A-Survey-B- C 1S -C- Nb3d5/2 and 3d3/2 -D- O1S -E- N1S.....</i>	163
<i>Figure V. 15 : Full XPS spectra for different erosions times. A-30 minutes. B-60 minutes. C-90 minutes and D-120 minutes.....</i>	164
<i>Figure V. 16 : C 1S contributions for different erosion times. A-30 minutes, B-60 minutes. C-90 minutes. D-120 minutes.....</i>	165
<i>Figure V. 17 : Nb 3d^{5/2} and Nb3d^{3/2} contributions for different erosion times. A-30 minutes, B-60 minutes. C-90 minutes. D-120 minutes.....</i>	166
<i>Figure V. 18 : O 1S contributions for different erosion times. A-30 minutes, B-60 minutes. C-90 minutes. D-120 minutes.....</i>	167
<i>Figure V. 19 : N 1S contributions for different erosion times. A-30 minutes, B-60 minutes. C-90 minutes. D-120 minutes.....</i>	168
<i>Figure V. 20 : Possible composition of the deposit, conducted by thermal ALD. The first compound written is the one in majority.....</i>	169
<i>Figure V. 21 : SEM images of the top of the wells, using back scattered electron detector, for a better appreciation of the deposit. Energy of the beam : 3kV, magnification 20.00 kX. A-PEALD recipe. B-Thermal ALD recipe.....</i>	170
<i>Figure V. 22 : SEM images of the bottom of the wells, using back scattered electron detector, for a better appreciation of the deposit. Energy of the beam : 3kV, magnification 20.00 kX. A-PEALD recipe. B-Thermal ALD recipe.....</i>	171
<i>Figure V. 23 : X-EDS spectra of the deposits, realized on Panex 30 carbon cloth, taken at 8,00 kV.....</i>	172

Figure V. 24 : XPS full spectra for A-1500. B-2000. C-2500 and D- 1500-Extended.....	173
Figure V. 25 : C1S peaks for A-1500. B-2000. C-2500. D-1500-Extended.....	174
Figure V. 26 : Nb 3d ^{5/2} and Nb 3d ^{3/2} peaks for A-1500. B-2000. C-2500. D-1500-Extended.....	175
Figure V. 27 : O 1S peaks for A-1500. B-2000. C-2500. D-1500-Extended.....	176
Figure V. 28 : Cyclic voltammetry, recorded in 0.2M LiClO ₄ DMSO, Ar purged, at 2 mV s ⁻¹ . Black line : Pristine Panex 30, Red line : 1500 cycles and green line : 2000 cycles.....	179
Figure V. 29 : Cyclic voltammetry, recorded in 0.2M LiClO ₄ DMSO, O ₂ saturated, at 2 mV s ⁻¹ . Black line : Pristine Panex 30, Red line : 1500 cycles and green line : 2000 cycles.....	180
Figure V. 30 : Full cell performances comparison between pristine Panex 30 and Electrode 4 of each batch.....	181
Figure V. 31 : SEM images of Electrodes 2 of each batch, recorded with 3 kV energy and a magnification of 500X, using ESB detector. A-1500. B-2000. C-2500. D-1500-Extended.....	182
Figure V. 32 : SEM image of a post-mortem Panex 30 Electrode, taken with an energy of 3.0k kV and a magnification of 5.00kX, Secondary Electrons detector.....	183
Figure V. 33 : SEM image of post-mortem Electrode 4-1500, taken with an energy of 3.0k kV and a magnification of 5.00kX. A- Secondary Electrons detector.B- Back Scattered Electrons detector.....	183
Figure V. 34 : SEM image of post-mortem Electrode 4-2000, taken with an energy of 3.0k kV and a magnification of 5.00kX. A- Secondary Electrons detector.B- Back Scattered Electrons detector.....	183
Figure V. 35 : SEM image of post-mortem Electrode 4-2500, taken with an energy of 3.0k kV and a magnification of 5.00kX. A- Secondary Electrons detector.B- Back Scattered Electrons detector.....	184
Figure V. 36 : SEM image of post-mortem Electrode 4-1500-Extended, taken with an energy of 3.0k kV and a magnification of 5.00kX. A- Secondary Electrons detector.B- Back Scattered Electrons detector.....	184
Figure V. 37 : X-EDS spectra of the post-mortem Electrodes 4. Black.-1500. Red-2000. Green-2500. Blue-1500-Extended, taken at 8,00 kV.....	185
Figure V. 38 : Y-primary axis : O ₂ ion current (A). Y-Secondary axis : Electrochemical current (mA).Electrolyte 0.2M LiClO ₄ DMSO, Ar purge. Scan rate 2mV s ⁻¹ , for pristine Panex 30 (A and B). Electrode 4 1500 cycles (C and D). Electrode 4 2000 cycles (E and F).....	186
Figure V. 39 : Y-primary axis : CO ₂ ion current (A). Y-Secondary axis : Electrochemical current (mA).Electrolyte 0.2M LiClO ₄ DMSO, Ar purge. Scan rate 2mV s ⁻¹ , for pristine Panex 30 (A and B). Electrode 4 1500 cycles (C and D). Electrode 4 2000 cycles (E and F).....	187
Figure V. 40 : Y-primary axis : O ₂ ion current (A). Y-Secondary axis : Electrochemical current (mA).Electrolyte 0.2M LiClO ₄ DMSO, O ₂ purge. Scan rate 2mV s ⁻¹ , for pristine Panex 30 (A and B). Electrode 4 1500 cycles (C and D). Electrode 4 2000 cycles (E and F).....	188
Figure V. 41 : Y-primary axis : CO ₂ ion current (A). Y-Secondary axis : Electrochemical current (mA).Electrolyte 0.2M LiClO ₄ DMSO, O ₂ purge. Scan rate 2mV s ⁻¹ , for pristine Panex 30 (A and B). Electrode 4 1500 cycles (C and D). Electrode 4 2000 cycles (E and F).....	189
Figure VI. 1: SEM image of the deposit, taken at an energy of 3.00 kV, using a back-scattered electron detector and a magnification of 5.00 kX (A) and 20.00 KX (B).....	199
Figure VI. 2: XPS characterization of the V ₂ O ₅ deposit. (A) global spectrum, and contributions of (B) C1s, (C) O1s and V2p, (D) O1s and (E) N1s.....	201
Figure VI. 3: Electrochemical behavior of the V ₂ O ₅ deposit, scan rate 5 mV s ⁻¹ . in Ar-purged (black), O ₂ -purged (red), and O ₂ -purged + Co salen (green) electrolyte.....	202
Figure VI. 4: O ₂ DEMS signal for A, C and E; CO ₂ DEMS signal for B,D and F. Primary Y-Axis: Ion current. Secondary Y-Axis: electrochemical current. Ar-purged (A &B). O ₂ -purged (C&D). O ₂ -purged + 1.75 mM Co salen (E&F). Scan rate 5 mV s ⁻¹	204

<i>Figure VI. 5: Scheme of self-discharge in a Li-O₂ system, without the use of a solution to prevent the crossing of the mediator to the negative side and its reaction with metallic lithium.....</i>	<i>206</i>
<i>Figure VI. 6: Scheme of self-discharge in a Li-O₂ system, with the pre-forming of an SEI to prevent the decomposition of the Mediator to the negative side.....</i>	<i>207</i>
<i>Figure VI. 7: Ideal case for a Li-O₂ full cell, where the self-discharge is suppressed thanks to a fully optimized, pre-formed Solid Electrolyte Interface.....</i>	<i>207</i>
<i>Figure VI. 8: Pictures of the samples right after their preparation. Left side: metallic lithium and DMSO. Right-Side: metallic lithium and EC:PC blend.....</i>	<i>209</i>
<i>Figure VI. 9: Pictures of the samples after four day of SEI formation. Left side: metallic lithium and DMSO. Right-Side: metallic lithium and EC:PC blend.....</i>	<i>209</i>
<i>Figure VI. 10: Results of the contact between Lithium and Co-salen electrolyte, after the pre-formation step of the SEI. Top picture: pre-forming with DMSO. Bottom picture: pre-forming with EC:DEC.....</i>	<i>211</i>
<i>Figure VI. 11: Full cell performances, with a pre-formed SEI when Co-salen is (or not) comprised in the electrolyte. Primary Y-axis: Cell voltage. Secondary Y-Axis: Cell current.....</i>	<i>212</i>
<i>Figure VI. 12: CV operated at 2 mV s⁻¹ with drawing of the full cell settings. Black without Co-salen, Red, with Co-salen.....</i>	<i>213</i>
<i>Figure VI. 13: Images of the un-mounted SEI pre-formed + Co-salen cell, in the glovebox.....</i>	<i>215</i>

List of Tables

Table I. 1 : Specific Energy for four metal air systems.....	15
Table I. 2 : Half peak potential of the first reduction process of oxygen in TEAClO ₄ non-aqueous solvents electrolyte. Data extracted from [40, 41].....	26
Table III. 1: BET measurements of the three high surface area materials. * The data for Panex 30 originates from the provider data sheet.....	65
Table III. 2: Vibration modes observed on high surface area carbon supports with Raman spectroscopy, as presented by Castanheira [3], and others [4–7].....	66
Table III. 3: Vibration mode position for the four materials. The average and deviance are calculated on at least three points (the aberrant values are eliminated).....	66
Table III. 4: Area of the vibration modes contribution and crystallite size calculation (equation III.1).....	67
Table III. 5: Markers of the active materials efficiency in Li-O ₂ Full cell design.....	71
Table III. 6: Fitted peak positions of the Raman contributions (D1, G, D2 and D3), for pristine & discharged Li-O ₂ positive electrodes.....	85
Table III. 7: Peak Areas for D1, G, D2 and D3 bands, for the pristine & discharged Li-O ₂ positive electrodes.....	86
Table IV. 1 : ΔE_p dependence on the scan rate for the Oxidation or the Reduction of Co(II)-Po.....	117
Table IV. 2 : Diffusion Coefficient for the Co(II)-Po in DMSO electrolyte.....	119
Table IV. 3: k° calculations, using fit of [10] for the oxidation of Co(II)-Po at several scan rates.....	121
Table IV. 4 : ΔE_p dependency on the scan rate for the oxidation of Co(II)-Salen.....	124
Table IV. 5 : Diffusion Coefficients for the Co-Salen in DMSO electrolyte.....	126
Table IV. 6: k° calculations, using fit of [10] for the oxidation of Co-Salen at several scan rates.....	127
Table V. 1 : Deposits conditions for the ALD window determination.....	152
Table V. 2 : Experiments conducted on Si (400) by PEALD recipe, with either 2000 or 5000 ALD cycles.....	154
Table V. 3 : Experiments conducted on Si (400) by thermal ALD recipe, with 5000 ALD cycles.....	154
Table V. 4 : Summary of the composition analysis of the samples, elaborated on Silicon (400), for both recipes.....	169
Table V. 5 : Depositions conditions for the cathodes, prepared with thermal ALD, at 400°C.....	172
Table V. 6 : Summary of the deposit composition of the electrodes analyzed.....	177

List of Acronyms

Acronyms	Definition
ALD	Atomic Layer Deposition
AN	Acceptor Number
BET	Brunauer, Emmett and Teller Surface Area determination method
CA	Chronoamperometry
CMC	Carboxymethyl cellulose
Co(II)-Po	5,10,15,20-Tetrakis(4-methoxyphenyl)-21H,23H-porphine cobalt(II)
Co-salen	N,N'-Bis(salicylidene)ethylenediaminocobalt(II)
CV	Cyclic Voltammetry
CVD	Chemical Vapor Deposition
DEC	Diethylene Carbonate
DEMS	Differential Electrochemical Mass Spectrometry
DMA	Dimethyl Acetamide
DMF	Dimethyl Formamide
DMSO	Dimethyl Sulfoxide
DN	Donor Dumber
EC	Ethylene Carbonate
NHE	Hydrogen Reference Electrode in Normal Conditions
GCPL	Galvanostatic Cycling with Potential Limitations
GPC	Growth Per Cycle
HSAB	Hard-Soft Acid Base
LCO	Lithium Cobalt Oxide
M	mol/L
MCB	Metal Cation Basicity
mM	millmoles / L
Mtoe	Million ton of Oil Equivalent
NMR	Nuclear Magnetic Resonance
OCV	Open Circuit Potential
OCV	Open Circuit Voltage
OER	Oxygen Evolution Reaction
OPV	Organic Photovoltaic
ORR	Oxygen Reduction Reaction
PC	Propylene Carbonate
PEALD	Plasma-Enhanced Atomic Layer Deposition
PEO	Polyethylene oxide
PEO	Polyethylene
PMMA	Poly (methyl methacrylate)
ppm	parts per millions
PS	Polystyrene
PTFE	Polytetrafluoroethylene
PVDF	Polyvinilidene Fluoride
PVP	Poly Vinyl Pyrrolidone
Ref	Reference

SCE	Saturated Calomel Electrode
SEI	Solid Electrolyte Interface
SEM	Scanning Electron Microscopy
TBA	Tetra-butyl Ammonium
TBTDEN	(tert-butylimido)bis(dimethylamino)Niobium
TEA	Tetra-Ethyl Ammonium
TEAP	Tetra-Ethyl-Ammonium-Phosphate
TEGDME	Tetra Ethylene Glycol Dimethyl Ether
XEDS	X-ray Energy Dispersive Spectroscopy
XPS	X-ray Photoelectron Spectroscopy
XRD	X-Ray Diffraction

Chapter I:

Non aqueous Li-O₂ batteries

Everything is Energy and that's all there is to it. Match the frequency of the reality you want and you cannot help but get that reality. It can be no other way. This is not philosophy. This is physics.

Albert Einstein.

Everything is Energy. This statement cannot be denied, and yet, the irony of our modern society is that we need more and more Energy for our every-day living. From cooking to lightning or transportation, human beings are strongly dependent to Energy. Yet, although there is plenty of energy on earth, we lack of available energy, and this problem is one of the major issues that mankind faces nowadays. In addition, this absolute need of Energy triggers increasing consumption of fossil fuels, charcoal and nuclear Energy, because these are the cheapest and most easily available energy sources. This strategy of course yields increasing pollution of air, water and soils, and will durably affect the Earth's climate. Because sustainable development is the only solution to fulfill both human needs and the preservation of our planet, green energy production must durably and massively come into the play. In this scope, electricity (the so-called white coal), and in particular renewable electricity, seems an appropriate vector; among others, "green" electric engines can be used as a replacement of fossil fuels-powered engines as a practical means to reduce our dependence on fossil fuels, and rapidly grow for both personal and public transportation. At present, nearly all the electric vehicles on the market are powered with batteries (exceptions are scarce, like the fuel cell-powered Toyota Mirai or battery/fuel cell hybrid Kangoo of Renault/Symbio FCell), and, unfortunately, the current Li-ion (and Li-metal) batteries do not have enough energy density and present too much safety issues for such applications. This has driven researchers from all around the world to put a great effort on beyond Li-ion batteries in order to find a technology that will allow users to drive longer distances without being forced to stop for time-consuming battery recharge. For such use, no candidates are as good as non-aqueous Li-oxygen batteries, which can develop up to 5200 Wh.kg⁻¹ [8].

I. Green pathways toward energy Storing

In our modern Society, the Energy demand is in constant evolution, as the growth rate of the population.

In 2015, the world population was estimated at 7.35 billion; it is forecast in a report from the United Nations to be close to 8.50 billion in 2030 [9], and is expected to approach 11 billion of persons in 2100, which raises questions on our energy supplies, as the fossil fuels are supposed to be fully consumed by 2230 [10] (from a report based on the fossil fuels consumption of year 2002, that may not be up-to-date).

In addition, a more concerning point is the (ever-growing) pollution generated by the use of those fossil fuels: in 2014, despite political/industrial efforts and awareness of society, CO₂ emissions were superior to 30 000 Mt [11]. It must be noted, that the overall production mostly accounts from OECD countries (nearly 10 000 Mt per year), and was almost constant from 1971 to 2014, while China and others Asian country (except for those included in OECD) sharply raised their emissions.

Giving such observations, it is clear that, only green energies will fulfill the issues of both the pollution and the energy demand, but viable solutions must be proposed, in order to sustain the living trend of our society.

a. Actual Energy Sources

i. Use in percent

Energy is a central issue in our modern society. Concerns about energy supplies are growing, while in the meantime, fossil fuels reserves dry-up at an increasing rate. As depicted on Figure I.1, the global energy consumption has more than doubled, from 1971 to 2014. Nowadays, energy sources varies from fossil fuels (Oil, Coal and Natural gas, largest part), Biofuels and wastes (second largest part), Nuclear (third largest part), and greener energies such as hydraulic, solar, wind (which account in less than 4% worldwide [11]).

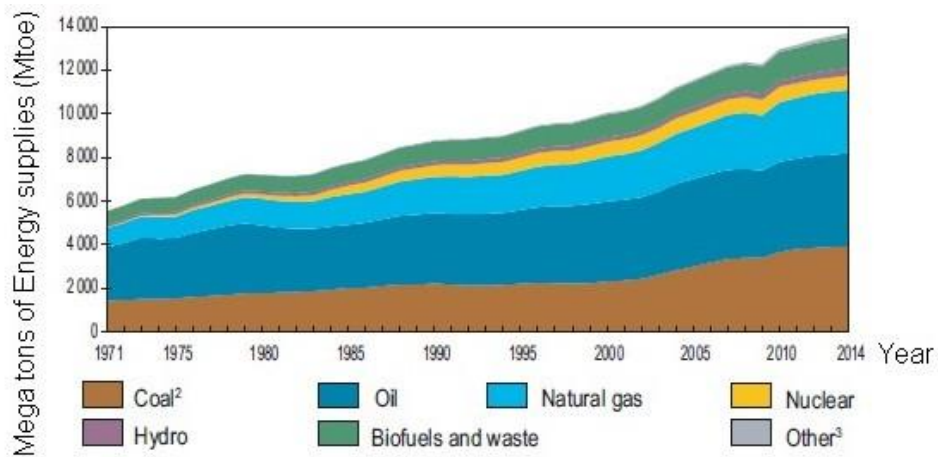


Figure 1. 1: Energy produced from various sources worldwide, presented as published by the International Energy Agency [4], reproduced with their permission.

It can be clearly seen that Fossil fuels account for more than 80% of the overall energy production. As discussed above, in 2002, fossil fuels were supposed to be fully consumed by 2230 [10], but at this time, nearly 8,000 Mtoe of energy was produced from fossil fuels, when nearly 11,110 Mtoe was produced in 2014. Giving data extracted from [10] and [11], 1,596,000 Mtoe of fossil fuels were available on Earth, in 2002.

A simple calculation was made in order to better evaluate the date on which Earth is supposed to run out of fossil fuels (fitting the Mtoe consumption of the past ten years, cumulated from 2002[11] give an equation, in which the available fossil fuels reserves, at the moment of 2002[10] can be introduced). Thanks to these calculations, the “extinction date” of the fossil fuels is supposed to be 2158 (72 years less than the prevision of [10]). If one needs to extend this period, two strategies exist:

- First, to lower the world’s energy consumption; this appears not easily feasible, because emerging countries such as China consume increasing levels of energy (as depicted on Figure 1) to expand and grow, being admitted that in addition, their population grows.
- Second, to rise the contribution of green energies (solar, wind, hydraulic, etc.), but also of nuclear energy (which is mandatory, because unlike most green energies, and like fossil fuels, nuclear power plants are not dependent on the environment (wind, sun), thus enabling to supply power peaks; hydraulic energies are only available for countries with seacoasts, or with large rivers, which narrow their use worldwide).

ii. Incidents and political/ safety issues

As discussed before, usage of fossil fuels not only triggers pollution by their main combustion products (carbon dioxide, nitrous oxides, etc.), but also, major safety, pollution and health issues, because of accidents linked to their exploitation, transportation, storage and transformation. As

presented in its corresponding safety data sheet [12], oil is carcinogen, toxic for reproduction, and heavily toxic for both aquatic and land life. Because of such harmful properties, oil spills always motivate great concerns, and local populations often are defiant to pipelines, constructed near their habitat and cultural places, as illustrated by the recent crisis at Cannonball, North Dakota, USA. In addition, the pollution generated by oil on aquatic life is not only due to spills but also to slow and chronic poisoning of the seas and ocean, from what is called “routine pollution”[13], when oil tankers proceed to the cleaning of the oil tanks, but also from the rejection of oil from the ships engine rooms, and from offshore production sites.

In addition, the acute pollution, generated by large spills (such as the Exxon Valdez in 1989), is responsible for sudden death of the ecosystem in spilled area (300 000 birds died because of the spill). Another major catastrophe can be also cited, as it is the largest one in our decade: the explosion of the Deepwater Horizon Oil rig. Because of both conception and human errors, the oil rig exploded in April, 20th 2010, leading to a spill equivalent de 4.9 million of barrels (780 million of liters). Not only this explosion impacted the ecosystem (eight American national parks were threatened from spill), but also it severely impacted the fishing industry (with a net loss of 2.5 billions of dollars) and the tourism (loss of 3 billion).

But, safety issues not only concern fossil fuels; nuclear power plant are also responsible for catastrophic events, such as Chernobyl, where the official casualties number accounted for the event, was determined in a very broad range from *ca.* 4000 (as published by a report of the UN of 2005) to 100,000 - 400,000 (according to Greenpeace estimates). More recently, the Fukushima catastrophe also triggered safety and health issues, along with the emerging of new anti-nuclear policies around the world (as depicted in France, where the anti-nuclear movements gain importance and supporters). However, the nuclear toll is nowhere close to the fatalities caused by other energy production means. As published in [14], the deadliest energy source (including catastrophes around the world), was the hydroelectric, when in 1975, 30 dams in central china failed in short succession, killing around 230,000 peoples. In addition, as illustrated by Figure 1.2, the second deadliest energy source is not nuclear power, but coal (fossil fuels), because of the death generated by pollution (in the US alone, 13,200 peoples die per year from fine particles emitted by coal power plants). This observation shows how the nuclear impact is over estimated by our society, and how the media truly relates the information concerning the real threat, from each energy sources (because for now, the safest energy power available is, indeed the nuclear, even though mankind still ignores how to handle nuclear wastes in the long-term).

Power risks

©NewScientist

For each unit of electricity produced, nuclear power is nowhere near as deadly as coal. The ranges on each power source indicate estimates from different studies, as collated by the IEA



Figure 1. 2: Power risks, presented as published by the New Scientist[7], reproduced with their permission

Because of the resentment of the population toward nuclear electricity, government policies tend to phase out for nuclear power (as illustrated by Germany, with a zero nuclear objective for 2022), and replacements solutions are both needed for fossil fuels power plants and nuclear energy. This naturally triggers a huge research effort, all around the world.

b. Replacement solutions for the electrical power grid

The urge for green energies for the supply of our power grid is facing new challenges: (i) lowering the cost of these energies, to be as close as possible to the cost of fossil fuels power/nuclear power plants, (ii) and finding ways to store this energy, in order to avoid any dependency of the power grid on the weather (for solar and wind energies for example). A screening of the available technologies is necessary to assess the feasibility and the usability of each available technology.

i. Green energies

Hydropower: This Energy is clean and renewable, and works on a very simple basis, from converting mechanical energy of the flowing water to electricity, by placing turbines on the water path [15]. It is also reversible, (when considering hydroelectricity from dams) thanks to the possibility of pumping back the water into the dam, when the electricity production is above the consumption, thus allowing the water to be passed again through the turbines when the energy demand on the grid rises. Another kind of hydroelectricity production that is not very common, is the wave power plant (as the one situated on the estuary of the Rance, in France, which can produce up to 240 MW of electricity, which

is equivalent to the electric consumption of Rennes, France). However, this kind of hydraulic power plants are still in their infancy, because the waves movements is not yet fully understood, thus this technology is not optimized.

The main disadvantages of such power plants are: the initial cost of the facility (much higher for coal power plants, for the same power yield), dependence on precipitations, changes in stream regimens (huge impact on wildlife), flooding, etc..

Still these technologies are among the cleanest ways, with the weakest impact on the environment, but suffer from a huge drawback: these power plants can only be installed on coasts (for wave power grids), or in mountainous areas, with rivers (for conventional dam power hydraulic power plants), which restrain their establishment in most countries, where coasts, rivers and mountains are rare (or nonexistent).

Solar power: Harvesting the power of the sun has become one of the greatest objective of the century. However, before the recent advances, with the finding of Organic Photovoltaic (OPV), this way of producing energy was not interesting, because, the production of solar panels was far more expensive than burning fossil fuels [15]. Also, the cost of OPV power plants is supposed to be matching those of conventional energy power plants by 2020, thanks to the research effort by the scientific community (the cost of thermal solar power plants is also supposed to match this trend [16]). As for now, two main problems remain for photovoltaic power plants: first their initial cost, which triggers a huge cost for its energy production: 0.2 \$/KWh in 2007 (When fossil fuels power plants cost around 0.7 \$/KWh) [16], second : the dependability of the electricity production on the weather (clouds or dust stop most of the suns radiations), but also on the time (no sun radiation during night time).

Wind Power: the generation of Electricity from the power of wind is pretty simple and is similar to the principle of hydraulic electricity production: the wind flow is converted into mechanical energy through a turbine, which produces electricity. However, unlike hydraulic systems and like the solar power, the electricity produced by wind power plants is weather-dependent (on whether there is wind or not), but also raises a lot problems, concerning the visual pollution triggered from such installations, their location (near forests, protected areas), and interference with nature (especially with birds; they interfere with their migration), and with signals such as radio and TV.

Geothermal Power: The principle of geothermal energy is based on the temperature gradient induced from the surface to a point under the surface [15] (usually 2000 meters underground), where the temperature is greater than at the surface. This gradient can be used directly (household heating), or in association with turbines: cold water is pumped under the surface, gets warmer (eventually evaporate), and returns at the surface with more energy, which can be converted, thanks to turbines, into electricity. For example, in Chevilly-Larue (France), a geothermal plant allows the heating and the supply of hot water of 21,000 households. The drawbacks of this way of producing energy is linked with the rarity of the available sites (geothermal energy can be found along plate boundaries), but also to issues concerning corrosion of the tubes deep under the surface, and can sometimes pull hazardous compounds trapped deep under the surface (hydrogen sulfide, mercury, ammonia, arsenic).

Biomass:

Biomass energy refers to the use of natural sources such as wood, food crops, but also residues from other industries such as agriculture and forestry residues, oil rich algae, municipal and industrial wastes.

According to Javid Mohtasham [15], biomass feed for power generation are paper mill residues, lumber mill scrap and municipal waste. But the biomass can also generate fuels, as corn grain (for ethanol production), and soybeans (for biodiesel). However, like the fossil fuels, most biomass generates carbon dioxide when consumed, and some also generate others greenhouse gases. Also, a major drawback that have risen lately is the competition between food crops and energy crops, which triggered a loss in food production. In conclusion, it is preferable to use biomass for both power and biofuel production, instead of fossil fuels, but the biomass cannot be used as the unique green energy sources, as it will eventually lead to major issues (such as population starving); it must therefore be considered in association with the others green energies sources, and used wisely, in order to complete a sustainable transition from fossil fuels.

ii. Solution for large scale energy storing

As discussed above, the versatility of the electricity production via green energies (PV, wind, etc.) suffers a huge drawback: storage systems must be used in order to store electricity. When the weather allows it (strong winds for wind energy, high sunshine for PV), these technologies must be used for production and store the produced energy and during peak consumption (or when the conditions for electricity productions are not fulfilled: nighttime for PV, lack of wind for solar). In this perspective, some solutions are already available in order to chemically store electricity and some examples will be presented below.

- Low Temperature electrolysis: As presented by Badwal et al. [17], water bounds can be split and both hydrogen and oxygen can be produced at temperatures below 100°C. The oxygen production is not relevant as oxygen is present in wide proportion in ambient atmosphere, but the advantage of producing hydrogen from water is the formation of ultra-pure hydrogen (a purity that is often required for current fuel cell systems) at the end of the electrolysis. Others advantages can also be cited: on site production, and low operating temperature (even at room temperatures). Strong drawbacks exist however, such as poor efficiency (50-55%, [17]: 4.26 Wh of energy are required to produce 2.94 Wh of hydrogen), and high costs of the electrolyzer (as for now, their catalysts comprise expensive platinum group metal (PGM) materials).

- High Temperature electrolysis: this time, the operating temperature ranges from 700°C to 800°C. the advantages of such technique is to gain in yield compared to low-temperature water electrolysis (4.03 Wh of energy are required to produce 2.94 Wh of hydrogen). Even though this gain can appear small, on a large scale, this could be the discriminating factor between LT and HT electrolysis. However, as pointed out by Badwal et al, this technology suffers from strong drawbacks: high temperature management, high investment and operating costs, poor lifetime and durability issues. It must be noted that for both LT and HT techniques, a huge issue is yet to be solved: the finding of a proper hydrogen storage technology. Hydrogen in both its gas and liquid form have a very low viscosity and an extremely high diffusivity [18], rendering leakages very hard to prevent, even on “leak-tight” systems, tested on nitrogen, and on leak-free systems (as hydrogen diffuses faster than any gases through materials); this increases both its transportation and storage costs, but also raises safety issues when a leak is present (extremely dangerous, as hydrogen is explosive).

- Redox flow batteries: as for fuel cells and electrolyzers, such systems are of great interest, thanks to a virtual unlimited capacity (the capacity is only limited by the tank volume) [19]. RFB systems are reversible: when too much electricity is present on the electrical grid, the battery can be charged; when peaks of consumption occur, the battery can be discharged. Their advantages are numerous: no self-discharge (the two electrolytes are stored in different tanks, and when electricity production is needed, pumps are switched on, both on the anodic and cathodic sides, which allows the discharge of the system), an easy monitoring of the State of Charge (SoC) of the Battery, via the cell potential, deep discharged does not affect the cell morphology nor its performances, and RFB are capable of rapid response, which allows them to follow the peak energy demand. Some drawbacks however exist: low power and energy density (not suitable for mobile applications), and precipitations problems that occur below 15°C and above 35°C, which triggers a

strict monitoring of the temperature. Various technologies exist such as Fe-Cr, VRB system (Vanadium/Vanadium battery: V(V)/V(VI) reaction at the positive; V(III)/V(II) at the negative). This technologies is currently used in various countries and a system of 5 MW (36 GJ) was installed in China, connected to the Woniushi wind power farm on May 23rd, 2013).

- Hybrid Flow Battery: These systems have very similar characteristics to the RFB devices. The only difference is that on one side (usually the negative side), the soluble materials are replaced by a solid, electrochemically active, electrode. Thus, the overall capacity of the battery only relies on the size of the installation. HFB systems have some advantages compared to RFB systems, such as a decreased size for the negative compartment (solid matter allow greater energy density by volume than saturated aqueous electrolytes), but suffers on the other hand of parasitic reactions (commons HFB systems usually comprises Zn at the negative side [17], and it is commonly known that Zn, in aqueous solutions, is not stable and slowly reacts with water, and oxygen traces).
- Li-Sulfur: As presented by Badwal et al. [17], Li-S systems have come of great interest, thanks to their high theoretical energy density: 1672 mAh g⁻¹. In a fully-packaged prototype, Li-S system can operate up to 700 Wh kg⁻¹ which is of high interest concerning energy storage. However, some issues remain such as solubility problems for the end discharge product (Li₂S), and redox shuttle of polysulfides from the positive to the negative side which triggers capacity losses (polysulfide: intermediate discharge products). However, those issues can (in principle) be solved thanks to additives, which put Li-S batteries as the next evolution for lithium-based batteries, with higher specific energy than Li-ion. However, due to the relatively restrained lithium resources worldwide, this technology is not suitable for large scale energy storing, but rather for smaller applications which require high energy densities.
- Metal-air systems provide the highest theoretical energy density (for non-aqueous Li-air : 5200 Wh kg⁻¹ [8], for non-aqueous Na air : 1105 Wh kg⁻¹ [17]); they however face strong challenges and are still in their infancy. For both technologies, the discharge product is an insulant (hard to re-oxidize) and a strong oxidant, which reacts readily with the positive electrode components [17] (carbon support, binder, solvent, salt, etc.). Also, the solvents that are commonly used in non-aqueous Li batteries are highly flammable, which raises a lot of safety issues, and the cyclability of the negative electrode is uncertain (metallic lithium forms dendrites during recharge, which can lead to cell failures by shortcuts). It must be noted that despite the large gap between the specific energy of Li-air and Na-air systems, Na-air are more attractive because sodium can be found in large amount anywhere around the globe, while lithium resources are smaller and located in specific locations (58% of the world resources are in Bolivia, and 27% in China), which might trigger geopolitical

issues. Thus, an extensive amount of research is necessary in order to solve these problems, in order to build a practical system.

c. Toward high energy systems for gasoline replacement in Mobile application

i. Fuel cells

Among Fuel cells, the most interesting technology for electric vehicle are Proton Exchange Fuel Cells. Such systems work with hydrogen at the negative electrode (oxidation of hydrogen) and oxygen at the positive electrode (reduction of oxygen harvested in air). The electrolyte of those systems are polymer resins (usually Nafion® or perfluorinated membranes), and their characteristics are very attractive [20] (low temperature operation, high current densities, tolerant to shocks and vibrations, no emission of NO_x or CO, and only bi-product: water). However, as for now, this technology suffers from a major drawback: a practical systems uses platinum-based catalysts on both the negative and positive electrodes and the MEA (Membrane-Electrode Assembly) represents on itself 80% of the cost of the stack. Moreno et al. [20], stated that, in 2013, the US department of Energy estimated the cost of PEMFC at \$55/KWh, and that in order to be competitive, the end price of PEMFC has to go below \$30/KWh. In order to do so, both the cost of the electrodes, the GDL (Gas Diffusion Layers) and the membrane have to be reduced. On the one hand, in the opinion of the authors, the determinant factor for the GDL and membrane costs is the volume, thus by enlarging their production, costs will be greatly reduced. On the other hand, the cost of the electrode is purely dependent on the cost of the catalyst (platinum). Several approaches are already investigated (non-PGM catalysts, core-shell platinum catalysts, alloying platinum with cheaper metals (palladium, Cobalt, etc.), but this not an easy task. Also, those systems operate on very pure hydrogen (hydrogen from petroleum reformates contains CO, which is one of the strongest poison for the negative electrodes), which also puts a hold on the use of such technologies. Hydrogen storage is also particularly demanding for transportation: one solution is the use of hydrides tanks [21], and especially magnesium hydrides tanks [21, 22]. Yet, this way of storing hydrogen suffers of the reversibility of the system (it is easier to adsorb hydrogen (exothermal) than to desorb it (endothermal), but a tank prototype has been designed lately which has proven a very good efficiency (around 90% [23]) which, makes magnesium hydrides tanks a relevant technology for PEMFC-powered vehicles, even though their mass has to be reduced (their mass-percentage of H₂ stored increased) to meet the needs. High-pressure H₂ storage (700 bar) in composite tanks is another option, but its usage imply severe safety measures in a practical vehicle, as hydrogen is highly explosive. Direct liquid fuel cells could also be an option, but these systems, although they do

not address most issues about fuel storage and transportation compared to H₂ [23, 24], are impeded by the kinetics of oxidation of their fuel.

ii. Lithium-Sulfur

As detailed in b ii., the Li-S battery technologies offer good performances in a fully-packaged system (700 Wh kg⁻¹ vs. 250 Wh kg⁻¹ for Li-ion), which can lead to an increased battery life for Electric Vehicles, thus increasing the available mileage for those vehicles. As detailed by Fotouhi et al. [24], for a Tesla Roadster battery pack, which operates with a LCO (lithium cobalt oxides) positive electrode, the range under normal driving conditions is around 245 miles. Replacing this technology by Li-S batteries stack of the same size, the range could be increased up to 3 times, thus greatly improving the range of electric vehicles. Considering the discharge reactions, the reduction of sulfur (S₈) is very complex and involves at least six [24] intermediates (known as polysulfide). By simplifying the scheme, the reaction at the positive (when fully discharged, no intermediates remaining) is equation (I.1):



At the negative, the reaction that take place is the oxidation of metallic lithium, equation (I.2):



Sulfur itself has a theoretical discharge capacity of 1675 mAh g⁻¹, while lithium can develop a capacity of 3861 mAh g⁻¹[24].

However, equation (I.1) is theoretical, and the main problem of Li-S systems is the redox shuttle formed by sulfur polysulfides species that cross over between the sulfur electrode and the metallic lithium, as depicted in Figure I.3. This phenomenon triggers efficiency losses by short-circuiting the external circuit and discharging directly the polysulfides onto the lithium. However, as explained by Badwal et al [17], existing solutions are already available to limit this phenomenon such as mesoporous silica, which adsorbs both polysulfides and sulfur and prevents major crossing to the lithium side. In addition, the dendrite formation on the lithium side in those systems have also been harnessed, with the use of fluorosulfonyl anions that helps forming a stable SEI.

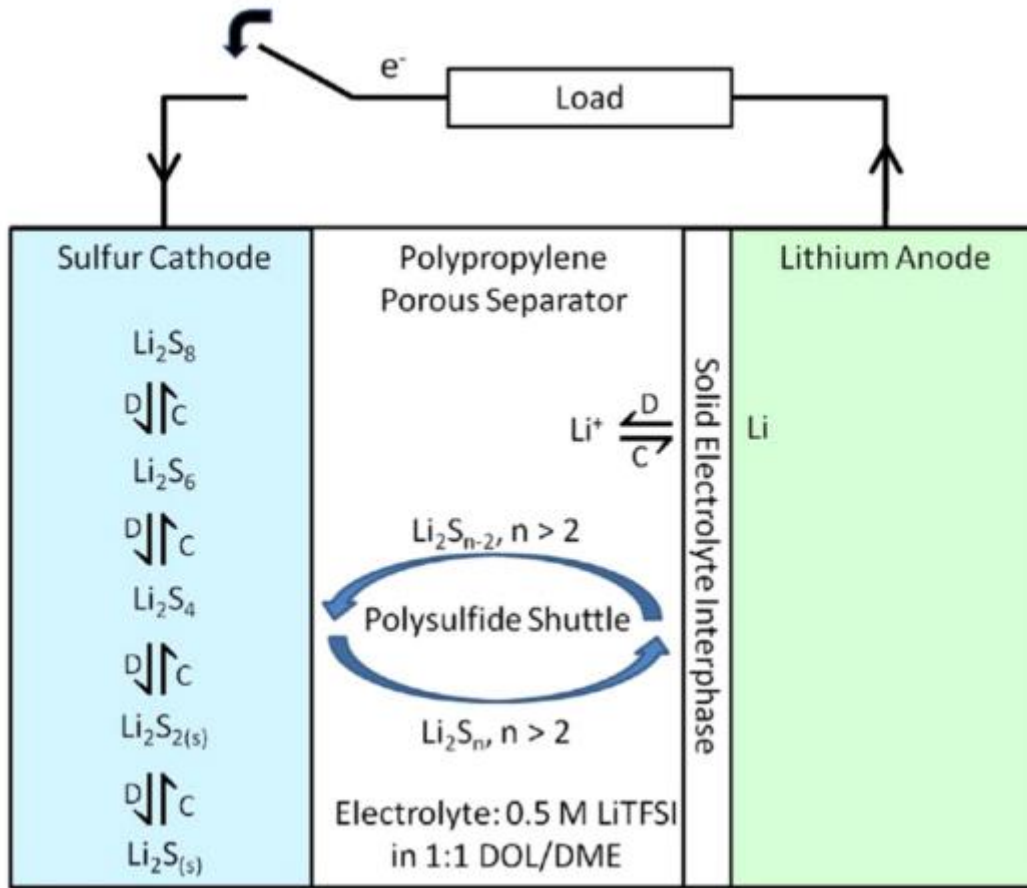


Figure 1.3 : Scheme of the discharge of a Li-S, battery as published in Fotouhi et al paper, reproduced from [17], with permission from the Renewable and Sustainable Energy Reviews

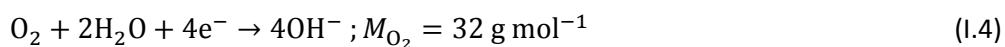
iii. Metal–air systems

The main advantage of metal air systems lies in the high theoretical capacity of oxygen. In order to better understand the potential of the ORR in electrochemical energy storing, the best is to assess two parameters: the capacity, and the specific energy. The capacity (equation 1.3) can be calculated by simple modifications of the Faraday's law and with a dimensional analysis

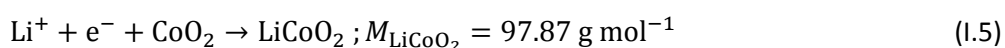
$$\text{Capacity} = \frac{z \times F}{M \times 3.6} [\text{mAh g}^{-1}] \quad (1.3)$$

With z the number of electrons exchanged; M the molar mass of the electroactive specie considered; m the mass of the electroactive specie considered; I the current and t the time

Applied to the oxygen reduction reaction (ORR) in alkaline condition, equation (1.4):



Or the reduction of LCO, amongst the more energetic oxidant for Li-ion batteries, equation (1.5):



The capacity can be estimated, if considering a 4 electrons total reduction (like in water medium), the theoretical capacity in the first case is around 3350 mAh g⁻¹, which largely outnumbers the capacity of Li-ion systems (for comparison, the capacity of Lithium Cobalt Oxide reaches 273 mAh g⁻¹).

Similar calculations can be made for the oxidation of metals (considered in aprotic electrolyte, except for zinc, which operates in alkaline medium), equation (I.6-I.9):



The capacity of these reducers reaches: Lithium: 3861 mAh g⁻¹; Magnesium: 2206 mAh g⁻¹; Aluminum: 2980 mAh g⁻¹; Zinc: 820 mAh g⁻¹. As a comparison, lithiated graphite can reach a capacity of 367 mAh.g⁻¹, which proves the interest for electrochemical systems that comprises metals as the negative. When considering the discharge voltages of those systems, Cheng et al reported the values obtained [25] (Li-O₂ : 3.35 V; Mg-O₂=3.09 V; Al-O₂=2.71 V; Zn-O₂=1.65 V).

By a simple calculation, the Specific energy (equation (I.10)) of those systems can be estimated :

$$\text{Specific Energy} = \frac{m_{\text{electrode}} \times z \times 96500 \times \Delta U_{\text{dis}} \times 1000}{m_{\text{system}} \times M \times 3600} \quad [\text{Wh. kg}^{-1}] \quad (\text{I.10})$$

With m_{system} the mass of the complete electrochemical chain ΔU_{dis} the discharge potential of the electrochemical chain.

Considering the calculation, some hypothesis will be made: first (the strongest one), it is considered that the mass of the positive and the negative electrode will be the same (this choice is usually not the one considered by battery suppliers, for economical, technological and safety reasons). The mass of the separator will be neglected (as usually, separators are ultra-thin polymers), and the mass of the “packaging” of the battery will be arbitrarily taken to 3 times the mass of the electrodes (for safety devices, leads, connections, etc.). Also, the electrodes charge will be considered equilibrated.

Thus, if considering the ORR, and the different hypothesis made:

$$\text{Specific Energy} = \frac{m_{\text{electrode}} \times z \times 96500 \times \Delta U_{\text{dis}} \times 1000}{5 \times m_{\text{electrode}} \times M \times 3600} \quad (\text{I.11})$$

With $z = 4$ and $M = 32$ for the oxygen and taking into account the ΔU_{dis} for each metal-air system:

Table I. 1 : Specific Energy for four metal air systems

Technology	ΔU_{dis} (V)	Specific Energy (Wh kg ⁻¹)
Li-O₂	3.35	2245
Mg-O₂	3.09	2071
Al-O₂	2.71	1816
Zn-O₂	1.65	1106

These very large specific energies highlight the potential of a fully developed metal-air system in contrast with the Li-ion and the lithium sulfur, where the specific energies reached are far below (250 Wh kg⁻¹ for Li-ion, 700 Wh kg⁻¹ for a fully-packaged Li-S system).

However, in contrast with the Li-S (on which most of the main issues have been solved), metal air systems (and especially non-aqueous metal air systems), have major issues, which are still yet to be solved. Among others, one must find active catalysts to enhance both the ORR and the OER [25], manage the reactive and insulating character of the discharge product, find solutions to enhance the recharge, etc. Those aspects will be discussed in the next section, focusing on the non-aqueous Li-O₂ system.

II. The Li-O₂ systems

As demonstrated in the previous part, the potential of Li-O₂ systems is huge for a large panel of applications. As the aim of this thesis is to understand and to solve major issues on the positive electrode (at least to try), some conventions of labeling will be applied: the positive electrode can be denoted “cathode” in the following discussion, as the positive electrode is the cathode for a cell in discharge.

a. Discovery of Li-oxygen batteries

The idea of using the Li/Li⁺ redox with the reduction of oxygen in a practical battery was first presented by Semkow and Sammells in 1987 [1]. At this time, they proposed to use molten salts as the electrolyte. This cell, described in Figure I.4 was operated from 600 to 850°C.

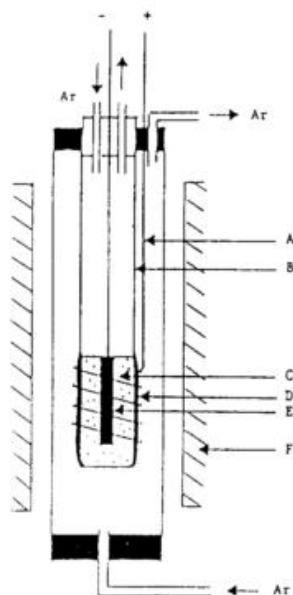


Figure 1.
Schematic drawing of lithium-oxygen secondary cell discussed in this work.
A. current collection from oxygen electrode
B. stabilized zirconia solid electrolyte
C. LiCl-LiF-Li₂O molten salt
D. La_{0.89}Sr_{0.10}MnO₃ oxygen electrode
E. lithium alloy negative electrode
F. furnace

Figure 1. 4 : Design of the Li-O₂ cell, operated by Molten Salts, as published in Semkov and Sammells paper, reproduced from [1], with permission from the Electrochemical Society

From this publication, very good performances were obtained (4,260 Wh kg⁻¹) at large current densities (Figure 1.5).

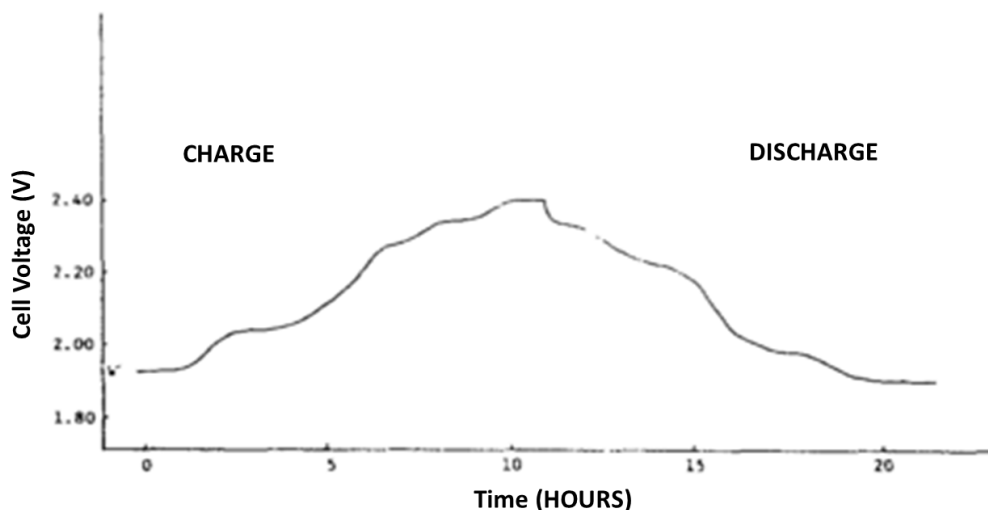


Figure 1. 5 : Galvanostatic cycling of the cell at 20 mA cm⁻², as published in Semkov and Sammells paper, reproduced from [19], with permission from the Electrochemical Society

Yet, the drawbacks of such technology are obvious: it is impeded by the complex handling of molten salts at high temperature (above 250°C for most molten salts), especially in interface with metallic lithium; because of this, their packing and handling rose safety issues.

As such, molten-salts Li-O₂ batteries could not be used as a power source for an Electric Vehicle (EV), but are of great (at least theoretical) interest for large-scale high-energy storage technology on the power grid [26, 27].

No more than 9 years later, Abraham and Jiang reported a Lithium-O₂ battery [8], which comprised a polymer electrolyte (Li/PAN), and could be operated at room temperature with a good remaining capacity after three cycles of charge/discharge. The design of the cell they used in the paper is reported on Figure I.6.

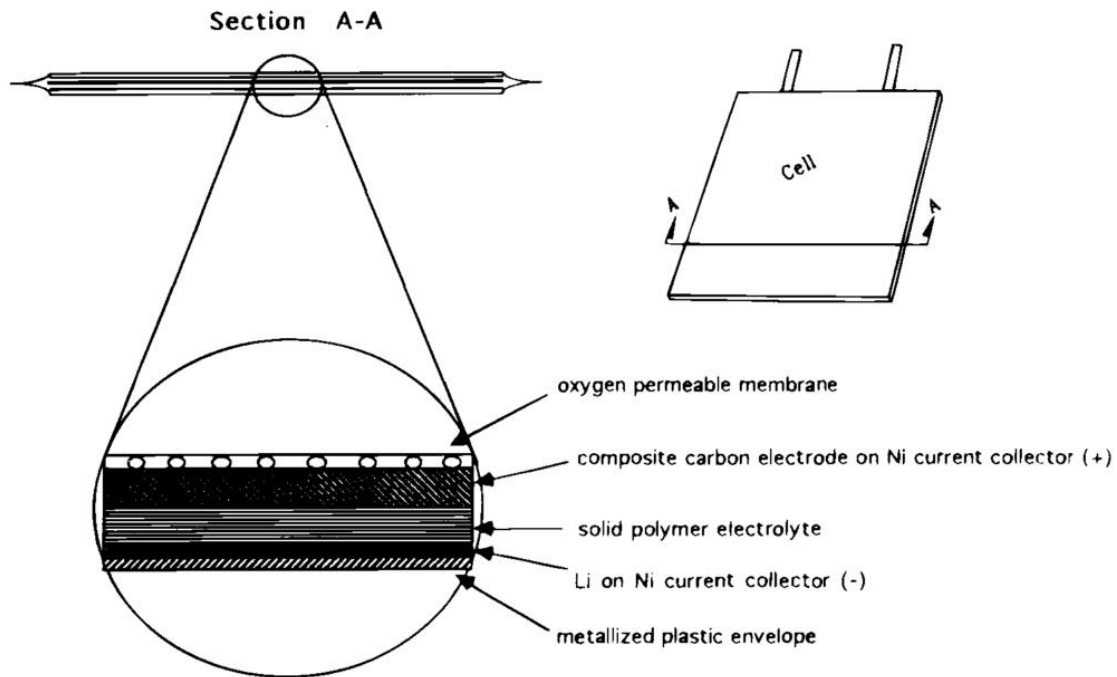


Figure I. 6 : Design of the Li-O₂ cell, presented as published by Abraham and Jiang, reproduced from [1], with permission from the Electrochemical Society

Such cell proved good performances at reasonable discharge current densities, as depicted on Figure I.7, where the carbon composite electrode consisted of chevron acetylene black, and where the oxygen source of the cathode was dry oxygen.

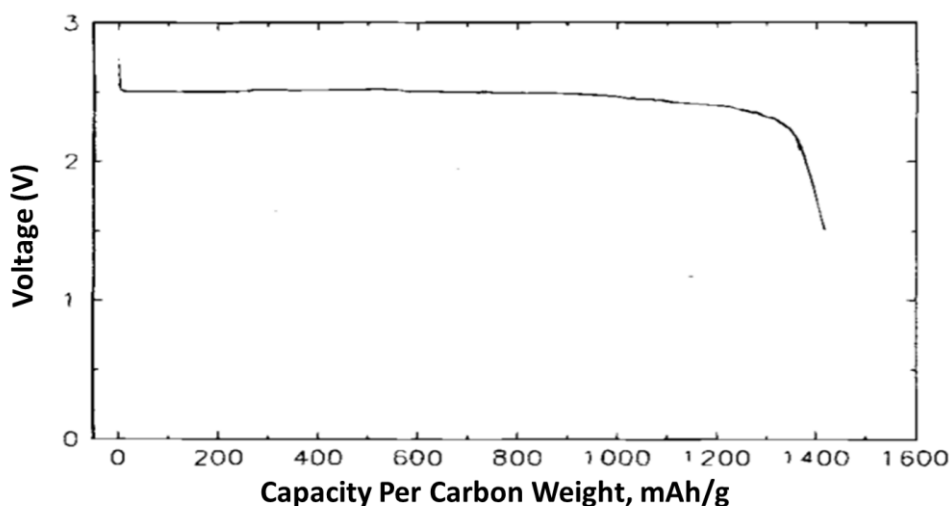


Figure 1. 7 : Discharge curve of the LI/PAN Li-O₂ cell at 0.1 mA cm⁻², presented as published by Abraham and Jiang, reproduced from [1], with permission from the Electrochemical Society

This early study highlighted that not all the carbons were equivalent for use as positive electrodes on such cells: when they changed the cathode material from chevron acetylene black ($S_{\text{BET}} = 40 \text{ m}^2 \text{ g}^{-1}$), to a graphite powder ($S_{\text{BET}} = 5 \text{ m}^2 \text{ g}^{-1}$), the available capacity decreased from 1 460 mAh g⁻¹ to 250 mAh g⁻¹ (Figure 1.8).

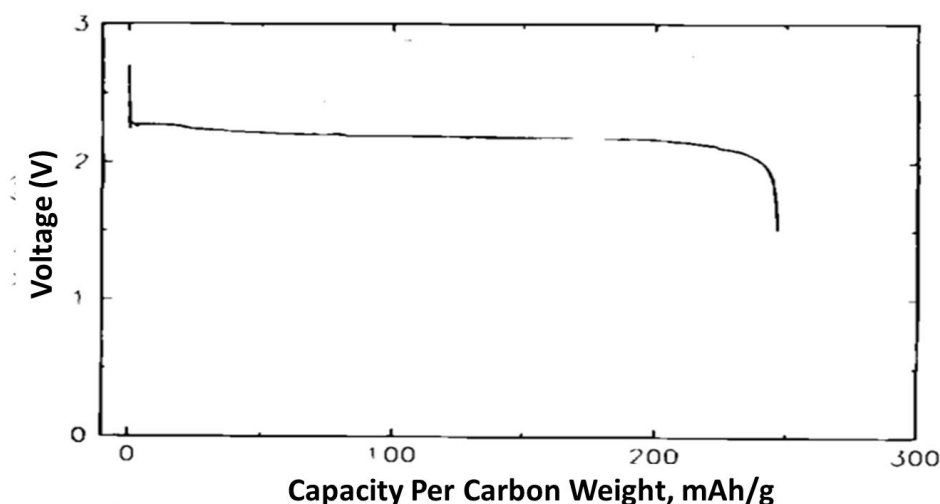


Figure 1. 8: Discharge curve of the LI/PAN Li-O₂ cell at 0.1 mA cm⁻², with a graphite cathode, presented as published by Abraham and Jiang, reproduced from [1], with permission from the Electrochemical Society

Although the authors were hoping that the main discharge product would be Li₂O (which leads to a specific energy of 5,200 Wh kg⁻¹, but this requires the 4-electron oxygen reduction reaction (ORR) to be complete), they discovered, thanks to Raman spectroscopy and a simple procedure with KMnO₄ solution (the discharged cathodes were put in 2.5 mM KMnO₄ solution and if present in contact with Li₂O₂, the purple color disappeared; when Li₂O was put in contact, the solution did not change in color (but it changes with Li₂O₂ samples)), that the main discharge product is Li₂O₂, which lowers the available energy delivered by a practical cell, versus the theoretical calculations, by a factor two. The Raman spectra of the discharge product is depicted on Figure 1.9, the peak at 795 cm⁻¹ being

characteristic of the O-O bonds of peroxide species. Despite this partial deception, this first study demonstrated the great interest of secondary (rechargeable) Li-O₂ systems (depicted in the Ragone diagram of Figure I.10): among advanced batteries, only the Li-O₂ systems can approach the performances of Internal Combustion Engines (ICE) in terms of energy density (and power density – as claimed in [28] – but this claim is yet to be demonstrated in practice). However, these promises are still only theoretical, and practical Li-O₂ systems face a lot of issues especially on the cathode side (it will be discussed in chap I part d), that still need to be overcome.

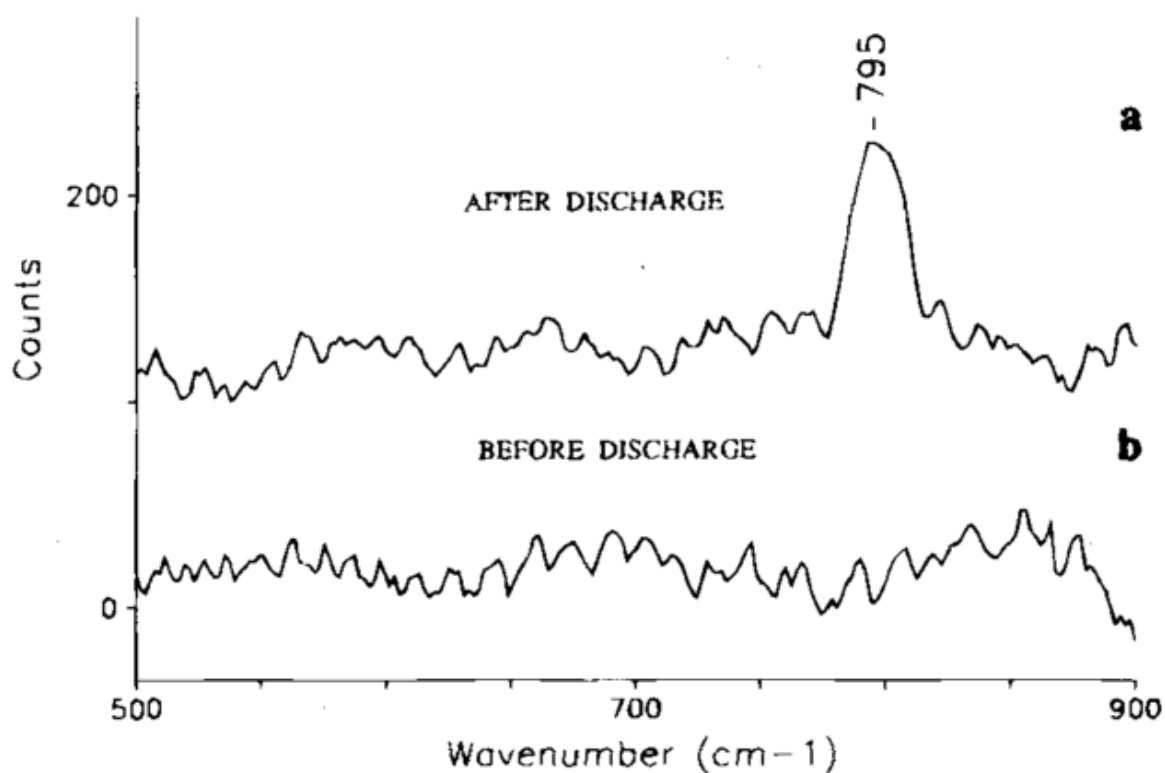


Figure I. 9 : Raman Spectra of a discharge Li-O₂ battery cathode. Presented as published by Abraham and Jiang, reproduced from [1], with permission from the Electrochemical Society

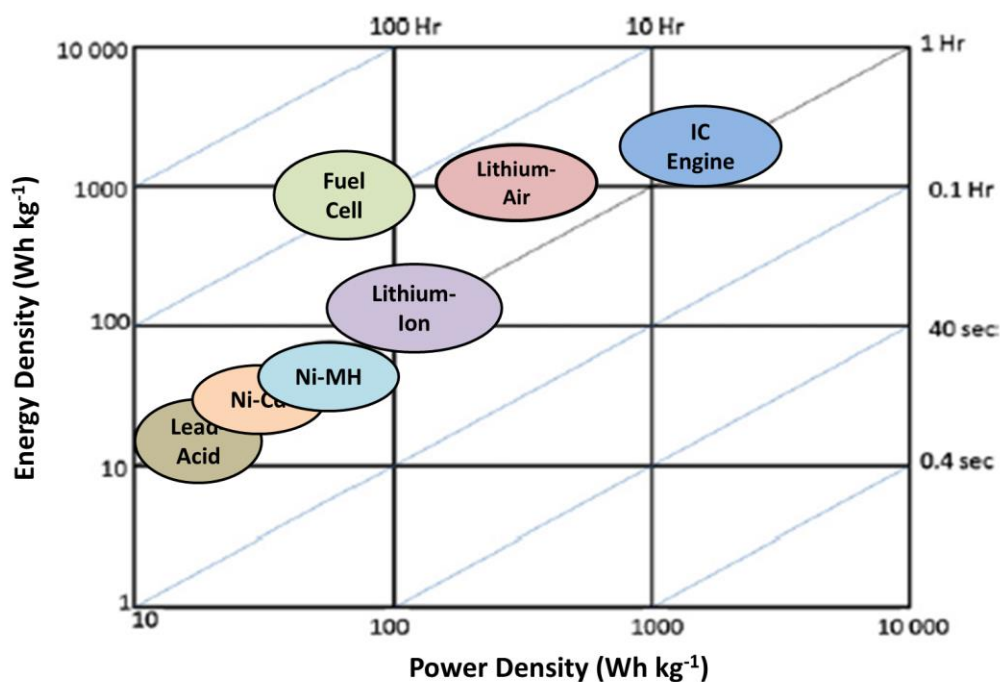


Figure 1. 10: Ragone diagram of some secondary batteries, fuel cells and ICE, presented as published by Padbury et al and Zhang, reproduced from [22], with permission from the Journal of Power Sources

It is clear that, in order to fully optimize the Li-O₂ technology, a full understanding of the mechanisms that occur on the electrodes must be conducted; thanks to the work of Zimmerman [29] and other groups [30–34], this understanding has immensely progressed, at least for the cathode [29].

b. ORR and OER mechanisms in aprotic medium

On the very infancy of the Li-O₂ system, Abraham et al, sensed well that the predominant discharge product was lithium peroxide [8]. However, the investigation of the individual steps of the ORR and OER mechanisms was only conducted in the late 2010s, and emerged with the hard/soft acid/base (HSAB) theory, promoted by Abraham's group.

i. ORR in Li⁺ and TEA⁺ containing electrolytes

The first study of the ORR in aprotic medium lasts from 1966, with a study by Johnson et al [35], where the impact of various cations in TEAP DMSO solution were quantified. Its main result showed that, in absence of alkali metal cation (only TEAP present), two electrochemical waves were observable (with half waves potentials respectively at -1.15 V vs. SCE and -2.5 V vs. SCE).

Along with other papers [36, 37], Johnson et al found that two consecutive one electrons processes were occurring in aprotic media, in presence of TEAP, where the first one (with the half wave potential measured at -1,15 V vs. SCE) was proven to be the reduction of oxygen into superoxide (I.12).

In their paper, Johnson et al attributed the second wave to the formation of peroxides (I.13), because the addition of proton in the media had the same effect than the addition of sodium or potassium cations: the second wave shifted at higher voltages, and the product formed in presence of the proton was characterized to be hydrogen peroxide. Thus, the second reduction was attributed to be the formation of peroxide.



However, in presence of lithium, the second wave disappeared, which was attributed by the authors to an impossibility to electrochemically form lithium peroxide. However, the main product during ORR, in Li^+ containing electrolyte was later characterized by Abraham et al and further confirmed by Laoire et al [30], in dimethyl sulfoxide media, and this product was determined to be lithium peroxide. Thus, as reported in the paper by Laoire et al, lithium peroxide must be produced by a chemical reaction directly from lithium superoxide (a disproportionation reaction), which was proven to be metastable (I.14):



It is thus clear that, in presence of lithium cations, the ORR proceeds via two simultaneous reactions (one electrochemical and one chemical) that occur as follows (I.15 and I.16):



As a consequence, the occurrence of the disproportionation reaction (I.16) hides a two electron-process; it corresponds to surface re-arrangements, as depicted on Figure I.11, and modeled by equations (I.17 and I.18).

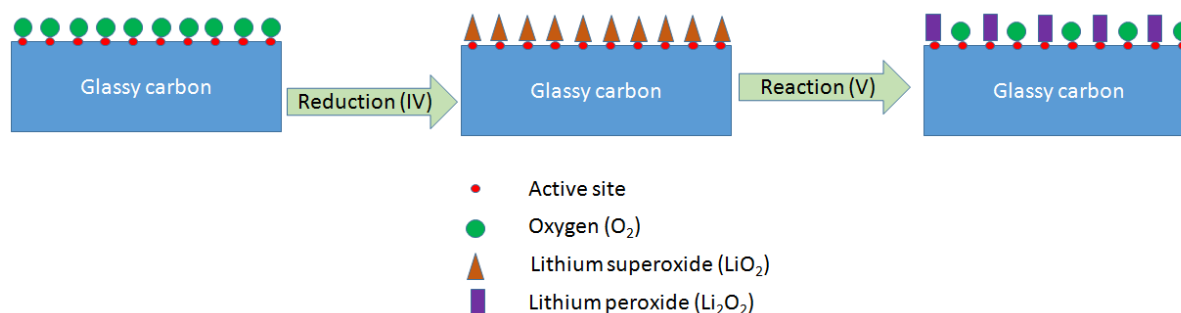


Figure I. 11 : ORR scheme in aprotic medium, in presence of Li^+

If U_n represents the number of active sites occupied by LiO_2 and n , the number of recombination of LiO_2 into Li_2O_2 , the overall electrons exchanged at the n^{th} step of recombination (e_n) is equal to:

$$e_n = 2 \times (U_n) \quad (I.17)$$

$$\text{With : } U_n = \frac{U_{n-1}}{2} + \frac{1}{2} \text{ and } U_0 = \frac{1}{2} \quad (I.18)$$

(at the first recombination, 50% of the overall active sites are unoccupied, while 50% are blocked).

However, various papers also proposed that an electrochemical reduction of the lithium superoxide is possible, forming lithium peroxide (I.19):



No studies have been able to confirm which path (consecutive electrochemical and chemical steps (I.15 and I.16), or two consecutive electrochemical steps (I.15 and I.19)), as for both paths, the overall number of electrons exchanged per O_2 molecule shall be worth two [38] (the oxygen that is re-emitted in reaction (I.16) is believed to be re-adsorbed readily, as it is re-emitted on the electrode). One could think that this re-emitted oxygen could be measured by differential electrochemical mass spectrometry (DEMS), but as two O_2 molecules are consumed by (I.15) for each molecule of lithium peroxide produced, in order to fulfill (I.16), one molecule of O_2 is consumed overall, when combining (I.15) and (I.16), so DEMS can only measure a consumption during ORR. Laoire et al claimed that the mechanisms in a Li^+ containing electrolyte is as follows [30], (Figure I.12):

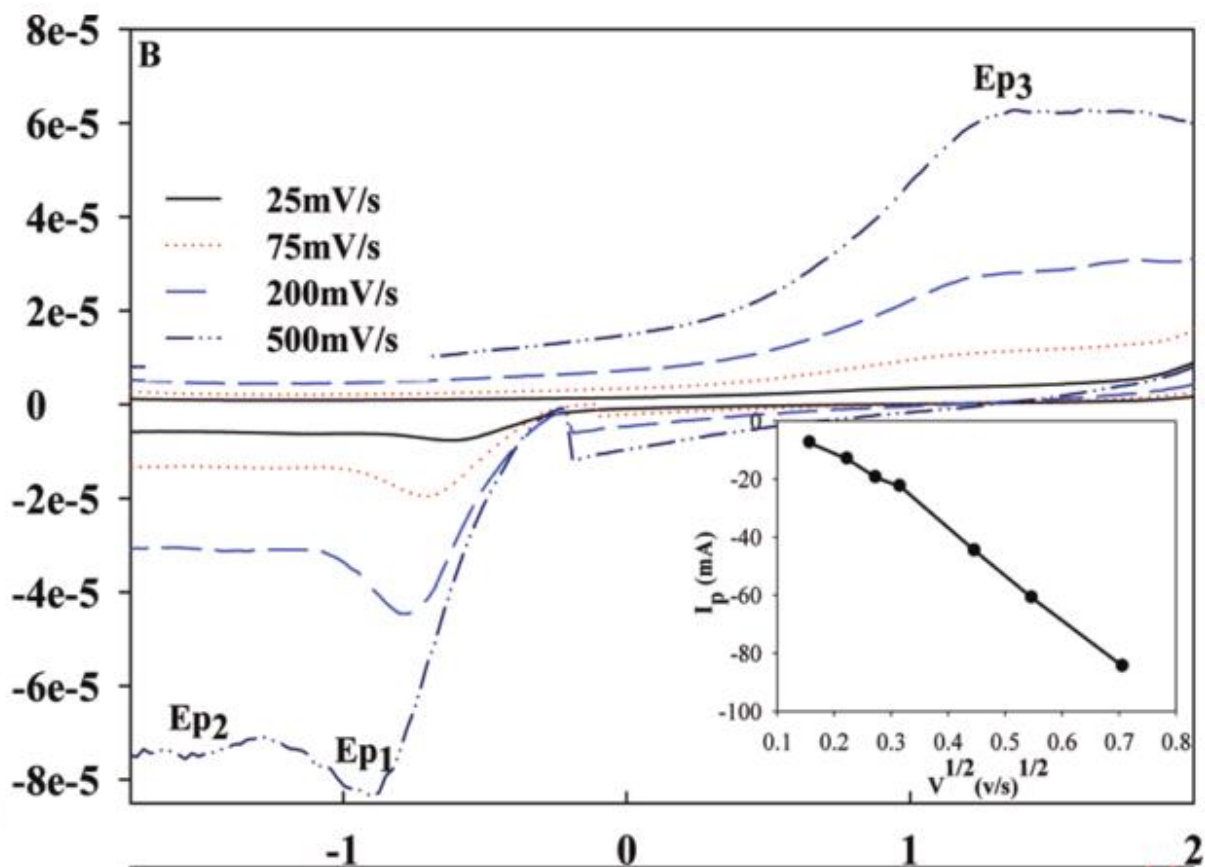
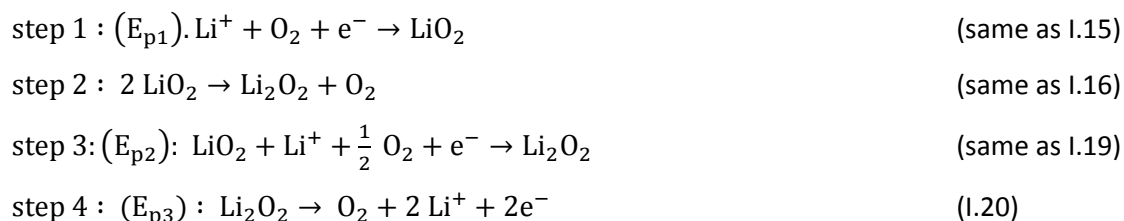


Figure I. 12 : Oxygen purged 0.1 M LiPF6 MeCN on GC at various scan rates, presented as published by Laoire et al , reproduced from [24] with permission from ACS



However, there is no such evidence that reaction (I.15) is really happening at E_{p1} , and in the author's opinion, both E_{p1} and E_{p2} are likely due to the consecutive reactions (I.15) and (I.16), or (I.15) and (I.19). As E_{p2} peak occurs at lower voltages, because larger toroids are formed, E_{p1} cannot be linked to superoxide formation only, as it is a metastable species, which has a very short lifetime (and E_{p1} is observed, even at lower scan rates). So, reaction (I.19), might happen at the same time than reactions (I.15) and (I.16), as their standard potentials are very close [30]. This statement is confirmed with a further publication of Laoire [39], where, in DMSO he changed the reverse potential (Figure I.13):

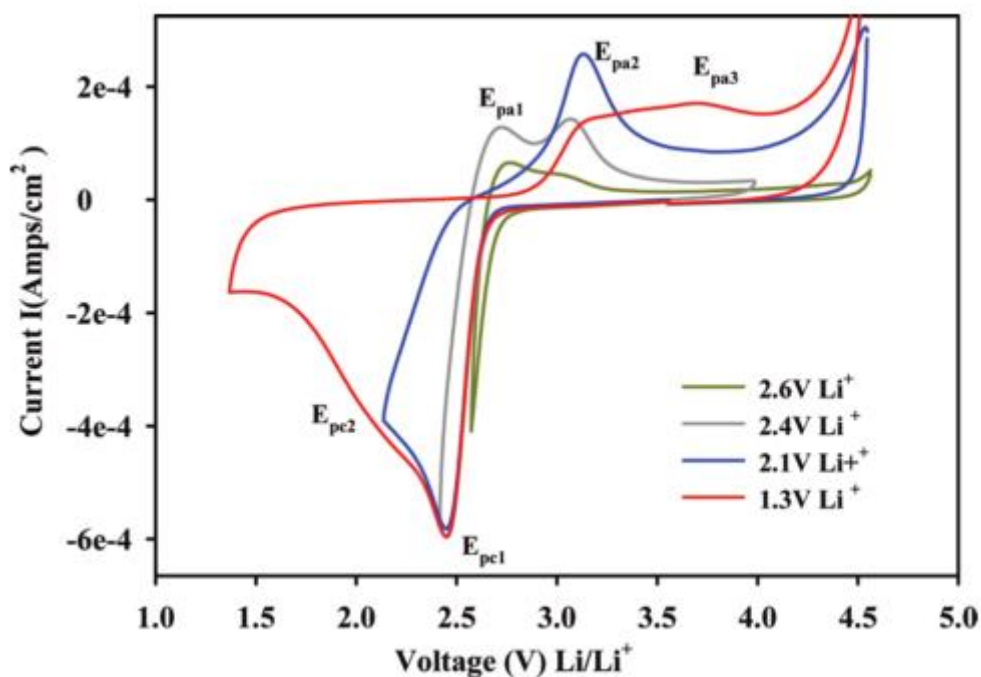


Figure I. 13 : 0.1 M LiPF6 DMSO at room temperature, on GC at 100 mV s⁻¹ with various reverse potentials, presented as published, reproduced from [33], with permission from ACS

In this publication, Laoire al claimed that the following reactions occurred:



However, among all the literature, even at very low potentials, physical characterizations of Li₂O was never produced after discharge of a Li-O₂ battery [38, 40–43], thus confirming that in a practical aprotic Li-O₂ system, the limit of 4 electrons per oxygen will most likely never be reached, and instead the final discharge product will be lithium peroxide. Consequently, Peaks Epc3 and Epa3 must originate from another phenomenon. A possible explanation could be the formation of larger particles (which is consistent, with a deeper rate of discharge), and those particles will be more difficult to re-oxidize, producing the broad peak Epa3.

Also, Laoire et al claimed that reaction (I.19) is occurring at Epc2, but even when the reverse scan occurs at 2.6 V vs. Li⁺/Li (which is just below the onset potential of the ORR), the peak Epa2 is seen in a small extent, thus meaning that lithium peroxide is produced before, either by the combination of

reactions (I.15) and (I.16), or by combination of reactions (I.15) and (I.19). Again, no evidence can discredit either one path or the other one because in the end, the same product (Li_2O_2) is formed, with the same amount of electrons exchanged.

ii. Hard Soft Acid Base (HSAB) theory

In the same publication [39], Laoire et al introduced a possible explanation of the variation of the ORR onset potential with different solvents, linked with the HSAB theory, first emitted by Pearson et al [44]. As explained in their paper, $\text{TEA}^+/\text{TBA}^+$ cations are considered to be Soft Lewis Acids, Li^+ cations are strong Lewis Acids, superoxide (O_2^-) is considered to be a moderate Lewis Base and peroxide (O_2^{2-}) is considered to be a strong Lewis Base. The authors also proposed that, considering the HSAB, peroxide will prefer strong acids (such as Li^+ , Na^+ , K^+) and superoxide will be stabilized by a soft acid (cations such as TEA^+ or TBA^+ for instance). In addition, in their papers, Laoire et al stated that the solvent has a similar effect on the stabilization of species such as superoxide and peroxide, and their respective basicity and/or acidity can be characterized by donor (DN) and acceptors numbers (AN). The DN scale for conventional Li- O_2 solvents is given in their paper as well as the AN scale (with their respective values in the brackets):

$\text{MeCN (14.1)} < \text{TEGDME (16.6)} < \text{DME(20.0)} < \text{DMSO (29.8)}$ (DN)

$\text{DME (10.2)} < \text{TEGDME (10.5)} < \text{MeCN (18.9)} < \text{DMSO (19.3)}$ (AN)

Consequently, the two effect, explained by the HSAB theory are as follows:

- AN number: the higher the AN number, the better the “solvation” of the anion associated with cation (*i.e.*: ClO_4^- ; PF_6^- , etc.), the higher amount of cations “available” to stabilize the superoxide and peroxide species;

- DN number: the higher the DN number, the stronger the Li^+ /solvent interactions, lowering the Li^+ acidity thus stabilizing the Li^+ /superoxide bound, which leads to an increased lifetime of lithium superoxide. Still, even in DMSO, LiO_2 is proven to be a metastable specie, and quickly undergoes chemical decomposition to form lithium peroxide, as presented in their paper, and in various other studies [33, 39, 45].

Also, they state that in DMSO, TBA^+ cations are poorly solvated, and as superoxide is that first specie produced during ORR, and is a moderately soft base, a strong interaction occurs between TBA^+ and O_2^-

, thus “preventing any further reduction to the peroxide form”. However, it has been proven, long time before the interest in metal air batteries, that the second reduction to peroxide is observed, but at much lower potentials (half wave potential for the second reduction around -2.5 V vs. SCE) [35–37].

As a consequence, they explain the chemical disproportionation of lithium superoxide to lithium peroxide by the incompatibility between the lithium cation (hard acid) and the superoxide (moderate base), the former rather transforming into lithium peroxide (association of the hard acid and the hard base), which is consistent with the experimental results, where the main discharge product is lithium peroxide, and lithium superoxide is sometime observed as a metastable specie [30, 33, 39, 42]. As explained in the work of Zimmerman [29], the AN scale correlates well with the half-wave potential of the first oxidoreduction of oxygen (in TBAClO₄), whereas the DN scale is completely uncorrelated with these half peak potential, as shown in Table I.2 and Figure I.14 (in the same electrolyte).

Table I. 2 : Half peak potential of the first reduction process of oxygen in TEAClO₄ non-aqueous solvents electrolyte. Data extracted from [40, 41]

Solvent	Donor Number	E_{1/2} vs SCE (V)
Acetonitrile	14.1	-0.85
DMF	26.6	-0.87
DMA	27.8	-0.9
DMSO	29.8	-0.77
Pyridine	33.1	-0.93

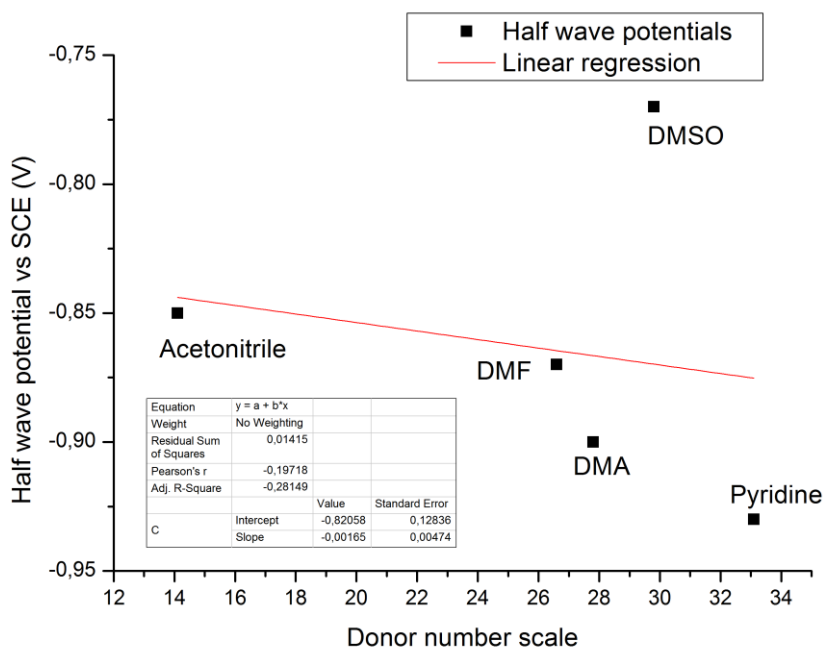


Figure I. 14 : Plot of the half wave potential of ORR (TBACIO4) versus the Donor Number of the solvent. Data used in Table1

However, the HSAB theory states that the higher the acceptor number, the better the stabilization of the superoxide. Also, as explained in the work of Zimmermann[29], the Donor number can play a role in the stabilization of the cation-superoxide pair, as high donor number solvents will lower the acidity of the cation (thus the reactivity of the cation-superoxide specie). For a given redox couple, if the reducer form is stabilized, the potential of the redox couple is supposed to shift to lower potential. The data shows that it is indeed the correct trend, but at least one solvent is the exact contrary (DMSO). Thus, problems are raised for the understanding of the stabilization of ORR products. One possible explanation can be that those two numbers are not determined in the same way.

On the one hand, the AN number is determined by the relative ^{31}P -NMR shift of triethylphosphine oxide shift, which is a strong Lewis base, in each solvent. On the other hand, the DN is based on the measurement of the coordination heat of those solvents (diluted in 1, 2-dichloroethane) with SbCl_5 (which is a hard Lewis Acid). While the AN scale is pretty much accepted by the community of scientists, some discrepancies exist for the DN scale as:

- The heat measured is an enthalpy, not a Gibbs energy (the entropy term of the Gibbs energy induce a non-linearity between those two);
- The measurements are made in diluted solution in 1,2-dichloroethane, so they might not reflect the actual Lewis Basicity of the solvent only but rather the mixture;
- SbCl_5 is a large hard Lewis acid, in contrary to alkali metal cations, so some differences in coordination behaviors between those two might exist.

In conclusion, if one truly wants to measure the basicity of a given solvent, a different number than the DN number must be used. In this perspective, a possible number that could explain well the basicity of the solvent toward alkali metal cation are MCB (Metal-Cation Basicity), which are a gas-phase measurement of the free energy of the pairing between the cation and a solvent. This scale is more relevant for the explanation of the HSAB theory than Donor Number, as here, the true pairing between a solvent molecule and the alkali metal cation is measured [46], and it is not an enthalpy, but a free energy. By computing MCB values [46] and half peak potential values of the ORR in those solvents [47], a drawing can be done (Figure I.15).

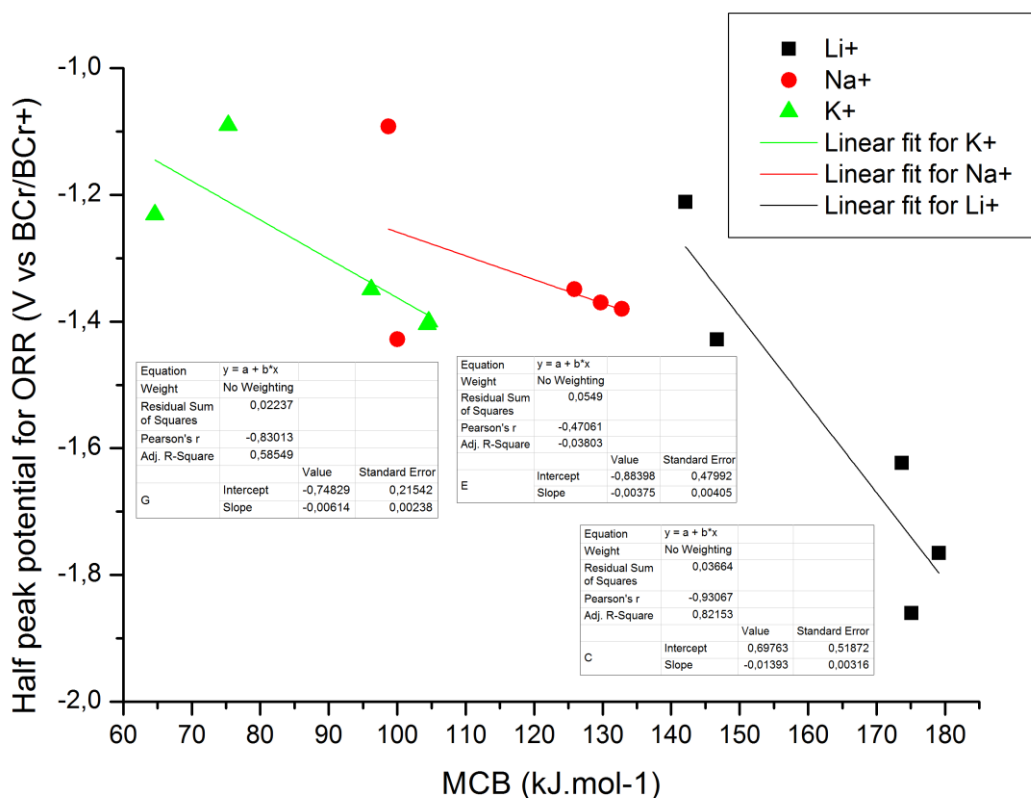


Figure I. 15 : Plot of half peak potential vs. MCB value, with pyridine. Data extracted from [42, 43]

Figure I.15 shows that still, no good correlation exists between the half peak potential of the ORR and the MCB values. However, by looking closer to those values, only one solvent seems responsible for the bad correlation: pyridine. By removing the pyridine contribution from the plot, a better correlation can be observed, for the three metal cations (Figure I.16).

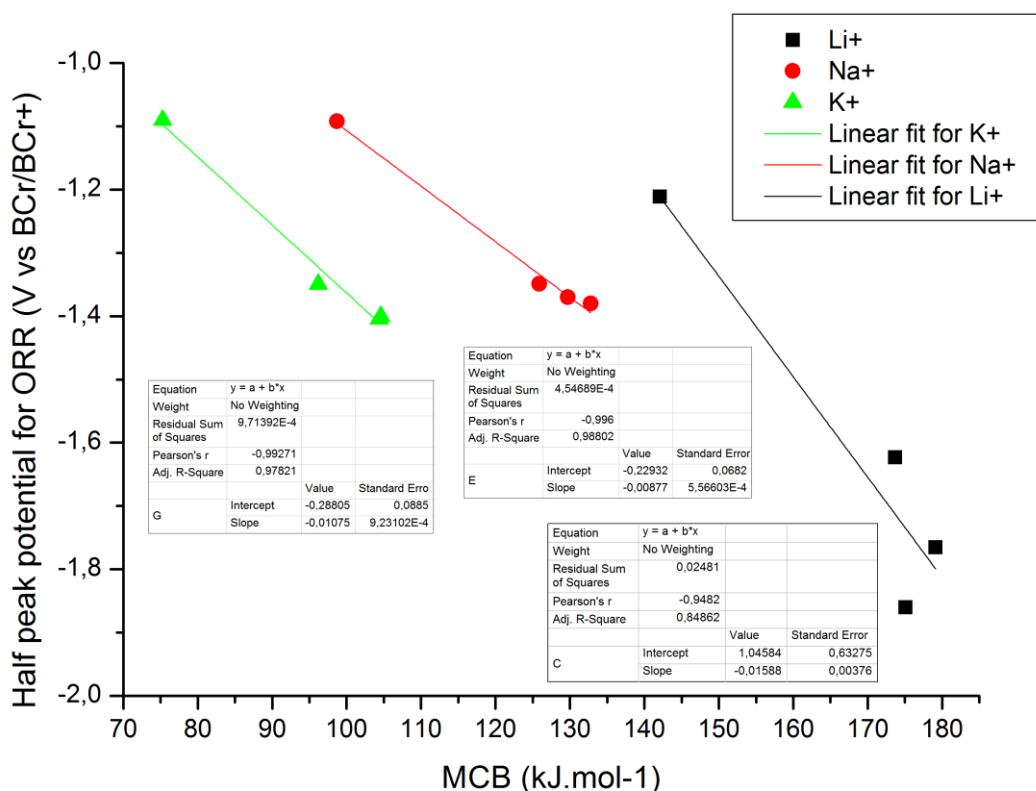


Figure 1. 16: Plot of half peak potential vs. MCB value, without pyridine. Data extracted from [42, 43]

A possible additional effect of pyridine (for example nucleophilic attack of superoxide on the heterocycle), is highlighted, which might affect the basic behavior of pyridine, in presence of superoxide/peroxide species. However, it must be noted that in some extent, every solvent is affected by nucleophilic attack of superoxide/peroxide [48], as those species are highly reactive and trigger strong challenges for the design of a practical system.

c. Effect of water

It is clear that, in a practical Li-O₂ system, water must be removed as much as possible, as it violently reacts with metallic lithium. But in addition, water also has a significant effect on the operation of the positive electrode (cathode). Usually, anhydrous solvents that are sold by chemical suppliers have water contents that range from 50 to 100 ppm. For example, in DMSO, a water content of 100 ppm is equivalent to 1.4 mM, which is in the same order of magnitude of the oxygen content at saturation in the same solvent. So, even in an “anhydrous” solvent, the water can significantly impact the cell behavior. The way in which the water affects the non-aqueous ORR can be compared to the impact of acids on ORR in non-aqueous medium [49]. In presence of an acid (HA), Andrieux et al proposed the following ORR pathway (I.24-26):



In aprotic solvents, water is considered as a weak acid ($\text{p}K_a = 31.24$ in DMSO [50]); so according to the HSAB theory, it should not interact a lot with superoxide and peroxide species. However, it is well known that water has a very strong affinity for anions, thus interactions between water and superoxide may occur, interactions that are not acid/base related, and a complex of the form $\text{O}_2^- \cdots \text{H}_2\text{O}$ is observed (on glassy carbon in acetonitrile [51]) leading to the following ORR pathway (1.27-29):



The subsequent formation of a stabilized, soluble superoxide complex, is allowing the growth of greater particles of Li_2O_2 (toroids), rather than a fully-covering homogeneous layer, which increases the capacity of the system [52, 53] (at least in discharge), but also the yield of the Li_2O_2 . However, the presence of water is not affecting only the solubility of the superoxide, it must also be noted that in water, lithium peroxide is not the stabilized formed, but LiOH is. Even with water amounts as high as 1%, the major discharge product detected on a carbon cloth is still Li_2O_2 [52], but in presence of another substrate such as $\text{Ru}/\text{MnO}_2/\text{SP}$ [54], a mix of $\text{LiOH}/\text{Li}_2\text{O}_2$ is detected on discharged cathodes, with water contents as high as 120 ppm.

In conclusion, traces of water allow an increased lifetime of superoxide species, thus allowing the formation of large Li_2O_2 (or LiOH) crystallites (the greater the water amount, the greater the particles, the greater the discharge capacity [52, 53]). However, it must be noted that water traces also trigger overpotential values during the charge of the battery [53], which is a serious issue for a practical system. In addition, although the stabilized discharge product is LiOH in hydrated electrolyte, it has been proven that still, the main discharge product is Li_2O_2 on conventional “carbon” cathodes [52, 53, 55], thus implying that somehow the formation of lithium hydroxide proceeds with a slow kinetics.

This statement is supported by the fact that in presence of MnO_2 lithium hydroxide is detected by XRD [54], and from a patent, where the reaction of Li_2O_2 with water vapor (which forms lithium hydroxide) was faster with the MnO_2 catalyst than without [56]. The fact that this catalyst has proven some very good performances in $\text{Li}-\text{O}_2$ design [57, 58] might be linked to this phenomenon.

d. Issues of Li-O₂ cathodes and improvement paths

The selected literature presented above demonstrates that, despite the efforts from the research community to build a practical Li-O₂ system, two main issues remain:

The first is the need to find a suitable electrolyte for a Li-O₂ practical system. Actually none are 100% stable toward the Li-O₂ discharge products [33] (lithium superoxide and peroxide). In the same line, the carbon cathode proved to be unstable toward lithium peroxide [32, 33], as it forms readily a monolayer of lithium carbonate, this issue being all-the-more prejudicial at the large potential values encountered during recharge.

The second is that, in a pure anhydrous electrolyte, and at high discharge rate, the deposit is a compact thin layer [52, 59], that will trigger sudden death of the cell, if the deposit thickness becomes greater than the electron tunneling distance. This issue is a big deal for both the automotive and stationary applications, as it triggers a very bad cyclability of the system, good cyclability being a prerequisite to the use of any battery in these applications.

*i. **Li-O₂ cathode components stability toward ORR products***

An electrochemical system, in order to be practically used, needs a stable electrolyte on both side (anode and cathode). For the Li-O₂ system, it is well known that in presence of carbonate solvents, lithium metal is producing a stable and thin Solid Electrolyte Interface (SEI), thus triggering a low irreversible loss on the lithium negative electrode [60, 61].

This stability on the lithium side is probably responsible for the early use of carbonate solvents in Li-O₂ systems [8]. However, in the past decade, carbonate solvents have been characterized to be highly instable toward products of non-aqueous ORR [38, 62–65], which leads to the formation of insoluble lithium alkyl carbonate salts. A possible reaction mechanism of superoxide on a cyclic alkyl carbonate (figure extracted from [65]) is depicted on Figure I.17.

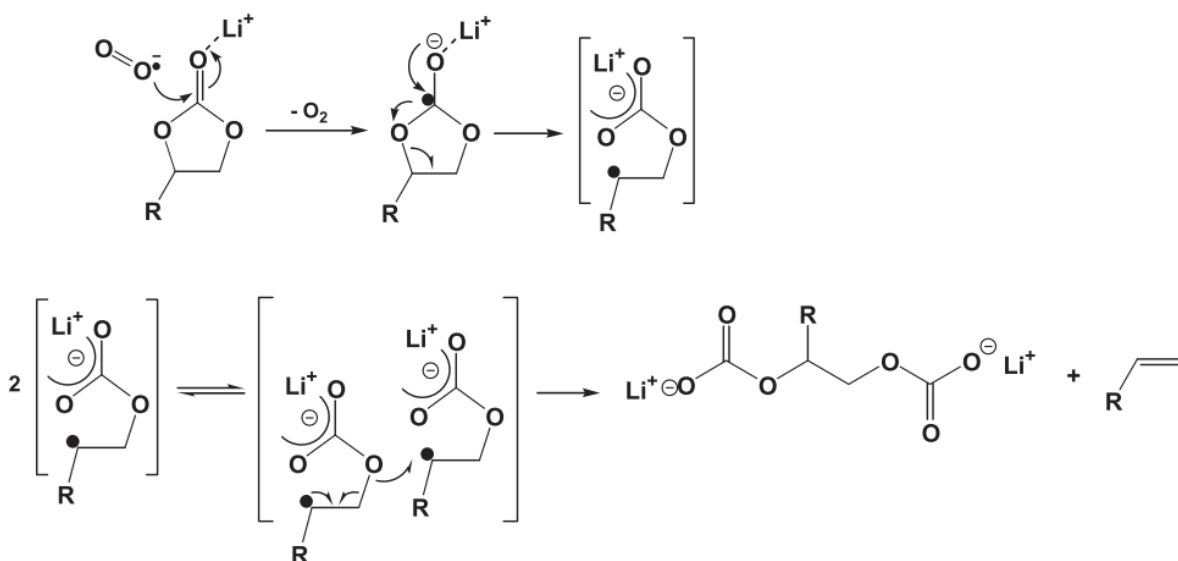


Figure 1. 17 : Nucleophilic attack of superoxide on an alkyl carbonate molecule : a possible pathway (scheme extracted from [61], reproduced with permission from Elsevier

In any case, the main discharge product in carbonate-based electrolyte was always either lithium carbonate (Li₂CO₃) or lithium alkyl-carbonate species (LiRCO₃) [33, 57, 62–65].

In addition to the reactivity of carbonate-based electrolytes, several studies have also characterized ether-based solvents as electrolytes (DME [32, 66] and TEGDME [57]), in which the main discharge product was, this time, lithium peroxide [32, 38, 57].

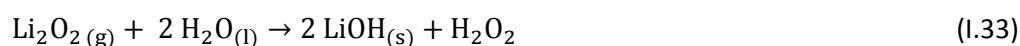
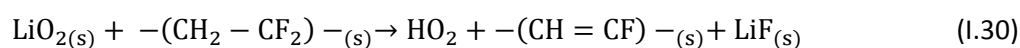
It was found that part of the ORR product are still decomposing ether-based solvents to form alkyl carbonate lithium salts, and it was supposed that these alkyl carbonates species were formed at the Li₂O₂/electrolyte interface [32] and formed a “crust” of LiRCO₃ on the Li₂O₂ particles. Another study, in which isotopic substitution was carried out on DEMS measurements showed that lithium acetate and lithium formate were produced as side reactions products [66].

Moreover, two studies pointed out that the lithium salts are also sensitive to ORR discharge products, which eventually decomposes. Younesi et al [57], have conducted a series of experiments where solvents (carbonates and TEGDME) along with salts (LiPF₆, LiClO₄ and LiBF₄) and binder (PVDF) were put in contact with lithium peroxide for two different time (10 min and 48 h) and then analyzed by XPS. The surface analyses allowed the authors to clearly identify decomposition products such as LiCl and Li_xCl_y (for LiClO₄ TEGDME electrolyte), LiF and Li_xBO_yF_z (for LiBF₄ EC/DEC electrolytes) and LiF, Li_xPF_y and Li_xPO_yF_z (for LiPF₆ EC/DEC electrolytes). It must be noted that for the PC electrolytes, alkyl carbonates were detected, which agrees with others papers [63–65].

Another study also reported the instability of LiBOB salt (Lithium Bis(oxalate)borate), which undergoes ring opening (probably similarly to that of propylene carbonate, depicted on Figure 1.17), and leads to the formation of lithium oxalate during the discharge of the Li-O₂ system [67].

Furthermore, the binder stability can also be an issue, considering the reactivity of both the lithium superoxide and lithium peroxide. Among the binder used in the literature, polyvinylidene fluoride (PVDF) is the most popular [40, 68], thanks to its properties (easy to process in an ink).

However, it has been proven lately by Black et al [69], that PVDF faces an attack from superoxide species, which leads to its deprotonation (reaction pathway: 1.30-33), and eventually to the *in situ* formation of water by disproportionation of hydrogen peroxide, which reacts to form lithium hydroxide (consistent with the literature, on the moisture effect in aprotic media [54, 70, 71]).



Such reactions prove that it is mandatory to prohibit the use of PVDF as binder for Li-O₂ cathodes, because of the chain reaction and the vicious cycle that occurs (each LiOH molecule that is formed forms in return hydrogen peroxide, which disproportionates to water and reacts with lithium peroxide to form lithium hydroxide).

One might say that the LiOH formation is not a bad idea, because a full 4 electrons reduction is thus achieved [54, 72], but the water shall not originate from the binder decomposition. Indeed, it will fatally lead to grain detachment, capacity losses, and because although this can possibly be positive during discharge, it is definitely not the case during charge and overall in terms of cyclability. Also, such system will be forced to work with a Liskon separator (or equivalent), to avoid any transfer of water to the lithium side of the cell.

As a following, the excellent study of Nasybulin et al [73], has evaluated the stability of a wide panel of polymers (PVDF,PS,PEO,PAN,PVC,PVP,PMMA,CMC, PTFE, PP and PE) toward superoxide (KO₂) and peroxide (Li₂O₂), by ball-milling those polymers with the reactive (superoxide or peroxide). After the ball-milling, XRD and XPS was performed.

From this study, only PTFE, PP and PE were stable (from XRD analysis) toward superoxide and peroxide, while the other polymers were decomposed, by nucleophilic elimination and formed mainly carbonates as decomposition products (PVP, PMMA, CMC, PS PEO). However, XPS analyses revealed that decomposition products were nevertheless found for PTFE and PP, while nothing was detected by XRD, meaning that they are slightly unstable toward ORR products, which compromises their use for a practical system, along with the others polymers.

From this study, it is now an evidence that the only usable binder for a practical Li-O₂ system is PE, and it is well known that PE is a polymer that is very hard to dissolve: it requires the use of “super solvents” [74, 75] such as toluene, xylene, acetone, under heat and stirring, especially for Ultra High molecular Weight PE (required grade to be used as a good binder).

Moreover, as published by McCloskey et al [32], carbon electrodes are facing a thermal reaction with lithium peroxide, which forms a monolayer of lithium carbonate, at each cycle. In their publication, the carbon electrode consisted of ¹³C, and 40% of the CO₂ evolved during the charging was ¹³CO₂. Such phenomena imply that the greater the surface area, the greater the amount of lithium carbonate produced, thus the faster the carbon cathode is consumed.

ii. Rate capability

As presented above (part a) the very first design of the Li-O₂ system proved that, in a practical Li-O₂ system (if considering a cathode fully stable toward ORR products), the end capacity is only limited by the surface area of the material on which the oxygen reduction will be conducted [8].

In this perspective, solutions such as graphene based cathode [42, 76–79], and metal organic frameworks [80–85] have been proposed as high-surface-area materials for the cathode side, and have proven some very good results concerning the rate capability. However, as discussed in the previous part of this chapter (II.d.i), all those solutions involve carbon-based cathodes, in which some were binder free [76–78, 84] and other comprised either PVDF or Nafion (the use of the latter in an aprotic Li-O₂ system raises some questions) as a binder on their carbon-based cathodes [79–83, 85], which are unstable toward ORR products.

It was concluded that this apparent good cyclability on carbon based cathodes was due to the very decomposition of the carbon material [32, 40] (CO₂ evolved during the charging at high potential), thus those electrodes are not good candidates for a long life secondary system (rechargeable and durable Li-O₂ battery).

Very few studies have highlighted carbon-free cathodes, such as nanoporous gold cathodes [86], and also TiC, SiC and TiN bound on stainless steel mesh cathodes [87]. For the nanoporous gold cathodes, the electrolyte was LiClO₄ in DMSO and some astonishing performances were obtained (100 cycles with nearly perfect 2.0 electrons per Oxygen for the 100th discharge and charge), and no evidence of LiCO₂H or Li₂CO₃ presence was detected by FTIR.

Unfortunately, gold cannot be considered a practical Li-O₂ battery cathode, for evident materials cost and availability reasons. For the other study [87], the electrolyte consisted of either LiClO₄/DMSO or LiPF₆/TEGDME with PTFE as a binder. Still, for this study, very good performances were reported (less than 1% of Li₂CO₃ formed in the LiClO₄/DMSO electrolyte), and also 2 electrons per oxygen molecules were exchanged for the discharge and the recharge.

However, those experiments were duplicated by McCloskey et al [40], and they were unable to reproduce the results claimed by the original publications. Instead, the ratio OER/ORR in coulometry achieved was 0.44 for the NPG and 0.45 for the TiC cathodes (carbon cathodes exhibits a ratio of 0.51), which clearly contrasts with the original claims. Also, by changing alone the cathode material does not prevent electrolyte/salt decomposition. It is thus mandatory to use a suitable solvent and suitable salt on robust cathodes.

Conclusion

This literature survey shows that Li-O₂ systems are very promising owing to their theoretical capacities. However, crucial issues are raised concerning the stability of the cell components, especially on the cathode side. In this perspective, only polyethylene must be used as the binder in a Li-O₂ cathode, to ensure long life stability and flexibility of the cathode [73]. Also, a better screening of the salts available is necessary, as the ones working in Li-ion systems are unstable in Li-O₂ cathodes [57, 67]. In addition, the carbon support, carbon being one privileged material for the cathode of a Li-O₂ battery (owing to its very low price, good conductivity, availability, etc.), is unstable toward ORR products. Thus, two strategies exist: carbon free electrodes [86, 87], but those solutions have proven to not be reproducible [40] (and also the use of metal such as gold is to be limited as much as possible, as it will rise sharply the cost of the system), or carbon-protected electrode. This solution has not been screened yet and the idea is to make a thin deposition of a stable (semi)conductor on high surface area carbon cathode, which will ensure a high end capacity, and no contact between the ORR product and the carbon support. A second strong issue of the cathode side (if not one of the strongest), is to enhance the charge/discharge cyclability of the cathode; this may not be achieved by changing the cathode material, but by adding a redox additive that will allow the transport of electrons in the solution (thus allowing the recharge of fallen Li₂O₂ particles and huge aggregates). This idea has not been extensively screened, and very few papers have presented a redox shuttle that can practically be used to enhance the charging of the cathode (to be efficient, the standard potential of the redox shuttle must be superior to the onset of the OER, in presence of Li⁺). To the author's knowledge, in the literature, only the TEMPO [88] and iodine [72, 89] solutions have their redox potentials correctly placed to work as a redox shuttle, and have proven to enhance the OER and therefore improved the cyclability. Yet, the idea will be to have an additive with the ability to help both the discharge (homogeneous catalysis or ORR) and the recharge (redox shuttle).

So to conclude, the present study will address two of the main issues suffered by non-aqueous Li-O₂ batteries: (i) the poor stability of the carbon cathode will be enhanced by thin metal-oxide deposits (as a protective but electron-conducting layer); (ii) the poor recharge ability of the cathode will be improved by using a redox mediator in the electrolyte. Both strategies will be described and practically assessed in the following chapters.

References

1. Semkow KW, Sammells AF (1987) A lithium oxygen secondary battery. *J Electrochem Soc* 134:2084–2085. doi: 10.1149/1.2100826
2. Schneider N, Deposition AL (2016) Atomic Layer Deposition (ALD) Atomic Layer Deposition (ALD) Principes généraux , matériaux. 33:
3. Rodrigues Castanheira LF (2014) Corrosion of high surface area carbon supports used in proton-exchange membrane fuel cell. Université Grenoble-Alpes
4. Ferrari AC, Robertson J (2000) Interpretation of Raman spectra of disordered and amorphous carbon. *Phys Rev B* 61:14095–14107. doi: 10.1103/PhysRevB.61.14095
5. Jawhari T, Roid A, Casado J (1995) Raman spectroscopic characterization of some commercially available carbon black materials. *Carbon N Y* 33:1561–1565. doi: 10.1016/0008-6223(95)00117-V
6. Nistor L, Landuyt J, Ralchenko V, et al (1994) Direct observation of laser-induced crystallization of aC: H films. *Appl Phys A Mater Sci Process* 58:137–144. doi: 10.1007/BF00332170
7. Robins LH, Farabaugh EN, Feldman A (1990) Line shape analysis of the Raman spectrum of diamond films grown by hot-filament and microwave-plasma chemical vapor deposition. *J Mater Res* 5:2456–2468. doi: 10.1557/JMR.1990.2456
8. Abraham KM, Jiang Z, Soc JE (1996) A Polymer Electrolyte – Based Rechargeable Lithium / Oxygen Battery. *Tech Pap Electrochem Sci technology* 143:1–5. doi: 10.1149/1.1836378
9. Melorose J, Perroy R, Careas S (2015) World population prospects. *United Nations* 1:587–92. doi: 10.1017/CBO9781107415324.004
10. Nevada CRC of (2002) World Fossil Fuels Reserves and Expected Consumption. 1–3.
11. International Energy Agency (2016) Key world energy statistics. *Statistics (Ber)* 80. doi: 10.1787/key_energ_stat-2016-en
12. Tesoro (2014) Material Safety Data Sheet Fuel Oil Tesoro.
13. Kloff S, Wicks C (2004) Gestion environnementale de l'exploitation de pétrole offshore et du transport maritime pétrolier: un document d'information à l'attention des parties prenantes de l'écorégion marine ouest africaine. *Comm l'UICN des Polit Environnementales, Économiques Soc – CEESP* 80.
14. McKenna P (2011) Fossil fuels are far deadlier than nuclear power. *New Scientist*
15. Mohtasham J (2015) Review Article-Renewable Energies. *Energy Procedia* 74:1289–1297. doi: 10.1016/j.egypro.2015.07.774
16. Delucchi MA, Jacobson MZ (2011) Providing all global energy with wind, water, and solar power, Part II: Reliability, system and transmission costs, and policies. *Energy Policy* 39:1170–

1190. doi: 10.1016/j.enpol.2010.11.045
17. Badwal SPS, Giddey SS, Munnings C, et al (2014) Emerging electrochemical energy conversion and storage technologies. *Front Chem* 2:79. doi: 10.3389/fchem.2014.00079
 18. Pritchard DK, Rattigan WM (2010) Hazards of liquid hydrogen RR769 Position paper.
 19. Alotto P, Guarnieri M, Moro F (2014) Redox flow batteries for the storage of renewable energy: A review. *Renew Sustain Energy Rev* 29:325–335. doi: 10.1016/j.rser.2013.08.001
 20. Guerrero Moreno N, Cisneros Molina M, Gervasio D, Perez Robles JF (2015) Approaches to polymer electrolyte membrane fuel cells (PEMFCs) and their cost. *Renew Sustain Energy Rev* 52:897–906. doi: 10.1016/j.rser.2015.07.157
 21. Schlapbach L, Züttel a (2001) Hydrogen-storage materials for mobile applications. *Nature* 414:353–358. doi: 10.1038/35104634
 22. Liu C, Li F, Ma L-P, Cheng H-M (2010) Advanced materials for energy storage. *Adv Mater* 22:E28-62. doi: 10.1002/adma.200903328
 23. De Rango P, Fruchart D, Marty P (2011) Le stockage solide de l'hydrogène au service des énergies renouvelables. *CNRS (Centre Natl la Rech Sci* 86–92.
 24. Fotouhi A, Auger DJ, Propp K, et al (2016) A review on electric vehicle battery modelling: From Lithium-ion toward Lithium-Sulphur. *Renew Sustain Energy Rev* 56:1008–1021. doi: 10.1016/j.rser.2015.12.009
 25. Cheng F, Chen J (2012) Metal–air batteries: from oxygen reduction electrochemistry to cathode catalysts. *Chem Soc Rev* 41:2172. doi: 10.1039/c1cs15228a
 26. Hartenbach A, Bayer M, Dustmann CH (2013) The Sodium Metal Halide (ZEBRA) Battery: An Example of Inorganic Molten Salt Electrolyte Battery. *Molten Salts Chem.* doi: 10.1016/B978-0-12-398538-5.00021-4
 27. Bouteillon J (2012) Constantes électrochimiques des sels fondus. 33:
 28. Padbury R, Zhang X (2011) Lithium–oxygen batteries—Limiting factors that affect performance. *J Power Sources* 196:4436–4444. doi: 10.1016/j.jpowsour.2011.01.032
 29. Zimmermann M (2015) Oxygen Reduction Reaction Mechanism on Glassy Carbon in Aprotic Organic Solvents.
 30. Laoire CO, Mukerjee S, Abraham KM, et al (2009) Elucidating the mechanism of oxygen reduction for lithium-air battery applications. *J Phys Chem C* 113:20127–20134. doi: 10.1021/jp908090s
 31. Allen CJ, Mukerjee S, Plichta EJ, et al (2011) Oxygen Electrode Rechargeability in an Ionic Liquid for the Li–Air Battery. *J Phys Chem Lett* 2420–2424. doi: 10.1021/jz201070t
 32. McCloskey BD, Speidel A, Scheffler R, et al (2012) Twin problems of interfacial carbonate formation in nonaqueous Li-O₂ batteries. *J Phys Chem Lett* 3:997–1001. doi: 10.1021/jz300243r

33. Luntz A, McCloskey B (2014) Nonaqueous Li–air batteries: a status report. *Chem. Rev.*
34. McCloskey BD, Scheffler R, Speidel A, et al (2011) On the efficacy of electrocatalysis in nonaqueous Li-O₂ batteries. *J Am Chem Soc* 133:18038–41. doi: 10.1021/ja207229n
35. Johnson E, Pool K, Hamm R (1966) Polarographic Reduction of Oxygen in Dimethylsulfoxide. *Anal Chem* 38:183–185.
36. Fujinaga T, Sakura S (1974) Polarographic investigation of dissolved-oxygen in non-aqueous solvent. *Bull Chem Soc Jpn* 47:2781–2786.
37. Sawyer D, Jr GC (1982) Effects of media and electrode materials on the electrochemical reduction of dioxygen. *Anal Chem* 2:1720–1724. doi: 10.1021/ac00248a014
38. McCloskey BD, Bethune DS, Shelby RM, et al (2011) Solvents ' Critical Role in Nonaqueous Lithium À Oxygen Battery. *J Phys Chem Lett* 2:1161–1166. doi: 10.1021/jz200352v
39. Laoire CO, Mukerjee S, Abraham KM, et al (2010) Influence of nonaqueous solvents on the electrochemistry of oxygen in the rechargeable lithium-air battery. *J Phys Chem C* 114:9178–9186. doi: 10.1021/jp102019y
40. Luntz AC, Mccloskey BD (2014) Nonaqueous Li – Air Batteries : A Status Report. *Chem Rev* 114:11721–11750. doi: 10.1021/cr500054y
41. Rahman MA, Wang X, Wen C (2014) A review of high energy density lithium-air battery technology. *J Appl Electrochem* 44:5–22. doi: 10.1007/s10800-013-0620-8
42. Black R, Adams B, Nazar LF (2012) Non-aqueous and hybrid Li-O₂ batteries. *Adv Energy Mater* 2:801–815. doi: 10.1002/aenm.201200001
43. McCloskey BD, Bethune DS, Shelby RM, et al (2012) Limitations in Rechargeability of Li-O₂ Batteries and Possible Origins. *J Phys Chem Lett* 3:3043–3047. doi: 10.1021/jz301359t
44. Pearson G (1963) Hard and Soft Acids and Bases. *J Am Chem Soc* 85:3533–3539. doi: 10.1021/ja00905a001
45. Trahan MJ, Mukerjee S, Plichta EJ, et al (2013) Studies of Li-Air Cells Utilizing Dimethyl Sulfoxide-Based Electrolyte. *J Electrochem Soc* 160:A259–A267. doi: 10.1149/2.048302jes
46. C. Laurence JF. GAL Lewis Basicity and Affinity Scales.
47. Solutions N, Copyright KI, GmbH WV, Isbns K (2002) Related Titles from WILEY-VCH Encyclopedia of Electrochemistry , Volume VI Supramolecular Electrochemistry Semiconductor Electrochemistry Handbook of Analytical Techniques. *Electrochemistry*. doi: 10.1063/1.2218844
48. Khetan A, Luntz A, Viswanathan V (2015) Trade-offs in capacity and rechargeability in nonaqueous Li-O₂ batteries: Solution-driven growth versus nucleophilic stability. *J Phys Chem Lett* 6:1254–1259. doi: 10.1021/acs.jpcclett.5b00324
49. Andrieux CP, Hapiot P, Saveant JM (1987) Mechanism of superoxide ion disproportionation in aprotic solvents. *J Am Chem Soc* 109:3768–3775. doi: 10.1021/ja00246a040

50. Olmstead WN, Margolin Z, Bordwell FG (1980) Acidities of water and simple alcohols in dimethyl sulfoxide solution. *J Org Chem* 45:3295–3299. doi: 10.1021/jo01304a032
51. Singh PS, Evans DH (2006) Study of the electrochemical reduction of dioxygen in acetonitrile in the presence of weak acids. *J Phys Chem B* 110:637–644. doi: 10.1021/jp055296f
52. Schwenke KU, Metzger M, Restle T, et al (2015) The Influence of Water and Protons on Li₂O₂ Crystal Growth in Aprotic Li-O₂ Cells. *J Electrochem Soc* 162:A573–A584. doi: 10.1149/2.0201504jes
53. Aetukuri NB, McCloskey BD, García JM, et al (2014) Solvating additives drive solution-mediated electrochemistry and enhance toroid growth in non-aqueous Li-O₂ batteries. *Nat Chem*. doi: 10.1038/nchem.2132
54. Li F, Wu S, Li D, et al (2015) The water catalysis at oxygen cathodes of lithium-oxygen cells. *Nat Commun* 6:7843. doi: 10.1038/ncomms8843
55. Xu J-J, Wang Z-L, Xu D, et al (2013) Tailoring deposition and morphology of discharge products towards high-rate and long-life lithium-oxygen batteries. *Nat Commun* 4:2438. doi: 10.1038/ncomms3438
56. Capotosto Jr. A, Petrocelli AW (1986) Use of Lithium Peroxide for Atmosphere Regeneration.
57. Younesi R, Hahlin M, Björefors F, et al (2013) Li-O₂ Battery Degradation by Lithium Peroxide (Li₂O₂): A Model Study. *Chem Mater* 25:77–84. doi: 10.1021/cm303226g
58. Zhang J, Luan Y, Lyu Z, et al (2015) Synthesis of hierarchical porous delta-MnO₂ nanoboxes as an efficient catalyst for rechargeable Li-O₂ batteries. *Nanoscale* 7:14881–14888. doi: 10.1039/C5NR02983J
59. Viswanathan V, Thygesen KS, Hummelshøj JS, et al (2011) Electrical conductivity in Li₂O₂ and its role in determining capacity limitations in non-aqueous Li-O₂ batteries. *J Chem Phys* 135:0–10. doi: 10.1063/1.3663385
60. Tobishima SI, Yamaki JI, Yamaji A, Okada T (1984) Dialkoxyethane-propylene carbonate mixed electrolytes for lithium secondary batteries. *J Power Sources* 13:261–271. doi: 10.1016/0378-7753(84)80034-8
61. Tarascon JM, Guyomard D (1994) New electrolyte compositions stable over the 0 to 5 V voltage range and compatible with the Li_{1+x}Mn₂O₄/carbon Li-ion cells. *Solid State Ionics* 69:293–305. doi: 10.1016/0167-2738(94)90418-9
62. Mizuno F, Nakanishi S, Kotani Y, et al (2010) Rechargeable Li-Air Batteries with Carbonate-Based Liquid Electrolytes. *Electrochemistry* 78:403–405. doi: 10.5796/electrochemistry.78.403
63. Freunberger SA, Chen Y, Peng Z, et al (2011) Reactions in the rechargeable lithium-O₂ battery with alkyl carbonate electrolytes. *J Am Chem Soc* 133:8040–8047. doi: 10.1021/ja2021747
64. Xu W, Viswanathan V V., Wang D, et al (2011) Investigation on the charging process of Li₂O₂-based air electrodes in Li-O₂ batteries with organic carbonate electrolytes. *J Power Sources*

- 196:3894–3899. doi: 10.1016/j.jpowsour.2010.12.065
65. Xu W, Xu K, Viswanathan V V., et al (2011) Reaction mechanisms for the limited reversibility of Li-O₂ chemistry in organic carbonate electrolytes. *J Power Sources* 196:9631–9639. doi: 10.1016/j.jpowsour.2011.06.099
 66. García JM, Horn HW, Rice JE (2015) Dominant Decomposition Pathways for Ethereal Solvents in Li-O₂ Batteries. *J Phys Chem Lett* 6:1795–1799. doi: 10.1021/acs.jpcllett.5b00529
 67. Lau KC, Lu J, Low J, et al (2014) Investigation of the Decomposition Mechanism of Lithium Bis(oxalate)borate (LiBOB) Salt in the Electrolyte of an Aprotic Li-O₂ Battery. *Energy Technol* 2:348–354. doi: 10.1002/ente.201300164
 68. Lu Y-C, Gallant BM, Kwabi DG, et al (2013) Lithium-oxygen batteries: bridging mechanistic understanding and battery performance. *Energy Environ Sci* 6:750–768. doi: 10.1039/C3ee23966g
 69. Black R, Oh SH, Lee J, et al (2012) Screening for superoxide reactivity in Li-O₂ batteries: effect on Li₂O₂/LiOH crystallization. *J Am Chem Soc* 134:2902–5. doi: 10.1021/ja2111543
 70. Cho MH, Trottier J, Gagnon C, et al (2014) The effects of moisture contamination in the Li-O₂ battery. *J Power Sources* 268:565–574. doi: 10.1016/j.jpowsour.2014.05.148
 71. Guo Z, Dong X, Yuan S, et al (2014) Humidity effect on electrochemical performance of Li-O₂ batteries. *J Power Sources* 264:1–7. doi: 10.1016/j.jpowsour.2014.04.079
 72. Liu T, Leskes M, Yu W, et al (2015) Cycling Li-O₂ batteries via LiOH formation and decomposition. *Science* (80-) 350:530–533. doi: 10.1126/science.aac7730
 73. Nasybulin E, Xu W, Engelhard MH, et al (2013) Stability of polymer binders in Li-O₂ batteries. *J Power Sources* 243:899–907. doi: 10.1016/j.jpowsour.2013.06.097
 74. Huseby TW, Bair HE (1968) Dissolution of polyethylene single crystals in xylene and octadecane. *J Appl Phys* 39:4969–4973. doi: 10.1063/1.1655894
 75. Poulakis JG, Papaspyrides CD (1995) The Dissolution Reprecipitation Technique Applied on High-Density Polyethylene .1. Model Recycling Experiments. *Adv Polym Technol* 14:237–242.
 76. Zhang W, Zhu J, Ang H, et al (2013) Binder-free graphene foams for O₂ electrodes of Li-O₂ batteries. *Nanoscale* 5:9651–8. doi: 10.1039/c3nr03321j
 77. Wang ZL, Xu D, Xu JJ, et al (2012) Graphene oxide gel-derived, free-standing, hierarchically porous carbon for high-capacity and high-rate rechargeable Li-O₂ batteries. *Adv Funct Mater* 22:3699–3705. doi: 10.1002/adfm.201200403
 78. Li Y, Wang J, Li X, et al (2012) Nitrogen-doped graphene nanosheets as cathode materials with excellent electrocatalytic activity for high capacity lithium-oxygen batteries. *Electrochem Commun* 18:12–15. doi: 10.1016/j.elecom.2012.01.023
 79. Choi CH, Lim HK, Chung MW, et al (2014) Long-range electron transfer over graphene-based catalyst for high-performing oxygen reduction reactions: Importance of size, n-doping, and

- metallic impurities. *J Am Chem Soc* 136:9070–9077. doi: 10.1021/ja5033474
80. Zhang W, Zhu J, Ang H, et al (2014) Fe-based metallopolymer nanowall-based composites for Li-O₂ battery cathode. *ACS Appl Mater Interfaces* 6:7164–7170. doi: 10.1021/am500158s
81. Chen W, Zhang Z, Bao W, et al (2014) Hierarchical mesoporous γ -Fe₂O₃/carbon nanocomposites derived from metal organic frameworks as a cathode electrocatalyst for rechargeable Li-O₂ batteries. *Electrochim Acta* 134:293–301. doi: 10.1016/j.electacta.2014.04.110
82. Wei Xia, Jinghan Zhu, Wenhan Guo, Li An DX and RZ (2014) Well-defined carbon polyhedrons prepared from nano metal–organic frameworks for oxygen reduction. *J Mater Chem A* 2:11606. doi: 10.1039/c4ta01656d
83. Zhang J, Wang L, Xu L, et al (2014) Porous cobalt-manganese oxide nanocubes derived from metal organic frameworks as a cathode catalyst for rechargeable Li-O₂ batteries. *Nanoscale* 7:720–6. doi: 10.1039/c4nr05865h
84. Cao L, Lv F, Liu Y, et al (2015) A high performance O₂ selective membrane based on CAU-1-NH₂@polydopamine and the PMMA polymer for Li-air batteries. *Chem Commun (Camb)* 51:1–4. doi: 10.1039/c4cc09281c
85. Hu X, Zhu Z, Cheng F, et al (2015) Micro-nano structured Ni-MOFs as high-performance cathode catalyst for rechargeable Li-O₂ batteries. *Nanoscale* 7:11833–11840. doi: 10.1039/c5nr02487k
86. Peng Z, Freunberger S a., Chen Y, Bruce PG (2012) A Reversible and Higher-Rate Li-O₂ Battery. *Science (80-)* 337:563–566. doi: 10.1126/science.1223985
87. Ottakam Thotiyl MM, Freunberger S a, Peng Z, et al (2013) A stable cathode for the aprotic Li-O₂ battery. *Nat Mater* 12:1050–6. doi: 10.1038/nmat3737
88. Bergner BJ, Schürmann A, Peppler K, et al (2014) TEMPO: A Mobile Catalyst for Rechargeable Li-O₂ Batteries. *J Am Chem Soc* 136:15054–15064. doi: 10.1021/ja508400m
89. Kwak W-J, Hirshberg D, Sharon D, et al (2015) Understanding the behavior of Li–oxygen cells containing Lil. *J Mater Chem A* 3:8855–8864. doi: 10.1039/C5TA01399B

Chapter II.

Experimental section

Every obstacle is destroyed through rigor – Leonardo Da Vinci

In this section, the principles of the techniques used in the manuscript will be detailed.

I. Electrochemistry

a. Washing of the glassware

The cell consisted of homemade glass cell (for the three-electrode, Differential Electrochemical Mass Spectrometry and Full cell setup). Prior any experiment, the glassware was thoroughly cleaned; to this goal, each cell was soaked at least for 12 hours in a H₂SO₄:H₂O₂ mixture (concentrated Caro's acid), carefully washed several times with ultrapure water (18.2 MΩ.cm), and placed to dry for at least 1 hour in a stove at 120°C. Concerning the glass frit, the procedure is extended, with a sonication process (the glass piece is placed with ultrapure water on both side of the frit, and sonicated for at least 15 minutes), followed by an additional washing (2/3 times) in ultra-pure water. The last step of the washing process is to apply pressure in the tube of the glass frit, with ultra-pure water in it (either with Oxygen/Argon, at 1 bar), to ensure that no Caro's acid remain in the frit. At this point, the piece is shaken to remove water and placed in the stove with the other glassware to dry.

b. Chemicals

All reagents used for electrochemistry were of electrochemical grade and stored upon delivery in an argon atmosphere Glovebox (MBraun Labmaster, water and oxygen level below 0.1 ppm). Lithium perchlorate (battery grade, dry, 99.99% trace metals basis), silver nitrate (anhydrous, 99.999%), Pyridine (anhydrous, 99.8%, < 30 ppm water), 1-Methyl-2-pyrrolidinone (anhydrous, 99.5%, < 50 ppm water) were purchased from Sigma Aldrich. Dimethyl sulfoxide (anhydrous, 99.8%, packaged under argon in re-sealable ChemSeal bottles, < 100 ppm water), was purchased either from Alfa Aesar, or from Sigma Aldrich (anhydrous grade < 0.005% water). Metallic lithium was purchased from Sigma Aldrich (99.9% trace metal basis, W 0.38mm x 23 mm). N,N'-Bis(salicylidene)ethylenediaminocobalt(II) (99%) was purchased from Sigma Aldrich. 5,10,15,20-Tetrakis(4-methoxyphenyl)-21H,23H-porphine cobalt(II) < 96.0% (HPLC) was purchased from Sigma Aldrich. Molecular sieves 3A (beads 2 mm) were purchased from Sigma Aldrich and use to further dry the solvents.

The Dimethyl Sulfoxide dried for at least two days on molecular sieves 3A, and subsequently filtered, in order to have water levels (measured by Karl Fisher titrations) as low as possible (below 80 ppm after the mounting of the cell).

c. Three-electrodes setup

The cell is homemade, out of Pyrex glass, with airtight ends (ensured either by a silicone septum or seal rings/ SVL caps). The working electrode consists of a glassy-carbon disk (\varnothing 5 mm), polished with diamond paste before each experiment (1 μ m) and sonicated in ethanol for 15 minutes to remove the traces of the diamond paste. The counter electrode consists of high surface area platinum, which is heated with a butane blowtorch to remove any trace of organic element on the platinum surface prior to the experiment (by pyrocatalysis). Concerning the reference electrode, the Ag/Ag⁺ couple was chosen over lithium, owing to its better stability. Silver nitrate was used at either 2 or 20 mM concentration, depending on the experiment (specified in the text), with a supporting salt (with the same concentration and nature than in the bulk electrolyte). Concerning the solvents used, a blend of 1:3 of Pyridine: DMSO was used, as pyridine has a special ability to solvate silver ions [1]. The reference compartment is separated from the bulk by a P5 glass frit to prevent (or limit as much as possible) transfer between the bulk and the reference electrolytes during the experiment.

The cell is prepared and mounted in Ar-glovebox (MBraun Labmaster Sp), with water and oxygen levels below 0.1 ppm. For the experiment, as no oxygen can be flushed in the glovebox (for reactivity issues), the cell is placed outside of the glovebox, in a home-made box, in which Argon (5.0) is flushed continuously. This box is made out of polycarbonate and is airtight, and can be connected to the potentiostat, thanks to proper connectors. This box is also equipped with gas connections, that allow to purge the cell either with argon (5.0) or oxygen (5.0). The purging is ensured by needles, through the cell septum. In order to prevent any transfer to the ambient atmosphere (thus water contamination), the outlet of the box and of the cell are connected to homemade bubblers, filled with hydrophobic oil.

d. Differential Electrochemical Mass Spectrometry

In this technique, a specific three-electrode setup is used. It is designed so that any gas, consumed or produced at the working electrode can be detected *operando*. It is thus of very high interest for the study of the Oxygen Reduction Reaction and Oxygen Evolution Reaction (ORR and OER).

i. Working Electrode preparation

Ink preparation was performed by mixing 20 mg of active material, with 1 milliliter of NMP/binder solution (the amount of binder was fixed as 80:20 of active material: binder ratio fulfilled for a dry electrode). The binder used in this study was Kynar HSV 900 (Arkema). The ink was dispersed by sonication for at least 1 h prior usage. A calibrated drop of 20 μ L of this ink was then deposited on a 6 mm diameter Panex 30 carbon cloth electrode (Zoltek). This electrode was then left to dry in a 60°C

stove for 6 hours and placed under dynamic vacuum overnight to ensure that neither NMP nor water was left on the carbon cloth before the experiment.

ii. Cell setup

As for the three-electrode setup, the DEMS cell is airtight, thanks to septum and seal rings/SVL caps. The working electrode consists of a glassy-carbon rod collector, pushing onto the carbon cloth (on which deposition of ink was made, or used pristine). The counter electrode consisted of a glassy carbon slab, and the same reference couple than the conventional three-electrode setup was used. In order to ensure that only gases could go into the DEMS (no solvent, which would destroy the turbomolecular pumps that ensure the ballistic trajectory of the gases to the MS quadrupole), two PTFE membranes (0.02 μm pore size, ca. 30 μm thick) are placed on the stainless steel frit. For a better understanding, a drawing of the DEMS cell is presented in Figure II.1.

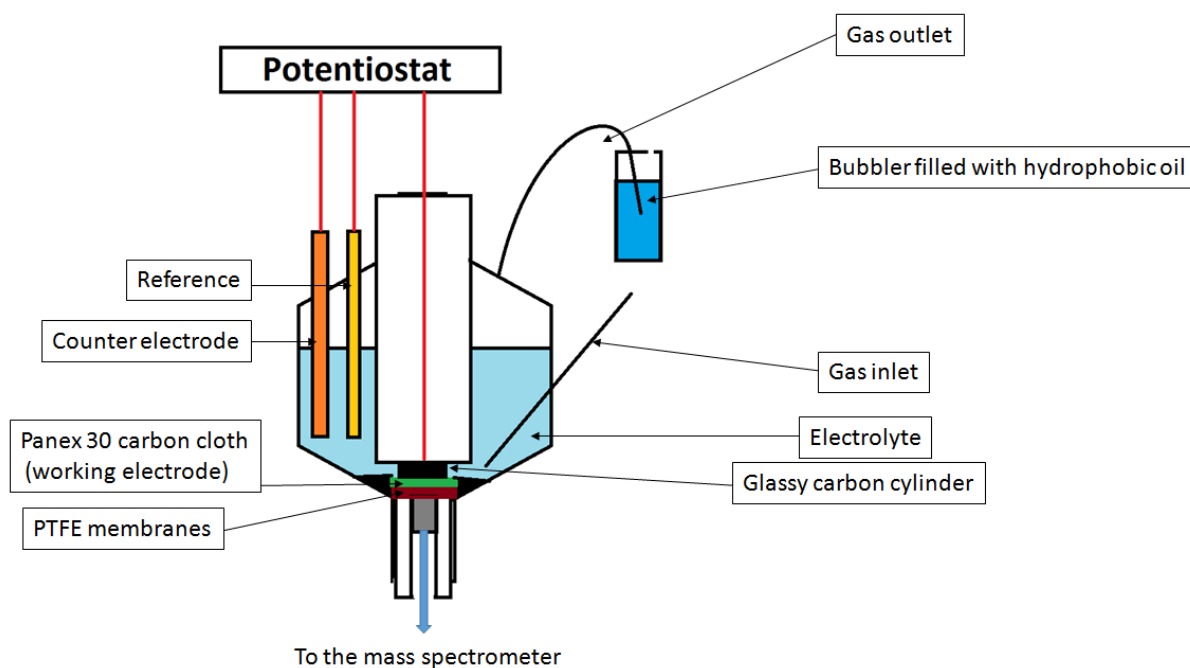


Figure II. 1: Scheme of the DEMS spectro-electrochemical cell

e. Full cell experiment

The full cell working electrode preparation is following the exact same procedure than for the preparation of the DEMS working electrode preparation (d.i). The full cell setup is a two-electrode airtight setup. The positive electrode consists of a glassy carbon disk, pressed onto the carbon cloth (used pristine or with an active material deposit). The separator used is Celgard K2045 (Polyethylene, 20 μm thick with an average pore size of 50 nm and porosity of 47%). The negative electrode was

metallic lithium, laminated onto a copper mesh, connected to a copper wire (new copper components are used for each new cell). The electrolyte consists of 1 M LiClO₄ DMSO. If an additive is added to the electrolyte, it will be specified in the text (see chapter six). For the full cell testing, the flushing of oxygen is conducted directly onto the working electrode, thanks to gas channels, parallel to the glassy-carbon rod. As for the three-electrode setup, the cell is placed in the Ar-Flushed box, and the outlets are connected to the hydrophobic oil filled bubblers.

f. Electrochemical testing

The electrochemical tests were conducted, thanks to a Bio-logic Potentiostat (Biologic SAS, models SP-300 or VMP-2), using EC-lab[®] software. For the DEMS and three electrodes cells characterizations, conventional electrochemical techniques such as cyclic voltammetry, chronoamperometry, and linear scan voltammetry were used. For the full cell, the technique used was a GCPL (galvanostatic cycling with potential limitations), which consisted of a discharge at a constant current, followed by the charging procedure. The charging procedure was selected as a classical CC-CV technique (a charging at a constant current, followed by a constant voltage step, at the cutoff potential). All the measurements were iR-corrected in dynamic mode (using the ZIR procedure in EC-Lab, with 85% iR compensation).

II. Characterization techniques

Different characterization techniques were used in the present thesis. Most of them were *ex situ*, but one was *operando*.

a. Differential Electrochemical Mass Spectrometry

The Differential Electrochemical Mass spectrometry (DEMS) experiments were carried out, using the Pfeiffer Vacuum PrismaPlus mass spectrometer (MS), connected to the biologic SP-300 potentiostat and the acquisition of the data was performed thanks to Quadera[®]. According to Baltruschat [2], DEMS allow to detect any gases produced or consumed on the working electrode surface, while conducting the experiment, placing this technique as a powerful *operando* technique. Thanks to this setup, various electrocatalysts could be tested for one application (for example, the Hydrogen Oxidation Reaction), and differences in desorption mechanisms could be spotted, by simply comparing the electrochemical signal, to the MS signal.

Various cell designs can be used for the study of thin layers or sputtering [2], but in every case, the main part of the installation remains. As a matter of fact, it is mandatory to isolate the electrolyte compartment from the mass spectrometer (which operates in high vacuum conditions). As such, two PTFE membranes with pores in the range of 20 nm are used [2], which have proven to effectively prevent liquid electrolyte crossing to the mass spectrometer (some vapor can cross them, though). Those two membranes are supported onto a stainless steel frit, mechanically separating the liquid and gas (vacuum) compartments. The vacuum system consists of a rotary pump, associated to two turbomolecular pumps (required for a MS vacuum), enabling a cascade of vacuum from the electrochemical cell to the MS quadrupole [2].

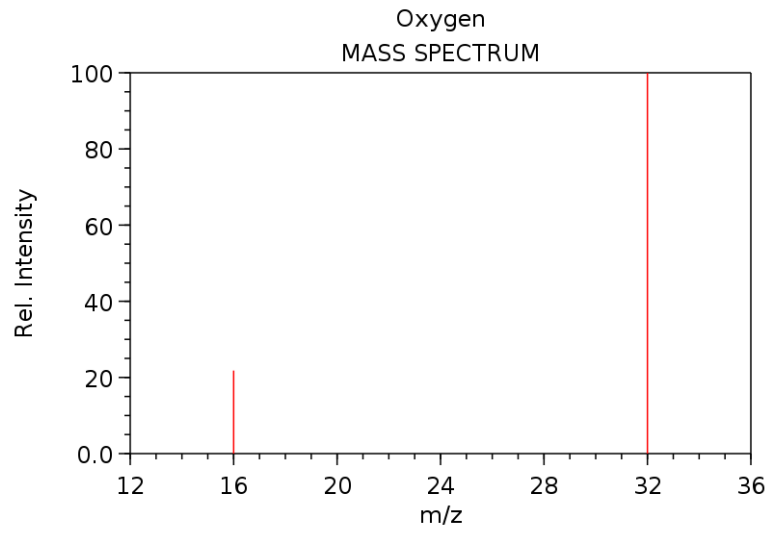
The MS principle allow to detect species at the spectrometer. The spectrometer detect compounds in respect to their mass to charge ratio [3, 4] (m/z), the mass here being the molar one. When a compound arrives at the spectrometer, in undergoes an electron ionization (equation II.1)



During this process, the M molecule undergoes fragmentations (thus breakage in the bounds). Two paths can occur, the first being the breakage of M into a radical and an ion with an even number of electrons. The second is the breakage of M into a molecule (no charge) and a new radical cation. As a consequence, each primary product undergoes fragmentation and so on (with different m/z that are characteristic of the incoming molecule M). All these ions are separately detected in the mass spectrometer, and the relative abundance versus the m/z is the signature of one compound.

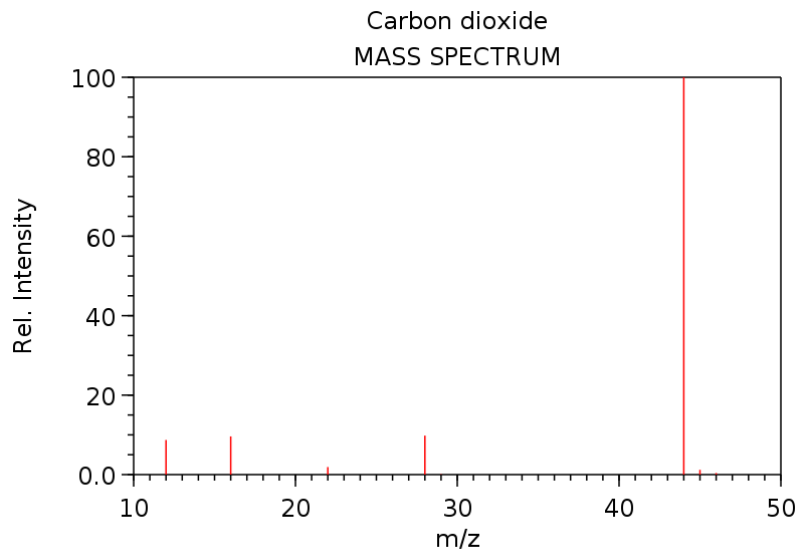
For each compound (for instance oxygen), the m/z corresponding to its molar mass (32 g/mol for oxygen) is always detected (thus for the O_2^{*+} specie), which render its detection very easy by the mass spectrometer. However it is mandatory to ensure that those fragments correspond only to the species at stake. In our case, the detection of either carbon dioxide or oxygen in Dimethyl Sulfoxide is aimed. It is thus mandatory to choose two m/z that can represent only the specie we want to detect.

The mass spectrum of Di-oxygen, Carbon Dioxide and Dimethyl Sulfoxide are subsequently depicted in Figures II.2-4.



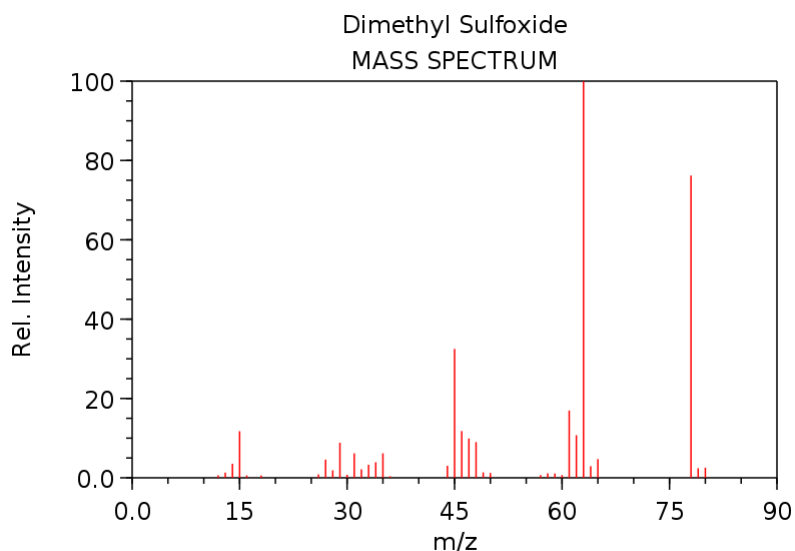
NIST Chemistry WebBook (<http://webbook.nist.gov/chemistry>)

Figure II. 2 : Mass spectrum of Di-oxygen.



NIST Chemistry WebBook (<http://webbook.nist.gov/chemistry>)

Figure II. 3 : mass spectrum of Carbon Dioxide

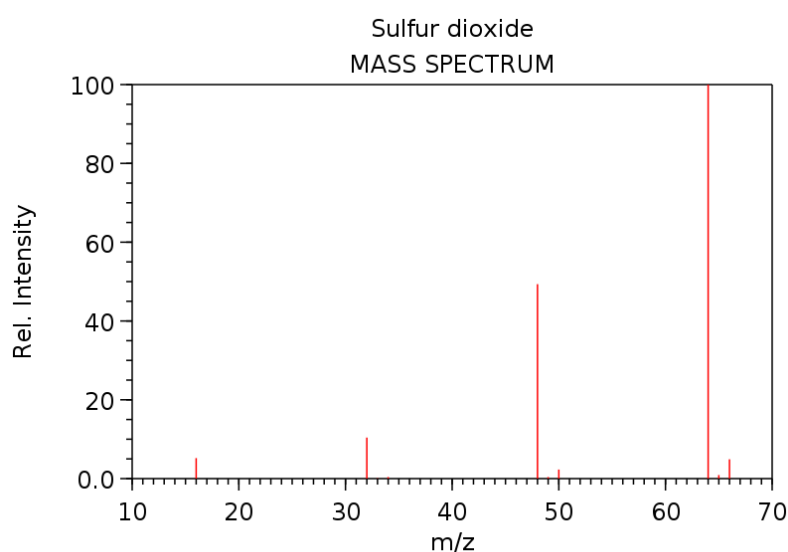


NIST Chemistry WebBook (<http://webbook.nist.gov/chemistry>)

Figure II. 4: mass spectrum of dimethyl sulfoxide

From Figures II.2 and II.3 it appears clearly that the m/z of 32 and 44 corresponds respectively (and only) to oxygen and carbon dioxide. Thus it will be the two “signature” m/z for these compounds. Concerning the Dimethyl Sulfoxide, various m/z can be detected, with a most intense m/z at 63. Dimethyl sulfoxide oxidation at high potential leads to the formation of dimethyl sulfone [5], which is a non-volatile, and insoluble specie (thus not detectable by DEMS as it will not cross the PTFE membranes). However, the authors of Ref [5] also speculate to the possible degradation of dimethyl sulfoxide into sulfur dioxide and methane, which are gaseous.

The mass spectrum of those compounds are depicted in Figures II.5 and II.6.



NIST Chemistry WebBook (<http://webbook.nist.gov/chemistry>)

Figure II. 5 : mass spectrum of sulfur dioxide

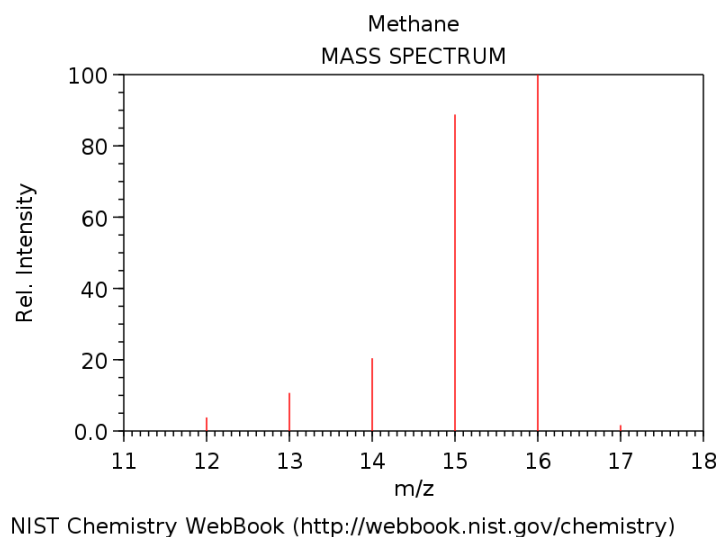


Figure II. 6 : mass spectrum methane

The more intense contributions for the sulfur dioxide are detected at a m/z of 48 and 64, whereas, the more intense signal can be registered at an m/z of 16 for methane. In this scope m/z values of 15, 16, 48 and 64 will also be selected in the program for their detection. In order to determine if the decomposition products are indeed detected by DEMS, linear scan voltammetries in Ar-purged electrolyte (0.2 M LiClO₄ in DMSO), with Panex 30 carbon cloth as the working electrode were conducted. The results in reduction (from OCV to -1.5 V vs. Ref) is presented on Figure II.7, and results in oxidation (from OCV to 1 V vs. Ref) is presented on Figure II.8.

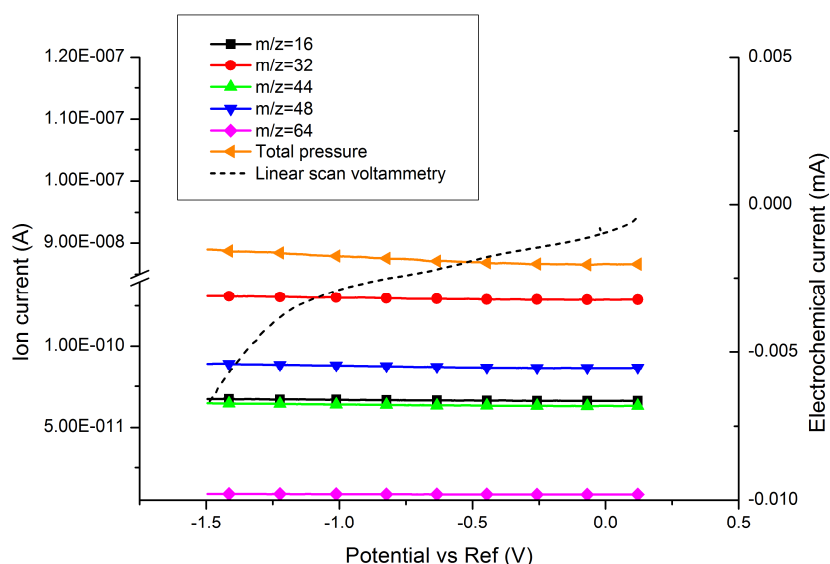


Figure II. 7: Differential Electrochemical Mass spectrometry experiment, from the Open circuit voltage to -1.5 V vs. Ref. primary Y-axis: Ion current of gases detected at the SEM; Secondary Y-axis: Electrochemical current. Scan rate of the LSV: 2 $mV s^{-1}$.

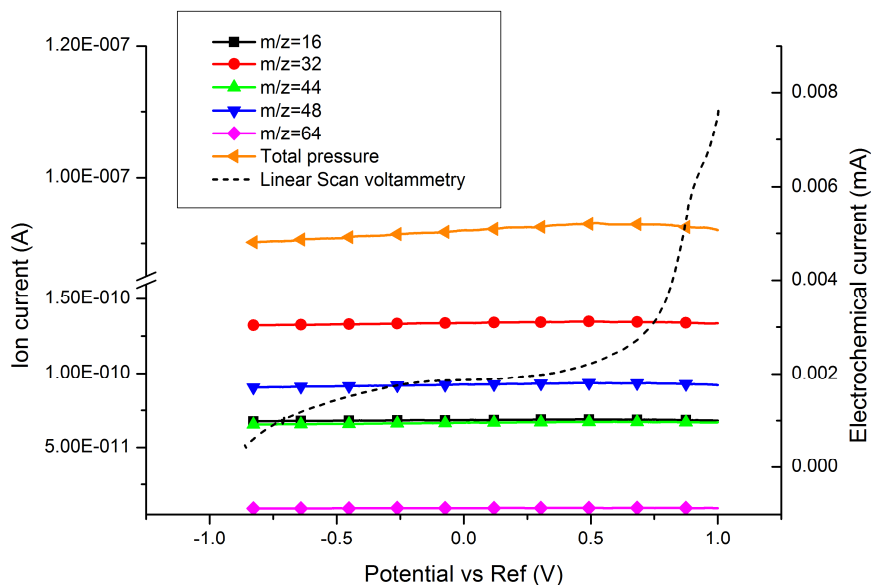


Figure II. 8: Differential Electrochemical Mass spectrometry experiment, from the Open circuit voltage to 1 V vs. Ref. primary Y-axis: Ion current of gases detected at the SEM; Secondary Y-axis: Electrochemical current. Scan rate of the LSV: 2 mV s^{-1} .

The results of Figures II.7 and II.8 support the theory of Krtil *et al* [5], as no m/z fragments of SO_2 ($m/z = 48$ and 64) and of CH_4 ($m/z=16$) are detected when the solvents oxidation and reduction occur. Thus, the decomposition product of DMSO at high potential is probably dimethyl sulfone, and as it is solid, it will never cross the PTFE membrane (thus, it is not detectable by DEMS). Also, no oxygen ($m/z=32$) nor CO_2 ($m/z=44$) are detected in Ar-purged media. The absence of detection of oxygen is normal as the electrolyte is Ar-purged (thus no ORR or OER can be observed), and the absence of CO_2 detection shows that the Panex 30 is resistant to corrosion at the “high potential” values experienced here (in the absence of O_2 and ORR products).

b. Raman Spectroscopy

Raman spectroscopy lies on a similar principle than IR spectroscopy [6]. A monochromatic light (LASER) irradiates the sample, the latter producing reflected, adsorbed and scattered radiations (which are called Raman scatter). Plotting the scattered radiations (intensity) versus the Raman shift (which is the difference between the frequency of the analysis and the one of the incident radiation, in cm^{-1}) allows a non-destructive analysis of the sample, and gives insight on the molecular composition of the sample (as very specific vibrational modes occurs for a given bound, for instance, O-O bounds scattering occurs at very specific wavelength (between 845 and 900 cm^{-1})).

In our case, Raman spectroscopy was used to analyze the contributions of the D and G bands of carbon materials (between 1200 and 1800 cm^{-1}), as various contributions, corresponding to either amorphous carbon, graphitic lattice, perfect graphitic lattice, or amorphous graphitic phase can be detected (and fitted) at very specific wavelengths [7–11].

The experiments were conducted *ex situ*, as the aim was to compare the differences between the pristine materials, versus the discharged one. The apparatus consisted of a Renishaw In-Via, working with an Ar-LASER (specific wavelength: 514 nm). The LASER power was set at 5 mW, and a transmission filter of 10% was used for the sample protection. The detector used on this device was a Peltier-cooled charge coupled device camera (CCD). The objective used for the analysis was a x 50 ULWD.

The samples were then fitted, thanks to LabSpec 4.18 (Horiba company), to conduct a fine analysis of the peaks, and were re-drawn using Origin (Origin lab®).

c. Field-Emission Gun-Scanning Electron Microscopy (FEG-SEM)

Scanning Electron Microscopy (SEM), in contrast with optical microscopy, uses electrons (which possess wavenumbers below the one of visible light), to carry analysis [12, 13]. In this scope, electrons are emitted by an electron gun, in strong vacuum conditions, and are directed to the sample. When those electrons encounter the sample, secondary electrons of lower kinetic energies are emitted. Those electrons poorly penetrate in the sample and can be deflected to the secondary electrons detectors with low potential differences (about 200-400 V): therefore, they give an information on the topography (morphology) of the surface (as the intensity of the signal depends both on the nature and the morphology of the substrate where the electron gun focus).

Another information can be obtained with backscattered electrons, as in contrast with the secondary electrons, they penetrate deeper in the sample, and are elastically backscattered, *e.g.* in the direction opposite to the incoming electrons. The rate of emission depends strongly on the atomic number: when the latter increases, so does the former. Thanks to this property, it is possible to obtain images with a chemical contrast and thus spot on the image zones where heavier elements are present versus zones where lighter elements are present (for instance a deposit of Niobium or Copper onto carbon).

In our case, the FEG-SEM was a Zeiss Ultra 55, specifically designed to enhance the image resolution at low beam energies (below 5 kV), thus limiting greatly the brightness of the image (as the lower the beam energy, the lower the amount of backscattered electrons detected). The detector used for the

morphological analysis was the InLens (a detector which is placed parallel to the electron gun, in the column), and were performed at 3 kV (at this energy, a very low amount of backscattered electrons will be detected), thus enhancing the quality of the morphological surface analysis (for this voltage, the brightness is mostly due to the morphological differences on the surface, for InLens detection of secondary electrons).

d. X-Ray Energy Dispersive Spectrometer (X-EDS)

The X-EDS experiments were conducted on the FEG-SEM Zeiss Ultra 55, using Bruker Esprit 2.1® software, with a resolution of 123 eV. The X-EDS spectra were then redrawn using Origin. X-EDS analysis allows the detection and quantification of specific elements [12, 14] (heavier than carbon), thanks to characteristic X-rays emitted by the sample. When the electron beam encounters the sample, various electrons and electromagnetic waves are emitted from the sample (including X-rays). Those X-rays are emitted following the following scheme (simplified here): when the electron beam encounters an electron from the inner (for example K shell) shell of the element, a vacant position is created. An electron from the outer shell (here L) comes into the vacant position, and it emits an X-ray, with an energy characteristic of the difference of energy between the outer shell and the inner shell, for one element. All elements (that can be detected by X-EDS) possess a K shell. Heavier elements (for $Z > 5$) possess K and L shell, and elements heavier than sodium ($Z > 11$) possess M shells. Thus, using a specific detector, it is possible to measure the energy of those characteristic X-rays, and to determine the elemental composition of the sample. It must be noted, however, that the precise chemistry of the sample cannot be determined by SEM X-EDS. For instance, if a sample contains niobium oxide, both niobium and oxygen will be detected by X-EDS, but the nature of the oxide cannot be detected (for example if it is NbO_2 or Nb_2O_5 ...etc.). Besides, the analysis can only be considered quantitative for smooth and homogeneous surfaces, and with dedicated references (which is not at all the case herein); as such, the present X-EDS analyzes will only be considered semi-quantitative.

e. UV-Visible Spectrophotometry

The principle of UV-Visible spectroscopy relies on the absorption of ultraviolet or visible radiations, by the analyzed sample [15]. This absorption can be detected in a large domain of wavelength (from 190 to 800 nm), which corresponds to the region of ultraviolet radiation (190 to 400 nm) and to the visible radiation (400 to 800 nm). The energy of the UV-Visible radiation is of about 6.5 to 1.5 eV,

which corresponds to energies of electronic transitions of molecules. Most molecules are in their fundamental vibrational states at ambient temperature [15], thus several rotations state can be occupied for one molecule, according to the law of Boltzmann. Those rotations states are absorbing at very specific wavelength and are characteristic of a molecule. The setup of a UV-Visible spectrometer is fairly simple. Firstly, the sample to be analyzed is placed in a cell (usually in quartz as no radiation is absorbed by the cell from 800 to 200 nm), and a radiation of a specific wavelength (and intensity I_0) is directed to the sample. When the radiation goes through the sample, it can absorb radiation (if a vibration mode occurs at this wavelength), which decreases the intensity of the incoming radiation. When the radiation passed all the way through the cell, it is analyzed by an electronic detector. The absorbance of the sample can be determined at this wavelength as: $A = \log(I_0/I)$, with I_0 , the intensity of the incident radiation, and I , the intensity detected by the detector. If the wavelength of the source is changed, the absorbance will change, and the UV-Visible spectra can be obtained, by plotting the Absorbance, versus the wavelength. It must be noted that the UV-Visible spectrum of any molecule is dependent on the solvent in which it is dissolved, as it interacts strongly with it. For this purpose, the UV-Visible spectrophotometry is rather used for a quantitative analysis (thanks to the Beer-Lambert law, where the Absorbance at a peak depends on the concentration of the sample C , the molar attenuation coefficient ϵ , and the length path of the cell: $A = \epsilon \cdot l \cdot C$) than for a qualitative analysis, as it is highly difficult to attribute a peak, to a vibration mode of the sample to analyses. Nevertheless, the impact of a reactant on a sample can be observed by UV-visible spectrometry (if the same solvent is used), as changes in the spectra might occur, which will indicate either a bounding or change in the chemistry of the sample. The spectrometer used for the experiments was a Varian Cary 50[®], with 1 cm wide quartz cells filled with the sample in an Ar-filled glovebox and isolated from the ambient atmosphere by PTFE caps. The software used for the data acquisition was Cary WinUv[®]. The data were then extracted and redrawn in Origin.

f. X-ray Photoelectron Spectroscopy (XPS)

The Spectrometer used for these analysis was a XR3E2 (vacuum generator), using a Mg K α (1253.6 eV) X-ray source. The power used was 300 W (15 kV, 20 mA), and the kinetic energy of the photoelectrons was measured thanks to a hemispherical electron analyzer. The experiments were conducted with strict conditions with very low pressure (below $10^{-9}/10^{-10}$ mbar), and performed with 0.1 eV increments, and 50 ms dwelling times. The charging effect was corrected thanks to the C1s peak. In the literature, the C 1s peak of C-H species (contamination carbon) is located at 285 eV [16].

Thus all the XPS spectra are corrected thanks to the shift value between the experimental value of the C 1s, from 285 eV. This shift varies from one experiment, to one other. The software used for the fitting of the peaks was Thermo Scientific™ Avantage, and the spectra along with the fits were redrawn, using Origin®.

Among the techniques that allow to analyse the composition of a sample, the XPS is one of the most reliable [17]. For this technique, mono-energetic photons (with an energy equals to $h\nu$, where h is the Planck constant and ν the frequency) are accelerated onto the sample to analyze. Photoelectrons are produced from the sample and can be analyzed by the spectrometer. The emitted photoelectrons are characterized by their kinetic Energy (E_c) and their wave vector $\hbar.k$ (where $\hbar = h/2\pi$ and $k = 2\pi/\lambda$, λ being the wavenumber of the photoelectron). The direction of emission is not a key parameter, except for single crystals (which will not be the case in the present thesis). An XPS spectrum is usually the plot of the number of photoelectrons detected (N , in counts) versus the kinetic energy of the photo-electron detected (E_c). As a matter of fact, the binding energy (of the atom stroke by the photon) can be measured thanks (equation II.2):

$$h\nu = E_1^F + E_c + \phi_{sp} \quad (II.2)$$

With $h\nu$, the energy of the photon sent by the source, E_1^F , the binding energy of the bound stroke by the photon, E_c , the kinetic energy of the photoelectron emitted by the sample (measured) and ϕ_{sp} , the end work of the spectrometer (which is a constant known for each spectrometer).

As such, the kinetic energy of the photoelectron emitted by the detector is directly proportional to the binding energy (as $h\nu$ is known, it is the energy of the photon sent by the source, and ϕ_{sp} is a constant), which depend only on the nature of the bound (thus the species evolved in the bound, at their oxidation state). Thanks to this property, it is possible to observe peaks on XPS spectra of s, p, and d bands. Each elements possess a band more intense than the others, (for instance for niobium, the most intense band correspond to the $3d_{5/2}$ orbital and is located in the region of 202-211 eV) [16]. The presence of the element in the sample is confirmed by the presence of the other bands of the elements, in the spectrum, each being observed in a specific energy range (of 10 eV). As an illustration, again with niobium, the bands of the following transitions (with their kinetic energy in eV) are expected: 3s (467 eV), $3p_{1/2}$ (376 eV), $3p_{3/2}$ (361eV), and $3d_{3/2}$ (205eV), $3d_{5/2}$ (202 eV), 4s (56 eV) and $4p_{1/2}$ (31 eV) [16].

It is the shift on the most intense band position that gives insight into the nature of the chemical bound involved: as an example for the $3d_{5/2}$, the positions expected for metallic niobium will be 202 eV, niobium nitride : 204 eV, niobium monoxide : 204 eV, niobium pentoxide (Nb_2O_5) : 207.5 eV [16]. Of course, the information will be completed by the analysis of the shift of the atom, bound with the

metal (as such oxygen for oxides, or nitrogen for nitrides, etc.), in order to confirm the nature of the bound (for instance for O1s: metal oxides: in the range of 528-531 eV, hydroxides: in the range of 531-532 eV, etc.).

XPS experiments also allow the detection of Auger electrons, which contribute to the XPS spectrum as well as the other XPS peaks. These electrons allow their own spectroscopic method, that will not be discussed here (as it was not used). Parasites peaks [17] can also be detected on the XPS spectrum such as:

- Satellites peaks due to the energy source: an X-ray source (or UV-Source) which non monochromatic, emits small peaks, before the most intense peak of the sample. They will be denominated as "sat".
- Peaks due to the loss of energy: those peaks are observable after all the most intense peaks of each elements, comprised in the sample. They are usually small variations of the baseline on a range of 15-20 eV. Those peaks will be denominated "Plasmon", as they originate mostly from the excitement of Plasmon (quantified oscillation of plasma).
- Satellites multi-electronic peaks: during the photo-ionization phenomenon, two electron processes have a certain probability to occur. This can be observed by the apparition of small satellites peaks, next to the most intense peak of each constituent of the sample, at lower kinetic energies.

g. Ellipsometry

The spectrometer used for these analysis an Accurion® nanofilm ep_3. The manipulations were conducted with a monochromatic light of 532 nm, in AOI mode (Angle Of Incidence), between 50 and 80 degrees. The step used was of 5 degrees and the fittings were conducted with an *n.k* fixed model (*n* and *k* values fixed, with a value of 0 for *k*).

Ellipsometry is a technique that allows the analysis of surface and thin films, based on the change on the light polarization, by reflection on a planar sample [18]. To simplify, a polarized light is directed to the sample; when it encounters the sample, it can be reflected (with the same angle to the substrate than the incident radiation, with however a change in the polarization of the light), or transmitted (change of the angle). The spectrometer analyses the intensity and the polarization of the reflected light and compares it to the light emitted. The physical parameters (thickness, optical density...) are calculated thanks to models and fitted to the experimental data. This method is widely used in the field of microelectronics for the measurement of thin layers [19], as it is a fast-non-destructive technique. However, the thickness measurements can only be conducted on homogeneous, highly

planar and conformal layers. If not, the values given by this method will be far from the actual value of the thickness of the deposit.

h. X-ray Diffraction

X-Ray Diffraction is a technique that allows the detection of crystalline material [20]. If a material is crystalline, it will diffract the X-Rays with clear peaks, which correspond to the "signature" of this material, in the crystalline form that it is analyzed (*i.e.* centered cubic, hexagonal...etc). The XRD pattern is obtained thanks to constructive interference, between the sample, and a monochromatic beam of X-Rays. Thus, a clear identification of a compound is feasible thanks to this non-destructive technique (if the sample is crystalline), and information such as the average crystallite size, strain and crystal defects can be obtained.

References

1. Vosburgh WC, Cogswell SA (1943) Complex Ions. VIII. Pyridine-Silver Ions. *J Am Chem Soc* 65:2412–2413.
2. Baltruschat H (2004) Differential electrochemical mass spectrometry. *J Am Soc Mass Spectrom* 15:1693–1706. doi: 10.1016/j.jasms.2004.09.011
3. Hoffmann E De, Stroobant V (2007) Mass Spectrometry - Principles and Applications. *Mass Spectrom Rev*. doi: 10.1002/mas.20296
4. Denat F, Umr I, Bp AS, Franck D (2005) Spectrométrie de masse. 33:
5. Krtil P, Kavan L, Hoskovcov I, Kratochvilov K (1996) Anodic oxidation of dimethyl sulfoxide based electrolyte solutions: An in situ FTIR study. *J Appl Electrochem* 26:523–527. doi: 10.1007/BF01021976
6. Barbillat J, Bougeard D, Buntix G, et al (1999) Spectrométrie Raman. *Tech. l'ingénieur* 33:
7. Rodrigues Castanheira LF (2014) Corrosion of high surface area carbon supports used in proton-exchange membrane fuel cell. Université Grenoble-Alpes
8. Ferrari AC, Robertson J (2000) Interpretation of Raman spectra of disordered and amorphous carbon. *Phys Rev B* 61:14095–14107. doi: 10.1103/PhysRevB.61.14095
9. Jawhari T, Roid A, Casado J (1995) Raman spectroscopic characterization of some commercially available carbon black materials. *Carbon N Y* 33:1561–1565. doi: 10.1016/0008-6223(95)00117-V
10. Nistor L, Landuyt J, Ralchenko V, et al (1994) Direct observation of laser-induced crystallization of aC: H films. *Appl Phys A Mater Sci Process* 58:137–144. doi: 10.1007/BF00332170
11. Robins LH, Farabaugh EN, Feldman A (1990) Line shape analysis of the Raman spectrum of diamond films grown by hot-filament and microwave-plasma chemical vapor deposition. *J Mater Res* 5:2456–2468. doi: 10.1557/JMR.1990.2456
12. JEOL company Scanning Electron Microscope A to Z.
13. Ruste J (2015) Microscopie électronique à balayage: Images, applications et développements. *Tech l'ingénieur* 33:24.

14. Despujols J (2000) Spectrométrie d'émission des rayons X. Fluorescence X. Tech l'ingénieur 33:18.
15. Breuil P, Bouchoux G (2014) Spectrophotométrie d'absorption dans l'ultraviolet et le visible. Tech l'ingénieur 33:20.
16. Moulder JF, Stickle WF, Sobol PE, Bomben KD (1992) Handbook of X-ray Photoelectron Spectroscopy. doi: 10.1002/sia.740030412
17. Hollinger G (1986) Spectroscopie de photoélectrons : XPS ou ESCA et UPS. Tech l'ingénieur-Archives 33:P2625 1-18.
18. Passaglia E, Stromberg RR, Kruger J (1964) Ellipsometry in the Measurement of Surfaces and Thin Films.
19. Agius B, Siejka J (1977) Analyse de données ellipsométriques provenant de l'investigation de films très minces absorbants et homogènes. Rev. Phys. appliquée 12:
20. Bunaciu AA, Udriștioiu E gabriela, Aboul-Enein HY (2015) X-Ray Diffraction: Instrumentation and Applications. Crit Rev Anal Chem 45:289–299. doi: 10.1080/10408347.2014.949616

Chapter III.

High Surface Area Carbon-based Materials for High Energy Li-O₂ cathodes: Advantages and Drawbacks

Nothing in life is to be feared, it is only to be understood. Now is the time to understand more, so that we may fear less. – Marie Curie

As discussed in the previous chapter, the Li-O₂ system is, ideally, among the bests technologies to solve the energy issues of our modern society, *e.g.* in the fields of transportation and large-scale energy storage. However, the advent of a practical Li-O₂ secondary system remains a theoretical promise, as it was proven that those systems are impeded by a number of practical barriers, which still have to be overcome. In order to store as much energy as possible, the cathode has to be made of high surface area and electron-conducting materials. At present, the “best” such materials that present sufficiently low cost and high abundance are carbon based (nanotubes, blacks, graphene, etc.). The validation of these materials, and by extension of low costs electrocatalysts based on them (not belonging to Pt-group metals, PGM), for Li-O₂ systems implies that they are active and stable in the adequate experimental conditions; the present chapter will provide such data for a portfolio of such materials.

I. Materials

Four materials are studied in this chapter. Three are metal organic frameworks (MOF), and will be labeled MOF, Phen-MOF and Basolite. The MOF and Phen-MOF materials are produced by the Northeastern University Center for Renewable Energy Technology (Boston, MA), and their recipes of preparation are confidential. The Basolite material refers to the ZIF-8, produced by BASF. The three materials were not used bare; they underwent the same procedure of pyrolysis prior usage in electrochemistry. For better clarity the MOF, Phen-MOF and Basolite labels refers to those materials that underwent pyrolysis. The fourth material is the carbon cloth (Zoltek PX 30® [1], a high-temperature carbonized cloth, *ca.* 406 μm thick, hereafter denoted by Panex 30), used either bare or as the conductive substrate on which the high surface area materials are deposited (for the full cells and DEMS studies).

The materials prepared and pyrolyzed by the Northeastern University Center for Renewable Energy technology (NUCRET) of Northeastern University (Boston, Massachusetts, United-States) were used as received (no transformation of the active material prior to the ink and electrodes processing).

a. Morphologies

SEM images of the carbon cloth and of the three materials at a macroscopic state are presented on Figure III.1, and at the micro-scale (10 kX, 3 kV) on Figure III.2. Because the materials are of different morphologies, the low-resolution images of Figure III.1 were not necessarily acquired at the same

magnifications and the same acceleration voltage (see legend below each micrograph), this matter of fact not preventing the materials' comparison.

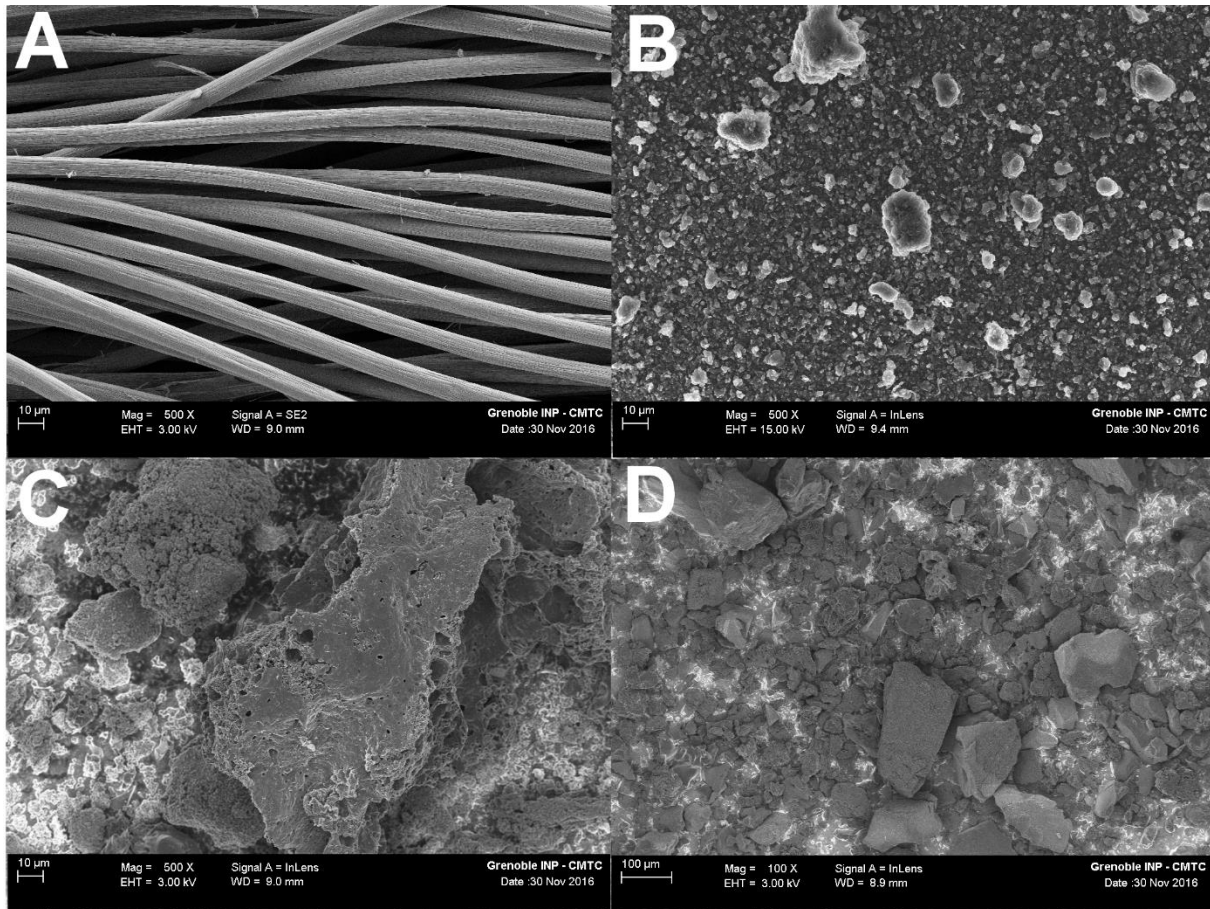


Figure III. 1: Scanning Electron Micrographs, taken at an accelerating voltage of 3 kV (Panex, MOF and Phen-MOF), or of 15 kV (Basolite) with a 500 X (Panex 30, Basolite and MOF) or 200 X (Phen-MOF) magnification. A-Panex 30 carbon Fibers.B- Basolite ZIF-8. C- MOF. D-Phen-MOF

Figure III.1-A displays the clean carbon fibers of the Panex 30 carbon cloth. For the Basolite (Figure III.1-B), some large particles can be observed (maximum size in one direction: 30 μm), but the essential of the material appear to be rather smaller particles (that most-likely constitute the larger aggregates). The MOF material (Figure III.1-C) is constituted of very large particles (greater than 125 μm in the longest direction), with smaller particles (about 10 μm), around the large ones. The Phen-MOF (Figure III.1-D), also bares very large particles (greater than 100 μm in the longest direction), and big particles (from about 50 μm). Overall, the particles appear round-like (for the Basolite), or with very sharp edges (for the MOF and Phen-MOF).

When the magnification is increased, it can be observed on the one hand that the Panex 30 surface (Figure III.2-A) area is smooth, with no or very little porosities (at that scale). On the other hand, with the same magnification, the Basolite and MOF materials (Figure III.2-B & C) have a similar granular

morphology: the large grains observed Figure III.1-B & C are indeed agglomerates of smaller nanoparticles. The Phen-MOF material has a different structure: its surface does not seem to be composed of nanoparticles, but rather of big non-spherical particles, roughened with nano-holes (Figure III.D). To summarize, unlike the Panex 30 cloth, the MOF, Phen-MOF and Basolite materials seem to be of high-surface area.

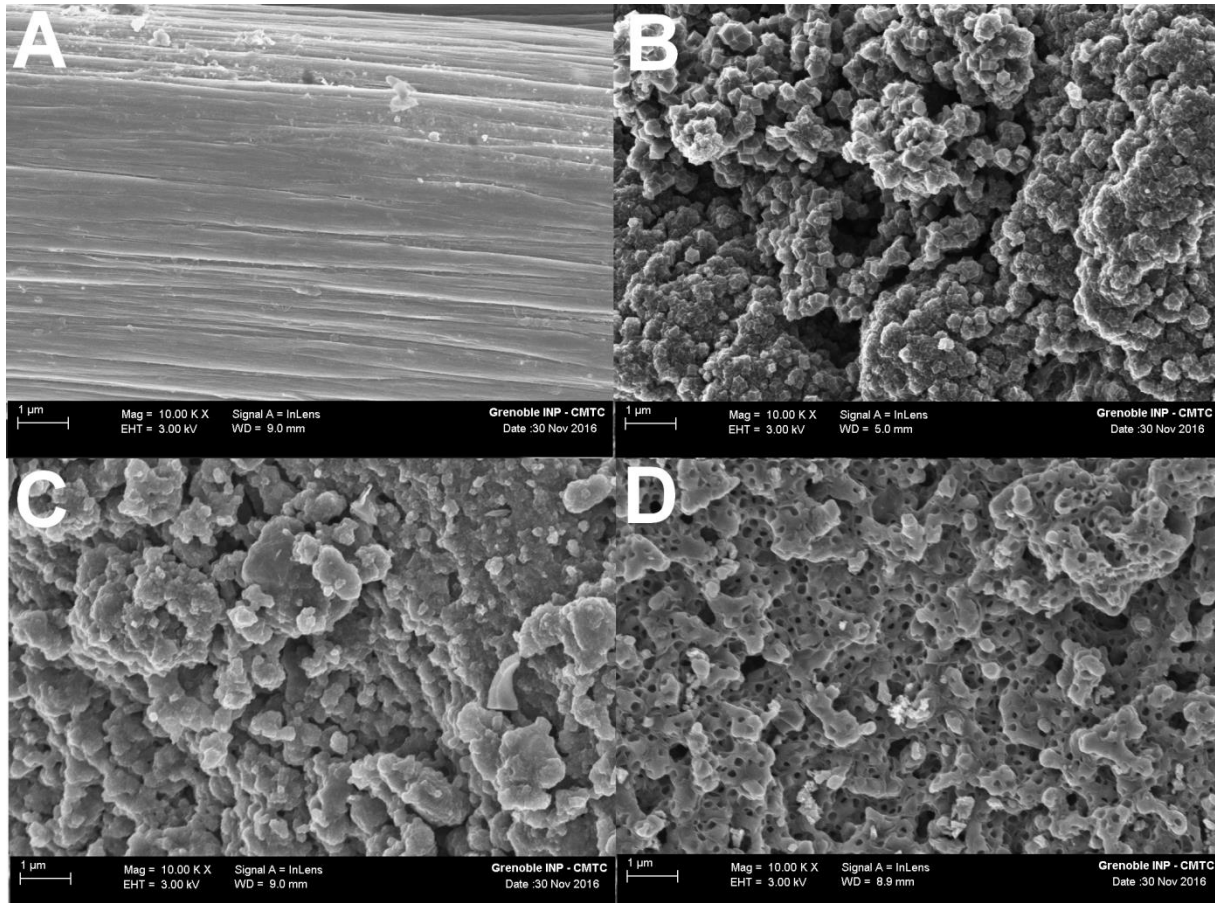


Figure III. 2: Scanning Electron Microscopy Pictures, taken at 3 kV, with a 10 kX magnification. A-Panex 30 carbon Fibers. B- Basolite ZIF-8. C- MOF. D-Phen-MOF

b. Surface areas

BET measurements of the three materials are presented in Table III.1. They confirm that Panex 30 is non-porous, unlike the three other materials. The three high-surface area materials have more or less the same average pore width; however, the Basolite and MOF are outclassing the Phen-MOF in terms of surface area. Thus, the best materials (in term of capacity) are expected to be Basolite and MOF, as more active surface area is expected (if following the conclusions of Abraham [2]), even if the BET area does not always scales with the electrochemically-accessible surface area [3, 4].

Table III. 1: BET measurements of the three high surface area materials. * The data for Panex 30 originates from the provider data sheet.

Label	Surface area (BET), $m^2 g^{-1}$	Adsorption average pore width, \AA
Panex 30*	ca. 0.01	
Basolite	1590	21.5
MOF	1630	22.5
Phen-MOF	959	19.9

c. Raman Spectroscopy

Raman spectroscopy of the pristine carbon cloth and of the three high surface area materials was also performed (using a LASER wavelength of $\lambda = 514 \text{ nm}$), and four representative spectra are presented in Figure III.3.

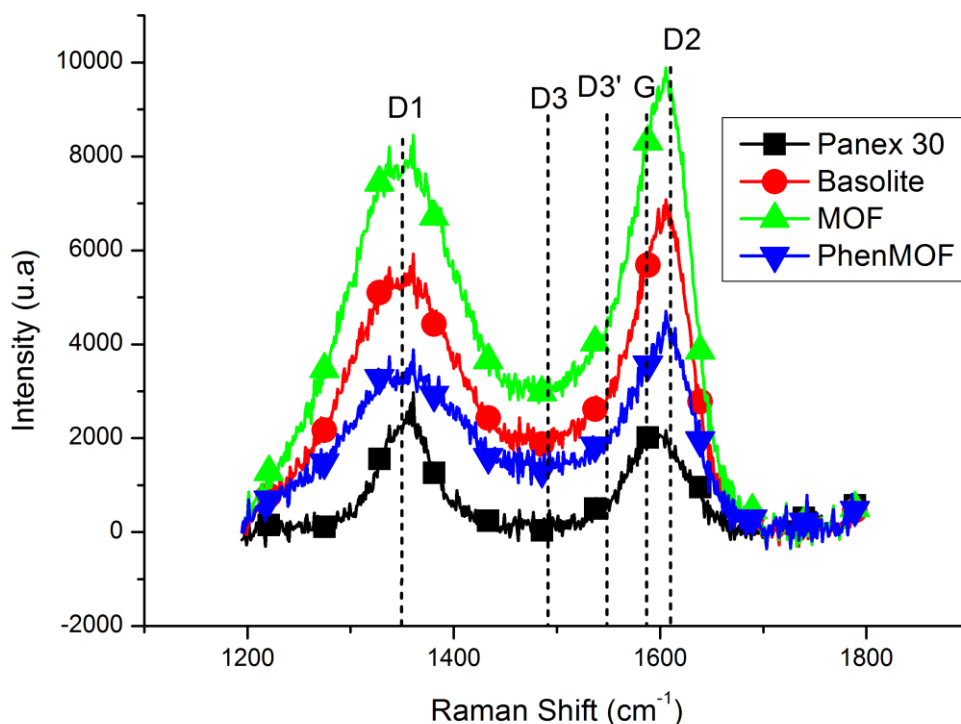


Figure III. 3: Raman spectra of the pristine materials, conducted with a LASER beam of 514 nm in the D and G bands region (from 1200 to 1800 cm^{-1}).

For each material, five Raman analyses were averaged, so an incertitude on the peaks position, height and width could be calculated. As presented in by Castanheira [5], several contributions of carbons chemistries can be recorded on a Raman analyse, the vibration mode correspondence being

presented in Table III.2. Examples of fits for pristine materials, in Labspec 4.18, are presented in Annexes 1.

Table III. 2: Vibration modes observed on high surface area carbon supports with Raman spectroscopy, as presented by Castanheira [5], and others [6–9]

Band	Raman Shift (cm ⁻¹)	Vibration mode
G	ca. 1585	Ideal graphitic lattice [6, 10]
D1	ca. 1350	Disordered graphitic lattice - graphene layer edge [6, 10]
D2	ca. 1610	Disordered graphitic lattice - surface graphene layer [5, 6]
D3	ca. 1495	Amorphous carbon [6, 10]
D3'	ca. 1550	Amorphous graphitic phase [7–9]
D4	ca. 1190	Polyenes, ionic impurities [6, 10]

As seen on figure III.3, no peaks are observed around 1200 cm⁻¹, thus no polyene or ionic impurities are comprised in the materials. The corresponding peaks for the materials, with the incertitude (deviance) on the average peak value for each contribution for the materials are summarized in Table III.3.

Table III. 3: Vibration mode position for the four materials. The average and deviance are calculated on at least three points (the aberrant values are eliminated)

Bands	Material			
	Panex 30	Basolite	MOF	Phen-MOF
D1 position (cm ⁻¹)	1354.8 ± 1.4	1351.1 ± 1.0	1353.5 ± 1.7	1355.1 ± 1.4
G position (cm ⁻¹)	1584.5 ± 3.6	1591.2 ± 0.4	1590.2 ± 4.9	1586.9 ± 1.0
D2 position (cm ⁻¹)	1610.5 ± 5.6	1614.1 ± 0.8	1615.4 ± 3.2	1614.0 ± 0.6
D3 position (cm ⁻¹)	no peak	no peak	no peak	no peak
D3' position (cm ⁻¹)	no peak	1546.7 ± 0.3	1543.5 ± 4.1	1538.8 ± 2.2

The peak of amorphous carbon (D3) is not observable in any of the present samples, but a broad Gaussian peak can be observed in the 1540-1550 cm⁻¹ region. The latter corresponds to amorphous graphitic domains (D3'). In order to ensure the presence of this phase in the samples, the area of the peaks is also monitored and presented in Table III.4, along with the crystallite size (L_a) of the three high surface area materials (Basolite, MOF and PhenMOF), determined by the Knight and White Formula [11] (equation III.1).

$$L_a(nm) = 4.4 \times (I_{D1}/I_G)^{-1} \quad (III.1)$$

Table III. 4: Area of the vibration modes contribution and crystallite size calculation (equation III.1)

Bands	Material			
	Panex 30	Basolite	MOF	Phen-MOF
D1 area	$(1.8 \pm 0.5) 10^5$	$(9.1 \pm 0.6) 10^5$	$(1.0 \pm 0.3) 10^6$	$(7.6 \pm 1.5) 10^5$
G area	$(9.0 \pm 3.7) 10^4$	$(2.2 \pm 0.3) 10^5$	$(2.5 \pm 0.7) 10^5$	$(1.7 \pm 0.4) 10^5$
D2 area	$(7.7 \pm 3.7) 10^5$	$(2.1 \pm 0.2) 10^5$	$(2.3 \pm 0.9) 10^5$	$(2.0 \pm 0.3) 10^5$
D3 area	0	$(2.3 \pm 0.2) 10^5$	$(2.4 \pm 0.5) 10^5$	$(1.8 \pm 0.6) 10^5$
Crystallite size (L_a , nm)	2.21 ± 0.58	1.08 ± 0.06	1.06 ± 0.07	0.96 ± 0.06

From a qualitative view-point, computing the results of Table III.3 and III.4 enables to conclude on several points. Firstly, the Panex 30 carbon cloth is completely graphitized, with no amorphous graphitic phase (D3') detected. Secondly, the high surface area materials all comprise amorphous graphitized phase (D3') in a non-negligible proportion, as the area of the corresponding peak is of the same order of magnitude than the G and the D2 contributions. Thirdly, for the four materials, the graphitic part is not ideal, and half of the area of the G band is attributed to ideal graphitic lattice (G), the other half to disordered graphitic lattice (disordered surface graphene layer - D2); this agrees with the fact that the D1 band (that account only to disordered graphitic lattice edges) is nearly perfectly fitted in the four cases.

From a quantitative view-point, the application of the Knight and White formula to the crystallite size calculation showed that the three high surface area materials have nearly the same crystallite size ($L_a = 1.0/1.1$ nm), whereas the Panex 30 carbon support exhibits a twice larger crystallite size ($L_a = 2.2$ nm), meaning a higher degree of graphitization than the three high surface area materials.

II. *Electrochemical properties*

a. Half Cells

The three high-surface area materials were tested in a three-electrode setup, using the same loading of catalysts (0.8 mg.cm^{-2}) on the Panex 30 substrate; of course, Panex 30, which was also used bare, was not considered at the same "catalyst" loading. The binder used to prepare inks of the MOF, Phen-MOF and Basolite was Arkema Kynar HSV900®, and the weight percentage of active material/binder was 80:20. The ink was prepared by dissolving both the active material and the binder in NMP and left under sonication for 2 hours. It was found that the ink had better

homogeneity when it was heated up to the boiling point of the mixture (with a cap on the top to prevent NMP evaporation), heavily shaken, and deposited right away after this step. The electrochemical characteristic of electrodes prepared in these manners, as tested in three-electrode setup in the DEMS cell, are presented in Figure III.4.

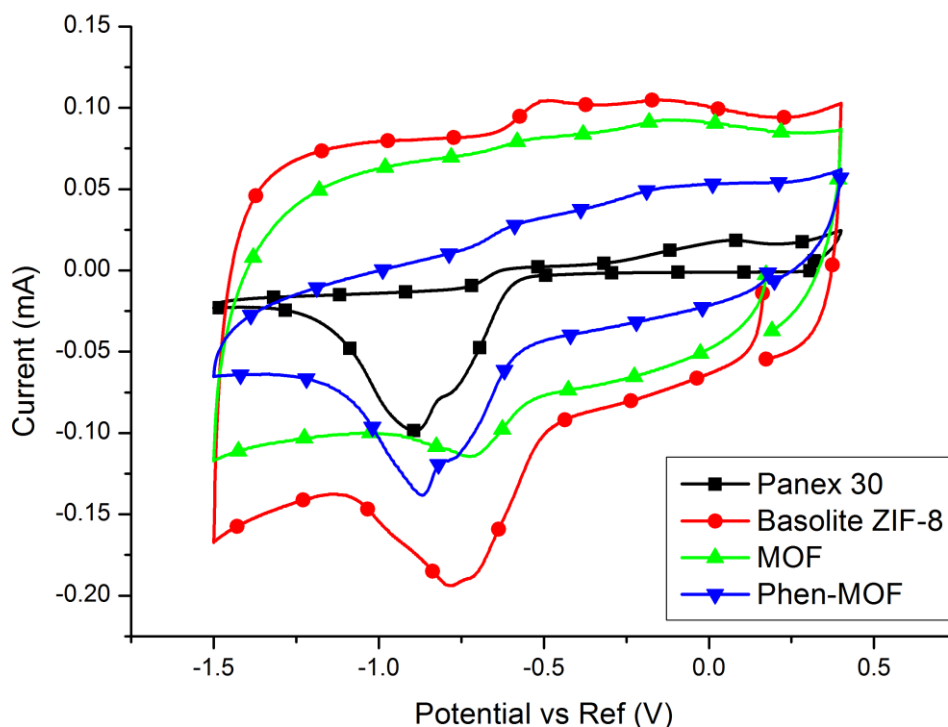


Figure III. 4: Voltamperogram obtained for the three catalyst materials in an O_2 -purged 0.2 M $LiClO_4$ electrolyte. The voltamperogram of the bare Panex 30 substrate is also given for comparison. Scan rate at 5 mV s^{-1} , KF below 100 ppm before the start of the experiment.

As explained above, the binder used for this experiment was PVDF. However, as presented in Chapter I, this polymer is unstable toward ORR discharge product and is prone to *in situ* water production during the experiment [12]. As detailed in this publication, the only stable polymer is polyethylene, which is very difficult to process in an ink, and often requires using super solvent, at the boiling point, to dissolve [13, 14]. This procedure was tried, with high molecular weight polyethylene, and from the author's experience, it was found very difficult to process an ink: as soon the active material was added to the polyethylene/toluene solution, the active materials did instantly precipitate with the polyethylene, ruining any possibility to deposit a correct thin layer of catalyst at the Panex 30 substrate. Thus, for the experiment recorded in Figure III.4, even though the cell was mounted dry (water content usually around 80 ppm at the beginning of the experiment), by the end

of the experiment, the water content could reach values as high as 800 ppm after electrochemistry, due to the decomposition of the PVDF [12].

Considering the performances, it can be seen on Figure III.4, that the ORR proceeds roughly at the same potential for the four materials (around -0.5 V vs. Ref). However, as the surface areas differs a lot from one material to one other, the ORR peak and double layer current densities exhibit different values. It seems at first sight, that the onset of ORR is sifted more positive when the BET area (see Table III.1) increases; nevertheless, this is only a rough estimate: the MOF and Basolite have almost the same surface area, and at the same loading the Basolite material shows greater ORR/OER and double layer currents, confirming that the BET surface area does not necessarily scales with the electrochemical active surface area [3, 4]. Also, compared to Panex 30, MOF and Phen-MOF, the Basolite material seems to enhance the OER, as an oxidation peak can be observed as low as -0.5 V vs. Ref. In order to truly assess if this peak is OER related, operando DEMS must be conducted.

b. Full cells

Inks of these materials were then prepared in NMP with a 80:20 ratio of active materials (per weight) versus binder (Kynar HSV 900), in N-Methyl-2-pyrrolidone, to perform full cell tests and complete these materials' characterizations. The experiments were conducted in DMSO electrolyte (DMSO: anhydrous grade, either from Sigma Aldrich or Alfa Aesar, stored in Ar Glovebox) and dried on 3 Å molecular sieves (Beads, Sigma Aldrich), with LiClO₄ (1 M) as the supporting salt (battery grade, Sigma Aldrich). The loadings used in those full cells were the same for the three materials (Basolite, MOF and Phen-MOF) and was chosen at 0.795 mg of active material per cm² of Panex 30 carbon cloth (geometrical area). Once the ink deposition was made, the electrodes were left to dry at 60°C overnight and placed under dynamic vacuum for 24 hours prior to be processed in the full cell. A bare Panex 30 cloth was also tested as benchmark. As described in section II.a, polyvinylidene fluoride is not stable toward non-aqueous ORR products [12], but it had to be used anyway, in order to be able control efficiently the loading of active material and the ink formulation/processing. However, in order to prevent further water production by polymer-decomposition, Celgard K2045 was used as the separator, as it is only composed of polyethylene (this material being highly stable toward non-aqueous ORR products). The negative electrode consisted of metallic lithium (Sigma Aldrich, ribbon, thickness × W 0.38 mm × 23 mm, 99.9% trace metals basis), laminated on a copper grid, connected to a copper wire. The cell was designed so that oxygen was flushed directly onto the cathode continuously, with airtight inlet and outlet (ensured by a silicon septum). Prior to launching the cell,

oxygen was flushed for at least 1 hour in the cell, and the cell was placed in an antechamber (glove-box like) and flushed continuously with argon to prevent/limit water contamination from ambient atmosphere. The Ar-flushing of the antechamber was maintained during the electrochemical procedure, as described below.

The charge and discharge currents were chosen to be of the same value (0.05 mA) in the four cases, corresponding to a relatively high charge/discharge rate (0.125 A g^{-1} , or 0.1 mA cm^{-2} geometrical). The charging procedure was designed as a CC-CV charge (Constant Current followed by a Constant Voltage). In order to limit carbon oxidation (which occurred above 0.5 V vs. Ref (*i.e.* 4.17 V vs. Li/Li⁺) for the three materials (Basolite, MOF and Phen-MOF), as detected by DEMS), the cut-off voltage was chosen at 4.2 V. The CV step time was limited at 20 hours with a cut-off current below $5 \mu\text{A}$. The Corresponding experiments are presented in Figure III.5.

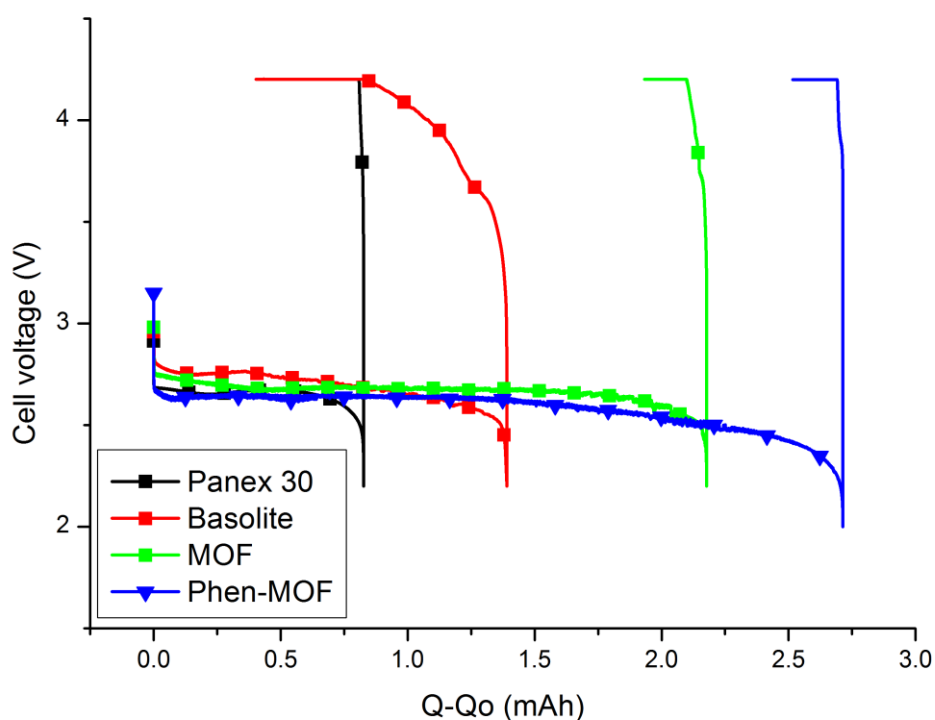


Figure III. 5: Full cell configuration; discharge at $-50 \mu\text{A}$, charge at $50 \mu\text{A}$; cutoff voltage: 4.2 V, maintained for 20 hours, for $I_{\text{charge}} > 5 \mu\text{A}$. One shall note that these very time-consuming experiments were not reproduced in multiple replicates.

The electrochemical performances were unattended: one would have expected that the discharge capacity would depend on the BET surface area, as described by Abraham *et al.* [2]. This was not experimentally observed, and the experimental discharge capacity followed a different pattern: Phen-MOF > MOF > Basolite >> Panex 30 (when for BET surface area: MOF > Basolite > Phen-MOF >>

Panex 30). The reason for this is probably linked to the presence of different reaction sites, which are responsible for the discharge onto the materials' surface. The important data, extracted from Figure III.5 are presented in Table III.5.

Table III. 5: Markers of the active materials efficiency in Li-O₂ Full cell design

Material	Discharge Capacity (mAh)	CC charge (mAh)	CV charge (mAh)	OER/ORR (%)
Panex 30	0.827	0.018	0.076	11
Basolite	1.391	0.556	0.432	71
MOF	2.177	0.081	0.163	11
Phen-MOF	2.714	0.022	0.199	8.2

On the one hand, Table III.5 demonstrates that the OER processes are really sluggish for Panex 30, MOF and Phen-MOF, as depicted by their very low OER/ORR efficiencies (11%, 11% and 8.2%, respectively), indicating that most of the discharged products remained at the end of the charging process. This might indicate that for those materials, the charging shall be done at higher potential, probably because of larger lithium peroxide particles. The latter hypothesis is supported by the fact that most of the charged capacity, for those materials, is occurring during the CV step (therefore, at 4.2 V). However, the cutoff potential cannot be raised up further as it was proven (and will be demonstrated hereafter) in the DEMS experiments, that CO₂ evolves at potentials above 0.5 V vs. Ref (*i.e.* above 4.2 V vs. Li/Li⁺). On the other hand, the Basolite exhibits much better roundtrip efficiency, with an OER/ORR efficiency of 71%; more interesting, most of the OER occurring at low potential (CC step capacity of 40% of the overall capacity), even though a large part also proceeds at higher potential (about 31%). In order to better understand this huge difference of behavior between the four materials, *post test* SEM imaging was conducted on those full cell cathodes after discharge (Figures III.6, III.8, III.10 and III.12). Prior the SEM analyzes, the cathodes were rinsed several time with anhydrous acetonitrile, and dried under dynamic vacuum to efficiently remove the electrolyte (salt + DMSO) from their surfaces, a procedure which shall keep unchanged the presence of ORR products (as Li₂O₂ is non-soluble and stable in Acetonitrile [15, 16]).

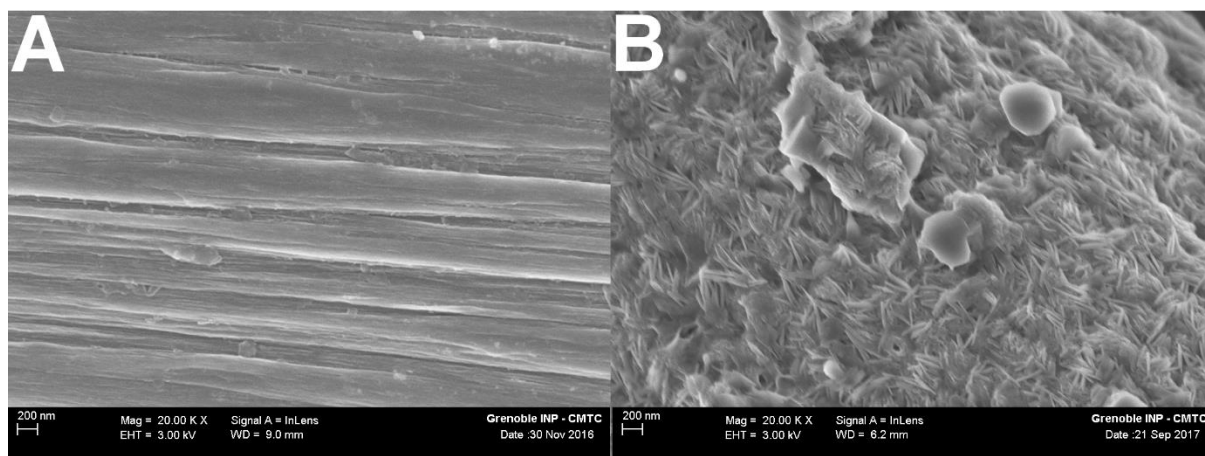


Figure III. 6: SEM micrograph of the surface of a Panex 30 cathode surface at an accelerating voltage of 3.00 kV, magnification 20 kX. A- pristine. B-post test

Figure III.6 shows that the initially smooth surface of Panex 30 (Figure III.6-A) is not observable anymore after discharge (Figure III.6-B). The discharge product morphology is very similar to what is observed in the literature for high depths of discharge (and high regimes of discharge) [17–19]. X-ray energy dispersive analyzes (XEDS) were also performed (Figure III.7): initially Panex 30 comprises only carbon (at least no other elements were observed, which may not rule out the presence of traces). However, the discharged Panex 30 cathode spectra (Figure III.7-B) show a predominant oxygen signal, which may be attributed to lithium peroxide (no CO_2 evolution on Panex 30 was detected by DEMS, which suggests that major carbonate formation is unlikely for this material – see later); sulfur and chloride are also detected. Sulfur may originate from the decomposition products of dimethyl sulfoxide [20] and chloride from either traces of supporting salt (lithium perchlorate) or from its solid decomposition products [21]. Fluorine was not detected, which can be understood by the fact that no PVDF was included in Panex 30 cathodes. Carbon is detected in minority (*versus* oxygen) after the discharge, demonstrating that the layer of Li_2O_2 is "thick" (it hides the underlying carbon).

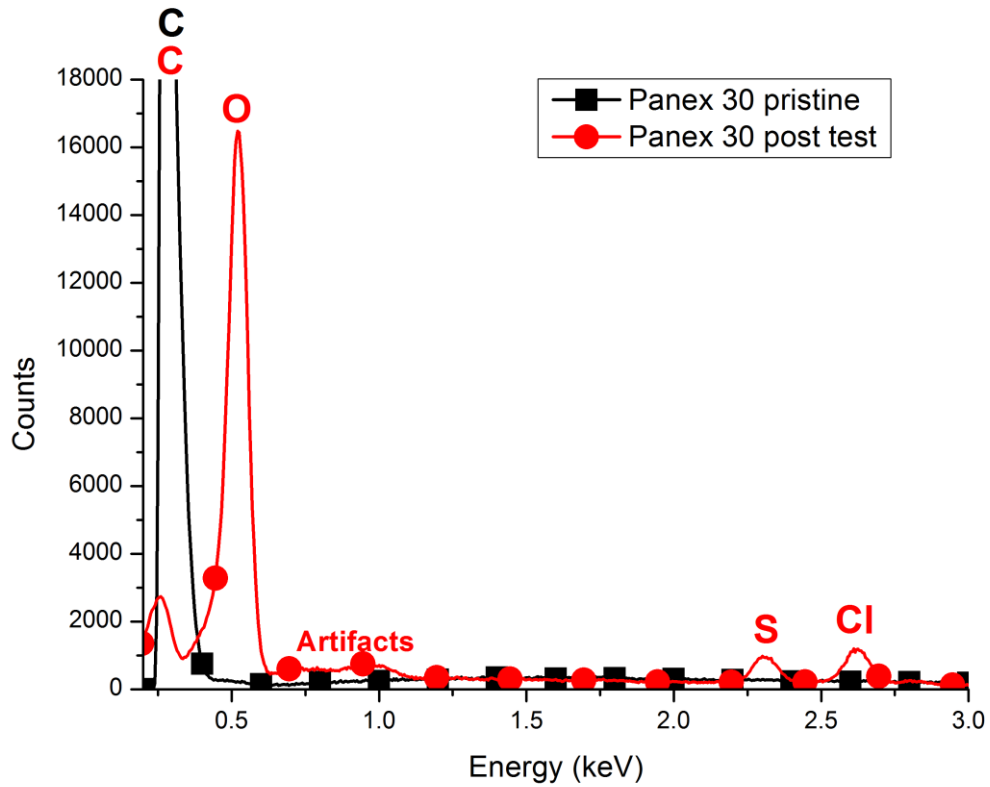


Figure III. 7: XEDS spectra of Pristine Panex 30 (black) and post test Panex 30 (red) cathodes

An identical survey was performed for the used active layers of the high surface area materials. SEM micrographs for Basolite and related XEDS spectra are presented in Figures III.8 and III.9.

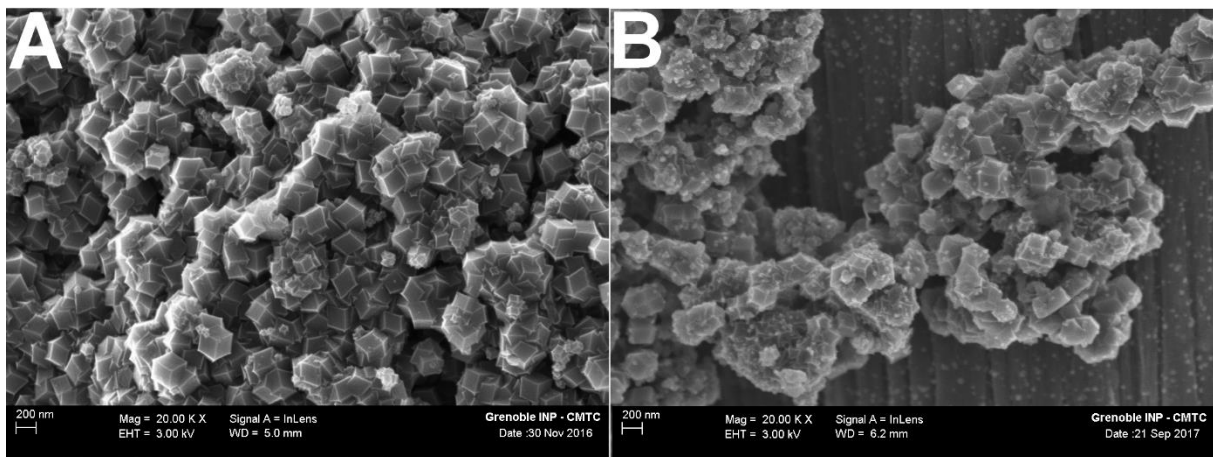


Figure III. 8: SEM micrographs of the surface of a Basolite cathode surface at an accelerating voltage of 3.0 kV, magnification 20 kX .A- pristine. B-post test

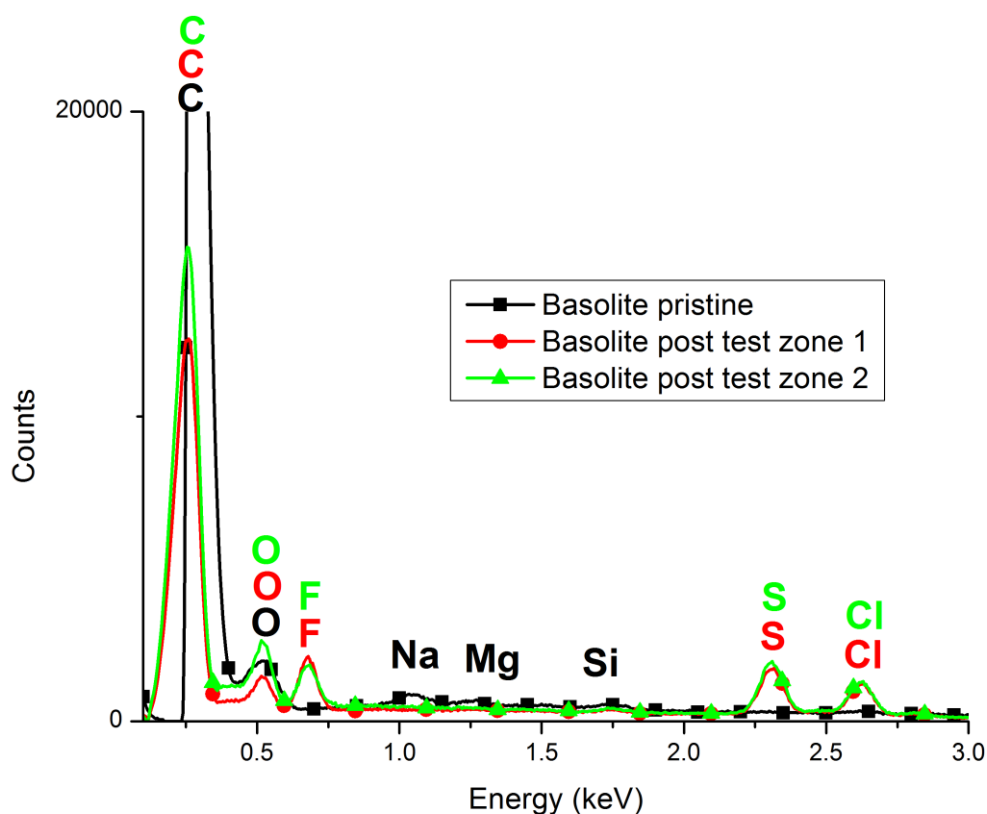


Figure III. 9 : XEDS spectra of Pristine Basolite (black) and post test (red and green) Basolite cathodes

Figure III.8 and III.9 reveal differences of behavior between the Basolite cathode and the Panex 30 cathode. Firstly, the Basolite particles have the shape of nanocubes and those latter are still observable after discharge (Figure III.8-A); the surface of the Panex 30 fiber on which they were deposited are also observed before and after discharge. By comparison with the previous case (Panex 30 Alone), this indicates that lithium peroxide deposition does not occur preferentially on the Panex 30 carbon fiber: the presence of the high-surface area Basolite nanocubes enabled to favor the formation of the discharge product on the Basolite, not on the Panex 30. Nevertheless, remainings of the discharge product can also be observed in the spaces between the nanocubes, indicating that the lithium peroxide has the ability to be formed in the pores between the Basolite particles as well. In other words, the formation of discharge product seems to proceed on any cm^2 available. As adding high surface area Basolite to low surface area Panex 30 greatly increases the overall surface area available for the reaction, this enabled the discharge to last *ca.* twice longer than for Panex 30 (Table III.5). In addition, this extra surface area available did yield smaller size of the lithium peroxide particles upon discharge (compared to those observed on Panex 30), in agreement with the SEM micrographs of Figure III.8. This morphology of the Li_2O_2 particles naturally eases the transport of

electrons and enables their near-complete re-oxidation more efficiently (in contrast with Panex 30 cathode alone), in line with the much better round-trip efficiency for Basolite than for Panex 30 (Table III.5). The XEDS measurements go in line with the conclusions for Panex 30 alone: sulfur and chlorine are observed and probably originate from the decomposition products of the lithium salt and solvent. However in this case, fluorine is also observed, because PVDF was included in the cathode formulation (the latter can be decomposed by lithium peroxide [21]). Finally, the trace elements comprised in the pristine electrode (*i.e.*: sodium, magnesium and selenium) are not observed anymore after discharge, which is not explained here.

The SEM micrographs and XEDS spectra for the MOF are presented in Figures III.10 and III.11.

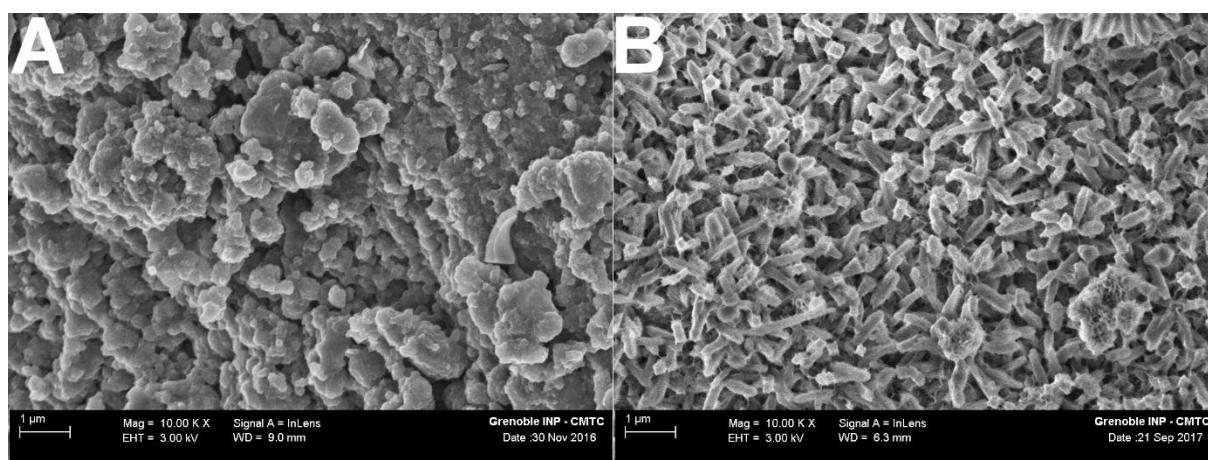


Figure III. 10: SEM micrographs of the surface of a MOF cathode surface obtained at an acceleration voltage of 3.0 kV, and a magnification of 10 kX. A- pristine. B-post test

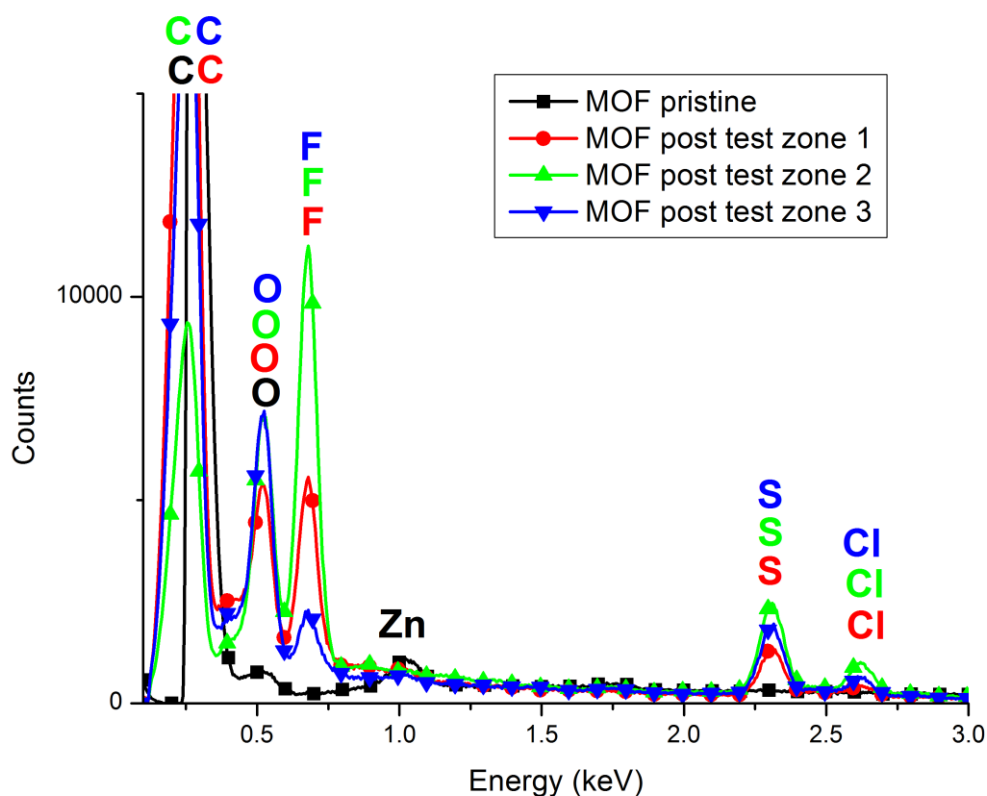


Figure III. 11: XEDS spectra of Pristine MOF (black) and post test (red, green and blue) MOF cathodes

The comparison between the pristine MOF cathode and the discharge one (Figure III.10) are consistent with the behavior in the full cell design: most of the capacity (89 %) could not be re-charged, and this can be accounted for by the fact that the surface of the initial material is not observed anymore on the *post test* micrograph (Figure III.10); instead, crystals of Li_2O_2 are fully covering the electrode surface (Figure III.10-B). The discharged product morphology also differs a lot from what was observed on Panex 30, where its shape resembled nano-flakes. Here, the discharged product has more a micro-rod shape. Also, concerning the pristine material, Zn was observed by XEDS (Figure III.11-A), as it is included in the recipe of the active material. This contribution disappeared on the discharged XEDS spectra, probably because the thickness of the discharged product (Li_2O_2) is too important to enable the detection of the elements of the active material itself (under the Li_2O_2 layer). As for the Basolite, fluorine, sulfur and chlorine are detected on the discharged cathode, probably for the same reason (fluorine from PVDF, sulfur from DMSO decomposition products and chlorine from the supporting salt contribution). In this case, the much larger surface area initially (in theory) available than for the Panex 30 alone did only play a favorable role in the discharge (much larger coulometry of discharge is monitored, Table III.5); it is likely that

the “superior” performance in discharge compared to the previous case of Basolite was a drawback for the recharge, the thickness of Li_2O_2 particles formed being too high to enable an efficient recharge, as accounted for the very modest roundtrip efficiency monitored (Table III.5).

Finally, SEM micrographs and related XEDS spectra for Phen-MOF are presented in Figures III.12 and III.13.

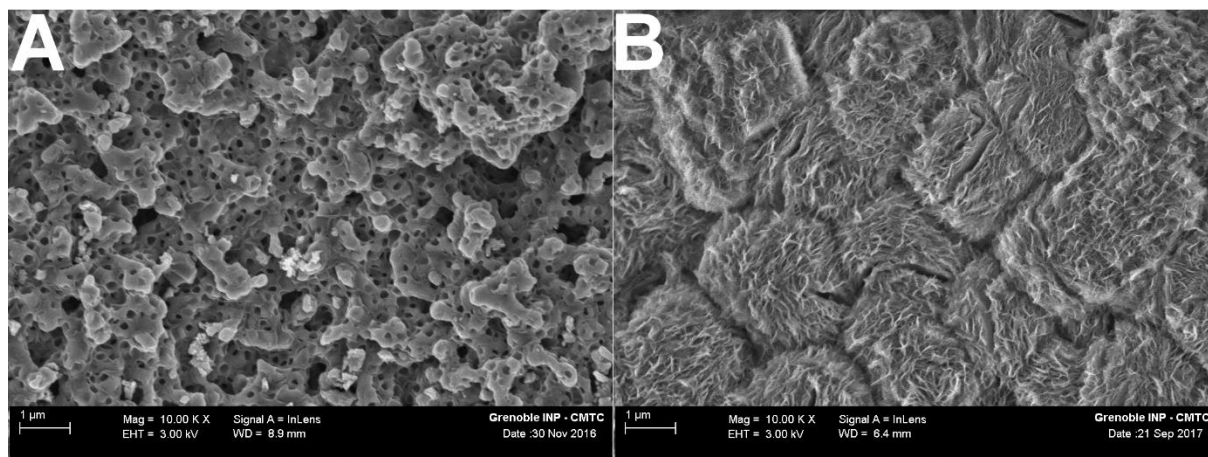


Figure III. 12: SEM micrograph of the surface of a Phen-MOF cathode surface, obtained at an accelerating voltage of 3.0 kV and a magnification of 10 kX. A- pristine. B-post test

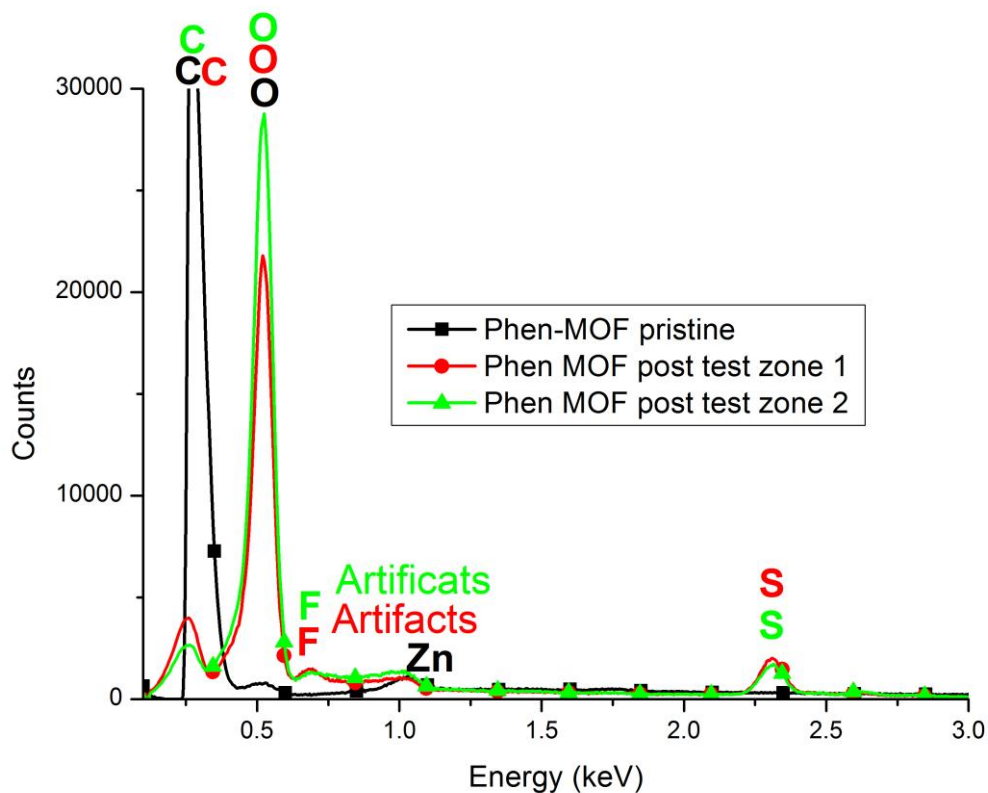


Figure III. 13: XEDS spectra of Pristine Phen-MOF (black) and post test (red and green) Phen-MOF cathodes

As for the MOF material, the SEM micrographs show completely different surface morphologies for the pristine material *versus* the discharged one, indicating a very large coverage of the initial material by Li_2O_2 crystals upon discharge. The behavior of the Phen-MOF therefore parallels that of the MOF. This is consistent to the bad charging process (more than 90% of the discharged product is still on the material surface, Table III.5). Concerning the discharged product morphology, it has more similarities with what is observed on the Panex 30 discharged cathode (Figure III.6-B) than with the MOF (Figure III.10-B), with nano-flakes observable on the surface. Concerning the XEDS analysis, the conclusions are the same than for the MOF: the comprised Zn and Silicon are not observable anymore on the discharged cathode, probably because of the thick deposit onto the electrode surface.

Also, in line with the observations on Panex 30, the deposit appear very thick, as the carbon is detected in minority for the post-test cathode versus the pristine one. Decomposition tracers of the solvent and binder are also observable onto the discharged cathode, as for the other materials.

c. DEMS

DEMS characterizations were performed on these materials to further assess their ORR/OER efficiency (via the monitoring of the O_2 signal), but also their durability in operation (via the monitoring of CO_2 evolution, the latter signing either electrolyte or electrode materials decomposition).

The DEMS characterization of the materials followed a strict procedure: firstly, a stabilization of the DEMS signal is required (at least for one hour and a half), and during this time, no electrochemistry is performed (open circuit potential), and Ar is flushed continuously in the cell to remove oxygen traces as much as possible and to prevent/limit possible water contamination. Then, five cycles were recorded in the Ar-purged electrolyte, from -1.5 to 0.4 V vs. Ref, at 5 mV s^{-1} . For the following step, the electrolyte was purged with purified oxygen (5.0) for at least 45 minutes and five other cycles were recorded in the same experimental conditions than for the Ar-purged experiments. Following this experiment, two cycles were monitored at the same scan rate, still in O_2 -saturated electrolyte, but by extending the upper reverse potential from 0.4 V vs. Ref to 0.7 V vs. Ref.

The O_2 DEMS signal of the first cycles (normal voltage window), associated to the electrochemical current is presented in Figure III.14.

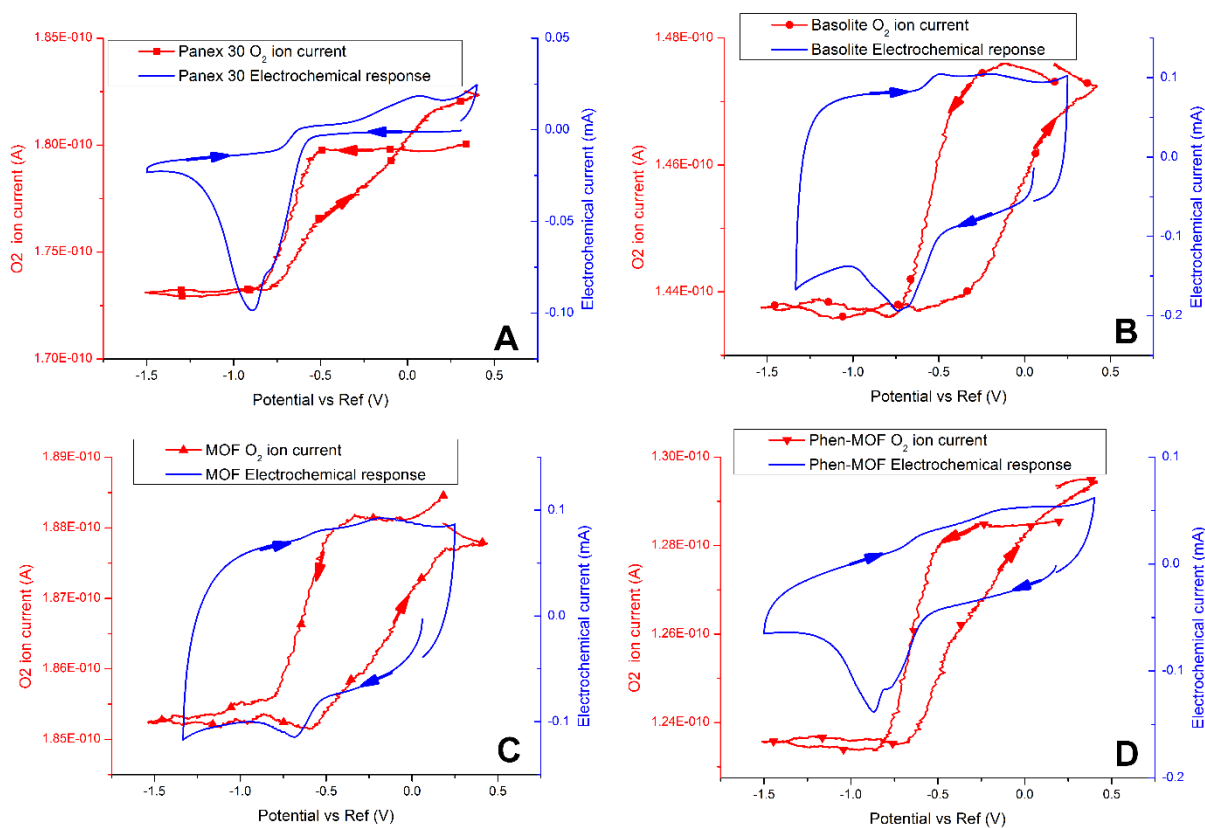


Figure III. 14: O₂ ion current (primary Y-axis) and faradic current (secondary Y-axis) monitored during the voltamperogram at 5 mV s⁻¹, in O₂-saturated 0.2 M LiClO₄ DMSO electrolyte. A-Panex 30. B-Basolite. C-MOF. D-Phen-MOF

Figure III.14 shows that the O₂ ion current starts to decrease at *ca.* -0.25 V/-0.35 vs. Ref during the ORR sweep for Basolite, MOF and Phen-MOF, while a lower value is monitored for Panex 30 (around -0.5 V vs. Ref). Surprisingly, the ORR electrochemical onset potential values do not seem to change: for the four materials, it is monitored at -0.5 V vs. Ref, indicating a discrepancy between the O₂ consumption (monitored in DEMS) and the ORR (electrochemical) current.

This premature O₂ consumption on the three high surface area materials might be linked to a small “electrocatalytic” effect, that could consist of adsorption of oxygen molecule on the high surface area Basolite, MOF and Phen-MOF particles *ca.* 0.15 - 0.25 V above the real (quantitative) ORR. The author does not speculate whether such an effect would have been observed as well on high surface area carbon black, for instance. Interestingly, the small electrochemical oxidation peak, monitored at -0.5 V vs. Ref during the OER for the Basolite does not match any detection of excess (released) O₂ next to the electrode, which probably indicates as well the formation of adsorbates on the catalysts surface upon OER, from the oxidation of Li₂O₂ particles (the same applies to MOF and Phen-MOF, in a lesser extent). On the contrary for Panex 30, the O₂ ion current perfectly matches the electrochemical signal (faradic current), which is a sign that no catalysis occurs for this material (at least owing to its

small surface area, but possibly also at all). These results suggest that upon ORR/OER on high surface area materials, oxygen adsorbs/desorbs at/from the surface and/or absorbs in the small pores; as a result, its consumption/release (and detection in DEMS) is favored/delayed in the earlier steps of ORR/OER, therefore explaining the delay between the faradic and mass spectrometry current values.

One could however claim that the faradic oxidation current could be linked to another parasitic process than the OER, *e.g.* the corrosion of carbon (and related CO₂ emission, as measured by McCloskey *et al.* [22, 23]). In order to test this hypothesis, the CO₂ DEMS signal was also recorded (Figure III.15).

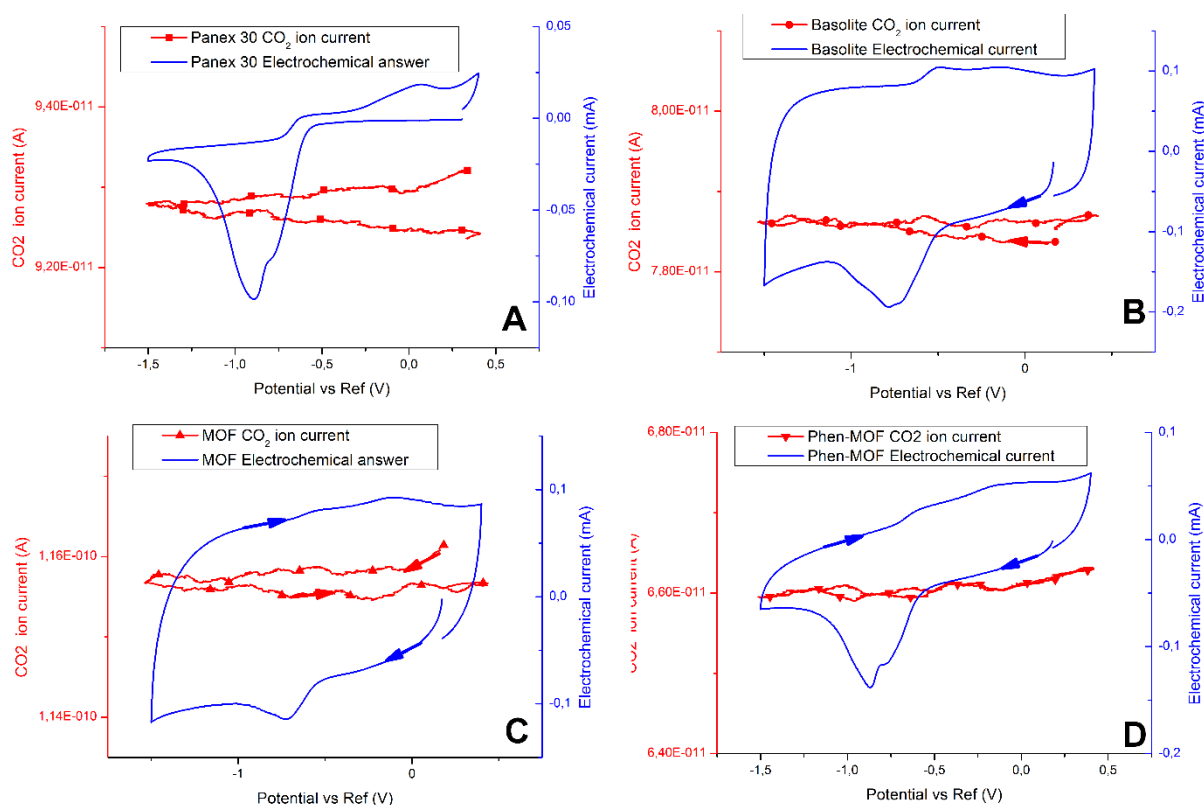


Figure III. 15: CO₂ ion current (primary Y-axis) and faradic current (secondary Y-axis) monitored during the first voltamperogram at 5 mV s⁻¹, in O₂-saturated 0.2 M LiClO₄ DMSO electrolyte. A-Panex 30. B-Basolite. C-MOF. D-Phen-MOF

Figure III. 15 clearly demonstrates that no CO₂ evolution occurs within the tested potential window in O₂-purged electrolyte, whatever the four materials tested (Panex 30, Basolite, MOF and Phen-MOF). This firstly demonstrates that the CO₂ evolution published by McCloskey *et al.* [23] might be electrolyte-dependent, as they used carbonates, or ether-based solvents (DME or TEGDME), instead of DMSO in the present case. The author points out that this does not prove the complete stability of DMSO, as a recent paper demonstrated that the DMSO-decomposition products are either solid or non-volatile [20] (thus not detectable by DEMS). Secondly, Figure III. 15 shows that carbon corrosion

is not at the origin of the oxidation current monitored in the OER region: the carbon support is stable in DMSO and LiClO₄ electrolyte; note that in McCloskey *et al.* [23] paper, it was proved that CO₂ was evolved both by the oxidation of lithium alkyl carbonates (originating from carbonates decomposition products) or lithium carbonates (originating from the carbon support).

This relative stability of the carbon electrode|electrolyte interface is however only partial: the high surface area materials are undergoing a strong CO₂ evolution during their first cycle, in Ar-purged electrolyte (Figure III.16). The latter is thus not related to any decomposition product of the carbon support from (electro)chemical action of lithium peroxide; instead, this probably highlights that a similar preferential oxidation of disordered graphitized area of carbon (evidenced in Raman for the three high surface area materials, see the initial section of this chapter) can occur, as monitored in PEMFC-like condition (as described by Luis Castanheira *et al.* [10]). Once these easily oxidizable groups are evolved into CO₂, the CO₂ detection stops (at least until more oxidizing conditions are experienced).

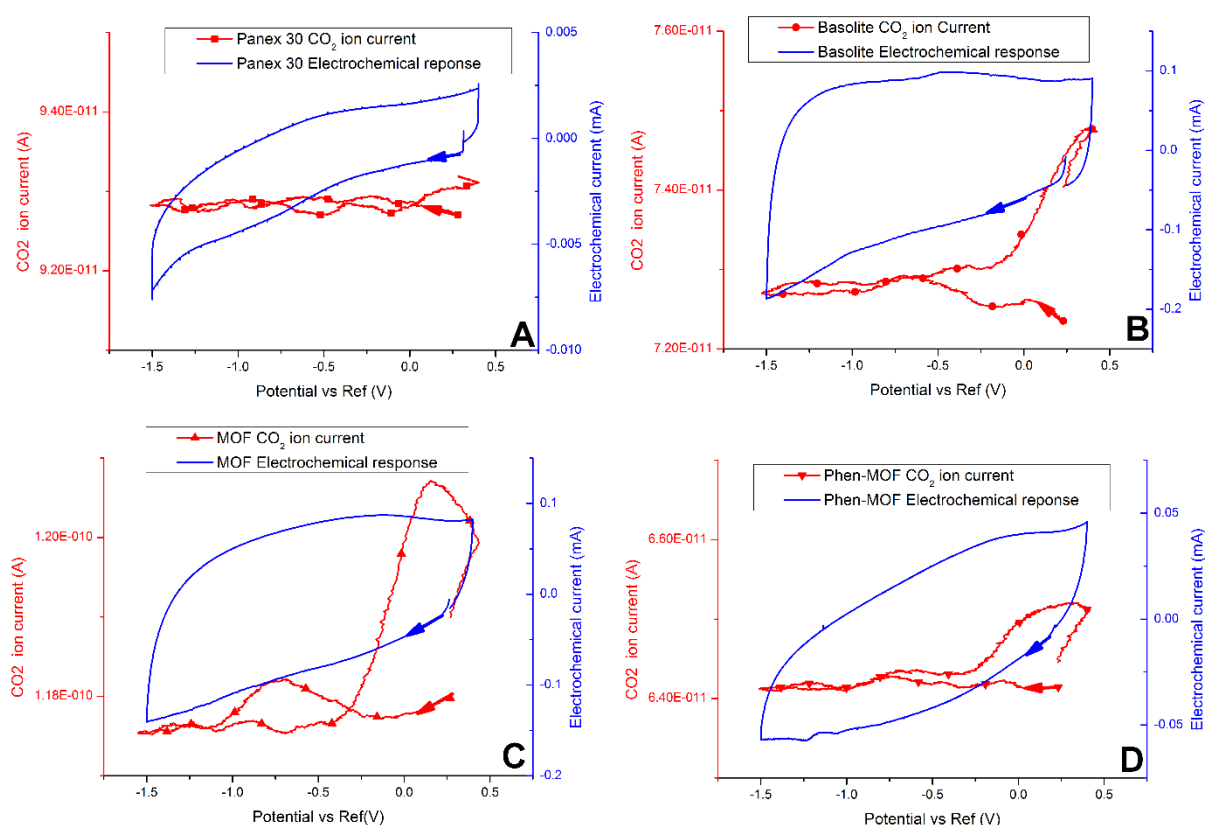


Figure III. 16: CO₂ ion current (primary Y-axis) and faradic current (secondary Y-axis) monitored during the first voltamperogram at 5 mV s⁻¹, in Ar-saturated 0.2 M LiClO₄ DMSO electrolyte. A-Panex 30. B-Basolite. C-MOF. D-Phen-MOF

More specifically, Figure III.16. shows that a detectable oxidation of the graphitized carbon is only occurring for the high surface area materials (Basolite, MOF and Phen-MOF), with a clear and strong

CO₂ evolution above -0.5 V vs. Ref. On the contrary, the Panex 30 carbon cloth itself seems to be rather resistant to this process and does not evolve any detectable carbon dioxide in these conditions. The same applies for the data of Figure III.15 and Figure III.16, which show that even when the Panex 30 is exposed to oxygen, no CO₂ evolution occur, confirming that this low-surface area material is non-negligibly resistant to carbon corrosion in the present electrolyte and potential window.

Compared to Figure III.15, when the upper reverse scan is increased to 0.7 V vs. Ref in O₂-purged electrolyte (*i.e.* more oxidizing conditions than experienced before), the picture changes and CO₂ evolution can be observed by DEMS on the three high surface area supports (but still nothing on Panex 30), as presented on Figure III.17.

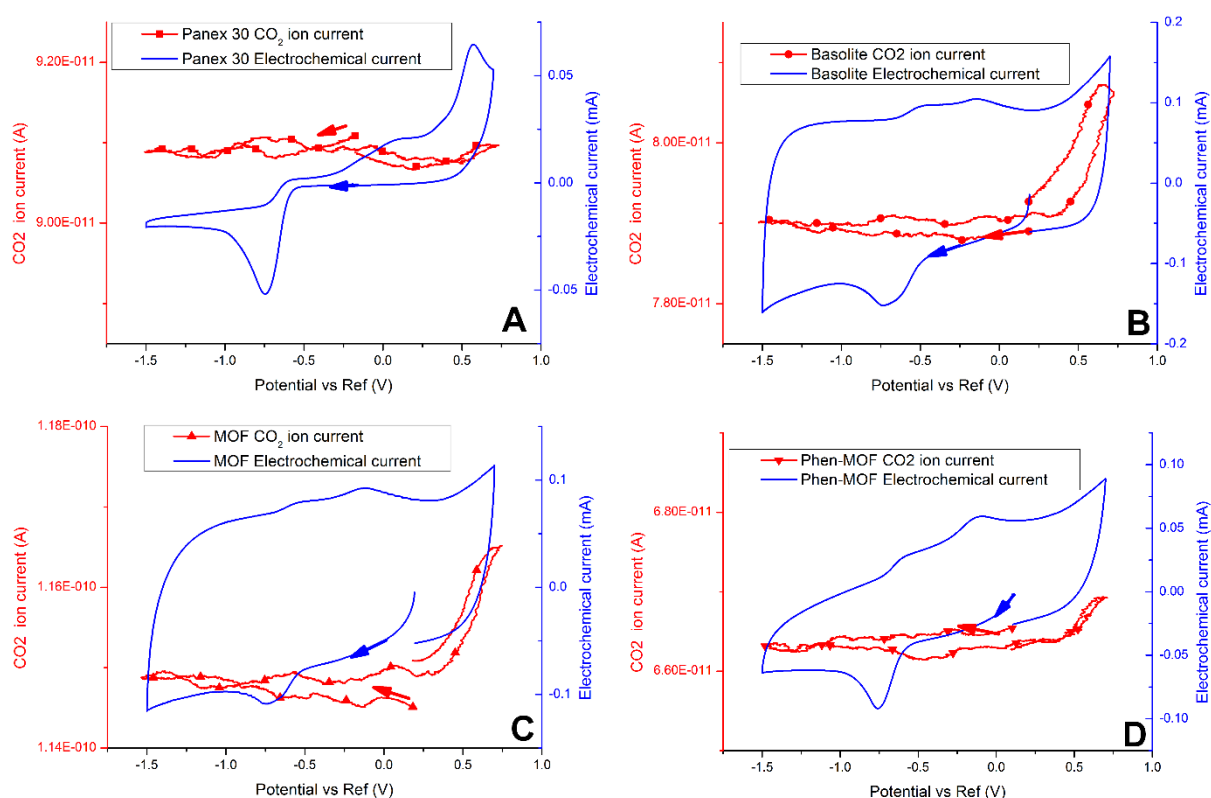


Figure III. 17: CO₂ ion current (primary Y-axis) and faradic current (secondary Y-axis) monitored during the first voltamperogram at 5 mV s⁻¹, upper reverse potential at 0.7 V vs. Ref, in O₂-saturated 0.2 M LiClO₄ DMSO electrolyte. A- Panex 30. B-Basolite. C-MOF. D-Phen-MOF

Figure III.17 indicates a clear CO₂ evolution monitored above 0.4 V vs. Ref when the reverse scan potential is increased to 0.7 V vs. Ref, especially for the Basolite, MOF and Phen-MOF materials. This is a probable indication of the decomposition of those materials by lithium peroxide into lithium carbonate, thus triggering reaction (III.2), in accordance with McCloskey's scheme [23]:



Again, no CO_2 is evolving on Panex 30 itself, as no carbon dioxide evolution can be observed for this material (Figure III.17-A), even with a higher reverse scan potential. This is another indication that this carbon cloth is rather resistant to both electrochemical corrosion and to lithium peroxide attack on its surface, which can be related to its high degree of graphitization (see Raman data above).

d. Comparative Raman

In an effort to explain the reason of the carbon dioxide evolution of the high surface area material, while the Panex 30 remained un-attacked, comparative Raman spectroscopy of the pristine and the discharged cathodes (the ones of the full cells in part II.b) was conducted. Comparative Raman for the Panex 30 cathode is depicted on Figure III.18. As for the pristine materials, the contribution could not be reproduced in Origin. As such, examples of fits for discharged materials in Labspec 4.18 are presented in Annexe 2.

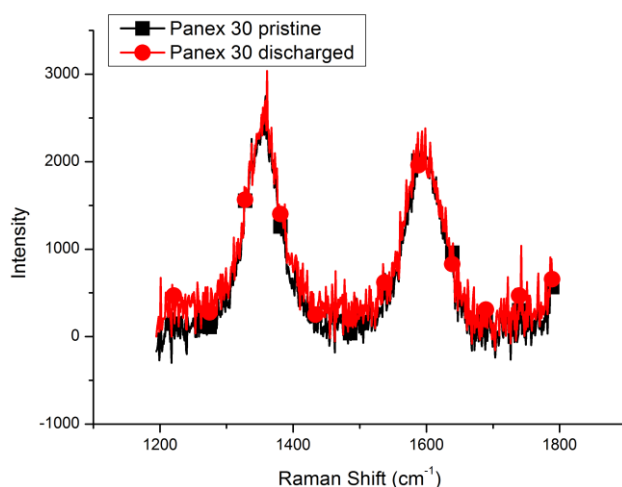


Figure III. 18: Raman spectroscopy, with a LASER beam of 514 nm, for a Panex 30 cathode -Pristine (black); -Discharged (red)

Figure III.18 shows that the discharge product (lithium peroxide) did not affect the signature of the G and D bands for the Panex 30 cathode. Although one cannot rule out superficial degradation of the Panex 30 cathode, this results demonstrates that the Panex 30 cathode essentially remained intact, which is a very good sign for the application and confirms the DEMS results.

The same comparison was conducted for Basolite (Figure III.19), MOF (Figure III.20) and PhenMOF (Figure III.21):

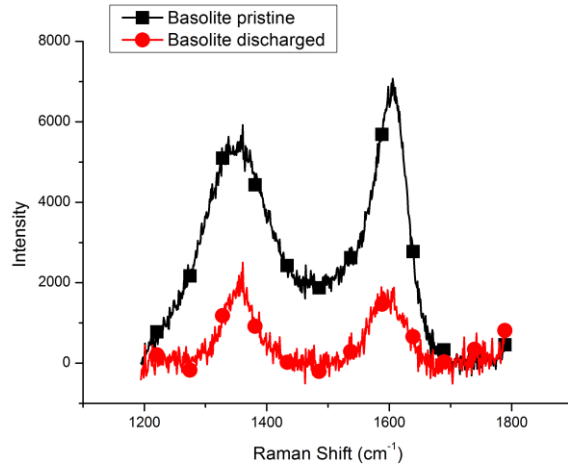


Figure III. 19: Raman spectroscopy, with a LASER beam of 514 nm, for a Basolite cathode -Pristine (black); -Discharged (red)

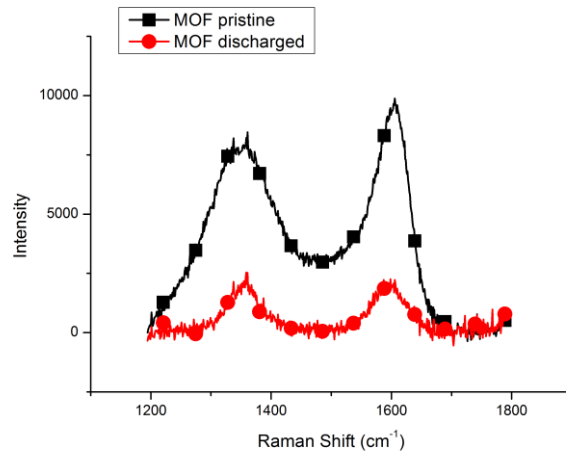


Figure III. 20: Raman spectroscopy, with a LASER beam of 514 nm, for a MOF cathode -Pristine (black); -Discharged (red)

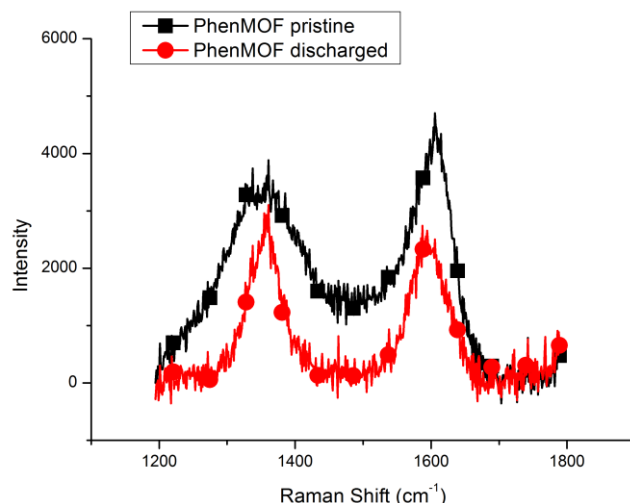


Figure III. 21: Raman spectroscopy, with a LASER beam of 514 nm, for a PhenMOF cathode -Pristine (black); -Discharged (red)

It is clear from Figure III.19, III.20 and III.21 that the Raman spectra of the discharge cathodes is different from the one of the pristine one, indicating a major impact of the discharge product (lithium peroxide), on the cathode texture. In order to better understand in which way it was impacted, the Raman spectra were fitted, similarly than in part a.iii. The corresponding results are presented in Tables III.6 and III.7. For the D3 peak on the discharged Phen-MOF cathode, the shift was fixed in the fittings parameter as otherwise, it was systematically impacting the G and D2 peaks shifts and areas.

Table III. 6: Fitted peak positions of the Raman contributions (D1, G, D2 and D3), for pristine & discharged Li-O₂ positive electrodes

Bands	Conditions	Positive Electrodes			
		Panex 30	Basolite	MOF	PhenMOF
D1 position (cm ⁻¹)	Pristine	1354.8 ± 1.4	1351.1 ± 1.0	1353.5 ± 1.7	1355.1 ± 1.4
	Discharged	1354.5 ± 0.4	1353.7 ± 0.3	1354.1 ± 0.1	1354.7 ± 0.4
G position (cm ⁻¹)	Pristine	1584.5 ± 3.6	1591.2 ± 0.4	1590.2 ± 4.9	1586.9 ± 1.0
	Discharged	1587.7 ± 2.9	1583.9 ± 0.5	1585.2 ± 3.9	1588.4 ± 3.8
D2 position (cm ⁻¹)	Pristine	1610.5 ± 5.6	1614.1 ± 0.8	1615.4 ± 3.2	1614.0 ± 0.6
	Discharged	1616.7 ± 3.1	1610.13 ± 3.1	1610.6 ± 7.1	1617.1 ± 7.3
D3 position (cm ⁻¹)	Pristine	no peak	1546.7 ± 0.3	1543.5 ± 4.1	1538.8 ± 2.2
	Discharged	no peak	no peak	no peak	1550 (fixed)

Table III. 7: Peak Areas for D1, G, D2 and D3 bands, for the pristine & discharged Li-O₂ positive electrodes

Bands	Conditions	Positive Electrodes			
		Panex 30	Basolite	MOF	PhenMOF
D1 area	Pristine	$(1.8 \pm 0.5) 10^5$	$(9.1 \pm 0.6) 10^5$	$(1.0 \pm 0.3) 10^6$	$(7.6 \pm 1.5) 10^5$
	Discharged	$(2.1 \pm 0.3) 10^5$	$(2.0 \pm 0.2) 10^5$	$(1.8 \pm 1.3) 10^5$	$(2.0 \pm 0.6) 10^5$
G area	Pristine	$(9.0 \pm 3.7) 10^4$	$(2.2 \pm 0.3) 10^5$	$(2.5 \pm 0.7) 10^5$	$(1.7 \pm 0.4) 10^5$
	Discharged	$(1.4 \pm 0.4) 10^5$	$(9.2 \pm 0.3) 10^4$	$(1.1 \pm 1.1) 10^5$	$(1.2 \pm 0.5) 10^5$
D2 area	Pristine	$(7.7 \pm 3.7) 10^4$	$(2.1 \pm 0.2) 10^5$	$(2.3 \pm 0.9) 10^5$	$(2.0 \pm 0.3) 10^5$
	Discharged	$(4.8 \pm 1.9) 10^4$	$(9.3 \pm 0.4) 10^4$	$(4.6 \pm 3.3) 10^4$	$(5.4 \pm 2.1) 10^4$
D3 area	Pristine	0	$(2.3 \pm 0.2) 10^5$	$(2.4 \pm 0.5) 10^5$	$(1.8 \pm 0.6) 10^5$
	Discharged	0	0	0	$(2.7 \pm 2.1) 10^4$

The results from Table III.6 and Table III.7 clearly demonstrate that the amorphous graphitic phase disappeared after the discharge for Basolite and MOF cathodes. Concerning the Phen-MOF, the D3 contribution did not disappear entirely, but its area largely decreased (by a factor of ten). It must be noted that for the electrodes on which the deposit was the thicker (*i.e.* MOF and Phen-MOF), a large uncertainty is obtained for the areas, probably because the thickness of the discharge product varies a lot (with large lithium peroxide particles on their surfaces of sizes greater than one micron, as seen on the *post mortem* SEM micrographs, see above). Although the wavelength of the LASER used for this experiment was 514 nm, and according to the literature, such LASER penetrates in the material up to 1 μm [24], the probable thickness of discharge product was probably on the same order of magnitude, which can affect the intensity of the Raman spectra.

It was proven during the DEMS experiments that only the high surface area materials were evolving carbon dioxide at high potential during the OER, in LiClO₄ DMSO electrolyte. Panex 30 itself appeared highly stable, with no CO₂ evolution at high potential (indicating no lithium carbonate formation [23]). In that case, Raman spectroscopy of the carbon cloth confirmed this trend: no differences is observed on the spectra between the pristine material and the discharged one. The stability of this material is surely linked to its high degree of graphitization, with no amorphous graphitic phase (D3), in agreement with the larger stability of graphitic carbons in PEMFC operation [5, 10, 25].

On the contrary, the high surface area materials all exhibit a strong contribution of the D3 peak on the pristine electrodes, contribution that completely disappeared from the Raman spectra on the discharged electrodes of the Basolite and MOF materials, and was considerably reduced for the Phen-MOF. Computing the behavior of the three high surface area materials and the Panex 30 by DEMS and Raman, it is highly suspected that the amorphous graphitic phase of the high surface area material is the one responsible for the CO₂ evolution during the OER (thus reactive toward lithium

peroxide). It is postulated that parts of this contribution is still observable for the Phen-MOF, owing to the larger initial particles of this material (as observed by SEM), whereas the Basolite and MOF particles are smaller (thus most of their amorphous graphitic phase can react with lithium peroxide).

So these results clearly demonstrate that a single discharge and related formation of Li_2O_2 is enough to severely (entirely or near-entirely) destroy the amorphous domains of high surface area carbon electrodes, therefore emphasizing the need for either their protection or the use of more graphitic carbons. It is likely that such destruction of the amorphous phase of carbon is linked to the formation of lithium carbonate [23] by reaction of the lithium peroxide with amorphous graphitic phase.

Conclusion

High surface area carbon-based materials, the use of which is recommended by Abraham *et al.* [2], were studied as cathode materials for Li-O₂ system. DEMS investigations demonstrated that those materials undergo a severe CO₂ evolution at high potential, even in inert atmosphere, which was firstly assumed to be linked to the oxidation of disordered graphitized area [10]. In addition, comparative Raman spectroscopy of the pristine and discharged materials, enabled to link the destruction of the amorphous phase of carbon to the formation of lithium carbonate [23], formed by the reaction of the lithium peroxide with amorphous graphitic phase. Of course, this puts at risk the usability of those materials in a practical Li-O₂ positive electrode, as the consumption of the positive electrode will lead to the cell failure, and this will be possible both during discharge (by reaction of Li₂O₂ with amorphous carbon) and in recharge (direct formation of CO₂ in oxidizing potential values). Full cell experiments, along with *post mortem* SEM and XEDS analyses also proved that possessing the greater surface area is not the key parameter to achieve a good OER/ORR efficiency (at least in the present experimental conditions, and for the present, disordered, carbon-based materials); rather, the morphology of the active material seems to play a role. As a consequence, it was proven that the better material in terms of roundtrip efficiency was the Basolite, which yields agglomerated nanocubes of Li₂O₂ upon discharge, with spaces between them, and this material was the only one to achieve a satisfying OER process (70% of the discharged capacity recovered). The other materials were unable to process a correct OER (as for the others, the OER/ORR efficiency is below 11%), SEM micrographs showing that in those cases, the discharge yields much larger Li₂O₂ crystals. For the Basolite, the different Li₂O₂ crystal geometry seems to show that the ORR occurred between the Basolite nanocubes, versus on the material surface for the other materials. However, unfortunately, only Panex 30 shows some material stability in operation, Basolite being subjected to severe corrosion of its amorphous domains.

In conclusion this study shows that a three-dimensional electronic percolation is essential for the OER to process efficiently, along with the absence (or at least really depreciated presence) of amorphous graphitic phase in the material to prevent the formation of lithium carbonate by reaction with Li₂O₂ in discharge and CO₂ at high charging potential values. Therefore, although the achieved performances are encouraging for the Basolite in terms of roundtrip efficiency in the first discharge/charge cycle, still nearly 30% of discharged capacity is not recovered, which is not acceptable in a practical system. It is thus mandatory to find a way to efficiently recharge such

cathodes (with a OER/ORR coulometry ratio as close to one as possible!), and one way to do so is to transport electrons in solution through redox mediation. Doing so is the goal of the next chapter.

References

1. Zoltek Corporation Technical Data Sheet Zoltek PX-30. <http://zoltek.com/wp-content/uploads/2017/01/PX30-Woven-Fabric.pdf>.
2. Abraham KM, Jiang Z, Soc JE (1996) A Polymer Electrolyte – Based Rechargeable Lithium / Oxygen Battery. *Tech Pap Electrochem Sci technology* 143:1–5. doi: 10.1149/1.1836378
3. Simon P, Gogotsi Y (2009) Materials for electrochemical capacitors. *Nanosci Technol* 320–329. doi: 10.1142/9789814287005_0033
4. Palacín MR, Simon P, Tarascon JM (2016) Nanomaterials for Electrochemical Energy Storage: the Good and the Bad. *Acta Chim Slov* 417–423. doi: 10.17344/acsi.2016.2314
5. Rodrigues Castanheira LF (2014) Corrosion of high surface area carbon supports used in proton-exchange membrane fuel cell. Université Grenoble-Alpes
6. Ferrari AC, Robertson J (2000) Interpretation of Raman spectra of disordered and amorphous carbon. *Phys Rev B* 61:14095–14107. doi: 10.1103/PhysRevB.61.14095
7. Jawhari T, Roid A, Casado J (1995) Raman spectroscopic characterization of some commercially available carbon black materials. *Carbon N Y* 33:1561–1565. doi: 10.1016/0008-6223(95)00117-V
8. Nistor L, Landuyt J, Ralchenko V, et al (1994) Direct observation of laser-induced crystallization of aC: H films. *Appl Phys A Mater Sci Process* 58:137–144. doi: 10.1007/BF00332170
9. Robins LH, Farabaugh EN, Feldman A (1990) Line shape analysis of the Raman spectrum of diamond films grown by hot-filament and microwave-plasma chemical vapor deposition. *J Mater Res* 5:2456–2468. doi: 10.1557/JMR.1990.2456
10. Castanheira L, Dubau L, Mermoux M, et al (2014) Carbon corrosion in proton-exchange membrane fuel cells: From model experiments to real-life operation in membrane electrode assemblies. *ACS Catal* 4:2258–2267. doi: 10.1021/cs500449q
11. Knight DS, White WB (1989) Characterization of diamond films by Raman spectroscopy. *J Mater Res* 4:385–393. doi: 10.1557/JMR.1989.0385

12. Nasybulin E, Xu W, Engelhard MH, et al (2013) Stability of polymer binders in Li-O₂ batteries. *J Power Sources* 243:899–907. doi: 10.1016/j.jpowsour.2013.06.097
13. Huseby TW, Bair HE (1968) Dissolution of polyethylene single crystals in xylene and octadecane. *J Appl Phys* 39:4969–4973. doi: 10.1063/1.1655894
14. Poulakis JG, Papaspyrides CD (1995) The Dissolution Reprecipitation Technique Applied on High-Density Polyethylene .1. Model Recycling Experiments. *Adv Polym Technol* 14:237–242.
15. Laoire CO, Mukerjee S, Plichta EJ, et al (2011) Rechargeable Lithium/TEGDME-LiPF₆/O₂ Battery. *J Electrochem Soc* 158:A302. doi: 10.1149/1.3531981
16. McCloskey BD, Scheffler R, Speidel A, et al (2011) On the efficacy of electrocatalysis in nonaqueous Li-O₂ batteries. *J Am Chem Soc* 133:18038–41. doi: 10.1021/ja207229n
17. Luntz A, McCloskey B (2014) Nonaqueous Li–air batteries: a status report. *Chem. Rev.*
18. Schwenke KU, Metzger M, Restle T, et al (2015) The Influence of Water and Protons on Li₂O₂ Crystal Growth in Aprotic Li-O₂ Cells. *J Electrochem Soc* 162:A573–A584. doi: 10.1149/2.0201504jes
19. Griffith LD, Sleightholme A, Mansfield JF, et al (2015) Correlating Li/O₂ Cell Capacity and Product Morphology with Discharge Current. *ACS Appl Mater Interfaces* 150316103008003. doi: 10.1021/acsami.5b00574
20. Sharon D, Afri M, Noked M, et al (2013) Oxidation of dimethyl sulfoxide solutions by electrochemical reduction of oxygen. *J Phys Chem Lett* 4:3115–3119. doi: 10.1021/jz4017188
21. Younesi R, Hahlin M, Björefors F, et al (2013) Li–O₂ Battery Degradation by Lithium Peroxide (Li₂O₂): A Model Study. *Chem Mater* 25:77–84. doi: 10.1021/cm303226g
22. Luntz AC, McCloskey BD (2014) Nonaqueous Li – Air Batteries : A Status Report. *Chem Rev* 114:11721–11750. doi: 10.1021/cr500054y
23. McCloskey BD, Speidel A, Scheffler R, et al (2012) Twin problems of interfacial carbonate formation in nonaqueous Li-O₂ batteries. *J Phys Chem Lett* 3:997–1001. doi: 10.1021/jz300243r
24. Brisset F (2006) *Microscopie électronique à balayage et Microanalyses*, 2008th ed. EDP Sciences, Saint-Martin d’Hères

25. Dubau L, Castanheira L, Chatenet M, et al (2014) Carbon corrosion induced by membrane failure: The weak link of PEMFC long-term performance. *Int J Hydrogen Energy* 39:21902–21914. doi: 10.1016/j.ijhydene.2014.07.099

Chapter IV:

Redox Shuttles: necessary additives for OER enhancement in Li-O₂ batteries.

The art and science of asking questions is the source of all knowledge

- Thomas Berger

The previous chapter made clear that enhancing the cyclability by heterogeneous catalysis in Li-O₂ cathodes has not been achieved yet. Indeed, the occurrence of two consecutive steps during the discharge processes (of electrochemical, E, and chemical, C, nature) can yield a full covering of the “catalyst” surface/sites with particles that are much larger than what would have been obtained if the formation of Li₂O₂ had been purely electrochemical (in that latter case, the growth of these particles would have been restricted by (i) the number of active sites/the surface area of the electrode and (ii) the (bad) electronic conductivity of Li₂O₂); this eventually prevents their electrochemical recharge (the charging takes place at the triple interface Li₂O₂|electrolyte|electrocatalyst), and therefore triggers incomplete recharge of lithium peroxide particles and related bad rechargeability of the Li-O₂ cathode, loss of cyclable lithium, capacity losses, etc. In consequence, electrocatalysts that had proven very efficient for the ORR/OER in alkaline medium (in this case, the electrode is never “passivated” by such solid products) were demonstrated inefficient (or at least not more efficient than glassy carbon) for the same reactions in non-aqueous environment [1]. Even though few papers published have clearly claimed a catalysis effect [2] (when most papers publish good performances in full cell by simple surface enhancement), using those materials in a practical Li-O₂ system can be questioned [1], as it will be of little help to prevent capacity losses because of inefficient recharge. To alleviate these issues, the mechanism of the discharge/charge processes at the oxygen electrode must be better understood, and a way to enhance and solve the cyclability of this electrode must be found. In this perspective, one potentially-interesting way to make the charging of those large (and therefore not perfectly “electrically-connected”) Li₂O₂ particles, and avoid irreversible capacity losses of the battery, is to “transport electrons” in solution. This transport can be achieved by using redox shuttle species.

I. Redox shuttle screening for Li-O₂ cathodes

a. Redox Shuttles: the ideal behavior

The idea of using a redox shuttle to enhance the charging process on a Li-O₂ cathodes has first been introduced (and patented) by Christensen *et al*, for the company Robert Bosch GmbH in 2011 [3]. After this discovery, a few papers have been published in this topic, and various chemistries and chemicals were used for this application: iodide [4, 5], 2,2,6,6- tetramethylpiperidinyloxy (TEMPO) [6], tetrathiafulvalene (TTF) [7], or tris[4-(diethylamino)phenyl]amine (TDPA) [8]. However, before

knowing which compound could be relevant as a redox shuttle for non-aqueous oxygen reduction/evolution reactions (ORR/OER), the processes at stake must be defined, as described below.

i. Mechanism of the redox shuttle

As detailed in Chapter one, the charging process involved in the direct conversion of lithium peroxide into oxygen is an electrochemical reaction (Equation IV.1):



As an electrochemical reaction, this reaction must proceed at the triple interface between the current collector (carbon), the electronically-insulating reactant (Li_2O_2) and the electrolyte, as illustrated in Figure IV.1.

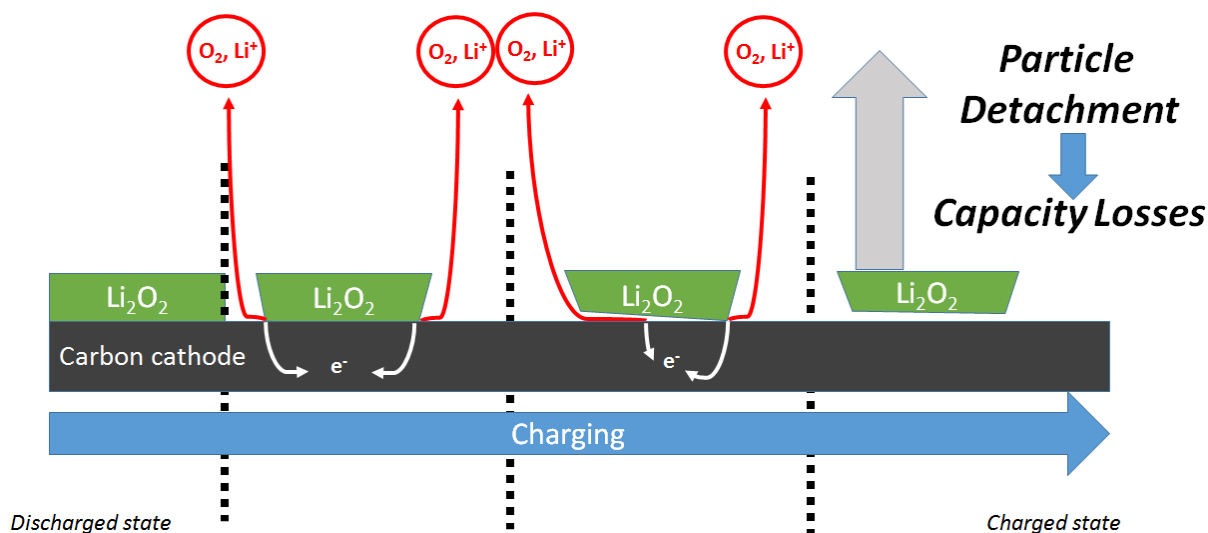


Figure IV. 1: Proposed scheme for the (electrochemical) OER process in the absence of a redox shuttle

In the charging process, as the Li_2O_2 oxidation only occurs at the triple interface (*i.e.* at the interface with the carbon electrode), only the “small” Li_2O_2 particles (small enough for electron tunneling in this large gap (5 eV) semi-conductor material) have a chance to be fully oxidized (back to O_2). Bigger particles (particles with dimensions greater than the tunneling distance of the electrons in Li_2O_2 [9]), can only be partially recharged (at the interface with the carbon support); the portion of the Li_2O_2 particle which is further from the carbon becomes electrically disconnected from the latter, leading to their fall in the electrolyte, both processes yielding irreversible capacity losses. In particular, the assumption that particles detachment indeed occurs in practical Li-O₂ battery cathodes is made on three observations:

- Firstly, McCloskey *et al* always measured OER/ORR coulometry ratio (by DEMS) around 0.5, for most solvents [10], signing an irreversible loss upon charge/discharge cycling.

- Secondly, most papers that “proved” high cyclability of Li-O₂ batteries dealt with high recharge potential values (above 4.2 V vs. Li/Li⁺), where the oxidation of the solvent/carbon electrode occurs; in particular, most of the papers dealing with “good charging performances” are conducted in TEGDME electrolyte [11–13], and Gittleson *et al* showed that TEGDME starts its (slow) oxidation above 4.0 V vs. Li/Li⁺ [14], the oxidation products of the solvent/carbon being capable to favor the complete oxidation of Li₂O₂ (but in a process that can only be sustained transiently in 3-electrode cells and is not practical in a real Li-O₂ battery).

- Thirdly, the same capacity of discharge is obtained in these papers after each recharge process, which proves that even though not all the current was used for the charging of Li₂O₂ particles (see item 1 above), the surface is freed again, which must follow the detachment of the incompletely recharged “big” Li₂O₂ particles from the electrode surface.

This short literature review shows that *ca.* half of the capacity is lost at each cycle for the Li-O₂ cathodes; this demonstrates the imperative need for a sustainable redox additive (*i.e.* not degradation products of the electrode/electrolyte), soluble in solution that can transport electrons in solution and chemically assist the recharge of large Li₂O₂ particles, these being either still attached to the electrode surface or disconnected/fallen in the electrolyte. The mechanism at stake in presence of a redox shuttle (labeled X) is detailed by Equations (IV.1 to IV.3):



where equation (IV.2) is the electrochemical OER at the triple interface, and equation (IV.4) involves the spontaneous chemical reaction between Li₂O₂ and the oxidized form of the redox shuttle, formed by equation IV.3. The latter reaction can proceed for any Li₂O₂ particle, even disconnected and/or fallen in solution.

This mechanism can be schematized as in Figure IV.2.

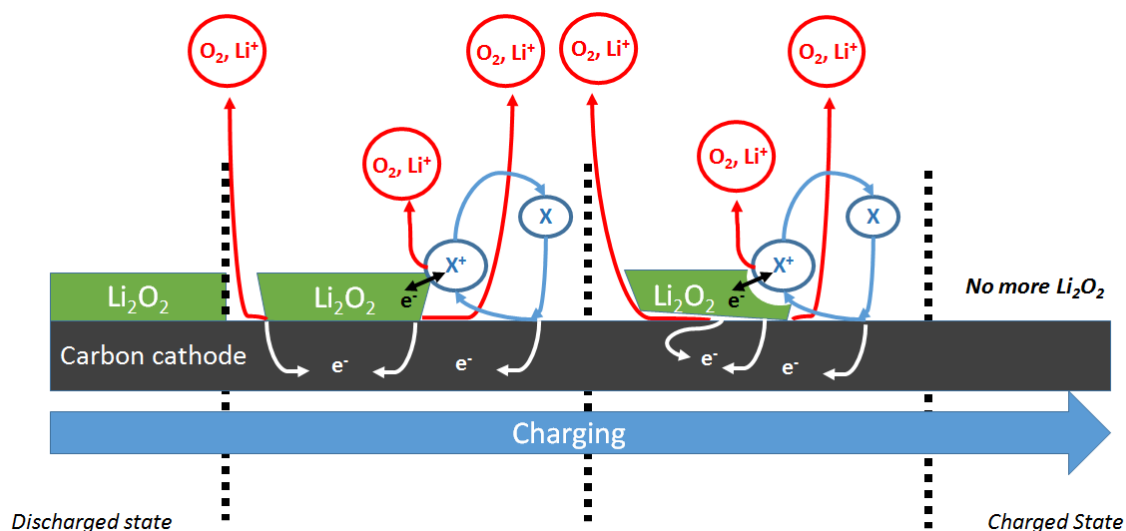


Figure IV. 2: Proposed scheme for the OER process in presence of a soluble redox shuttle to chemically assist the recharge of Li_2O_2

The advantage of the addition of the redox shuttle is, on a theoretical point of view, to be capable to favor the complete recovery of the surface, through the re-oxidation of big (and/or detached) lithium peroxide particles.

ii. Required electrochemical behavior

In order to have an efficient redox shuttle for the OER processes, some characteristics are essential:

- Firstly, the redox shuttle must be (at least partially) soluble and mobile in the electrolyte (otherwise it will not reach detached particles and big aggregates). The larger its solubility and diffusion coefficient, the larger its efficiency to assist the recharge of Li_2O_2 (supposedly).
- Secondly, the redox kinetics of the redox shuttle must be fast, so that it does not further slow down the OER processes (that are already sluggish).
- Thirdly and most importantly, the redox potential of the mediator must be correctly placed, so it (i) enables the reactions targeted, (ii) remains within the stability window of the electrode/electrolyte and (iii) has enough driving force to oxidize the lithium peroxide particles.

In order to have a better insight of the required voltage window, one can draw a simulated voltage scale with the redox couple in presence (Figure IV.3)

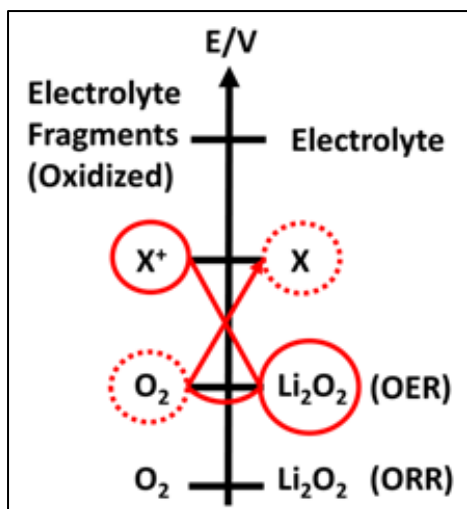


Figure IV. 3: Scheme of the potential scale of the ORR/OER processes, comprising a well-chosen redox shuttle

Two lines are positioned on the voltage scale to illustrate the irreversible kinetics of the ORR/OER processes in non-aqueous solution. Plain-red circles represent the species in presence and dashed circles the ones that are produced upon redox mediator-assisted recharge. It can be easily observed that the reaction between X^+ and Li_2O_2 is spontaneous in the case where the potential of the X^+/X redox couple exceeds that of O_2/Li_2O_2 (in practice is above the onset potential of the OER). However, it is also clear that this potential must stay within the voltage window of the electrolyte (and electrode).

More practically, the electrochemical behavior of the ORR/OER processes on GC, as measured in a 0.2 M LiTf DMSO electrolyte, can be confronted to the required electrochemical behavior of the redox shuttle (Figure IV.4).

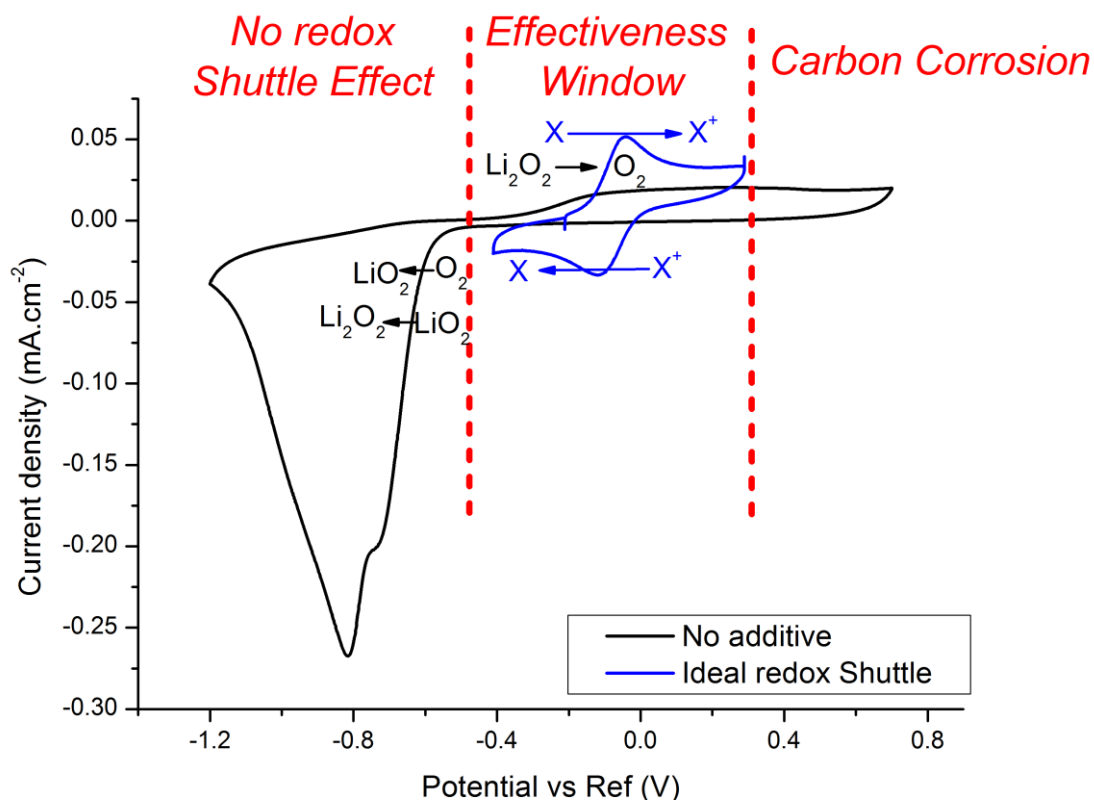


Figure IV. 4: Cyclic voltamperogram of a glassy-carbon electrode in O_2 -purged (5.1 grade), 0.2 M $LiClO_4$ DMSO electrolyte. Scan rate 5 mV s^{-1} . Reference: $Ag/AgNO_3$ (2 mM in 0.2 M $LiClO_4$ DMSO). Added is a simulated cyclic voltamperogram of a useful redox mediator to assist the recharge of Li_2O_2 .

The different domains of electrochemical activity (or inactivity) are depicted on Figure IV.4, and show how finding a proper redox shuttle is not an easy task: the voltage window applicable is only of 0.5 V vs. Ref (in DMSO electrolyte), as at too-high potential, the electrode/electrolyte is decomposed, leading to CO₂ and then lithium carbonate in a process that would both destroy the electrode/electrolyte and further passivate it. Another aspect that can be observed on Figure IV.4 is that the driving force of the redox shuttle is highly impacted by its concentration (and therefore the peak currents associated to the redox shuttle), which is mostly limited by its solubility in the electrolyte used. Thus the redox shuttle screening must also account on this parameter.

iii. System restrictions

In conventional lithium battery systems, the separator used is an ultrathin porous polyethylene, polypropylene or multilayered (PE/PP) membrane. The most known brand which distributes these separators is the Celgard Company, which offers various grades in term of thicknesses, porosities, composition, surface treatments, *etc.* These separators are designed to be as thin as possible, in order to limit their impact on the total mass of the battery. The ideal electrolyte forms a thin, protective, Solid Electrolyte Interface (SEI) layer with the lithium negative electrode [15], while the oxygen is supposed to be reduced only at the carbon electrode (cathode in discharge, anode in charge).

The best solvents for the SEI formation are carbonated solvents [16]; unfortunately, this class of compounds is prohibited in Li-O₂ systems, as they easily form Lithium carbonates with lithium peroxide, upon the discharge at the positive electrode [17]. So, the current solvents that are used in practical Li-O₂ batteries are not carbonated solvents, and are therefore less prone to form a thin SEI layer covering the lithium surface, which remains ill-protected by such an imperfect SEI. Thus, parasitic reactions can occur at the regions of the lithium electrode that are unprotected, such as the direct reduction of oxygen on lithium (formation of lithium peroxide and oxide from the O₂ species crossing over the electrolyte from the positive electrode); this naturally lowers the amount of “cyclable lithium”, and in an open system can in the end provoke the total consumption of the metallic lithium and cause the death of the cell.

Such parasitic reaction scheme is detailed on Figure IV.5, where Li₂O is supposed to be formed directly on the lithium surface. To prevent or at least mitigate this severe issue, one must find means to protect the lithium negative electrode, by either a layer of Li⁺ conductive ceramics (*e.g.* LISICON [18–21] and/or by a better engineering of the solvent for non-aqueous Li-O₂; finding a solvent that is stable to both the ORR products at the high (oxidizing) potential of the positive electrode and metallic lithium (which is at very reducing potential values) may however be a difficult task.

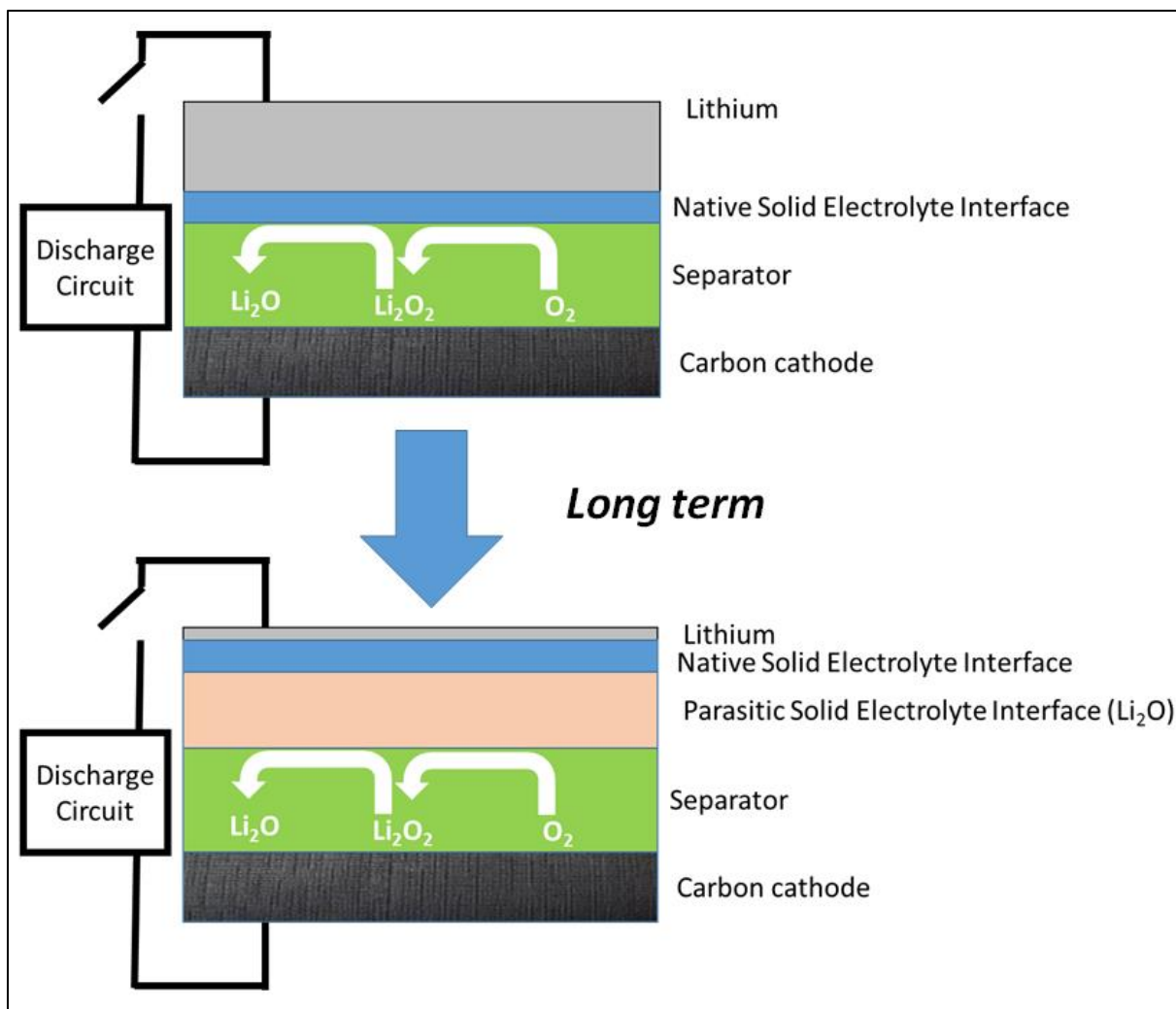


Figure IV. 5: Scheme of the parasitic reactivity of lithium with dissolved oxygen, in a Li-O₂ battery with an oxygen-saturated electrolyte

Using a redox shuttle (a strong oxidant in its oxidized state, in order to promote the recharge of Li₂O₂) puts more stress on the technology: the redox shuttle diffusion to the lithium side must be prevented, as it is susceptible to render complex both the overall charge/discharge mechanisms and compromise the safety of system. If the oxidized moiety of a redox shuttle crosses over from the positive to the negative electrodes during the charging process, this will impact not only the efficiency of the additive for the oxidation of lithium peroxide but also provoke a severe consumption of cyclable lithium, as depicted on Figure IV.6.

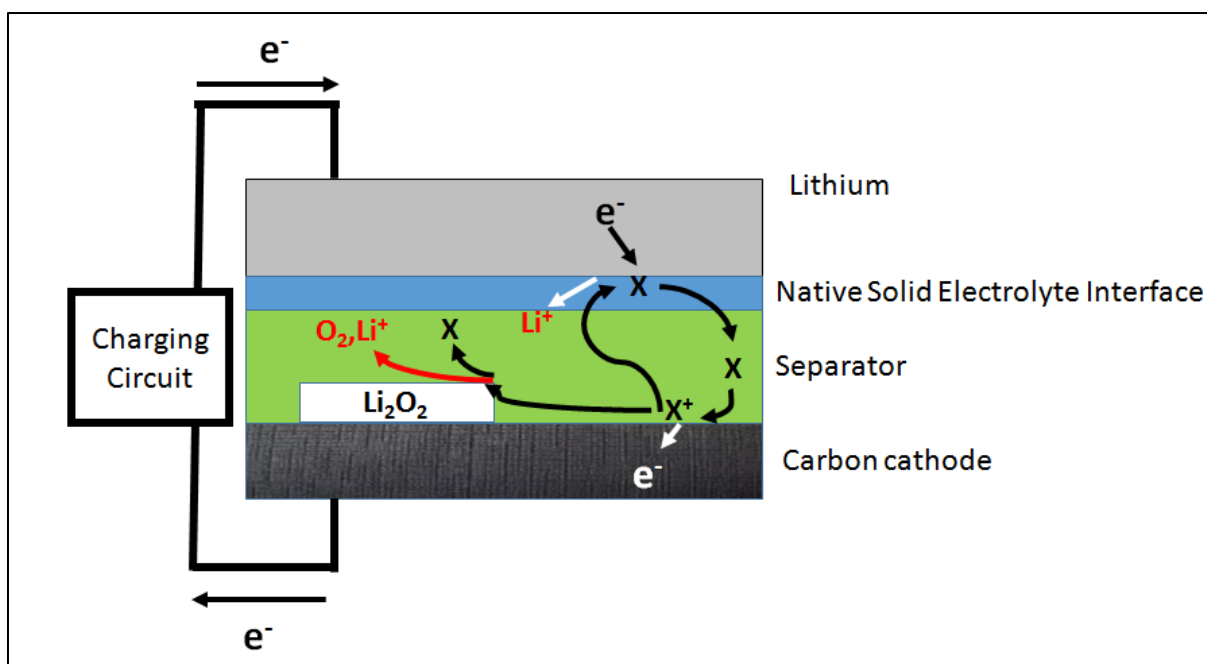
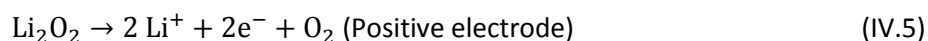
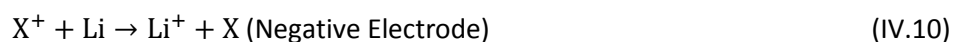
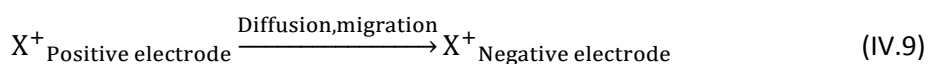


Figure IV. 6: Undesired mechanism of the reaction between the redox and the negative (lithium) electrode

The desired reactions during the charging process are given by the sequence of equations (IV.5 to IV.7) at the positive electrode, and equation (IV.8) at the negative electrode.



whereas the unwanted path occurs as the sequence of equations (IV.6), (IV.9) and (IV.10).



To be more specific, this unwanted path triggers two important problems: (i) the loss of the coulombic efficiency of the redox additive and (ii) an “infinite recharge phenomenon” at the end of the charging process. In the latter case, the positive electrode generates X^+ species that can react with Li to form Li^+ , a reaction that can proceed as long as some Li remains at the negative electrode, which means that this apparent “infinite recharge” may entirely deplete the negative electrode if the diffusion/transport of the oxidized form of the redox shuttle to the lithium negative electrode cannot be prevented.

In conclusion, it is mandatory for the use of redox shuttle additives in solution, to efficiently block the contact between the metallic lithium and the electrolyte containing the redox additive. Several possibilities are mentioned in the literature [22–24], such as the use of NaSiCON type membranes (Li⁺ conducting ceramics); these are indeed able to efficiently (physically) separate the positive and the negative electrode compartments. However, their poor conductivity to Li⁺ cations ($5 \cdot 10^{-4} \text{ S cm}^{-1}$), coupled to their brittleness (and therefore need for sufficiently large thickness) are clear hindrances to their practical usage: it results in large Ohmic resistance of the cell. Besides, these compounds show non-negligible reactivity toward metallic lithium, and secondary protection of the lithium electrode is necessary (*e.g.* LIPON and/or polymer electrolyte layers [25–27]). Another solution, which is, in the author's opinion the best, would be to pre-form a fully-covering/protecting SEI layer on the lithium negative electrode, in order to avoid any direct contact with the electrolyte and in particular the oxidized form of the redox additive. This solution involves a lot of system engineering but will offer a better reliability for a practical system. However, this topic (of protection of the lithium negative electrode) is beyond the subject of this thesis, and no solution for this issue will be presented in this chapter, but some paths for further research will be presented in chapter VI.

b. Unfruitful selection of potential redox mediators

The screening of compounds that are electrochemically active in non-aqueous solution, at high potentials for potential use as redox shuttle for Li-O₂ batteries is not an easy task. As stated above, various parameters impact the usability of an additive for this purpose. Herein are presented experiments that proved unsuccessful for such selection, but these are nevertheless described, as they paved the way to the discovery of interesting compounds.

The reference solution used in these experiments were 20 mM Ag/AgNO₃ in 0.2 M TBAClO₄ electrolyte. The solvent used for the reference was the same used in the experiment (either DMSO or ACN). The working electrode was plain 5 mm-diameter glassy-carbon and the counter electrode was high surface area platinum.

i. Potassium Ferrocyanide

Potassium Ferro cyanide was believed to be the perfect candidate as a first try, thanks to its redox potential, situated within the required voltage window [28].



Considering the Reference Potential used in our experiments, it gives a redox transition expected at -0.34 V vs. Ref, which did put great hope for this compound.

The electrolyte used for the testing of the redox mediation of this compound was chosen to be TBAClO₄. It is well-known that in presence of the latter salt, only a one electron, fast reversible ORR/OER can be achieved [29]. According to the HSAB theory, the subsequently formed superoxide in TBAClO₄ is soluble and less reactive which completely contrast with the main discharge product in lithium-containing electrolyte (lithium peroxide) [29, 30]. Thus, if the ORR/OER features are hindered in this experiment electrolyte, it will mean that poisonous reactions occur (as the ORR/OER is here highly reversible and happen at much lower potentials). Even though the ORR/OER features were not hindered in this experiment, the first drawback encountered was when the potassium ferrocyanide was dissolved in the electrolyte (20 mg in 20 mL): even after two days, a very small portion of it was dissolved. Still, it satisfies the requirement of the redox additive as it is partially soluble (the best is high solubility for better efficiency). The results obtained are presented in Figure IV. 7.

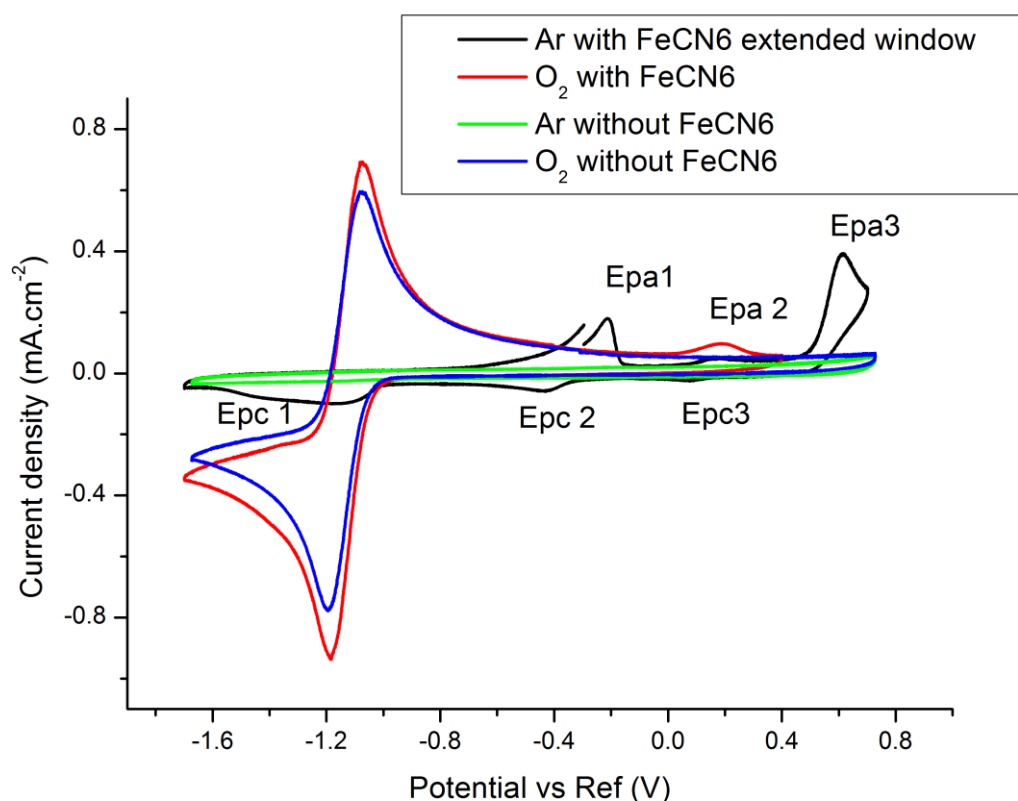


Figure IV. 7: Oxidoreduction activity of potassium ferrocyanide in 0.2 M TBAClO₄ DMSO, 100 mV s⁻¹

The electrochemical response of the ferrocyanide couple in Ar-purged electrolyte (black curve) shows that the mechanisms are much more complicated than expected. Three anodic redox peaks and three cathodic redox peaks are observed. One might associate the "reversible" couple E_{pa1}/E_{pc2} to the reaction (IV.2), and this would be the desired behavior. However, the presence another "reversible" couple E_{pa2}/E_{pc3} is unexpected, as well as the occurrence of irreversible anodic (E_{pa3}) and cathodic (E_{pc1}) peaks that could be linked to irreversible degradation reactions of the ferrocyanide additive at high/low potential values in this reaction medium.

In addition, when the electrolyte is purged under oxygen (red curve), the electrochemical features of the ferrocyanide couple, that were clearly seen under argon, disappear in profit to the ORR/OER processes only. As a result, nearly the same electrochemical response with and without ferrocyanide additive is monitored when the electrolyte is oxygen-purged or not (with: red curve; without: blue curve), demonstrating that the redox shuttle additive does not play its role.

Therefore, the ferrocyanide compound does neither fulfill the fast kinetics simple mechanism property, nor the stability required for a redox shuttle additive, and in consequence is not operating as desired; thus, it will not be studied further.

ii. Benzoquinone

Compounds such as p-benzoquinones show excellent redox behavior, within the required voltage window for a redox shuttle in a Li-O₂ battery. Tetra-bromobenzoquinones were proven very efficient toward the simultaneous detection of ascorbic acid, dopamine and uric acid [31]. For the present application, the tetrabromobenzoquinone revealed a very fast redox kinetic around 330 mV vs. ENH [31], which is slightly above the lower limit of the required voltage window (0.2 V vs. ENH or -0.5 V vs. our Ag/AgNO₃ reference). Being admitted that having a redox shuttle that is as stable to ORR products as possible is highly desired, the first compound tested was p-tetrafluorobenzoquinone: C-F bounds are indeed very robust, thus making, at least theoretically, the compounds less prone to decomposition upon attack by Li₂O₂. The study medium was 0.2 M TBAClO₄ in acetonitrile (TBAClO₄ salt was chosen for the same reason than for the study of K₄Fe(CN)₆, and the cyclic voltammeteries were performed at 100 mV s⁻¹. Results in Ar-purged electrolyte are depicted in Figure IV.8. Two consecutive redox activities can be observed for the p-tetrafluorobenzoquinone species (equations IV.12 and IV.13).

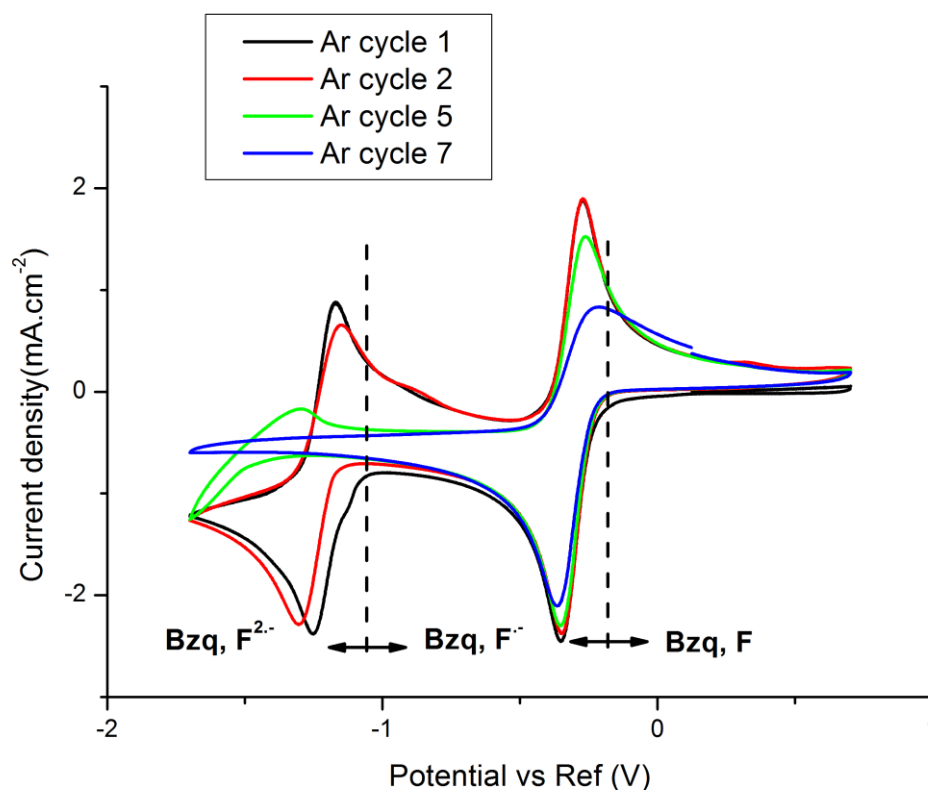
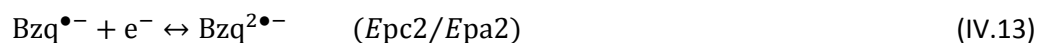


Figure IV. 8: Voltamperogram obtained for a glassy-carbon electrode in an Ar-purged electrolyte composed of 5.5 mM TetraFluoroBenzoquinone in 0.2 M TBAClO₄ in acetonitrile, at 100 mV s⁻¹. The plot puts into evidence the self-poisoning of the electrode.

Figure IV.8 demonstrates that an unwanted mechanism occurs, as the second redox activity (Epc2/Epa2) becomes more and more irreversible upon cycling; it is totally inactive at cycle 7. It can also be seen at the 7th cycle, that even the first redox activity (Epc1/Epa1) is affected by this phenomenon. In other words, the electrode is gradually (and with fast kinetics) self-poisoned in presence of the Tetrafluoro-p-benzoquinone. This behavior puts a great threat on the usability of this compound as the redox shuttle. Yet, the experiments were continued and the electrolyte saturated by oxygen (Figure IV.9).

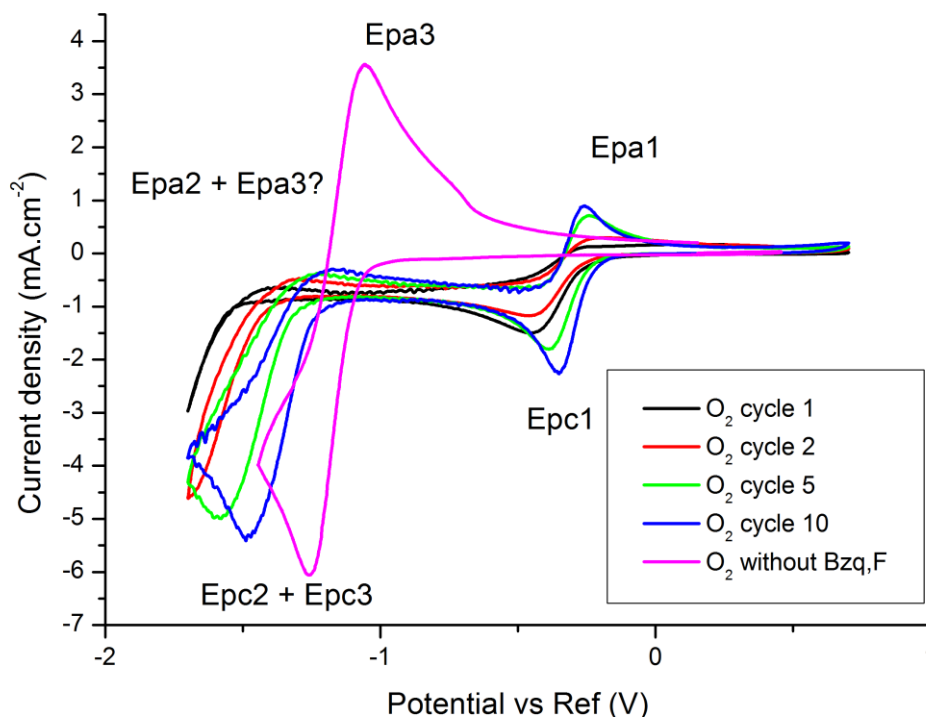


Figure IV. 9: Voltamperogram obtained for a glassy-carbon electrode in an O_2 -purged electrolyte composed of 5.5 mM TetraFluoroBenzoquinone in 0.2 M $TBAClO_4$ in acetonitrile, at 100 mV s^{-1} .

The first redox activity (E_{pc1}/E_{pa1}) gains more and more current from cycle 1 to cycle 10 (Figure IV.9), which totally contrasts with the experiment in Ar-purged medium (Figure IV.8). Also, both E_{pa2} and E_{pa3} are absent from these experiment. A possible mechanism to account for these phenomena (decreasing activity in Ar-purged electrolyte and increasing activity in O_2 -purged electrolyte) can be proposed.

The fluorinated benzoquinone has fluorine atoms, instead of hydrogen ones on the cycle. It is well-known that fluorine is strongly electronegative (it attracts electrons), thus increasing the reactivity of the radicals ($Bzq,F^{\bullet-}$ and $Bzq,F^{2\bullet-}$) formed during reactions (IV.12) and (IV.13).

As a consequence, the inductive effect of the fluorine atoms is more powerful than the mesomeric effect (which normally occur thanks to the benzene ring), which might lead to direct radicals recombination on the surface of the electrode.

Consequently, it is highly probable that a layer of the adsorbed "chains" of benzoquinones is clogging the electrode surface (which induces a decrease of the active surface), thus decreasing the redox apparent activity of the redox compound on the electrode.

When the ORR begins in an electrolyte purged under oxygen, superoxide species are produced; these are very reactive and might attack the O-O bond between the adsorbed benzoquinones, and as the superoxide is a smaller, highly reactive radical, the recombination path between the latter and the $Bzq^{2\bullet-}$ species becomes predominant versus the recombination of $Bzq^{2\bullet-}$ on itself. Thus, both *Epa2* and *Epa3* disappear, and the active surface area is recovered, thereby enabling (again) the first oxidoreduction peaks of the benzoquinone.

In order to test this hypothesis (that the recombination between the superoxide and the $Bzq^{2\bullet-}$ occurred), another benzoquinone species was tested: the tetrachloro-p-benzoquinone, on which the inductive effect of chlorine is less powerful than for its fluorinated counterpart. The results are presented on Figure IV.10.

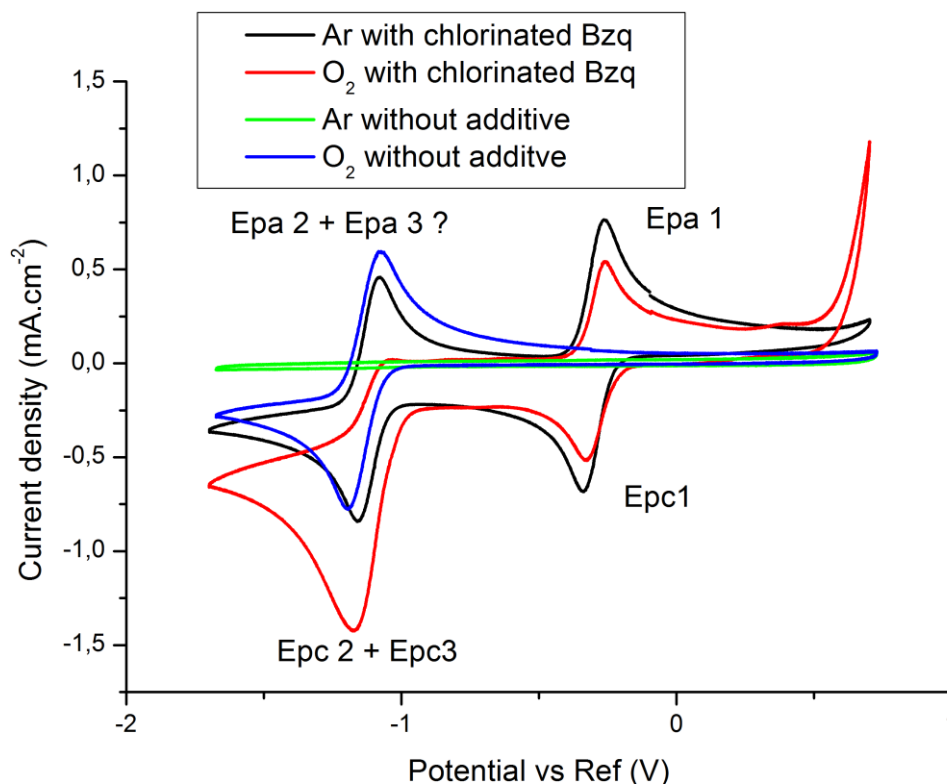


Figure IV. 10: Voltamperogram obtained for a glassy-carbon electrode in an O_2 -purged electrolyte composed of 3 mM TetraChloroBenzoquinone in 0.2 M $TBAClO_4$ DMSO, 100 mV s^{-1} . Evidence of Strong Reactivity with ORR product

The obtained results are unequivocal: the extinction of *Epa2* and *Epa3* in presence of the tetrachloro-p-benzoquinone under oxygen purge is also occurring for the chlorinated benzoquinone, which confirms that an additional mechanism takes place between the ORR product and the radical formed at *Epc2* ($Bzq, Cl^{2\bullet-}$). Also, the inductive effect is suppressed, when fluorine atoms are substituted by chlorine ones, as depicted on Figure IV.11.

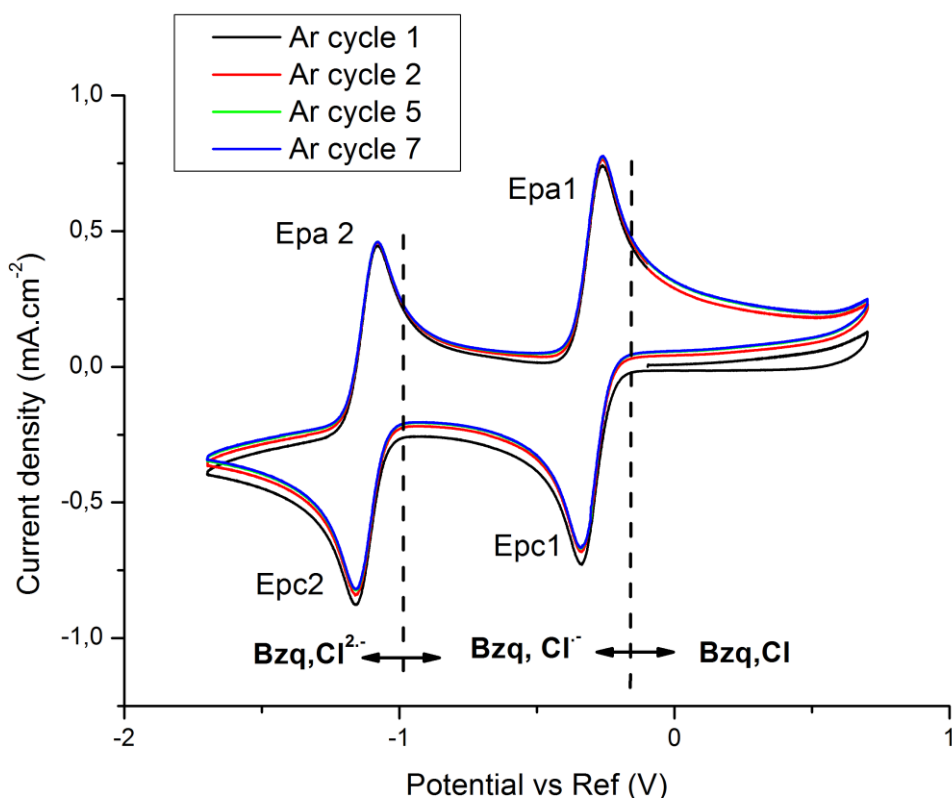


Figure IV. 11 : Voltamperogram obtained for a glassy-carbon electrode in an Ar -purged electrolyte composed of 3 mM TetraChloroBenzoquinone in 0.2M TBAClO₄DMSO, purged at 100 mV s⁻¹. No self-poisoning is observed.

Considering the results depicted from Figures IV.8 to IV.11, it appears that the TetraChloroBenzoquinone (Bzq,Cl) is of better interest than the TetraFluoroBenzoquinone (Bzq,F), as a full reversibility is obtained in Ar-purged media (see Figure IV.11), which opposes the behavior of the Bzq, F (Figure IV.). However, the recombination between the bi radical (Bzq,Cl^{2•-}) and the superoxide is still occurring in O₂-purged electrolyte (Figure IV.10), which compromises the usability of the family of benzoquinone compounds for use as redox shuttles. Pushing more the understanding, it is assumed that, in order to avoid the latter recombination, redox mediator must exhibit a redox activity, without the formation of a radical (the formation of either an anion or a cation will be preferred).

iii. Chromium difluoride

Chromium difluoride was of high interest also, at the Cr³⁺/Cr²⁺ redox activity is usually very fast (in aqueous medium). However, the redox potential of this transition is -0.41 V vs. ENH (corresponding to -1.1 V vs. Ref) [28] in aqueous solution, which is outside the required voltage window (lower limit:

0.2 V vs. ENH/0.49 V vs. Ref). At the time, these compounds were tried anyway, in the hope that the redox potential of this transition could appear at higher voltage values in non-aqueous media.

As CrF₂ was insoluble in the 0.2 M TBAClO₄ DMSO electrolyte (the grains remained in the bottom of the flask for 1 week, without any change in color that would have had indicated some solubilization), it was decided to immobilize this compound in the solid form at the glassy-carbon electrode. To that goal, an ink (Vulcan XC72/Kynar HSV900/CrF₂, with mass percentage: 48/27/25 in N-Methyl-2-pyrrolidone 20 mg of carbon for 1 mL) was prepared and a calibrated drop (20 μL) was deposited on the electrode; it was then dried in an oven at 85°C for 2 hours and put under dynamic vacuum for at least 30 minutes. The experiments were conducted in the same electrolyte (0.2 M TBAClO₄ DMSO) at 100 mV s⁻¹, and the results are presented in Figure IV.12.

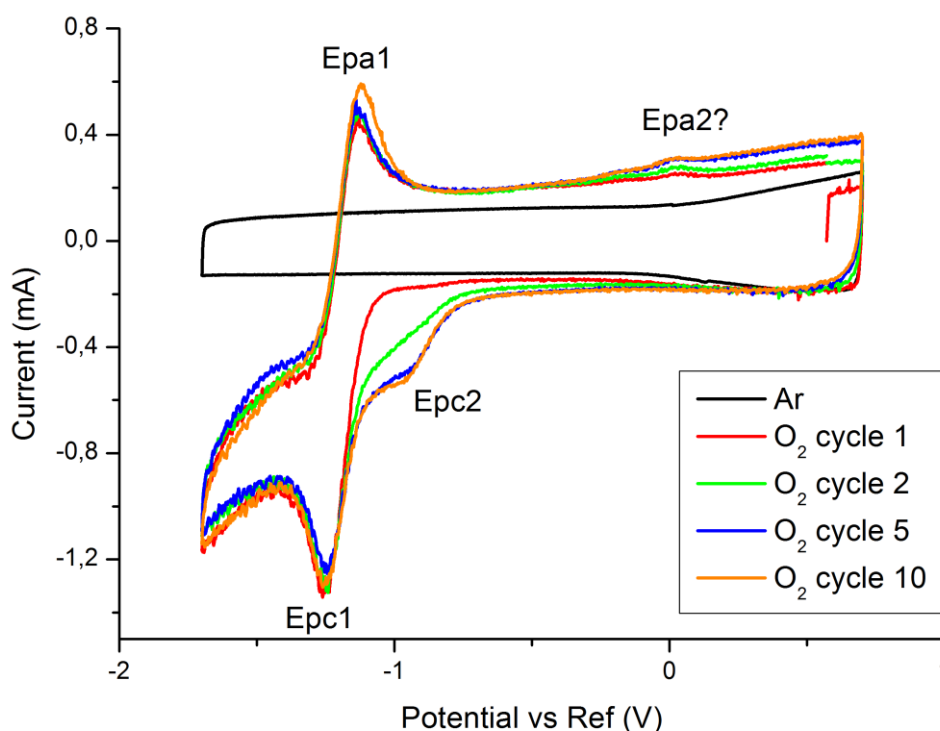


Figure IV. 12: Voltamperogram obtained for a glassy-carbon electrode in an O₂-purged electrolyte with the chromium difluoride ink in 0.2 M TBAClO₄ DMSO at 100 mV s⁻¹

For the Ar-purged experiment (black curve), only the double layer response of the high surface area carbon electrode was observed, showing that the CrF₂ compound is not electrochemically active in this medium. Then, the electrolyte was purged under oxygen (45 minutes). The electrochemical response for the first cycle (red curve) only accounted for the superoxide formation (Eq. IV.14).



During the cycling of the electrode, a second contribution appeared for the reduction and did stabilize (from the green curve – cycle 2—to the orange one - cycle 10). This contribution (E_{pc2}) occurs at around -0.75 V vs. Ref. A small oxidation also appears (E_{pa2}) and is probably related to the oxidation of the compound formed at E_{pc2} .

As the CrF_2 is not soluble in the electrolyte (see above), the first cycle is only active with the large cation TBA^+ . However, according to the HSAB theory (see chapter 1), ORR products have a stronger affinity with smaller cation. Therefore, if a superoxide species encounters a chromium cation, it will bound with the latter, rather than with the TBA^+ . It is therefore postulated that the E_{pc2}/E_{pa2} contributions are accounted for by the association of the ORR products with chromium cations. Despite its interest and as the subject of the present thesis focus on $Li-O_2$ cathodes, not on $Cr-O_2$ cathodes, this “activity” was disregarded and considered not interesting. It must also be noted that the ORR in presence of lithium occurs at much higher potentials than E_{pc2} , which completely discards this compound to be used as a redox shuttle.

c. Useful compounds to be used as redox shuttles in $Li-O_2$ batteries

As explained above, the benzoquinone was the only compound with the redox activity correctly placed in the required window. However, it was proven inefficient, owing to radical recombination. Thus, the screening of the redox shuttle continued, compounds where either the oxidized or reduced form was a radical being excluded. Two efficient compounds have been selected: the first is 5,10,15,20-Tetrakis(4-methoxyphenyl)-21H,23H-porphine cobalt(II). This compound is classed under the compound family named porphyrins. Thus it will be labeled Co(II)-Po for the rest of the present work. The second compound, which will prove highly efficient, is denominated N,N'-Bis(salicylidene)ethylenediaminocobalt(II). It is also known as salcomine or Co-salen, and will be denominated by the latter term for the rest of the present work. The subsequent molecules structure is presented in Figure IV.13.

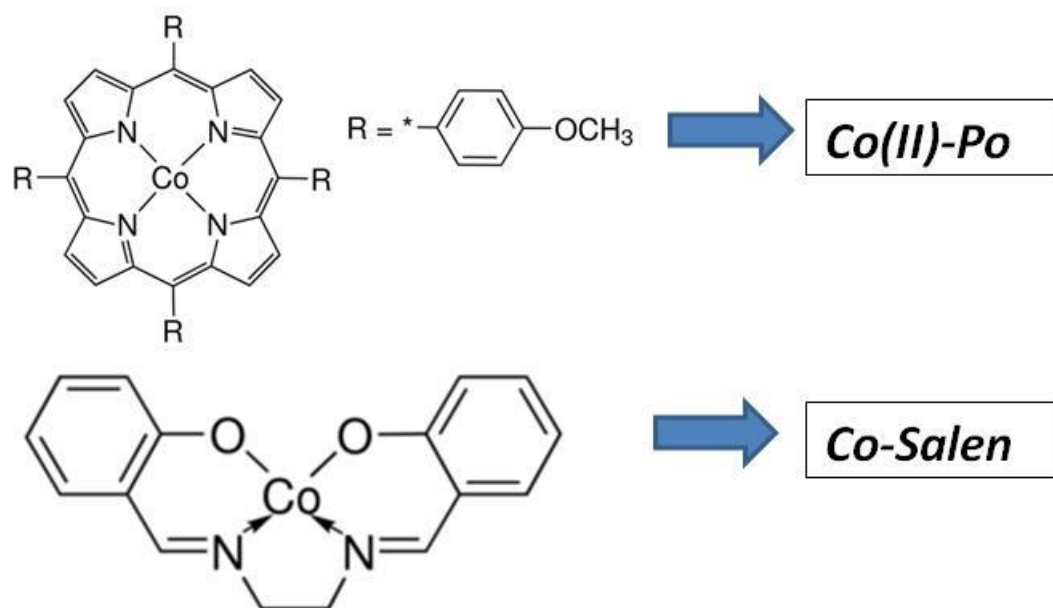


Figure IV. 13 : Chemical Structure of Co(II)-Po and Co-Salen

Electrolytes were prepared with these two compounds. For the former one, 34 mg of Co(II)-Po was dissolved in 20 mL of 0.2 M LiClO₄ DMSO. However, even after one week, some black solid particles remained in the electrolyte, meaning that the latter was saturated in Co(II)-Po, but also that the true Co(II)-Po concentration could not be asserted with precision. If all the Co(II)-Po was dissolved, the corresponding concentration would have been of 2 mM. Thus, it can only be assumed that the true Co(II)-Po concentration is below this value. As for the Co(II)-Po, 18 mg of Co-salen were dissolved in the same electrolyte (this time no particles remained in the solution, leading to a concentration of dissolved Co-salen of 2.8 mM). The activity of both compound is depicted on Figure IV.14.

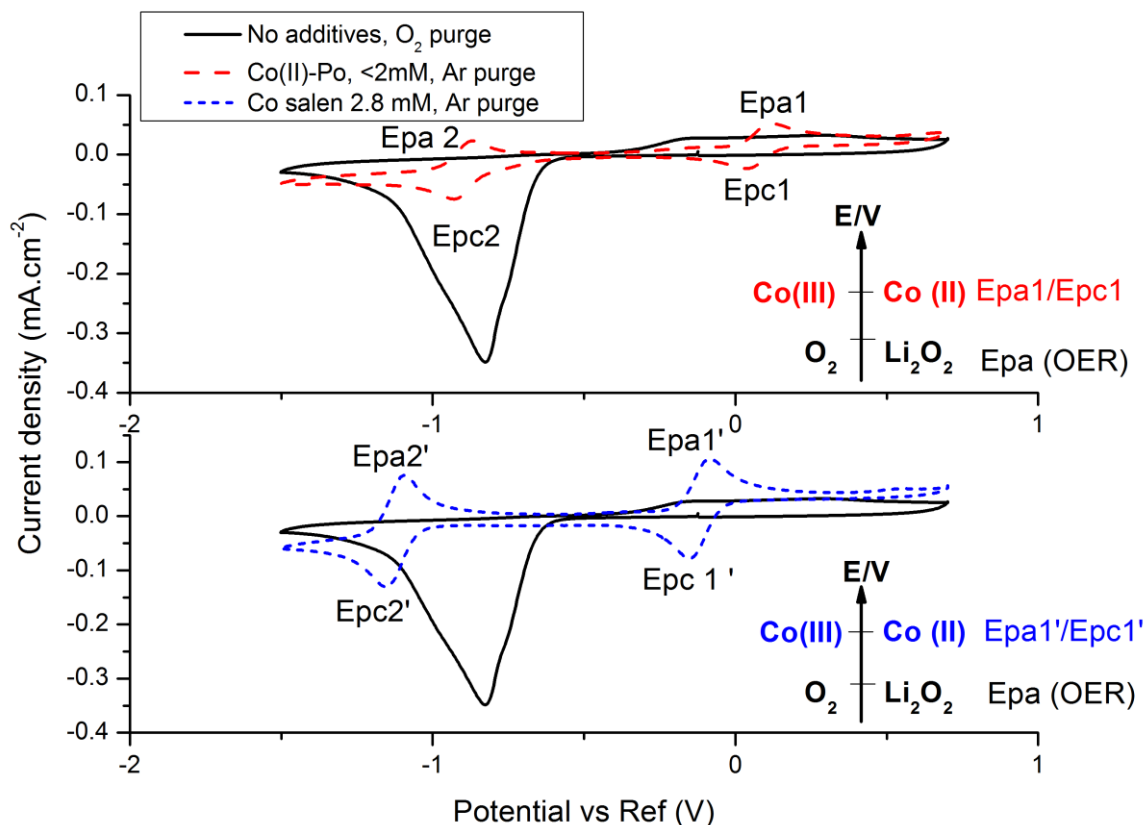


Figure IV. 14: Voltamperogram obtained for a glassy-carbon electrode in an O_2 -purged electrolyte of 0.2 M $LiClO_4$ DMSO, in presence of either $Co(II)$ -Po (red dashed line) or Co -salen (blue short dashed line), or without additives (plain line) 5 mV s^{-1} , Karl-Fisher titration of water traces below 100 ppm

As seen on Figure IV.14, the E_{pa1}/E_{pc1} activity of $Co(II)$ -Po, and the $E_{pa1'}/E_{pc1'}$ activity of Co -salen are ideally placed for an application as redox shuttle for the OER. As the cobalt is in (+II) state in the pristine compounds, this transition is relative to the $Co(III)/Co(II)$ couple. Thus, the $Co(III)$ form of the additive is expected to react with the remaining Li_2O_2 on the electrode surface, or in the solution (gamma rule, see Figure IV.14). In order to assess that this redox activity of both compound can be profitable for use as a redox shuttle, a regeneration experiment was conducted for “discharged” glassy-carbon electrodes. The scan rate used in these experiments was taken very low (5 mV s^{-1}), in order to see features as close as possible to a practical system. Firstly, five scans on a full voltage window were conducted in order to efficiently discharge the glassy-carbon electrode (*i.e.* form Li_2O_2 from ORR) and therefore passivate its surface. Then, ten cycles in the OER region were performed (no further ORR, so only the lithium peroxide, produced during the first step can be re-oxidized). After this, a scan on the full voltage window was performed and compared to the initial scan (of the first step), when the electrode surface was pristine. A similar benchmark experiment, conducted without additives, was made for comparison, as depicted in Figure IV.15.

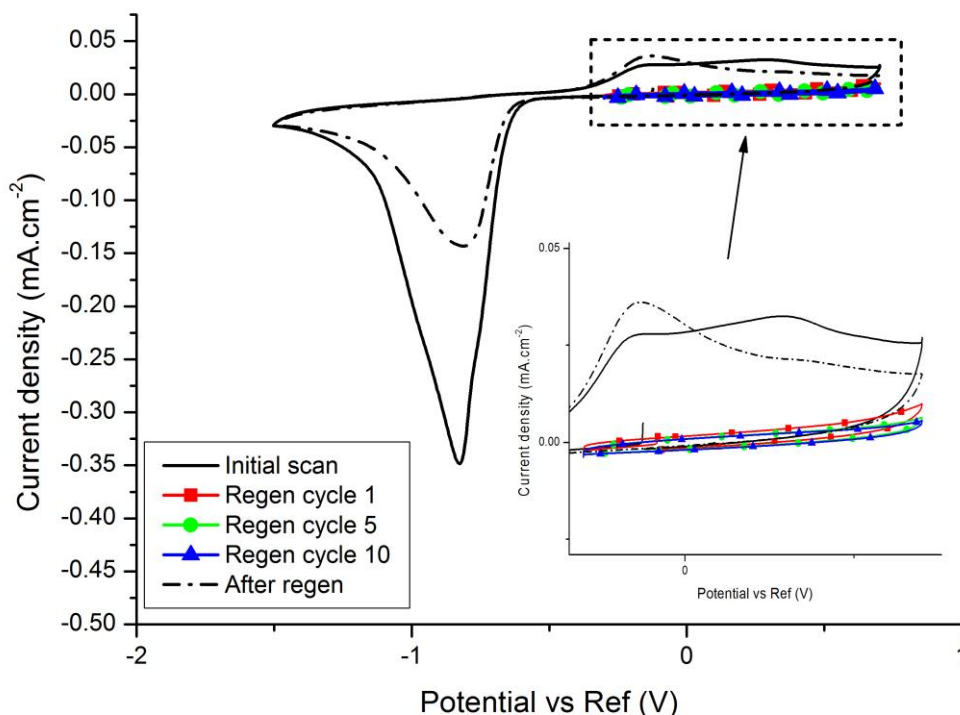


Figure IV. 15: Voltamperogram obtained for a glassy-carbon electrode in an O_2 -purged electrolyte. Regeneration experiment conducted in 0.2 M $LiClO_4$ without additives, 5 mV s^{-1} , KF below 100 ppm

Figure IV.15 indicates that the Initial scan and the scan after the regeneration step are very different: the ORR peak current density after the regeneration step dropped to $-0.15 \text{ mA}\cdot\text{cm}^{-2}$ (compared to $-0.35 \text{ mA}\cdot\text{cm}^{-2}$ on a fresh electrode), indicating that without additives, the electrode surface cannot be regenerated. In other words, the recharge is not efficient in absence of redox shuttle (at least in this potential window).

i. Oxygen fixation for Co(II)-Po and Co-salen

An unexpected phenomenon was observed for both compounds as they fix oxygen on their cobalt core [32, 33]. In order to assess the difference in bounding strength between the cobalt and oxygen, UV-Visible spectroscopy was conducted. In the subsequent experiment, the exact concentration of Co(II)-Po and Co-Salen is not known precisely, as the scope of this experiment is to observe the shifts in the UV-Vis Spectra, when the solution is purged by oxygen, or by argon. The corresponding results are presented on Figure IV.16.

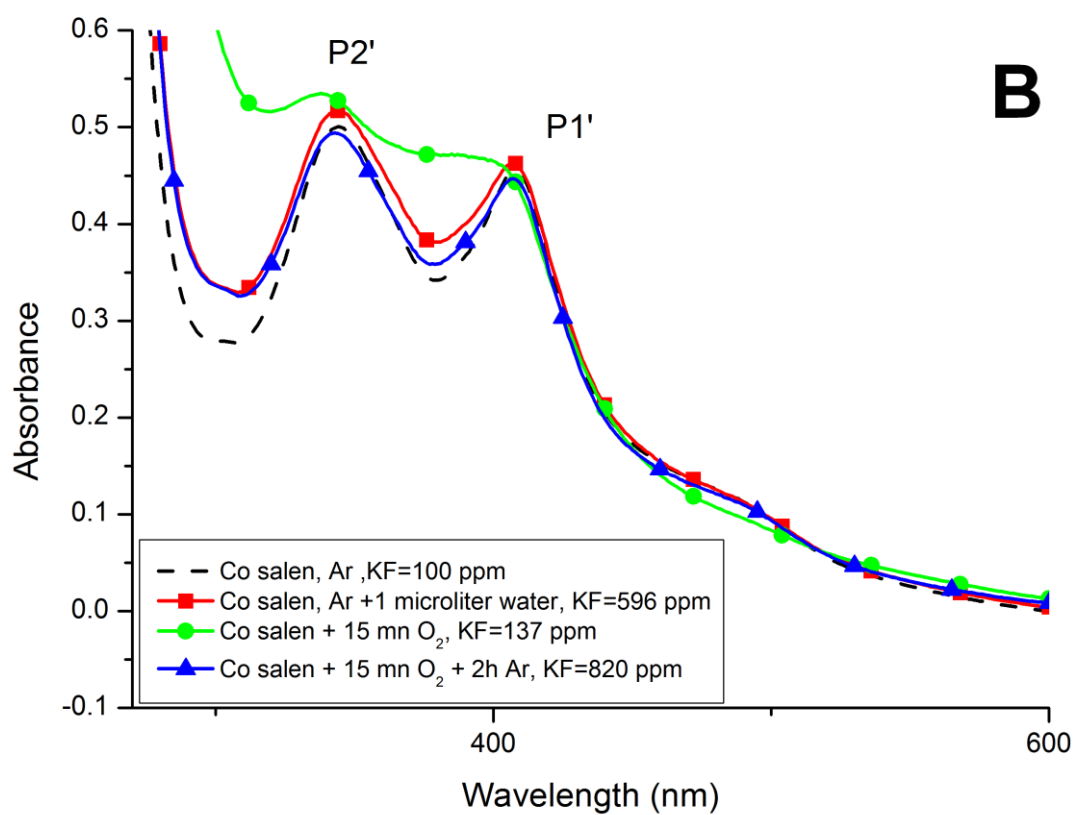
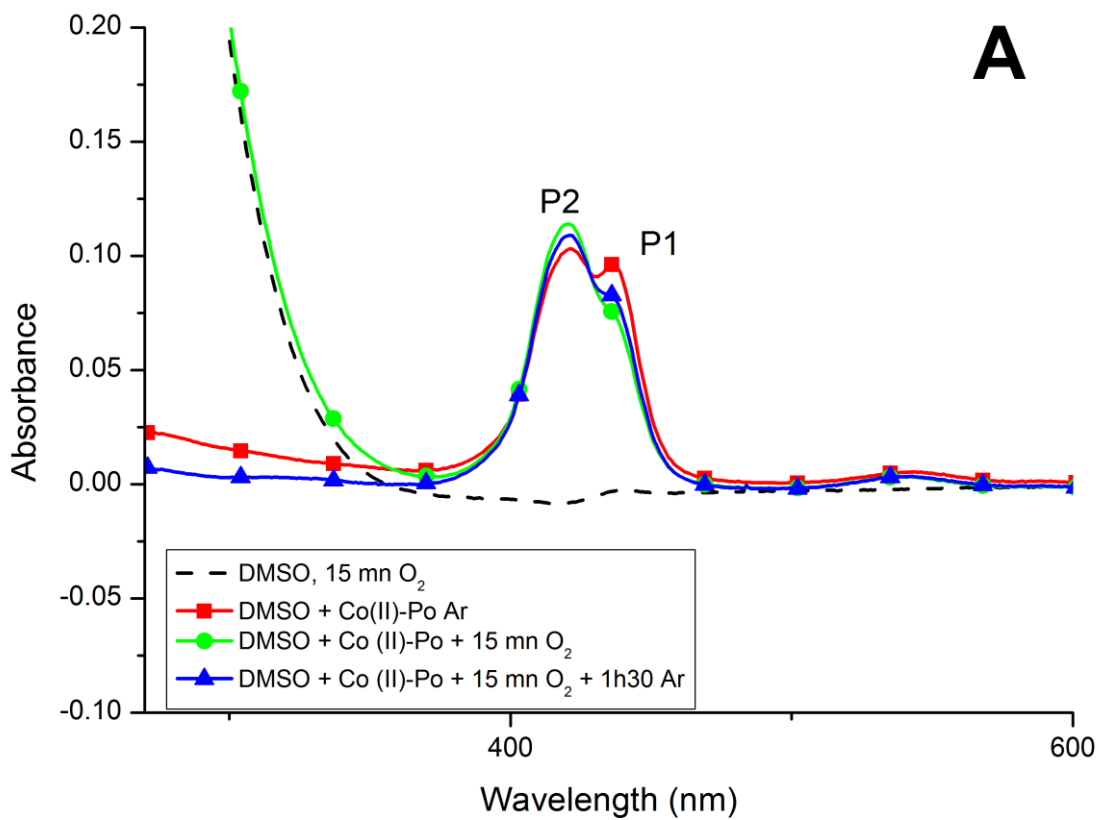


Figure IV. 16: UV-Visible spectra of A-Co(II)-Po and B-Co-salen in the presence/absence of O_2

Two contributions are visible for the Co(II)-Po spectrum on Figure IV.16-A: the P1 contribution at 437.2 nm and the P2 contribution at 420.15 nm. However, as published by Holze *et al*, only one contribution is expected for the Soret band of the Co(II)-Po [32] (in acetone, the corresponding peak was occurring at 411.5 nm). When the solution is purged under oxygen for 15 minutes, the P1 contribution decreases and the P2 rises. Once the solution is purged back with argon for two hours, the P1 peak rises again and P2 decreases, but even though the solution is now Ar-saturated, the spectrometric trace does not come back to its initial state. It is thus assumed that the P2 contribution is linked to the complex formation between the Co(II)-Po and oxygen and that the P1 contribution corresponds to the pristine porphyrin. As the heights of P1 and P2 are dependent on the purging of the solution, it is highly probable that an equilibrium exists between the pristine porphyrin and the porphyrin paired with oxygen (equation IV.15):



For the Co-salen, a similar complex is formed (already described in the literature, in KOH and DMSO [33]), but this time, the process is completely reversible, as seen on Figure IV.16-B: the shape of the UV-Vis spectrum is completely different under argon and oxygen atmospheres. When the solution is purged back with argon, a small increase of the baseline is observed at 350 nm, but this may be ascribed to some water contamination. To check this hypothesis, the first solution (that had never been purged with oxygen), was deliberately contaminated by water, and the two traces perfectly matched, meaning that the small increase of the baseline at 350 nm was due to the water. This small bias does however not change the conclusions: a complex forms between Co-salen and oxygen, and this complex formation is fully reversible (as shown in equation IV.16):



From this experiment, it can be concluded that the bounding strength between the oxygen and the cobalt core is stronger in Co(II)-Po than in Co-Salen (as the spectrum does not come back to its initial state, even after two hours of Ar-purging), which is also supported by the fact that the Co(II)-Po had the ability to "trap" the oxygen traces in the solution, even though the latter was intensively purged under argon and dried on molecular sieves upon the experiment.

ii. Co(II)-Po

The same electrochemical procedure was applied for the Co(II)-Po, and the results are depicted on Figure IV.17.

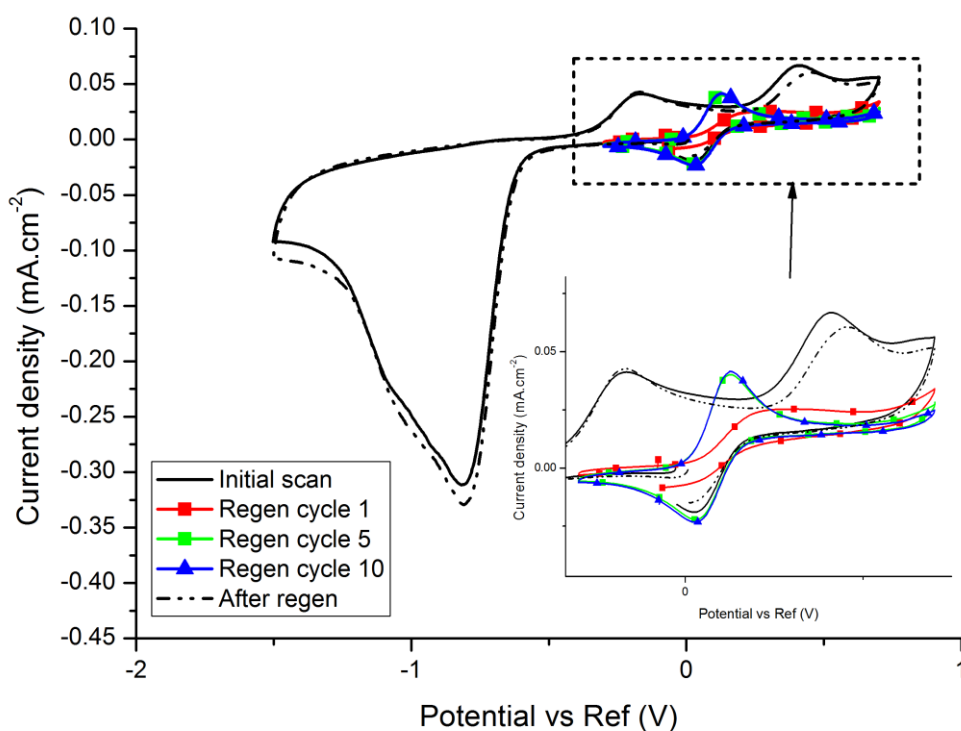


Figure IV. 17: Voltamperogram obtained for a glassy-carbon electrode in an O_2 -purged electrolyte. Regeneration experiment conducted in 0.2 M $LiClO_4$ containing < 2 mM $Co(II)-Po$, 5 $mV s^{-1}$, KF below 100 ppm

The results of the regeneration experiment in an electrolyte containing $Co(II)-Po$ are drastically different than without additives. The trace after the regeneration step (dashed line) is almost similar (in terms of ORR peak) than for the fresh electrode (plain line), showing that the regeneration step worked efficiently. In addition, during the regeneration step, the E_{pa1}/E_{pc1} peaks are gradually increasing from cycle 1 to cycle 10 (see the zoom inserted), which can only be explained by the fact that the active surface is progressively recovered. This signs the efficient “removal” of the solid passivating products (Li_2O_2) on the latter by $Co(II)-Po$, demonstrating that this compound can be used as a redox shuttle in $Li-O_2$ batteries.

-Mass transport and kinetic parameters determination:

The number of electrons exchanged for the oxidation and for the reduction of the $Co(II)-Po$ are estimated thanks to Figure IV.18.

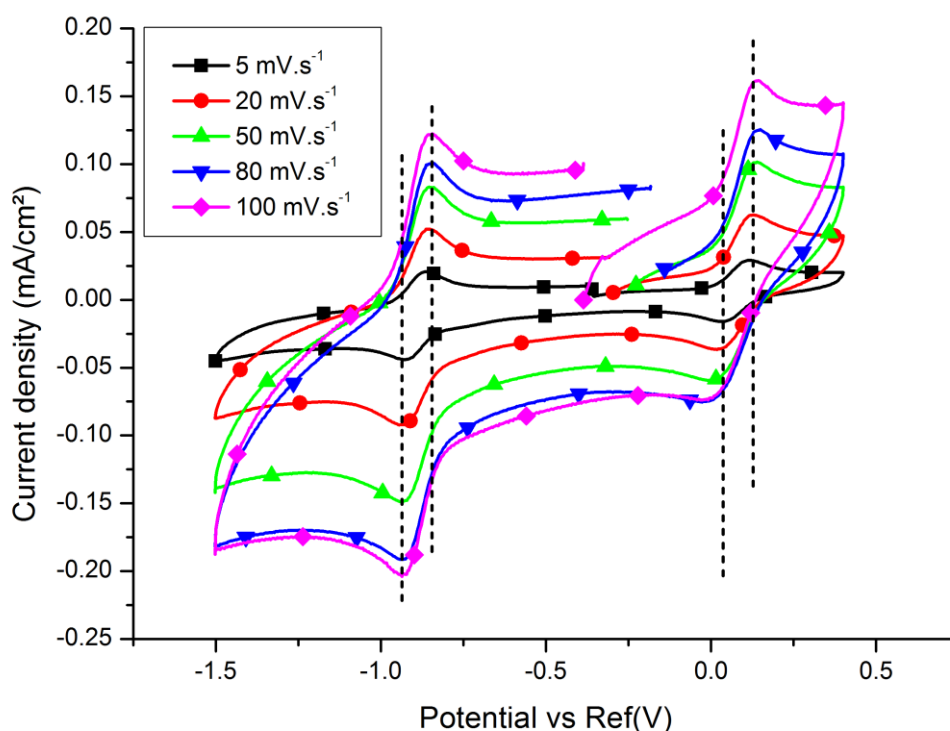


Figure IV. 18: *iR*-corrected voltamperogram obtained for a glassy-carbon electrode in an Ar-purged electrolyte comprising less than 2 mM of Co(II)-Po in 0.2 M LiClO₄ in DMSO. The scan rates varies from 5 to 100 mV s⁻¹.

Figure IV.18 shows that the oxidation of Co(II)-Po is quasi-reversible (the difference between the oxidation peaks and the reduction peaks is increasing with the scan rate [34]). On the contrary, the reduction of Co(II)-Po seems to be fully reversible (at least in this range of potential scan rates), as the peak positions are not scan rate-dependent.

The differences between the oxidation and reduction peaks (ΔE_p) for both the oxidation of the Co(II)-Po and the reduction of the Co(II)-Po are gathered in Table IV.1.

Table IV. 1 : ΔE_p dependence on the scan rate for the Oxidation or the Reduction of Co(II)-Po

Scan Rate (mV s ⁻¹)	ΔE_p Oxidation (mV)	ΔE_p Reduction (mV)
5	83	69
20	112	82
50	137	87
80	170	87
1000	184	88

As shown in Table IV.1, the oxidation of the Co(II)-Po is quasi-reversible and the reduction seems to be more reversible (even though a slight increase can be seen between 5 and 50 mV s⁻¹). Also, as in the two cases, the ΔE_p values are greater than 60 mV, the number of electrons exchanged (n) for both the oxidation and the reduction steps must be one, in agreement with equation IV.17 (the system here is quasi-reversible, but at a slow scan rate, a quasi-reversible system behave like a fast reversible system, (*i.e.* 5 mV s⁻¹)).

- For a reversible reaction : $\Delta E_p = \frac{59}{n}$ (mV)[34] (IV.17)

In order to assess the diffusion behaviors of the Co(II)-Po and the Co-salen, rotating disk electrode experiments were performed in diffusion-convection regime. The electrolyte consisted of 100 mL of 0.2 M LiClO₄ DMSO, with either 24 mg of Co-salen or, 21 mg of Co(II)-Po. Concerning the electrochemical procedure, the experiments were iR-corrected dynamically. The experiments consisted of an Open Circuit Voltage stabilization of 5 minutes, followed by a Linear Scan Voltammetry from the OCV to -1.5 V vs. Ref. Then, a new stabilization OCV was recorded for five minutes and a LSV was applied from the stabilization potential to 0.4 V vs. Ref. Five points were recorded in terms of mass-transport: no rotation, 500, 1000, 1500 and 2000 revolutions per minute. The corresponding experiment for Co(II)-Po in Ar-purged medium are depicted on Figure IV.19.

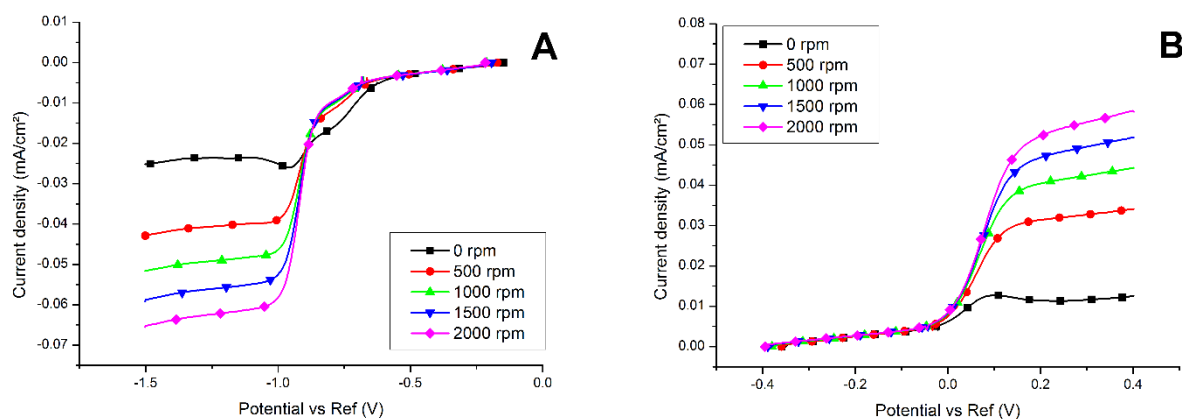


Figure IV. 19: Linear Scan Voltammeteries, in 0.2 M LiClO₄ DMSO, 0.265 mM Co(II)-Po, at 5 mV s⁻¹. Ar-purged medium. A- From OCV to -1.5 V vs. Ref. B-From OCV to 0.4 V vs. Ref

The Levich law (IV.18) is valid for a rotation rate comprised between 100 rpm and 10 000 rpm [34]. Thus, for the point at 0 rpm, the current density is arbitrarily taken at 0 mA cm⁻². The Levich plots are presented in Figure IV.20.

$$j_{lim}(A\text{ cm}^{-2}) = 0.620 \times n \times D^{2/3} \times \nu^{-1/6} \times C \times \omega^{1/2} \quad (IV.18)$$

With: n the number of electrons, D the diffusion coefficient (cm² s⁻¹), ν the kinematic viscosity (cm² s⁻¹), C the analyte concentration (mol cm⁻³) and ω the rotation rate of the RDE (rad s⁻¹).

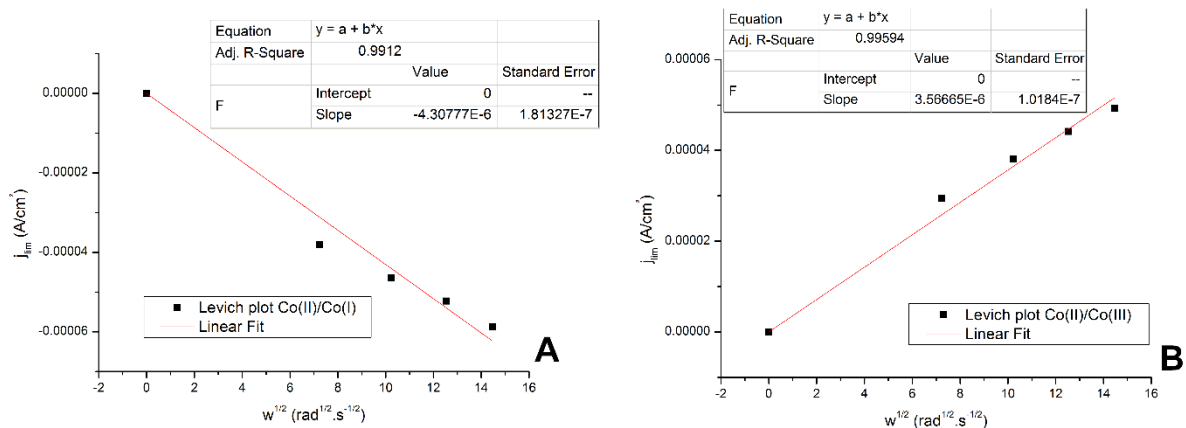


Figure IV. 20: Levich plot for A- Reduction of Co(II)-Po to Co(I)-Po . B- Oxidation of Co(II)-Po to Co(III)-Po

Taking in consideration that in both cases, the number of electron exchanged is equal to one, and assuming that the kinematic viscosity of the electrolyte is the one of DMSO ($0.018 \text{ cm}^2 \text{ s}^{-1}$ [35]) the diffusion coefficient of the Co(II)-Po for its reduction and oxidation can be calculated from the Levich slopes (Table IV.2).

Table IV. 2 : Diffusion Coefficient for the Co(II)-Po in DMSO electrolyte

Reaction	Co(II)-Po concentration (mol cm^{-3})	Diffusion coefficient ($\text{cm}^2 \text{ s}^{-1}$)
Reduction	$2.65 \cdot 10^{-7}$	$1.64 \cdot 10^{-6}$
Oxidation	$2.65 \cdot 10^{-7}$	$1.24 \cdot 10^{-6}$

The results from Table IV.2 show that the Co(II)-Po has a slower diffusion coefficient for its oxidation than for its reduction. Yet, this difference (24%) can be attributed either to a parasitic effect of the reduction of oxygen traces (that cannot be removed entirely from the solution), or to some distortions of the background. However, it is its oxidation that is of interest here, as it is the Co(III)-Po form that will react with lithium peroxide to enhance oxygen evolution. The subsequent slow diffusion coefficient can be explained by the size of the additive, which is rather a big molecule and thus moves slower than smaller molecules (*e.g.* compared to ferrocene, which exhibits a diffusion coefficient close to $4.9 \cdot 10^{-6} \text{ cm}^2 \text{ s}^{-1}$ in DMSO [36]).

The activity in oxygen-saturated electrolyte, under rotation, was also investigated and the related experiment is depicted on Figure IV.21.

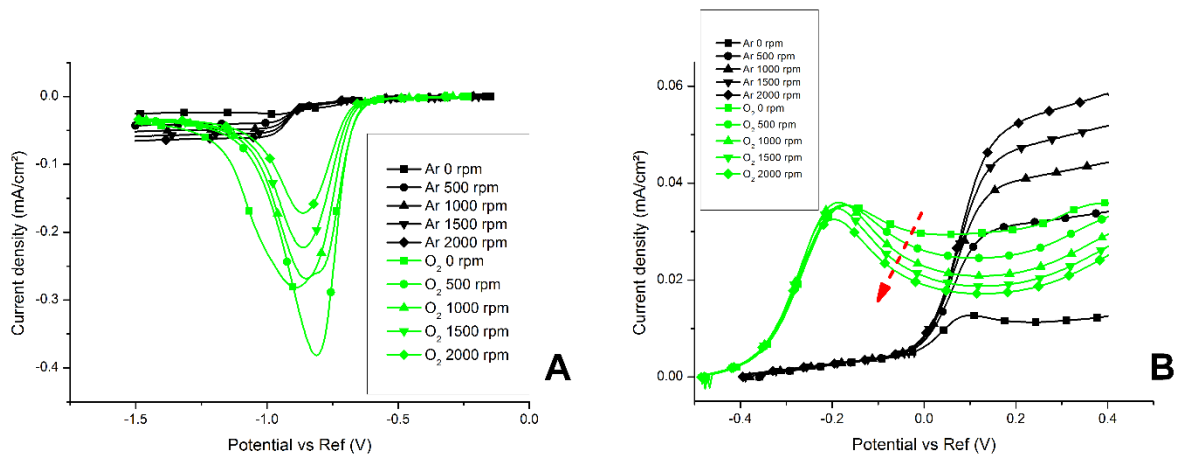


Figure IV. 21: Linear Scan Voltammograms, in 0.2 M LiClO₄ DMSO, 0.265 mM Co(II)-Po, at 5 mV s⁻¹ Ar (black) and O₂ (green) purged media. A-From OCV to -1.5 V vs. Ref. B-From OCV to 0.4 V vs. Ref

The ORR experiments of Figure IV.21-A show that even though the rotation is increased (O₂ transport enhanced at the electrode's surface), the ORR peak current density decreases from -0.3 mA cm⁻² (no rotation) to -0.15 mA cm⁻² (2000 rpm). This indicates that the electrode surface is rapidly covered (and passivated) by a layer of Li₂O₂. When the OER is performed, the current density at the end potential is expected to increase as the rotation rate increases. The present tendency indicates the opposite, as from no rotation to 2000 rpm, less current is obtained in the OER region. This indicates that the surface is not efficiently recovered and that the redox shuttle effect is not occurring as expected.

It is postulated that this inefficiency is only due to the relatively low content of Co(II)-Po in the electrolyte (required to dissolve all of it and to calculate its diffusion coefficient), as compared to the case of the three-electrode setup (20 mg was put in 20 mL of 0.2 M LiClO₄ DMSO, here only 21 mg in 100 mL of the same electrolyte). Knowing the diffusion coefficient, the rate constant for the oxidation of the Co(II)-Po can be estimated, using the Nicholson and Shain technique, and especially the fit technique proposed by Dragu *et al* [37], and calculating the ψ parameter (equations IV.19 to IV.22).

$$\psi = x_0 \left(\frac{A_1 - A_2}{\Delta E_{peak} - A_2} - 1 \right)^{\frac{1}{p}} \quad (IV.19)$$

$$a = \frac{nF}{RT} v \quad (IV.20)$$

$$k^0 = \frac{\psi \sqrt{\pi \cdot a \cdot D}}{\gamma^\alpha} \quad (IV.21)$$

$$\gamma = \left(\frac{D_O}{D_R} \right)^{\frac{1}{2}} \quad (IV.22)$$

With x_0 , A_1 , A_2 and p tabulated values ($x_0 = 0.0688$; $A_1 = 432.91$ mV; $A_2 = 59.55$ mV and $p = 0.9938$)

In the present case, several hypothesis must be made: $D_O = D_R$ (thus $\gamma = 1$) and $\alpha = 0.5$. Using the values listed in table IV.1 for the oxidation, the rate constant for the oxidation of Co(II)-Po can be estimated (Table IV.3).

Table IV. 3: k° calculations, using fit of [10] for the oxidation of Co(II)-Po at several scan rates

Scan rate (mV s ⁻¹)	ΔE_{peak} (mV)	ψ	a	k° (cm s ⁻¹)
5	83	1.044	0.195	$1.05 \cdot 10^{-3}$
20	112	0.426	0.779	$8.53 \cdot 10^{-4}$
50	137	0.265	1.947	$8.40 \cdot 10^{-4}$
80	170	0.165	3.116	$6.60 \cdot 10^{-4}$
100	184	0.138	3.895	$6.19 \cdot 10^{-4}$

The average value for the rate constant was determined to be $(8.03 \pm 1,71) \times 10^{-4}$ cm² s⁻¹.

Compared to other cobalt complex values (for instance Co(bpy)₃, which exhibits a rate constant of about 0.0416 cm s⁻¹ [37]), this value is smaller, indicating a quasi-reversible couple, but which tend to behave as a fast-reversible couple at lower scan rates.

iii. Co-salen

As for the Co(II)-Po, the same electrochemical procedure was applied and the corresponding results are depicted on Figure IV.22.

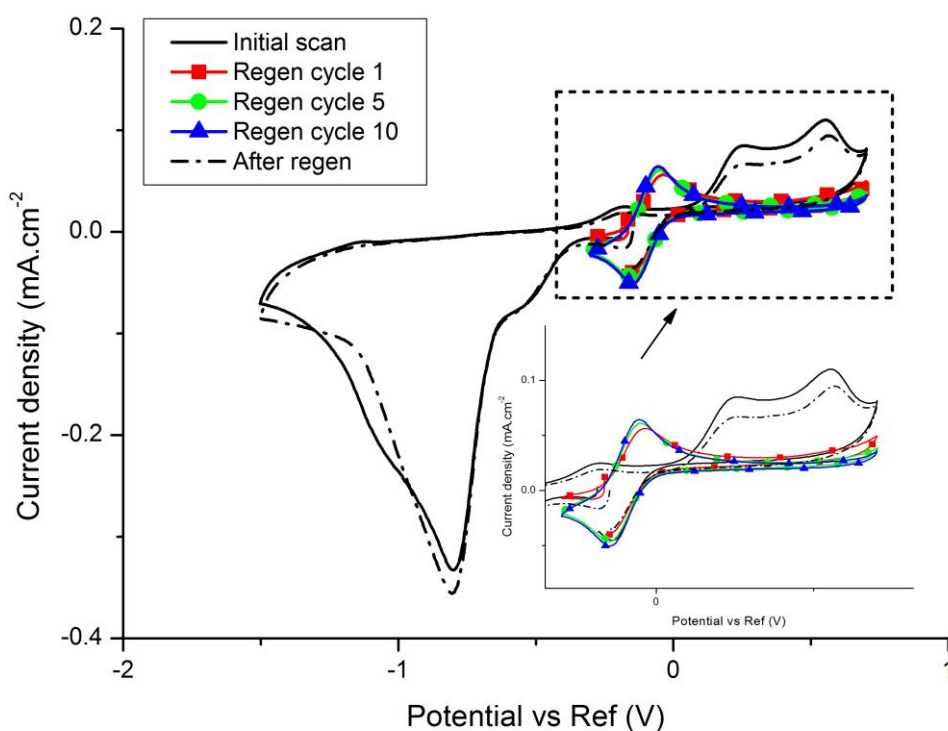


Figure IV. 22: Voltamperogram obtained for a glassy-carbon electrode in an O_2 -purged electrolyte. Regeneration experiment conducted in 0.2 M $LiClO_4$ containing 2.8 mM Co-Salen, 5 mV s^{-1} , KF below 100 ppm

The results of Figure IV.22 are as spectacular than with Co(II)-Po: the “after regeneration” trace and the trace on a pristine electrode are almost superposed in the ORR region, again meaning that an efficient surface recovery was possible in presence of the Co-salen. From the zoom on the OER region, one sees that the cathodic/anodic current densities of the $E_{pc1'}/E_{pa1'}$ transition are also increasing from the first cycle to the tenth cycle, but the passivation reached in the course/after the ORR in the previous cases, is much less of an issue with Co-salen in solution. This demonstrates that the redox shuttle effect is occurring *in situ*, even on the full cycles with Co-salen. This can be explained by the fact that more additives molecules are available in the vicinity of the electrode surface, owing to the larger solubility of this compound than for Co(II)-Po: the $E_{pc1'}/E_{pa1'}$ current densities are almost doubling those of the E_{pc1}/E_{pa1} (more Co-salen can be dissolved in the electrolyte than for Co(II)-Po).

-Mass transport and kinetic parameters determination:

As for the Co(II)-Po, the number of electrons exchanged (n) for the transition Co(II)-salen/Co(III)-salen is estimated by performing various scan rates in Ar-purged medium (Figure IV.23).

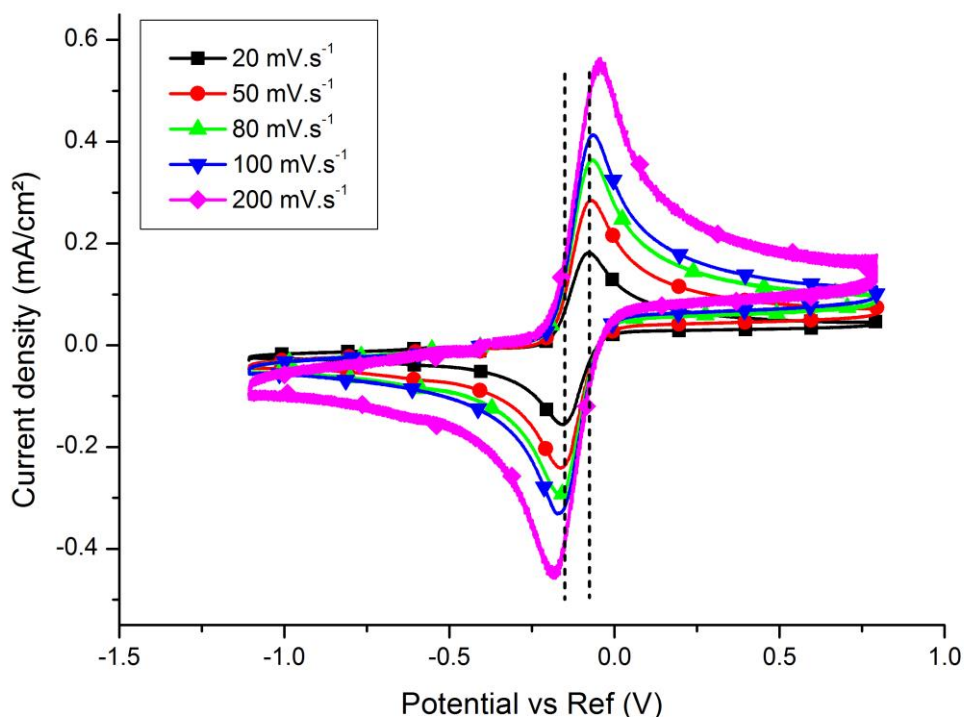


Figure IV. 23: *iR*-corrected voltamperogram obtained for a glassy-carbon electrode in an Ar-purged electrolyte comprising 3.8 mM of Co-salen, in 0.2 M TBAClO₄ in DMSO. The scan rates varies from 20 to 200 mV s⁻¹.

It is clear from Figure IV.23, that the redox activity of Co-salen is quasi-reversible, as when the scan rate increases, so does the difference between the oxidative and reductive peaks. It can also be seen that the second redox activity (which occurs at lower potential), is not visible. This can be explained by the fact that in this experiment, TBAClO₄ is used instead of LiClO₄, and that some interactions between the latter (probably with the lithium cation) and the Co-salen, allows the second redox activity to occur at higher potentials, while it is not possible in TBAClO₄ electrolytes; this effect is probably linked with the formation of ion pairs [38]. In order to prove this point, the same Co-salen content was dissolved in 0.2 M LiTf and compared with 0.2 M TBAClO₄ (Figure IV.24). This figure fully validates this explanation: the second redox activity of the Co-salen appears in a lithium-containing electrolyte.

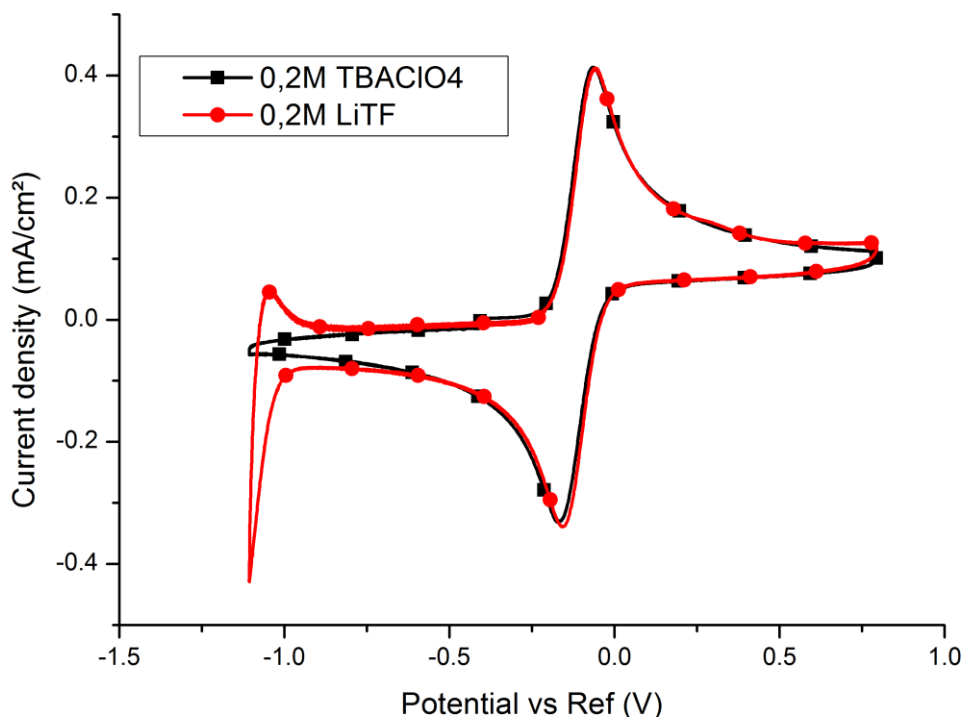


Figure IV. 24: *iR*-corrected voltamperogram obtained for a glassy-carbon electrode in an Ar-purged electrolyte comprising 3.8 mM of Co-salen, in either 0.2 M TBAClO₄ (Black) or 0.2 M LiTf (Red) in DMSO, 100 mV s⁻¹.

The values for the variation of ΔE_p with the scan rate (corresponding to Figure IV.23), are presented in Table IV.4.

Table IV. 4 : ΔE_p dependency on the scan rate for the oxidation of Co(II)-Salen

Scan rate (mV s ⁻¹)	ΔE_p Oxidation (mV)
20	79
50	88
80	99
100	104
200	142

As for the Co(II)-Po, the ΔE_p is greater than 60 mV, and grows with the scan rate. Thus, the oxidation kinetics of Co(II)-Salen is quasi-reversible and it is assumed that the number of electrons exchanged for the Co(II)/Co(III)-Salen transition is one (consistent with the literature [33, 38]). For the reduction of Co(II)-Salen to Co(I)-Salen, the number of electrons exchanged is also assumed to be one, as in the previous chapter, the ΔE_p was measured around 80 mV at 5 mV s⁻¹.

Rotating-disk electrodes experiment were performed in 0.2 M LiClO₄, with 0.74 mM of Co-Salen, and the corresponding results are presented in Figure IV.25.

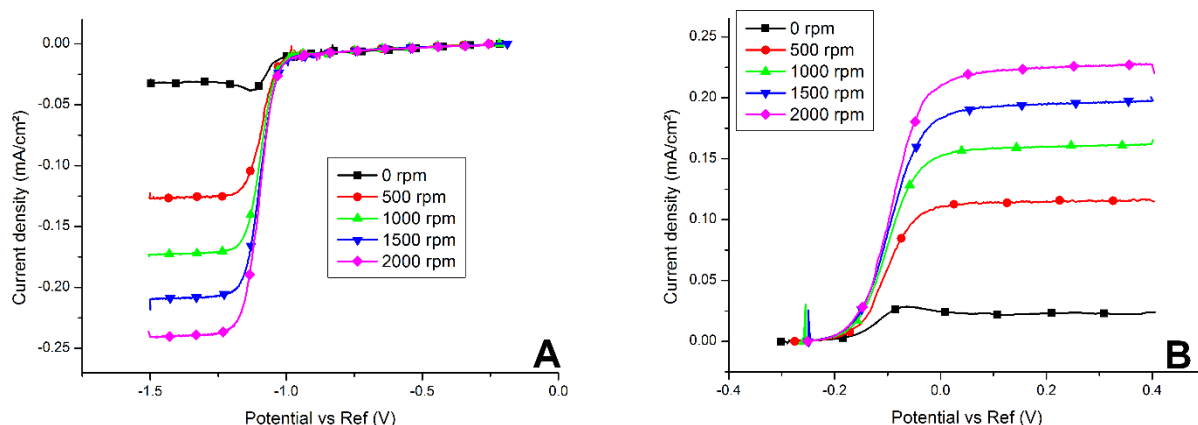


Figure IV. 25: Linear Scan Voltammeteries, 5 mV s⁻¹ in 0.2 M LiClO₄ DMSO, 0.74 mM of Co-Salen, Ar-purged medium. A-From OCV to -1.5 V vs. Ref. B-From OCV to 0.4 V vs. Ref

The behavior shown on Figure IV.25 clearly shows a process obeying Levich equation (no passivation of the electrode occurs, and clear dependence of the limiting current density to the rotation rate of the electrode is monitored). As the rotating disk electrode revolution rate is comprised between 100 and 10 000 rpm, the Levich law can be applied (Equation IV.18), and the corresponding Levich plots can be drawn by plotting the limiting current densities with the square root of the rotation rate (Figure IV.26).

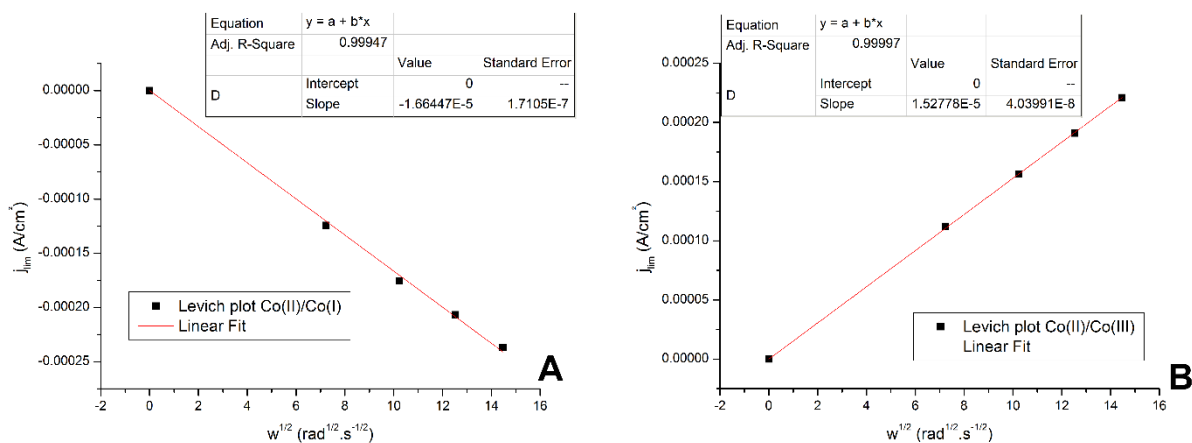


Figure IV. 26: Levich plot for A- Reduction of Co(II)-Salen to Co(I)-Salen . B- Oxidation of Co(II)-Salen to Co(III)-Salen

The diffusion coefficient of the oxidation of Co(II)-salen to Co(III)-salen and the reduction of Co(II)-salen to Co(I)-salen are calculated thanks to the same hypotheses than for Co(II)-Po (viscosity of the electrolyte equal to the one of pristine DMSO, number of electrons exchanged equals to one...); the slopes of the Levich Plots and their values are presented in Table IV.5.

Table IV. 5 : Diffusion Coefficients for the Co-Salen in DMSO electrolyte

Reaction	Co-salen concentration (mol cm ⁻³)	Diffusion coefficient (cm ² s ⁻¹)
Reduction	7.40 10 ⁻⁷	2.66 10 ⁻⁶
Oxidation	7.40 10 ⁻⁷	2.35 10 ⁻⁶

As for the Co(II)-Po, the diffusion coefficients determined correspond to a slow-moving molecule, compared to ferrocene (for instance). Also, as for the Co(II)-Po, the diffusion coefficient of the Co(II)-salen is larger for its reduction than for its oxidation (13%), which can be explained in a similar manner than for Co(II)-Po, by background distortions, or reduction of O₂ traces. The results in an O₂-saturated electrolyte are presented in Figure IV.27.

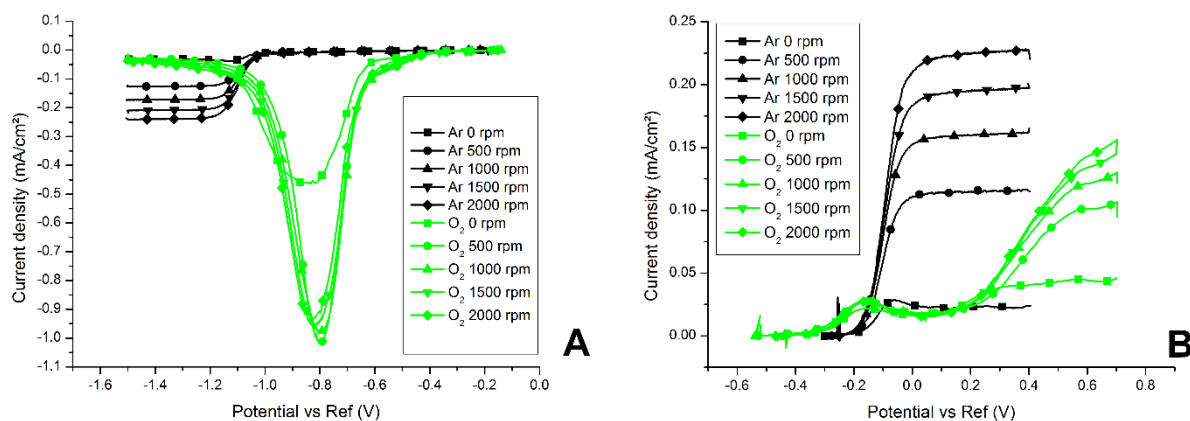


Figure IV. 27: Linear Scan Voltammeteries, 5 mV s⁻¹ in 0.2 M LiClO₄ DMSO, 0.74 mM Co-Salen, Ar (black) and O₂ (green) purged media. A-From OCV to -1.5 V vs. Ref. B-From OCV to 0.4 V (or 0.7 V) vs. Ref

For the reduction experiment, (Figure IV.27-A), the ORR peak current density (green line) increases from no rotation to the presence of a rotation, as expected. However, the trace for 500 rpm and the other rotation rates (1000, 1500 and 2000 rpm) are almost the same, indicating that the transport of O₂ to the electrode in the electrolyte is not the limiting step (but rather the charge transfer kinetic of the ORR scheme limits the reaction). It must be noted, though, that in opposition with the experiments with Co(II)-Po, the ORR current density is not decreasing (or by a very little value), which proves that the redox shuttle effect is to some extent working here. The OER experiments (Figure IV.27-B) support this conclusion: the OER current of the oxidation of Li₂O₂ itself is not increasing with the rotation rate (which is normal as the transport of species to the electrode is not supposed to increase the oxidation of a solid product on the electrode), but when going at higher potential values, the current is rotation-rate dependent, (the greater the rotation rate, the greater the current

density); this proves that some of the surface has been freed, which can only be explained by a true efficiency of the Co-salen to enhance the recharge.

Considering the differences between Co(II)-Po and Co-salen, and comparing the values between Table IV.2 and Table IV.5, it is clear that the Co-salen has a greater diffusion coefficient than Co(II)-Po, which is probably linked to the fact that the Co-salen is a smaller molecule than Co(II)-Po, enabling it to move faster in solution. In addition, from a practical point-of-view, both the oxidation of Co(II)-Po and Co-salen are quasi-reversible, as their ΔE_p grow from low to high potential scan rates. Thanks to the determination of the diffusion coefficient, and with the experiment with the different scan rates (Table IV.4), the standard rate constant can also be determined for the oxidation of the Co-Salen, using the same equations than for the Co(II)-Po (equations IV.19 to IV.22) and the same hypotheses ($D_O = D_R$ and $\alpha = 0.5$). The calculations data are gathered in Table IV.6.

Table IV. 6: k° calculations, using fit of [10] for the oxidation of Co-Salen at several scan rates

Scan rate (mV s ⁻¹)	$\Delta E_{peak}(mV)$	ψ	a	k° (cm s ⁻¹)
20	79	1.275	0.779	$3.06 \cdot 10^{-3}$
50	88	0.847	1.947	$3.21 \cdot 10^{-3}$
80	99	0.590	3.116	$2.83 \cdot 10^{-3}$
100	104	0.515	3.895	$2.76 \cdot 10^{-3}$
200	142	0.245	7.790	$1.86 \cdot 10^{-3}$

Considering the rate constant values for the oxidation of Co-Salen, an average value of k° is of $(2.74 \pm 0.53) \cdot 10^{-2} \text{ cm s}^{-1}$. This value, compared to the one obtained for the Co(II)-Po, is more than three times higher, indicating a faster kinetic process.

Combining all the results from the Rotating disk electrode experiments and Randles-Sevcik ones (no rotation but different scan rates), one concludes that the Co-salen exhibits (i) a higher diffusion coefficient (better transport to the electrode), but also (ii) a higher standard rate constant (faster kinetics process for the oxidation of Co-Salen than Co(II)-Po), along with (iii) a better solubility. These characteristics demonstrate that the Co-salen is the best redox shuttle candidate (much better than Co(II)-Po), which has already been demonstrated in the present chapter. Now, another effect is also stressing more this better behavior of the Co-salen compound, as discussed in the next part: the ORR homogeneous catalysis of Co-salen.

II. OER enhancement mechanisms of Co(II)-Po and Co-salen - How the Co salen is beneficial for both the OER and ORR

The screening of potential redox shuttles identified in the first part of this chapter indicated that two compounds are of high interest for the enhancement of the OER. However, the understanding of the precise mechanisms of this enhancement is not complete yet, and as such more characterizations are needed. In this scope, Differential Electrochemical Mass Spectroscopy along with UV-Visible spectroscopy and analytical electrochemistry were used to unravel those mechanisms.

a. Enhancement pathway of the OER for Co(II)-Po and Co-Salen

As previously shown, the recovery of the carbon electrode surface occurred during the cyclic voltammetry experiments for both Co(II)-Po and Co-salen redox mediators. In order to better assess the usability of those compounds in a practical system, complementary discharge experiments, using a DEMS setup, were performed. To be more specific, a chronoamperometry was conducted for 20 minutes, at the potential of the ORR peak current density (-0.8 V vs. Ref), yielding a severely discharged (passivated) carbon electrode. Then, five cycles were performed (at 5 mV s⁻¹), only in the OER region, and the O₂ ion current was followed by the mass spectrometer, in order to compare the oxygen emission with those additives versus without. The DEMS signal of the ORR chronoamperometry is depicted in Figure IV.28.

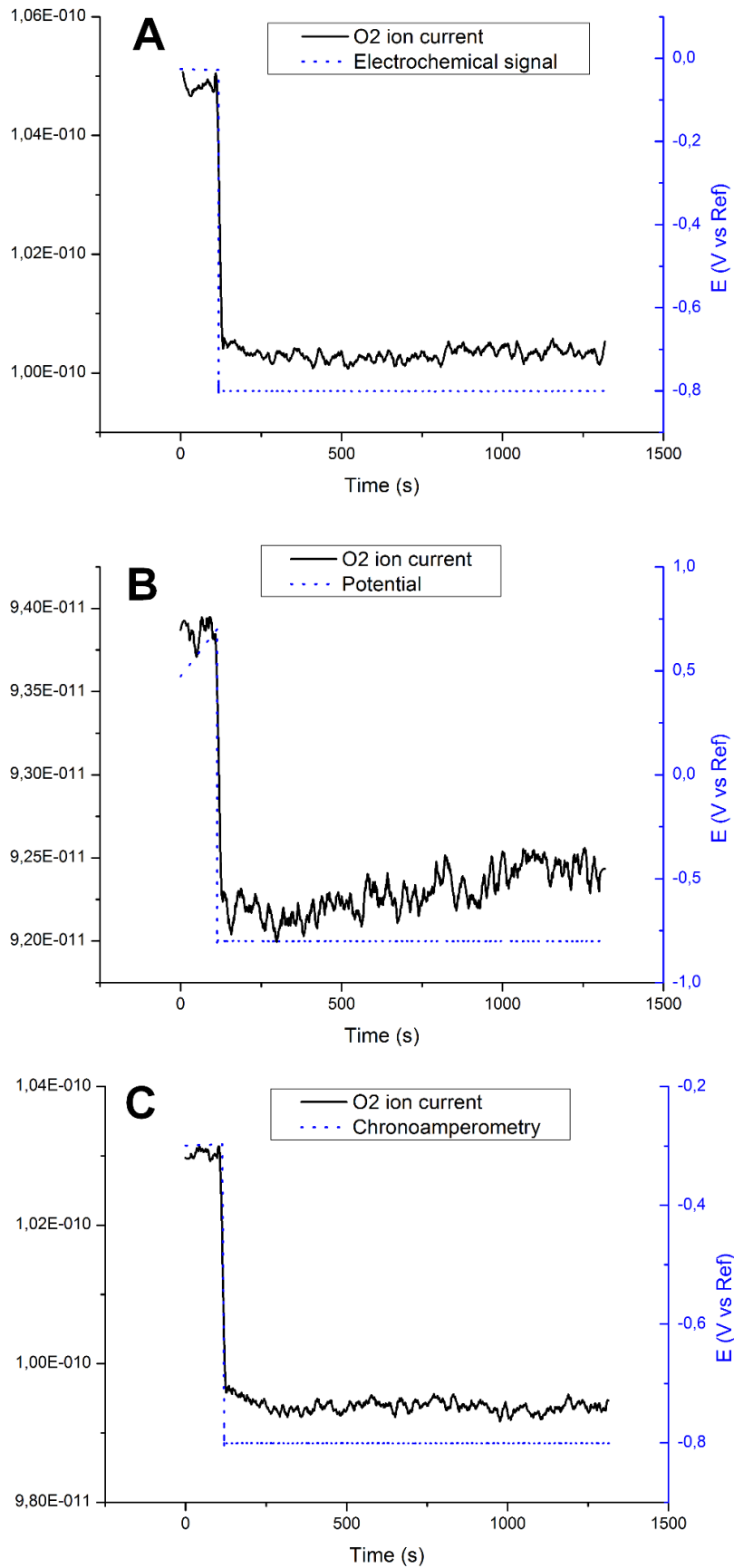


Figure IV. 28: O₂ ion current (primary Y-axis) and potential (secondary Y-axis) monitored during the ORR chronoamperometry experiment for A-Without additives. B-With Co(II)-Po. C-With Co-Salen, in 0.2 M LiClO₄ DMSO

As observed on Figure IV.28, once the potential drops from the Open Circuit Voltage, to -0.8 V vs. Ref, the O₂ ion current drops, which shows that O₂ is consumed at the carbon electrode, following the occurrence of the ORR on the electrode surface. As a result, lithium peroxide is produced, probably by the well-known ORR pathway [29, 39–41] (following equations IV.23-25), leading to the gradual passivation of the electrode:



Then, the five voltammetric cycles of regeneration (OER) are recorded (Figure IV.29).

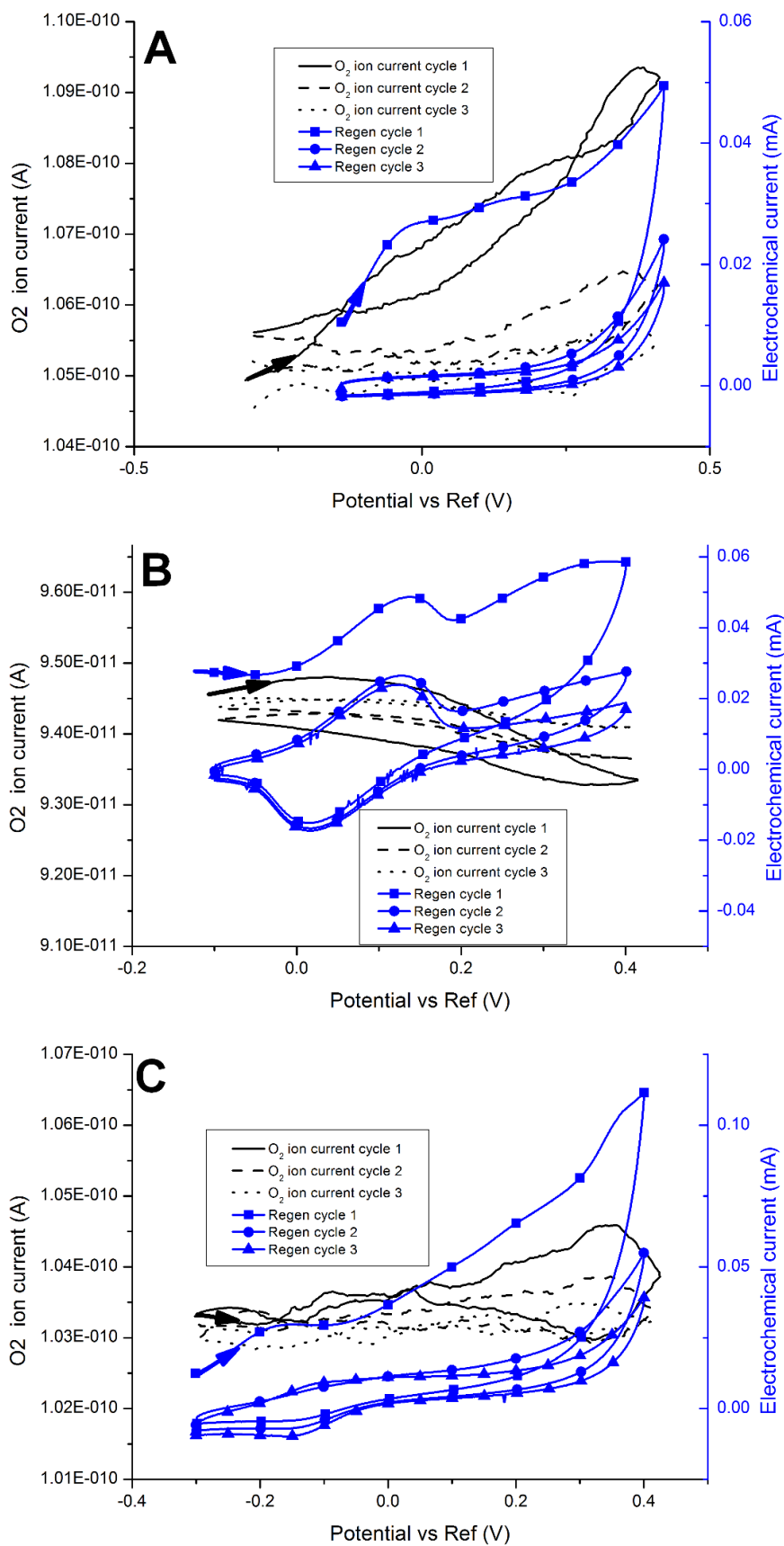
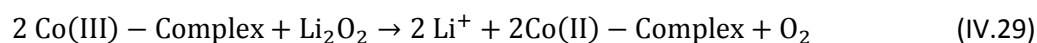
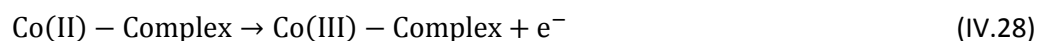


Figure IV. 29: O_2 ion current (primary Y-axis) and potential (secondary Y-axis) monitored during the OER regeneration experiment at 5 mV s^{-1} . For A-Without additives. B-With Co(II)-Po. C-With Co-Salen, in 0.2 M LiClO_4 DMSO. KF below 350 ppm.

Without additive (Figure IV.29-A), a perfect match is observed, between the oxygen released during the OER and the electrochemical oxidation current. As the main discharge product in an anhydrous electrolyte must be Lithium peroxide, the subsequent OER global reaction is:



However, in the cases of the Co(II)-Po and Co-salen containing electrolyte, the electrochemical current and O₂ ion current do not match (Figure IV.29-B and C). This observation, as surprising and not expected as it may be, does not mean that those redox shuttles are not working, though: the electrochemical signals indeed clearly show an OER enhancement. So, one could speculate that in presence of either the one or the other redox compound, the oxygen signal is hindered: even though more electrochemical current is recorded, less oxygen is detected (and mostly noise is detected). This observation, on the other hand, is simply explained by the fixation of the oxygen molecules on the cobalt core (as presented in the previous part, Figure IV.16), which shows that the OER enhancement must occur in the same manner for the Co(II)-Po and the Co-Salen mediators (for more clarity, the complex will be noted Co(II)-complex in both cases in the following equations), and is probably occurring as follows:



In this mechanism, oxygen molecules have a strong affinity with the redox complexes; as these complexes are present in solution at concentrations that are near-similar to the oxygen solubility in the electrolyte and as the electrolyte is in excess in the DEMS experiments, one understands that upon O₂ evolution at the electrode surface in the “recharge”, the redox mediators “instantly” trap this evolved O₂ to form the O₂ – Co(III) – Complex, which explains why the detection of O₂ is hindered during the DEMS experiment. Computing those DEMS results, with the O₂-Saturated RDE experiments realized above (Figures IV.21 and IV.27), it is clear that the amount of Redox shuttle, dissolved in solution, is a key parameter. In the rotating-disk electrode experiment for Co(II)-Po, the redox shuttle effect was not observable, with a concentration of Co(II)-Po of 0.265 mM. On the other hand, with an increased content of Co(II)-Po (as seen on Figure IV.17, and on the DEMS experiments, on Figure IV.29), probably in the range of 1-2 mM, the redox shuttle effect is effective. Comparing those values with the oxygen concentration at saturation in DMSO (2.1 mM [42]), it becomes clear that, in order to be efficient, a redox shuttle must be dissolved in the same range of concentration

than oxygen (when the content was about ten times lower for the Co(II)-Po, the redox shuttle effect was not achieved). Therefore, in a practical system (working with DMSO), it will be a requirement to dissolve at least a content of one or two millimole per liter of the redox shuttle, for the effect to proceed.

b. ORR Homogeneous catalysis of Co-Salen

As explained above, a reversible complex is formed between oxygen and the Co-salen. As published by Ortiz *et al* [33], a catalytic effect is observed between Co-salen and oxygen molecules, this catalytic effect still being observed in presence of lithium cations. This effect can be observed in three-electrode setup and is inducing a huge gain on the ORR potential (Figure IV.30):

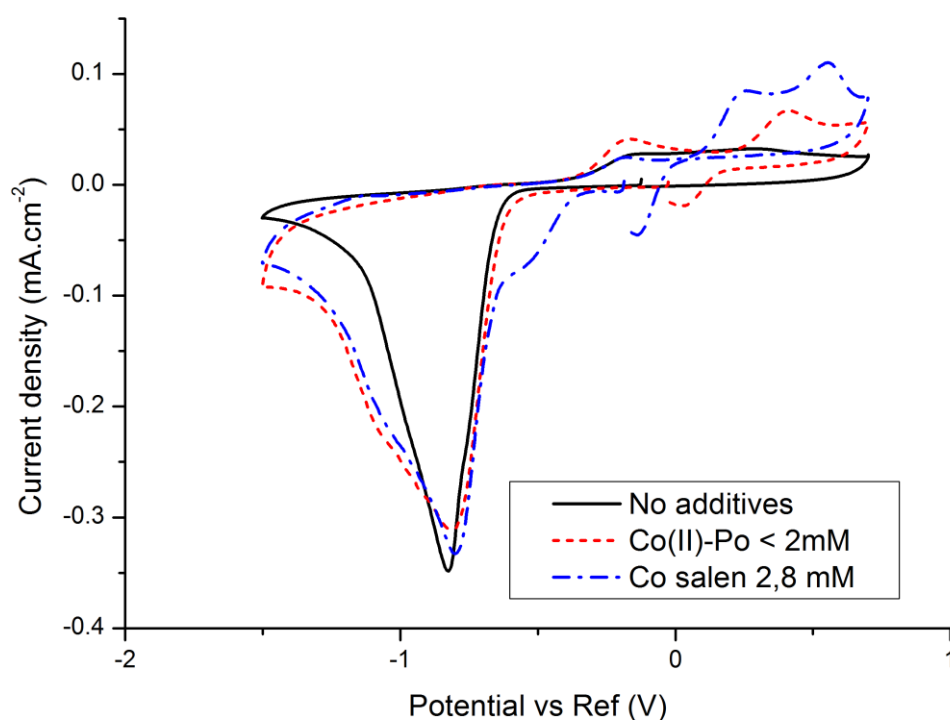
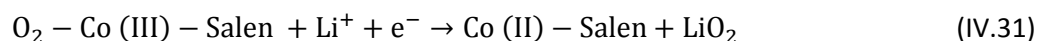


Figure IV. 30: Initial voltamperogram of the glassy-carbon electrode in 0.2 M LiClO₄ DMSO O₂-purge, $v = 5 \text{ mV s}^{-1}$. Solid line: no additives; red short Dashed line: Co(II)-Po-; dot-dashed line blue line: Co-salen, KF titrations below 100 ppm

As seen on figure IV.30, the addition of Co(II)-Po is not triggering any catalytic effect, even though a complex is also formed (as proven in the previous sections). However, the Co-salen induces a new reduction feature, occurring 230 mV above the ORR onset potential: Epc3. As published by Ortiz *et al*

[33], this effect is due to the reduction of the complex. Thus, in presence of oxygen and in a lithium-containing electrolyte, lithium superoxide is produced according to equation (IV.31):



As it is well-known that lithium peroxide is unstable, it is thus highly probable that it disproportionates into lithium peroxide, far above the potential of its production without the Co-salen (equation IV.32).



In order to verify that this catalytic effect is occurring, *in situ* DEMS was carried out. In this scope, very slow linear scan voltammetries were conducted (2 mV s^{-1}), firstly from the Open Circuit Voltage to -1.5 V vs. Ref , and then from the new OCV (ten minutes stabilization) to 0.7 V vs. Ref . The corresponding experiment is presented on Figure IV.31.

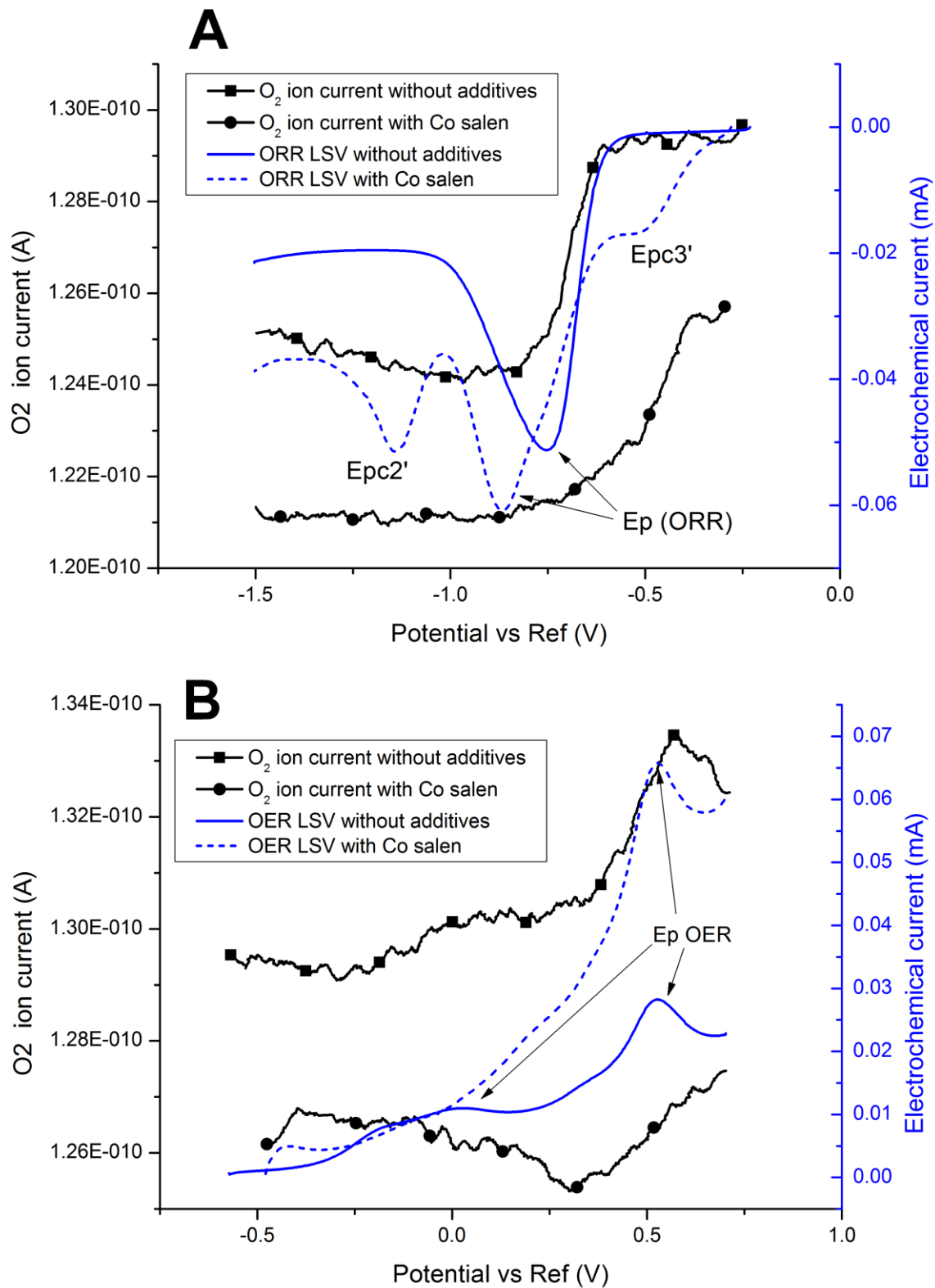
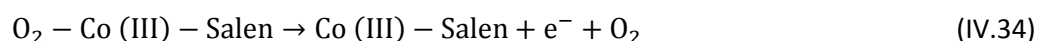


Figure IV. 31: O_2 ion current (primary Y-axis) and electrochemical current (secondary Y-axis) monitored during DEMS Linear Scan Voltammetries experiments 2 mV s^{-1} , in $0.2\text{ M LiClO}_4\text{ DMSO}$. Electrolyte with Co-salen: 2.1 mM . A- ORR LSV recording from OCV to -1.5 V vs. Ref. B-OER LSV from OCV (10 minutes after ORR LSV), to 0.7 V vs. Ref. Karl Fisher at the beginning of the experiment: 80 ppm ; at the end: 300 ppm .

Figure IV.31-A shows that the oxygen depletion at the electrode surface is perfectly matching the electrochemical current in both cases (without additives and with Co-salen). This implies that oxygen is also consumed above the ORR without additive, probably when the complex is reduced at E_{pc3} (equation IV.30), as the +II state is retrieved for the cobalt core. This probably induces reaction (IV.33), that happens simultaneously than reactions (IV.31) and (IV.32):



Concerning the OER, the observations are the same than in the part II.a: the oxygen signal is hindered in presence of the Co-salen complex, even though more faradic (electrochemical) current is produced. However, the end potential here was fixed slightly above the value monitored in the previous data, and a slow rise of the oxygen current can be observed above 0.3 V vs. Ref. One might imagine that this slow rise can be linked to the oxidation of the complex, linked with oxygen (equation IV.34):



However, the DEMS itself is not sufficient to prove that this reaction is indeed occurring, *in situ* Infrared or UV-Visible spectroscopy might be of good help, which is was beyond reach in the time frame of this PhD and could be performed in the future.

This homogeneous catalysis effect, combined with the redox shuttle effect might be the solution to a strong issue concerning the non-aqueous Li-air technology. As McCloskey put forth interrogations on the efficacy of heterogeneous catalysis for Li-O₂ cathodes [1, 22], one can question the usability of the best ORR electrocatalysts to enhance the charge/discharge of Li-O₂ batteries, as these materials will be covered by a layer of lithium peroxide and shall only be efficient in the first cycle of discharge/charge (the better their efficiency to assist ORR, the thicker the Li₂O₂ layer at their surface). However, if the ORR electrocatalyst is soluble in solution (which is the case for the Co-salen), and if the same compound has the ability to recover the surface (proved here), then the issues related to electrocatalysis (even heterogeneous catalysis) appear much less detrimental. Nevertheless, a lot of efforts still have to be conducted to develop such electrocatalysts of non-aqueous ORR, as these electrocatalysts cannot be carbon-based, carbon being easily decomposed by lithium peroxide [17] (along with solvents [17, 41, 43], salts [44, 45], etc.).

Finally, as CO₂ formation by degradation of the electrode/electrolyte by Li₂O₂ is a severe issue (see Chapter one), the CO₂ ion current was also monitored in presence of the Co-salen additive in solution; the results are depicted on Figure IV.32.

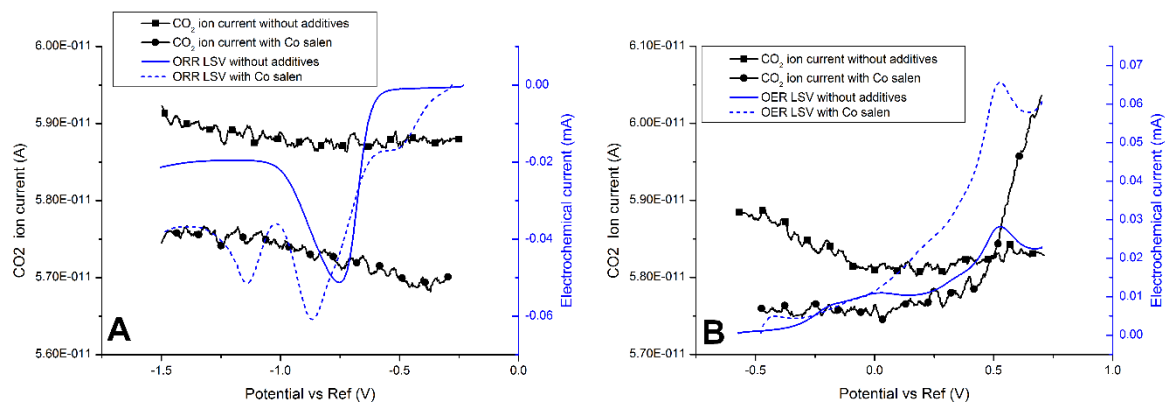


Figure IV. 32: CO_2 ion current (primary Y-axis) and electrochemical current (secondary Y-axis) monitored during DEMS Linear Scan Voltammetries experiments, 2 mV s^{-1} in 0.2 M LiClO_4 DMSO. Electrolyte with Co-salen: 2.1 mM . A- ORR LSV recording from OCV to -1.5 V vs. Ref. B-OER LSV from OCV (10 minutes after ORR LSV), to 0.7 V vs. Ref. Karl Fisher at the beginning of the experiment: 80 ppm ; at the end: 300 ppm .

The results from Figure IV.32 are unequivocal: no CO_2 is evolved in 0.2 M LiClO_4 DMSO electrolyte during the ORR (Figure IV.32-A) and CO_2 is evolved in the OER, above 0.5 V vs. Ref in presence of the Co-Salen (IV.32-B), when it is not without additive. This proves that the CO_2 is evolved rather because of the additive decomposition at higher potential than because of the decomposition of the carbon support or base electrolyte [17]. This demonstrates that the upper electrode potential value must be kept below 0.5 V vs. Ref in presence of the Co-salen additive, otherwise this additive will suffer irreversible decomposition. This is not a severe drawback, as this compounds was proven effective to assist the recharge (OER from Li_2O_2) below 0.4 V vs. Ref (see previous section).

Conclusions:

The necessity of using redox shuttle additives dissolved in the cathode electrolyte to favor the complete recharge of Li_2O_2 was demonstrated, as otherwise the charging processes would suffer from sluggish kinetics and remain incomplete, triggering a risk of capacity losses at each cycles. Several families of compounds were tested, and only two compound were proven efficient, the others being either inappropriate (no oxidoreductive activity in the required voltage window), or not applicable in a Li-O_2 cathode (strong reactivity of the additive with ORR product). These two compounds are 5,10,15,20-Tetrakis(4-methoxyphenyl)-21H,23H-porphine cobalt(II) and N,N'-Bis(salicylidene)ethylenediaminocobalt(II), and their activity were demonstrated in model experiments.

It was proven thanks to DEMS and UV-Visible spectroscopy that both compounds have the ability to bind with oxygen, which render the OER enhancement detection by DEMS difficult. However, the positive redox shuttle effect (enhancement of the OER) was proven for both compounds in three-electrode setup: regeneration experiments allowed to recover the cyclic voltammetry trace (low scan rate) of the glassy-carbon (and carbon cloth) electrode after discharge and charge than on a fresh electrode (this cannot be achieved in anhydrous electrolyte, without OER redox shuttles in solution). Determination of diffusion coefficients and standard rate constants was performed for both compounds and it was found that in both case, the Co-salen outperforms the Co(II)-Po, which exhibited slower diffusion coefficient, solubility and oxidation kinetics. All these aspects make of Co-salen a very good redox additive to assist the recharge in non-aqueous Li-air batteries. Interestingly, the Co-salen has also proven beneficial for the ORR, as it allows an homogeneous catalysis (the reduction of the complex with oxygen proceeds at 230 mV higher values than the ORR onset potential without any additives), which places this additives amongst the best (if not the best) for the use as both redox-shuttle for the OER and in-solution ORR electrocatalyst. Nevertheless, this additive is prone to decomposition at high potential values (above 0.5 V vs. Ref); this is however not a serious issue for the application, as it is efficient to assist the recharge, even when the electrode potential window is restricted in terms of upper limit: limiting the OER end-potential at 0.4 V vs. Ref does not (or very little) impact the recharge process.

Yet, in a practical system, the cathode will not be glassy-carbon or Zoltek Panex 30 (even though these support are resistant toward lithium peroxide, they exhibit a very low surface area), and it was proven in Chapter two that high surface area carbons are prone to decomposition by lithium peroxide. Thus the issue of the carbon protection is not solved by the addition of a soluble redox

shuttle in solution and must be investigated. A cathode protection by Atomic Layer Deposition will be proposed and presented in the following chapter.

References

1. McCloskey BD, Scheffler R, Speidel A, et al (2011) On the efficacy of electrocatalysis in nonaqueous Li-O₂ batteries. *J Am Chem Soc* 133:18038–41. doi: 10.1021/ja207229n
2. Trahan MJ, Jia Q, Mukerjee S, et al (2013) Cobalt Phthalocyanine Catalyzed Lithium-Air Batteries. *J Electrochem Soc* 160:A1577–A1586. doi: 10.1149/2.118309jes
3. John F. Christensen, Paul Albertus, Boris Kozinsky, Timm Lohmann, Jens Grimminger, Jasim Ahmed M (2013) Lithium battery with charging redox couple.
4. Kwak W-J, Hirshberg D, Sharon D, et al (2015) Understanding the behavior of Li–oxygen cells containing Lil. *J Mater Chem A* 3:8855–8864. doi: 10.1039/C5TA01399B
5. Liu T, Leskes M, Yu W, et al (2015) Cycling Li-O₂ batteries via LiOH formation and decomposition. *Science* (80-) 350:530–533. doi: 10.1126/science.aac7730
6. Bergner BJ, Schürmann A, Pepler K, et al (2014) TEMPO: A Mobile Catalyst for Rechargeable Li-O₂ Batteries. *J Am Chem Soc* 136:15054–15064. doi: 10.1021/ja508400m
7. Chen Y, Freunberger S a, Peng Z, et al (2013) Charging a Li-O₂ battery using a redox mediator. *Nat Chem* 5:489–94. doi: 10.1038/nchem.1646
8. Kundu D, Black R, Adams B, Nazar LF (2015) A Highly Active Low Voltage Redox Mediator for Enhanced Rechargeability of Lithium–Oxygen Batteries. *ACS Cent Sci* 1:510–515. doi: 10.1021/acscentsci.5b00267
9. Viswanathan V, Thygesen KS, Hummelshj JS, et al (2011) Electrical conductivity in Li₂O₂ and its role in determining capacity limitations in non-aqueous Li-O₂ batteries. *J Chem Phys* 135:0–10. doi: 10.1063/1.3663385
10. McCloskey BD, Bethune DS, Shelby RM, et al (2012) Limitations in Rechargeability of Li-O₂ Batteries and Possible Origins. *J Phys Chem Lett* 3:3043–3047. doi: 10.1021/jz301359t
11. Hu X, Zhu Z, Cheng F, et al (2015) Micro-nano structured Ni-MOFs as high-performance cathode catalyst for rechargeable Li-O₂ batteries. *Nanoscale* 7:11833–11840. doi: 10.1039/c5nr02487k
12. Zhang J, Luan Y, Lyu Z, et al (2015) Synthesis of hierarchical porous delta-MnO₂ nanoboxes as an efficient catalyst for rechargeable Li-O₂ batteries. *Nanoscale* 7:14881–14888. doi: 10.1039/C5NR02983J

13. Shui J-L, Karan NK, Balasubramanian M, et al (2012) Fe/N/C composite in Li-O₂ battery: studies of catalytic structure and activity toward oxygen evolution reaction. *J Am Chem Soc* 134:16654–61. doi: 10.1021/ja3042993
14. Gittleson FS, Sekol RC, Doubek G, et al (2014) Catalyst and electrolyte synergy in Li–O₂ batteries. *Phys Chem Chem Phys* 16:3230. doi: 10.1039/c3cp54555e
15. Peled E (1979) The Electrochemical Behavior of Alkali and Alkaline Earth Metals in Nonaqueous Battery Systems—The Solid Electrolyte Interphase Model. *J Electrochem Soc* 126:2047. doi: 10.1149/1.2128859
16. Ota H, Sakata Y, Inoue A, Yamaguchi S (2004) Analysis of Vinylene Carbonate Derived SEI Layers on Graphite Anode. 1659–1669. doi: 10.1149/1.1785795
17. McCloskey BD, Speidel A, Scheffler R, et al (2012) Twin problems of interfacial carbonate formation in nonaqueous Li-O₂ batteries. *J Phys Chem Lett* 3:997–1001. doi: 10.1021/jz300243r
18. Padbury R, Zhang X (2011) Lithium–oxygen batteries—Limiting factors that affect performance. *J Power Sources* 196:4436–4444. doi: 10.1016/j.jpowsour.2011.01.032
19. Black R, Oh SH, Lee J, et al (2012) Screening for superoxide reactivity in Li-O₂ batteries: effect on Li₂O₂/LiOH crystallization. *J Am Chem Soc* 134:2902–5. doi: 10.1021/ja2111543
20. Lim HD, Song H, Kim J, et al (2014) Superior rechargeability and efficiency of lithium-oxygen batteries: Hierarchical air electrode architecture combined with a soluble catalyst. *Angew Chemie - Int Ed* 53:3926–3931. doi: 10.1002/anie.201400711
21. Badwal SPS, Giddey SS, Munnings C, et al (2014) Emerging electrochemical energy conversion and storage technologies. *Front Chem* 2:79. doi: 10.3389/fchem.2014.00079
22. McCloskey BD, Addison D (2016) A viewpoint on heterogeneous electrocatalysis and redox mediation in nonaqueous Li-O₂ batteries. *ACS Catal* 778:acscatal.6b02866. doi: 10.1021/acscatal.6b02866
23. Bhatt MD, Geaney H, Dwyer CO (2014) and theory. 12093–12130. doi: 10.1039/c4cp01309c
24. Rahman MA, Wang X, Wen C (2014) A review of high energy density lithium-air battery technology. *J Appl Electrochem* 44:5–22. doi: 10.1007/s10800-013-0620-8
25. Xiaohua Yu, J.B. Bates, G.E. Jellison, Jr. and FXH (1997) A Stable Thin-Film Lithium Electrolyte : Lithium Phosphorus Oxynitride. 144:524–532.

26. Bates JB, Dudney NJ, Neudecker B, et al (2008) Thin-film lithium and lithium-ion batteries. 135:33–45.
27. Ribeiro JF, Sousa R, Sousa JA, et al (2012) Rechargeable Lithium Film Batteries – Encapsulation and Protection. *Procedia Eng* 47:676–679. doi: 10.1016/j.proeng.2012.09.237
28. Sarrazin J, Verdaguer M (1998) L'oxydoréduction. Concepts et expériences, May 5th 19.
29. Laoire CO, Mukerjee S, Abraham KM, et al (2009) Elucidating the mechanism of oxygen reduction for lithium-air battery applications. *J Phys Chem C* 113:20127–20134. doi: 10.1021/jp908090s
30. Zimmermann M (2015) Oxygen Reduction Reaction Mechanism on Glassy Carbon in Aprotic Organic Solvents.
31. Zare HR, Nasirizadeh N, Mazloum Ardakani M (2005) Electrochemical properties of a tetrabromo-p-benzoquinone modified carbon paste electrode. Application to the simultaneous determination of ascorbic acid, dopamine and uric acid. *J Electroanal Chem* 577:25–33. doi: 10.1016/j.jelechem.2004.11.010
32. Holze R (1991) Surface Raman spectroelectrochemical studies of oxygen reduction catalysts. 36:999–1007.
33. Ortiz B, Park SM (2000) Electrochemical and spectroelectrochemical studies of cobalt salen and salophen as oxygen reduction catalysts. *Bull Korean Chem Soc* 21:405–411. doi: 10.1016/S0013-4686(00)00363-7
34. Bard AJ, Faulkner LR, York N, et al (1944) *Electrochemicals methods: Fundamentals and Applications*. Electrochem I Faulkner, Larry R. doi: 10.1016/B978-0-12-381373-2.00056-9
35. Lebel RG, Goring DAI (1962) Density, Viscosity, Refractive Index, and Hygroscopicity of Mixtures of Water and Dimethyl Sulfoxide. *J Chem Eng Data* 7:100–101. doi: 10.1021/je60012a032
36. Janisch J, Ruff A, Speiser B, et al (2011) Consistent diffusion coefficients of ferrocene in some non-aqueous solvents: Electrochemical simultaneous determination together with electrode sizes and comparison to pulse-gradient spin-echo NMR results. *J Solid State Electrochem* 15:2083–2094. doi: 10.1007/s10008-011-1399-3
37. Dragu D, Buda M, Vişan T (2009) Cyclic voltammetry simulation using orthogonal collocation: Comparison with experimental data and measuring the electrochemical rate constant. *UPB Sci*

- Bull Ser B Chem Mater Sci 71:77–90.
38. Brisard GM, Manzini M, Lasia A (1992) Kinetics of the electroreduction of Co(salen) in DMSO. *J Electroanal Chem* 326:317–322. doi: 10.1016/0022-0728(92)80518-9
 39. Laoire CO, Mukerjee S, Abraham KM, et al (2010) Influence of nonaqueous solvents on the electrochemistry of oxygen in the rechargeable lithium-air battery. *J Phys Chem C* 114:9178–9186. doi: 10.1021/jp102019y
 40. Trahan MJ, Mukerjee S, Plichta EJ, et al (2013) Studies of Li-Air Cells Utilizing Dimethyl Sulfoxide-Based Electrolyte. *J Electrochem Soc* 160:A259–A267. doi: 10.1149/2.048302jes
 41. Luntz AC, Mccloskey BD (2014) Nonaqueous Li – Air Batteries : A Status Report. *Chem Rev* 114:11721–11750. doi: 10.1021/cr500054y
 42. Sawyer D, Jr GC (1982) Effects of media and electrode materials on the electrochemical reduction of dioxygen. *Anal Chem* 2:1720–1724. doi: 10.1021/ac00248a014
 43. García JM, Horn HW, Rice JE (2015) Dominant Decomposition Pathways for Ethereal Solvents in Li–O₂ Batteries. *J Phys Chem Lett* 6:1795–1799. doi: 10.1021/acs.jpcllett.5b00529
 44. Lau KC, Lu J, Low J, et al (2014) Investigation of the Decomposition Mechanism of Lithium Bis(oxalate)borate (LiBOB) Salt in the Electrolyte of an Aprotic Li-O₂ Battery. *Energy Technol* 2:348–354. doi: 10.1002/ente.201300164
 45. Younesi R, Hahlin M, Björefors F, et al (2013) Li–O₂ Battery Degradation by Lithium Peroxide (Li₂O₂): A Model Study. *Chem Mater* 25:77–84. doi: 10.1021/cm303226g

Chapter V:

Carbon protection by Atomic Layer Deposition of Nb₂O₅

The Science of Today is the Technology of Tomorrow

-Edward Teller

As one solution was proposed in the last chapter to solve the charging issue of Li-O₂ cathodes, one other main issue of Li-O₂ batteries remains: the protection of the carbon cathode. If one wants to prevent its decomposition (high-surface-area carbon can be decomposed by contact with Li₂O₂ and/or at the high potential values encountered in recharge, see chapter two), two strategies exist: either the material of the cathode is changed (two examples are presented in the literature with gold nanoparticles [1], and a screening of TiC, SiC and TiN cathodes [2]), or the carbon material has to be protected. The advantage of carbon over TiC, SiC and TiN is that it can exhibit much higher surface area, and the main advantage over gold nanoparticles is that it is way cheaper.

In the present work, it was imagined to protect the carbon material by a thin layer of stable metal-oxide in these conditions. Two materials were selected: Nb₂O₅ and V₂O₅. In the present chapter, Nb₂O₅ is particularly under focus; it exhibits a bandgap of about 3.7 eV [3], and an appropriate technique for its deposition as thin-layer is atomic-layer deposition, which has been proven efficient to make highly-conformal deposits on rough surfaces, with a high control of the thickness [4, 5]. In this scope, two ways of elaboration are tested: Plasma-Enhanced Atomic layer Deposition (PEALD), which allows to work at lower temperature, yields more directive deposition [6]) and thermal ALD, which is non-directive but proceeds at higher temperature and slower growth-rate. Those techniques will be first investigated on a model surface (silicon 400), and then transferred to a carbon substrate that proved interesting for the Li-O₂ system, the Zoltek® Panex 30 carbon cloth.

I. Atomic Layer Deposition: Principles

The atomic Layer Deposition technique was born in the late 1970s [7, 8], in order to fulfill the needs of electroluminescent panels. For this industry, very thin layers of dielectric and luminescent products were needed on large surfaces. Suntola and his team had the idea of introducing sequentially elementary precursors, which allowed a perfect control of the thickness, unlike the other deposition techniques available at that time (such as cathodic pulverization/vaporization).

The ALD is derived from a technique, invented in the late 1920's: the chemical vapor deposition (CVD). Both techniques use elementary precursors and rely on the chemisorption of the latter on the surface onto which the deposit is targeted. However, the CVD process is not introducing sequentially the precursors, which are flowed concomitantly in the reactor and are reacted at much higher temperature. As a consequence, the growth-rate of CVD deposits is much higher than for ALD deposits, but suffers from issues that are not occurring in ALD (inclusions of particles in the deposited

layer, heterogeneous thickness, non-conformal-deposits, etc.). A scheme for an atomic layer cycle is presented on Figure V.1.

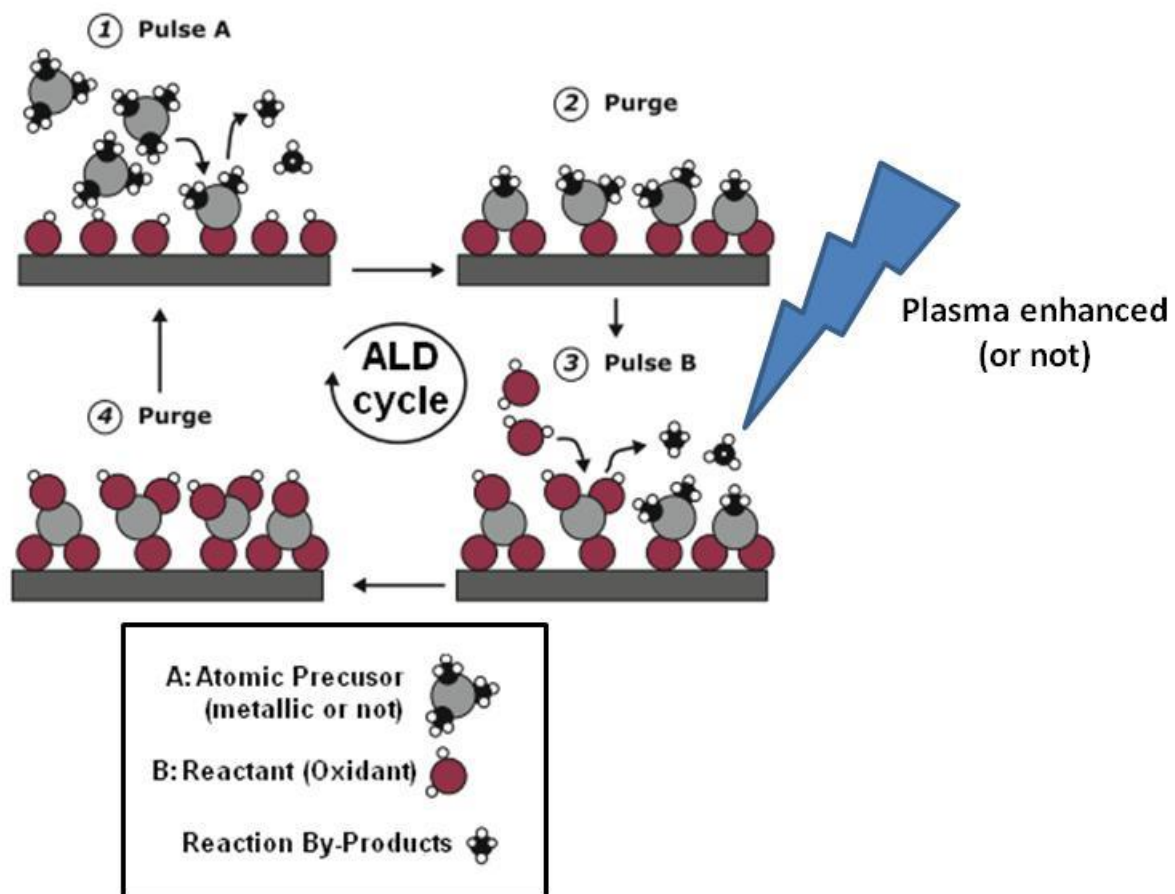


Figure V. 1: ALD cycle scheme for two precursors for a oxide formation recipe, reproduced from [8], with permission from Les techniques de l'ingénieur.

The first step is the pulse of the reactant A in the reactor. During this step, some of the precursors can chemisorb on the surface and generate by-products following their (partial) decomposition. During the second step, the remaining reactant A (which has not reacted, yet) and the gaseous by-products are flushed out from the reactor chamber by an heavy-pumping: this is a purge (step 2). Then, the oxidant (reactant B) is introduced (pulsed) in the reactor and reacts on the substrate surface (step 3), in the same fashion than reactant A, during the first step (chemisorption). Then, in the same manner than for the second step, a heavy-pumping flushes the gaseous by-products and remaining reactant B precursors (Step 4). All those steps characterize one ALD cycle. It can be easily understood that the thickness of the deposit will be thus strongly linked (and controlled) by the number of ALD cycles in a given process.

Unlike other gas-phase depositions techniques, deposits are conducted in mild conditions of temperature ($25 < T < 600^{\circ}\text{C}$), which allows deposition on "fragile" and sensitive substrates such as polymers, biological materials, etc.

Several parameters are crucial for the elaboration of a thin-layer by ALD: the temperature of the deposition, the reactivity of the precursors (reactants A and B have to react on each other irreversibly to produce self-limiting reactions onto the substrate), the pulse time (the best time might differ from reactant A to reactant B) and the purge time (which has to be as small as possible to limit the cycle time, but long-enough to purge unreacted/non-adsorbed reactant molecules). The parameter that defines best the efficiency of the deposition (at a given temperature) is the Growth per Cycle (GPC), expressed in Angström per cycle (\AA cycle^{-1}). In theory, the GPC is about the size of a monolayer on the surface, but usually, the surface has to be activated first (the activation depends on the temperature, the nature of the reactants and of the substrate). This dependence (also called "ALD window") is illustrated by Figure V.2.

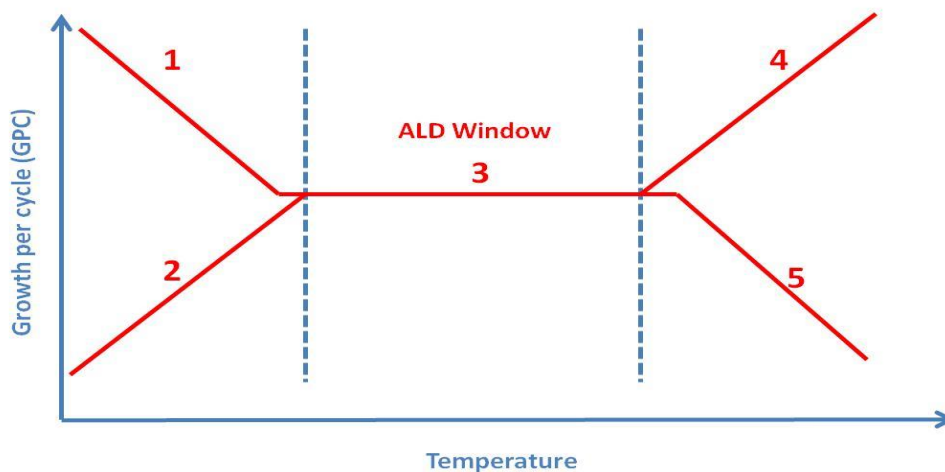


Figure V. 2: Determination of the ALD window; Dependence of the GPC on the Temperature

Five zones can be observed on Figure V.2. The first zone (1) corresponds to the condensation of one of the reactant on the substrate surface (which favors the deposition as the reactant is not gaseous anymore, and more can be retained on the surface). The second zone (2) corresponds to the case where the temperature for the deposition is not high enough to support the activation of the deposition; usually, this zone is called the kinetic regime and the deposition rate is proportional to the exponential of the activation energy [7] ($e^{-\frac{E_a}{RT}}$): thus the higher the temperature, the greater the GPC. The third Zone (3) is the ALD window: the temperature does not impact the deposition as the substrate is hot enough (no condensation nor activation) and the GPC can only be limited in this region by the pulse/purge time of each precursor, as the limiting step is the chemisorption of each

reactant within the ALD cycle. This zone is substrate-dependent and precursor-dependent: it might not be seen or it can be very narrow for a given reaction on a given substrate [5, 8]. The fourth zone (4) corresponds to the case where the precursor is decomposed on the substrate before reacting with the surface. The fifth zone (5) can be explained by several effects: precursor desorption, sublimation of the deposit, *etc.*

Usually, one of the reactant is an elementary precursor of the material needed to be deposited, at the same oxidation state and the other reactant supplies the needed element to complete the layer (e.g. oxygen or nitride). For instance, if one wants to deposit Al_2O_3 , the reactant A will be an elementary precursor, comprising aluminum in the +III state, and reactant B could be an oxygen supplier (H_2O , N_2O , O_2 , *etc.*). It must be noted that if one wants to make nitride depositions, as oxides will always be favored versus nitrides, no oxygen atoms must be present in both reactant A and B. Several families of ligands are available for the metallic precursors, as depicted on Figure V.3.

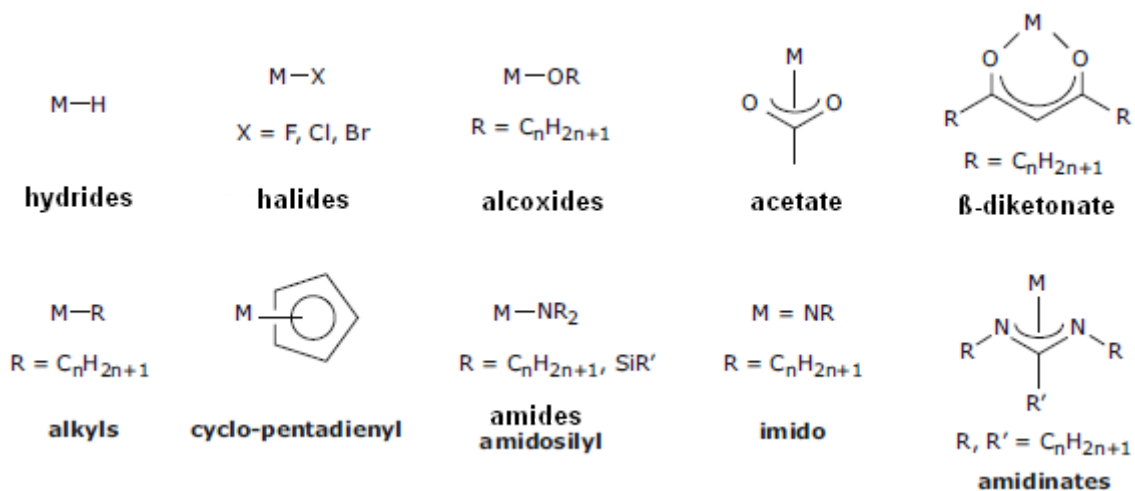


Figure V. 3: Ligands available for metallic cation precursors, reproduced from, with permission from [7], with permission from *Les techniques de l'ingénieur*

The reactivity of the metallic precursor (in terms of kinetics of the deposition), does not depend on the ligand, as the reactants are introduced sequentially in the reactor. However, major characteristics of the metallic precursor depend on the ligand, such as the stability of the precursor at the temperature of the deposition and the sublimation/evaporation temperature (if the sublimation temperature of the precursor is above that required for the deposition, the precursor will condensate on the substrate and on the reactor walls, which must be avoided). Also, in general, halide precursors are avoided, as by-products can produce gaseous acids (such as HCl , HBr , HF , *etc.*), which can corrode the substrate and/or the reactor, and produce *in situ* etching of the film [9]. Also,

the impact of both the pulse-time and purge-time of a reactant can have a great impact on the thickness of a deposit, as shown on Figure V.4:

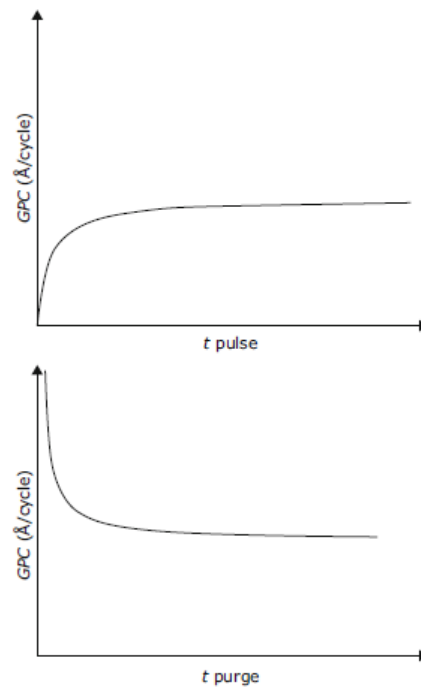


Figure V. 4: Impact of the pulse-time and purge-time of the reactants on the Growth rate of an ALD deposit; reproduced from [7], with permission from Les Techniques de l'ingénieur.

It is mandatory, if one wants to be independent to the pulse-time, to have long-enough pulse-time to fully adsorb the reactant on the substrate surface [8, 10]; if not, the deposit will take longer to proceed, as parts of the substrate surface will be covered by reactive adsorbates. Also, if the purge-time is not sufficient, remaining of the other reactant will be in the reactor, and gas-phase reactions will occur (CVD-like), leading to larger GPC, but with risk of non-homogeneities in the deposit.

II. Deposits of Nb_2O_5 on Silicon: a model study

Nb_2O_5 was chosen over other materials, for three reasons: firstly, a line with a niobium precursor was available on the ALD reactor, thus no changes in the reactor setup was required. Secondly, oxides were chosen over nitrides, as oxides will always be preferentially formed to nitrides, and most of the time, nitride films comprises oxides (because of oxygen traces in the precursors, or in the gases, etc.); therefore, oxides will likely be more stable in the operating conditions of a $Li-O_2$ positive electrode. Thirdly, Nb_2O_5 oxide have the ability to intercalate lithium ions, and can be used as a positive electrode in Li-ion systems [11]. This behavior can be used in our advantage, for a symbiotic effect:

Li-ion-like insertion/de-insertion of Li^+ for power delivery, and aprotic reduction/evolution of oxygen for high energy density). Finally, a large panel of study focuses on the deposition of Nb_2O_5 nanofilms in the literature [12–17], proving that deposition of this material is achievable by Atomic Layer Deposition.

In this study, the niobium precursor was (tert-butylimido)bis(dimethylamino)Niobium (TBTDEN), his formula being presented in Figure V.5.

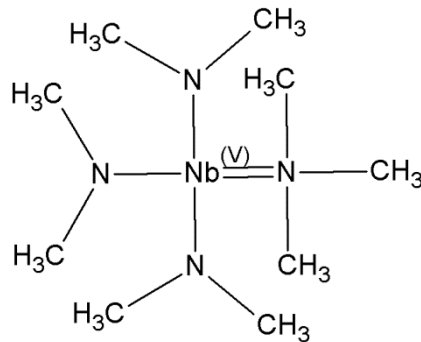


Figure V. 5: Chemical structure of the niobium Precursor (TBTDEN)

Two ways of depositions were investigated and compared in this study:

- Thermal Atomic Layer Deposition, with N_2O as the oxidant (Reactant B).
- Plasma Enhanced Atomic Layer Deposition (PEALD), with a plasma of oxygen as the oxidant.

The equipment used for the deposition (for both recipes) was a Picosun™ R-200 advanced. A large range of temperature can be applied with this machine (from 50 to 500 °C). Also, the strong advantage of this equipment is linked to a very homogeneous temperature in the reactor, which allows (in principle) a uniform deposit on the sample.

a. Surface morphology of Nb_xO_y deposits

i. Surface morphologies

The surface morphology of the deposits were analyzed by surface SEM and images of the best deposits (in terms of thicknesses at the better elaboration temperature) are presented on Figure V.6.

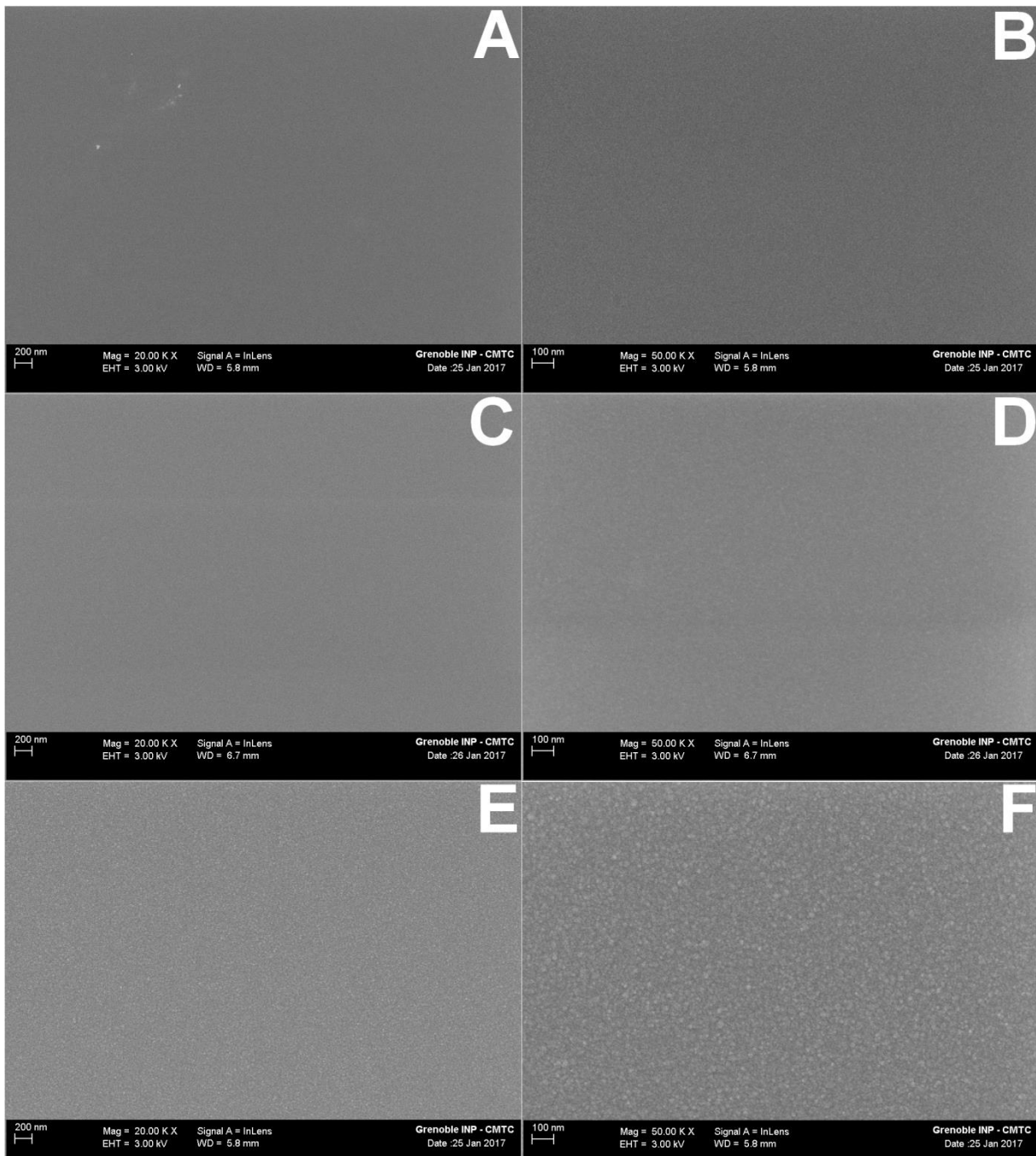


Figure V. 6 SEM pictures taken with a tension of 3 kV, at either a magnification of 20.00 kX (A,C,E) or 50.00 kX (B,D,F).
 Images of pristine Silicon (A & B), PEALD at 225°C and 2000 cycles (C & D), ALD thermal at 375°C, 5000 cycles

Figure V.6 shows that the pristine silicon is very flat, even at high magnification (Figure V.6-B). The observation is the same for the PEALD deposit: the surface appears as smooth as for the pristine silicon at high magnification (Figure V.6-D), indicating a process that is highly conformal. However, a small roughening of the surface appeared for the deposition, conducted with the thermal ALD (compared to PEALD and pristine silicon at 50.00 kX, Figure V6.F). This is probably linked to the

higher temperature required for the thermal ALD to proceed, as it will be presented here-after for the ALD window determination.

ii. Atomic Layer Deposition window

In order to characterize an ALD process, it is common to find if an ALD window exists (or not). To do so, the pulse and purge times for the reactants are fixed with reasonable values, to be sure that each cycle does not depend on the pulse or on the purge time (see part I). Here, similar conditions than in the work of Blanquart et al [12] were chosen for the precursor and oxidant purge times: they used a pulse/purge ratio of 0.7 s/1.0 s for the TBTDEN and of 1.0 s /1.5 s for oxygen (which was their oxidant). To verify that the conditions of pulse and purge time were sufficient, those times were increased and the corresponding conditions are presented in Table V.1; it must be noted that our group used before the TBTDEN, which was tough to evaporate (evaporation/transport temperature of 100°C), thus the Boost® feature of Picosun was used. This feature consists of a strong pulse of N₂ (400 sccm for 0.7 s) during the precursor pulse-time, which increases greatly its transport into the reactor. Otherwise, the flow is fixed at 80 sccm in the lines (of the precursor and oxidant, during their pulse-time).

Table V. 1: Deposits conditions for the ALD window determination

Recipe	TBTDEN pulse-time (s)	TBTDEN purge-time (s)	Oxidant pulse-time (s)	Oxidant purge-time (s)
PEALD	1.1	2	12	2
Thermal ALD	1.1	2	4	4

Deposits were realized on flat, microelectronic grade silicon (400), at either 5000 or 2000 cycles (the number of cycles has, in theory no impact for the ALD window determination), and the thicknesses of the deposits were evaluated by cleaving the samples and analyzing them with SEM on the cleaved spine. Two examples of the thicknesses measurements by SEM are presented on Figure V.7. Three measurements were carried out for each sample and a deviance was subsequently calculated.

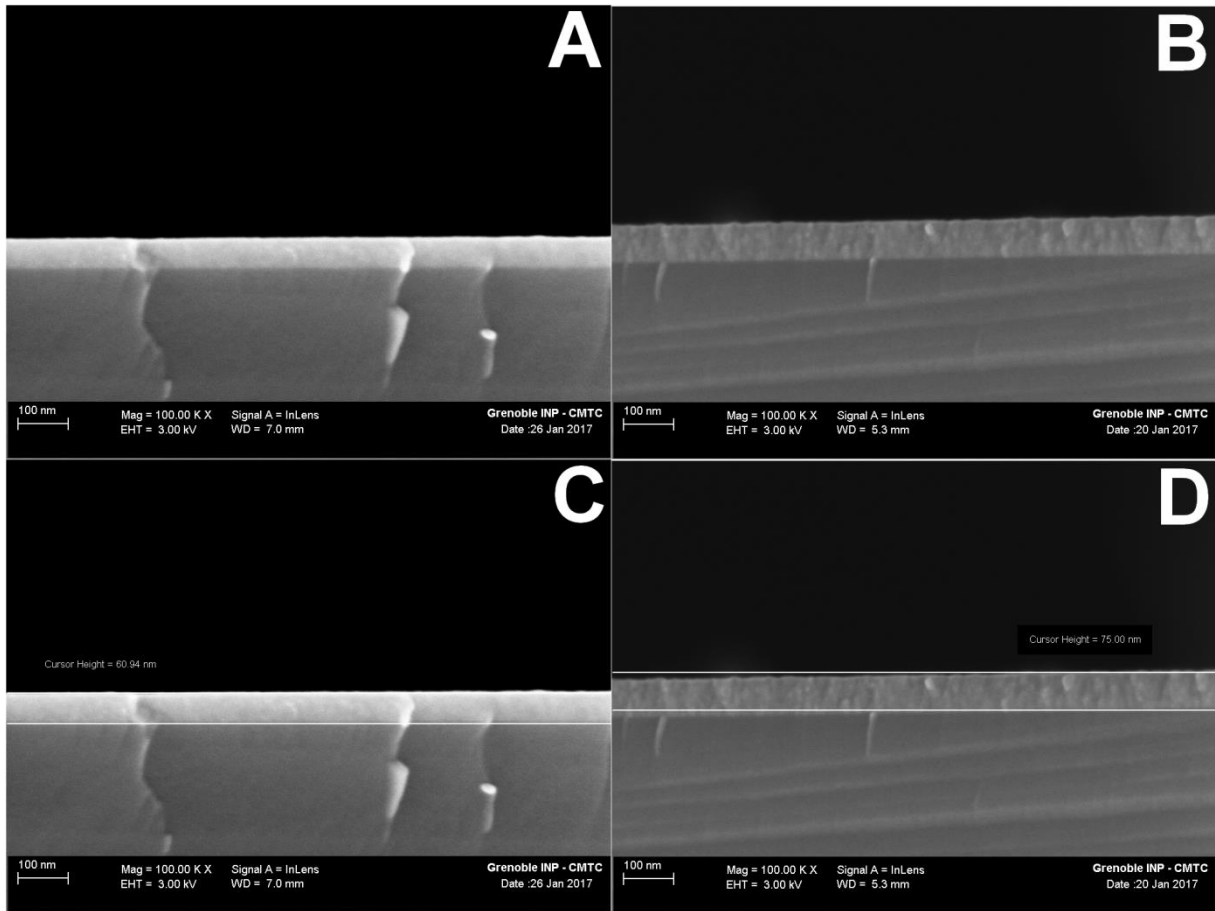


Figure V. 7: SEM thicknesses determination. Tension 3 kV, magnification 100.00 kX. PEALD at 225°C, 2000 cycles, picture without cursors (A), with (C). Thermal ALD at 375 °C, 5000 cycles, Picture without cursors (B), With (D)

The deposits are clearly observable by SEM (Figure V.7); it is thus very easy to determine their corresponding thicknesses, at different temperatures. The latter can also be determined by Ellipsometry. The corresponding results are presented on Table V.II (for elaboration by PEALD) and Table V.III (for elaboration by Thermal ALD).

Table V. 2: Experiments conducted on Si (400) by PEALD recipe, with either 2000 or 5000 ALD cycles

Temperature (°C)	100	125	150	175	200	225	250	275	300	350
Number of cycles performed	5000	5000	5000	2000	5000	2000	5000	2000	5000	2000
Thickness measurements by SEM (nm)	192	173	168	62	157	61	148	60	58	52
SEM measurement deviance (nm)	6	4	2	6	3	2	4	5	1	2
Thickness measurements by Ellipsometry (nm)	185	173	170	54	160	52	151	49	49	43
Deviance SEM/Ellipsometry measurements (nm)	3	0	1	4	2	5	1	6	5	4

Table V. 3: Experiments conducted on Si (400) by thermal ALD recipe, with 5000 ALD cycles

Temperature (°C)	250	275	300	325	350	375	400	425
Thickness measurements by SEM (nm)	0	0	0	29	47	78	54	42
SEM measurement deviance (nm)	0	0	0	1	4	3	4	1
Ellipsometry thickness (nm)	3	4	16	19	27	26	120	23
Deviance SEM/ Ellipsometry	1	2	7	10	15	28	40	14

The deposits are highly conformal and the deviance obtained, for the SEM measurements, was rather due to the appreciation of the delimitations of the deposit/substrate and deposit/void. The ellipsometry measurements for the PEALD recipe (Table V.2) are supporting the measurements conducted by SEM with a very low difference between the former and the latter (of about the same value for the reading of the deposit thickness on the SEM pictures).

However, the ellipsometry measurements for the thermal ALD recipe show a strong deviance with the measurements by SEM (up to 40 nm). The ellipsometry is very sensitive to the surface of the sample (roughness) and to the homogeneity of the deposit [18, 19]. As presented on Figure V.6, the sample roughness of the thermal ALD recipe appears greater than the one of pristine Si (400) or of the PEALD. Also, heterogeneities in the deposit can be held responsible for this deviance of thickness measured from ellipsometry. As the measurements of the thickness by SEM is more reliable, it is this

value that will be used to plot the growth per cycle (GPC, in \AA cycle^{-1}) versus the temperature, a value that enables to find the ALD window (if available) and the conditions of the deposition (Figure V.8).

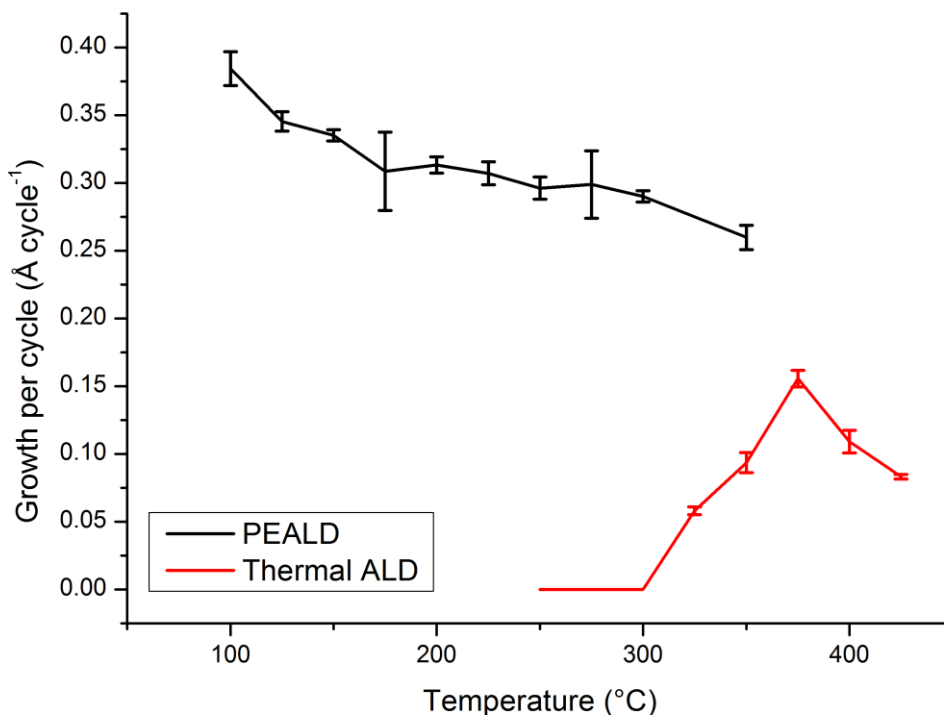


Figure V. 8: ALD window determination for the PEALD (black) and the thermal ALD (red)

As depicted on Figure V.8, the PEALD allows a greater GPC than the thermal ALD, which was expected (plasma enhances the reactivity, thus increasing the GPC at lower temperatures [4, 6, 10]). The trend for the PEALD seems to be: (1) condensation of the precursor at low temperature (as the GPC is greater at 100°C than at 125°C); then (2) a rather large and stable ALD window can be observed from 125°C to 300°C (with GPC varying from 0.33 \AA per cycle to 0.3 \AA per cycle); (3) at 350°C, a GPC of 0.26 \AA per cycle is obtained, which might indicate either a sublimation of the product, or the precursor desorption. However, if it was really the case, then at the same temperature, the elaboration by thermal temperature was supposed to occur too (as it is the same end-product that is supposed to be deposited). As it is not the case, it is postulated that the point at 350°C, for the PEALD process, is still comprised within the ALD window (but some effect might have perturbed the deposition). The ALD thermal process, on the other hand, does not seem to exhibit any ALD window, as the GPC grows, to its maximum (at 375°C) and then sharply decreases, indicating (this time), either the sublimation of the product or desorption of the precursor because of the high temperatures.

b. Composition of the deposits for the two recipes (Thermal ALD and PEALD)

The chemistry of the deposits was determined by using two different techniques. Firstly, by X-EDS (determining if elements such as Niobium, Nitrogen and Oxygen could be detected), then by X-Ray Diffraction and finally by X-Ray Photoelectron Spectroscopy (see chapter material and method). For the last technique, two materials of each recipe were analyzed (as this technique is costly and time consuming). X-EDS of the deposits, conducted by PEALD and thermal ALD are presented on Figures V.9 and V.10.

i. X-EDS analysis

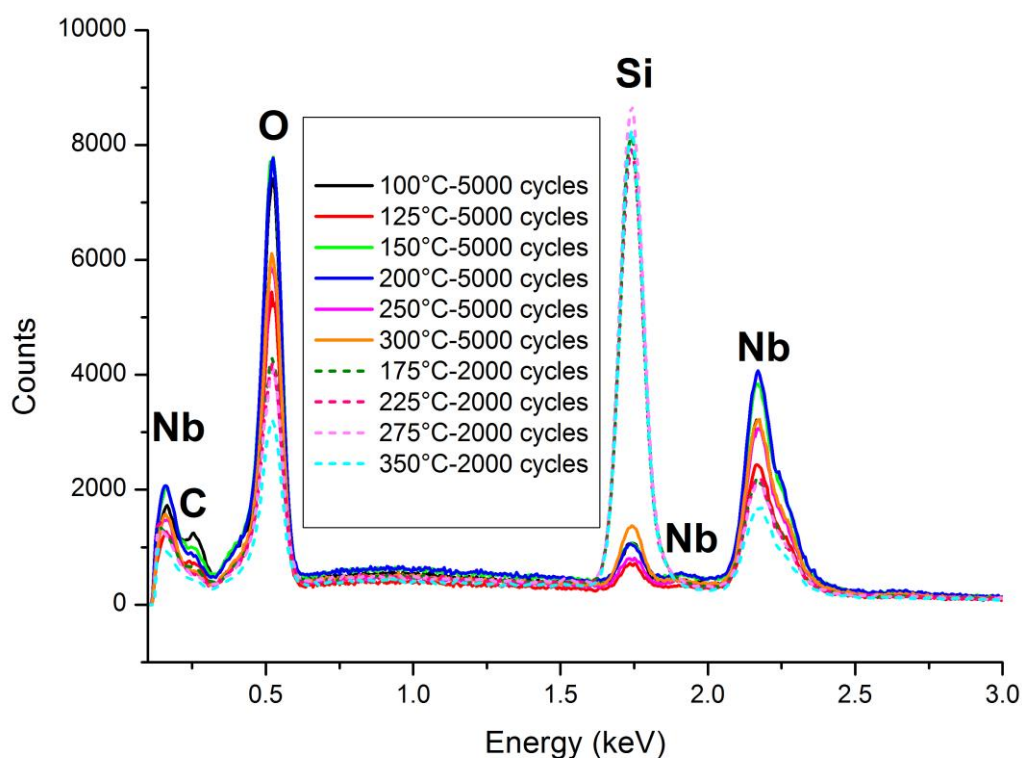


Figure V. 9: X-EDS of the samples for the PEALD recipe, conducted at 8.00 kV

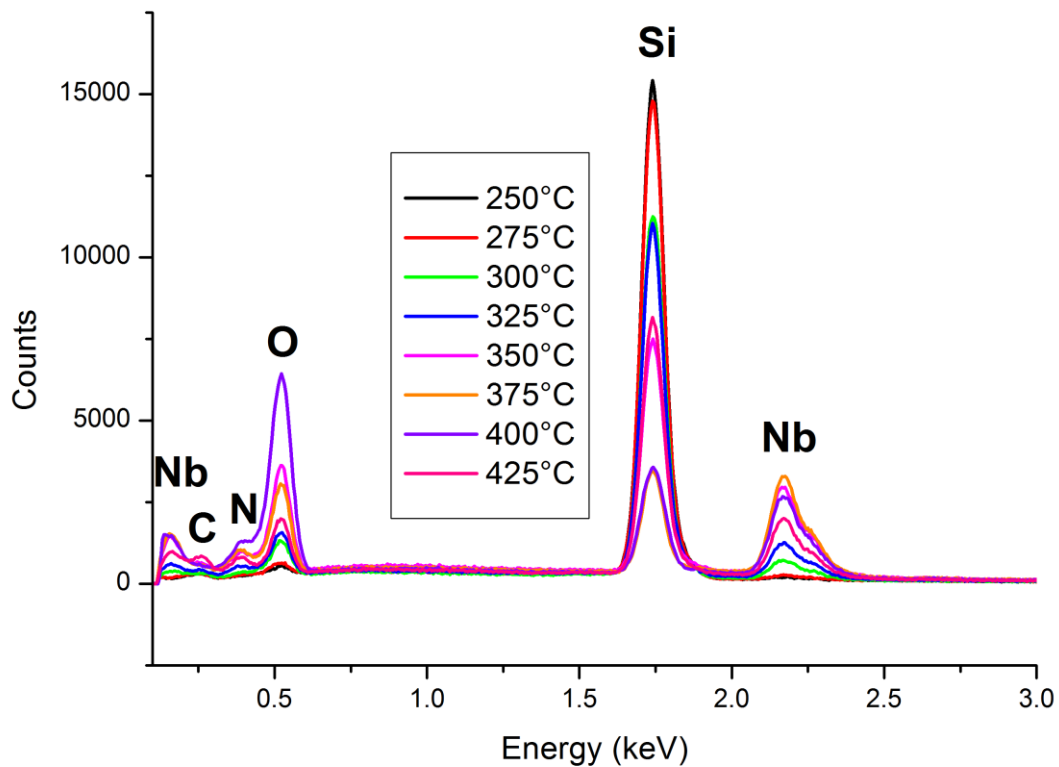


Figure V. 10 : X-EDS of the samples for the thermal ALD recipe, conducted at 8.00 kV

For the PEALD recipe (Figure V.9), the contributions of Niobium, Carbon, Oxygen and Silicon can be detected. Carbon probably originates from contamination [20], whereas it is postulated that niobium and oxygen are due to the deposit. Interestingly, for the thermal ALD deposition (Figure V.10), the same contributions are detected (Niobium, Carbon, Oxygen and Silicon) but another element is detected: Nitrogen. As this element is included in the oxidant (N_2O), it is probable that the deposit chemistry changed. Also, it can be seen in both recipes, that the peak height of silicon is inversely proportional to the ones of niobium and oxygen (and nitrogen for the thermal ALD recipe). As the beam encounters the sample, both the deposit and the substrate are penetrated by the electrons. Thus, the greater the thickness of the deposit, the lower the contribution of the substrate and the greater the contribution of the deposit. As the contribution of nitrogen is proportional to the thickness of the deposit, it is postulated that it is comprised within the deposit (as if it was only comprised on the extreme surface, the contribution of nitrogen would not change).

ii. XRD analysis

The X-Ray Diffraction pattern of three deposits of each recipe are presented in Figures V11.

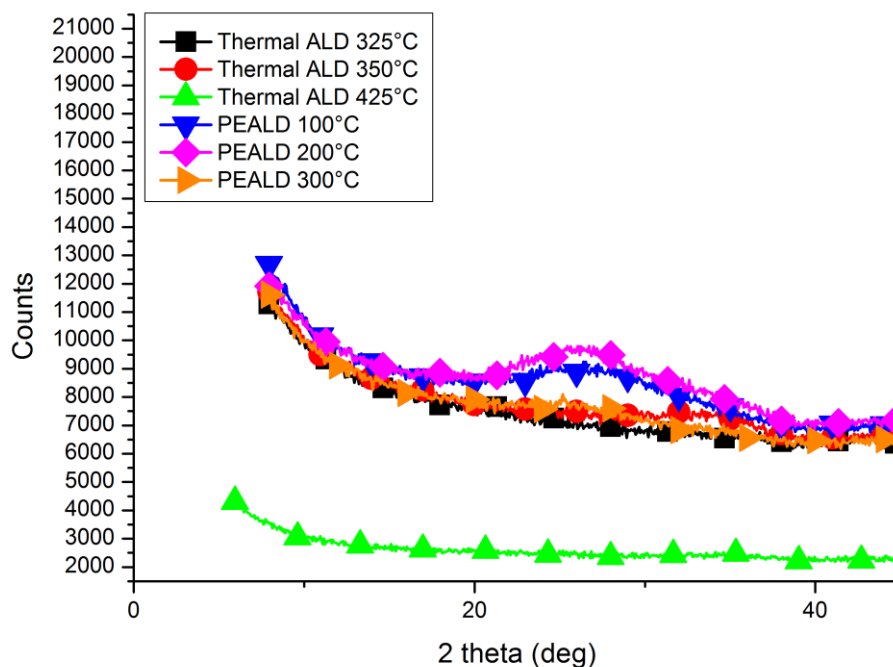


Figure V. 11: XRD pattern of Thermal ALD recipe and PEALD, measured by θ , 2θ , with a K alpha 1 copper X-Ray source.

The XRD results of the two recipe give insight on the deposit crystallinity. For example, crystalline niobium pentoxide (supposed nature of the deposit) possess strong XRD patterns in the region of $2\theta=20-40^\circ$ [21–23]. In our case, no strong XRD features are observed, indicating that the deposits are rather amorphous than crystalline. In order to give a better insight on the chemistry of the deposit, X-Ray Photoelectron Spectroscopy (XPS) was conducted on the PEALD sample elaborated at 200°C (5000 cycles), and on the thermal ALD sample elaborated at 400°C (5000 cycles).

iii. XPS analysis

The XPS results are presented on Figure V.12 for the PEALD and on Figure V.13 for thermal ALD.

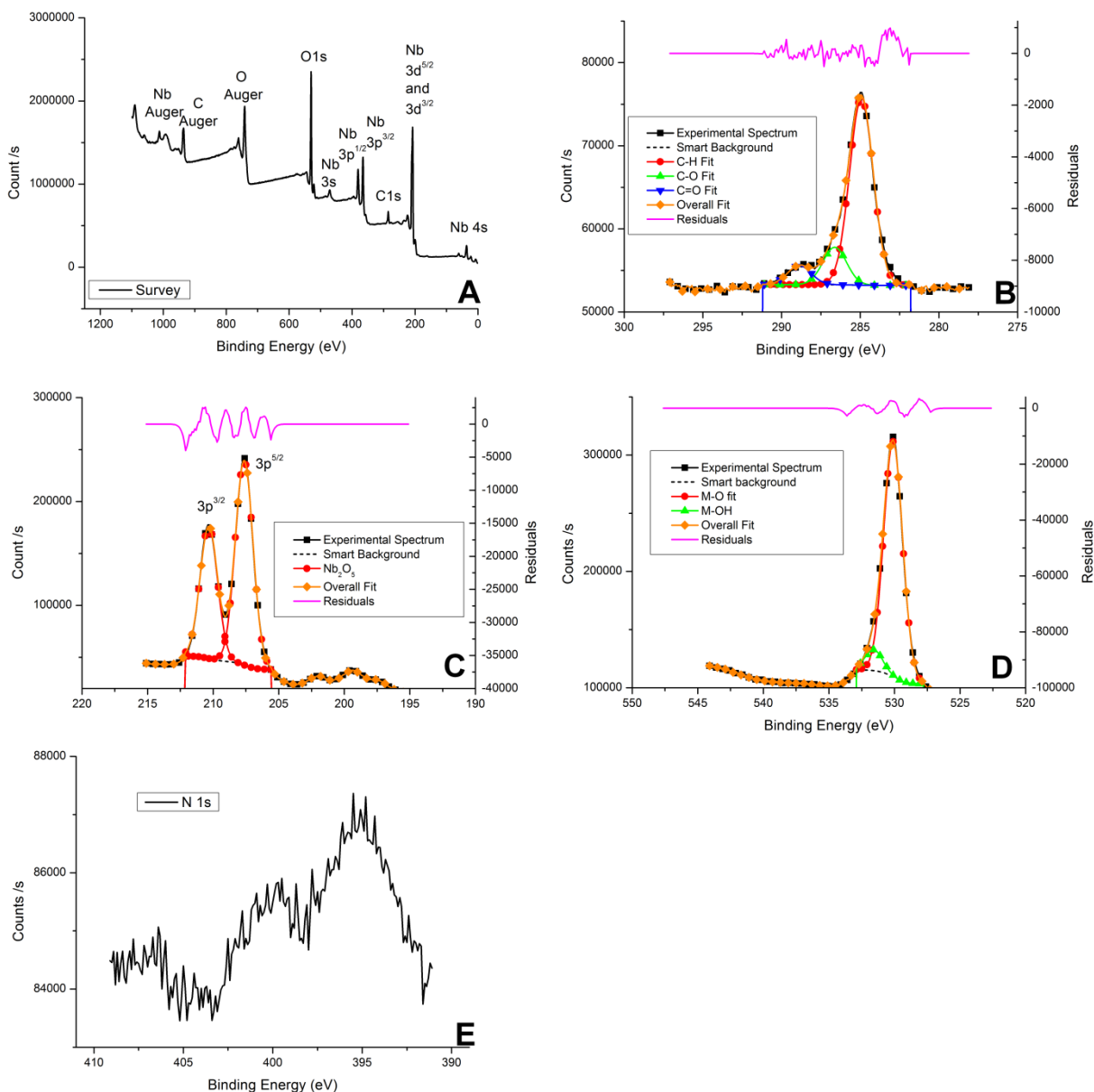


Figure V. 12: XPS surface analysis of PEALD sample at 200°C, 5000 cycles. A-Survey, B- C1s, C- Nb3d5/2 and 3d3/2, D- O1s and E- N1s

The survey for the PEALD sample (Figure V.12-A), shows that mainly the contributions of niobium and oxygen are detected (along with contamination carbon [20, 24]). The C1s spectra (Figure V.12-B), shows three contributions: at 285 eV is the contribution of C-H species [24]. the peak at 286.4 eV is accounted to C-O adsorbed species and at 289 eV, C=O adsorbed species. Figure V.12-C shows that only one contribution is sufficient to correctly fit the Nb^{5/2} and Nb^{3/2} spectra, indicating that only one form on niobium is present on the surface. The peak energy of the Nb^{5/2} is located at 207.5 eV, which corresponds to niobium pentoxide (Nb₂O₅) [24–30]. It must be noted that in any case and for any species, the difference between the peaks Nb^{5/2} and Nb^{3/2} is of 2.7 eV [24] (fixed parameter to

integrate in the fits). The O1s peak (Figure V.12-D) exhibits three contributions; the first, located at 530.5 eV, corresponds to metal oxides (here probably Nb-O bound [24, 28, 31]). The lower contribution at 531.5 eV, is linked to metal hydroxides [24] (formation of niobium hydroxides on the surface). The N1s spectra show the presence of adsorbates on the surface of the sample (as the signal is very noisy). The contribution around 400 eV is attributed to adsorbed N-N bound [24], and for the contribution at 395 eV, several papers linked this transitions to metal nitrides (niobium nitrides) [24, 32, 33]. It is postulated that, as ALD proceeds thanks to the chemisorption of the precursors, this contribution is accounted for remaining of the niobium precursor (TBTDEN) chemisorbed on the surface of the sample (as it comprises Nb-N bounds).

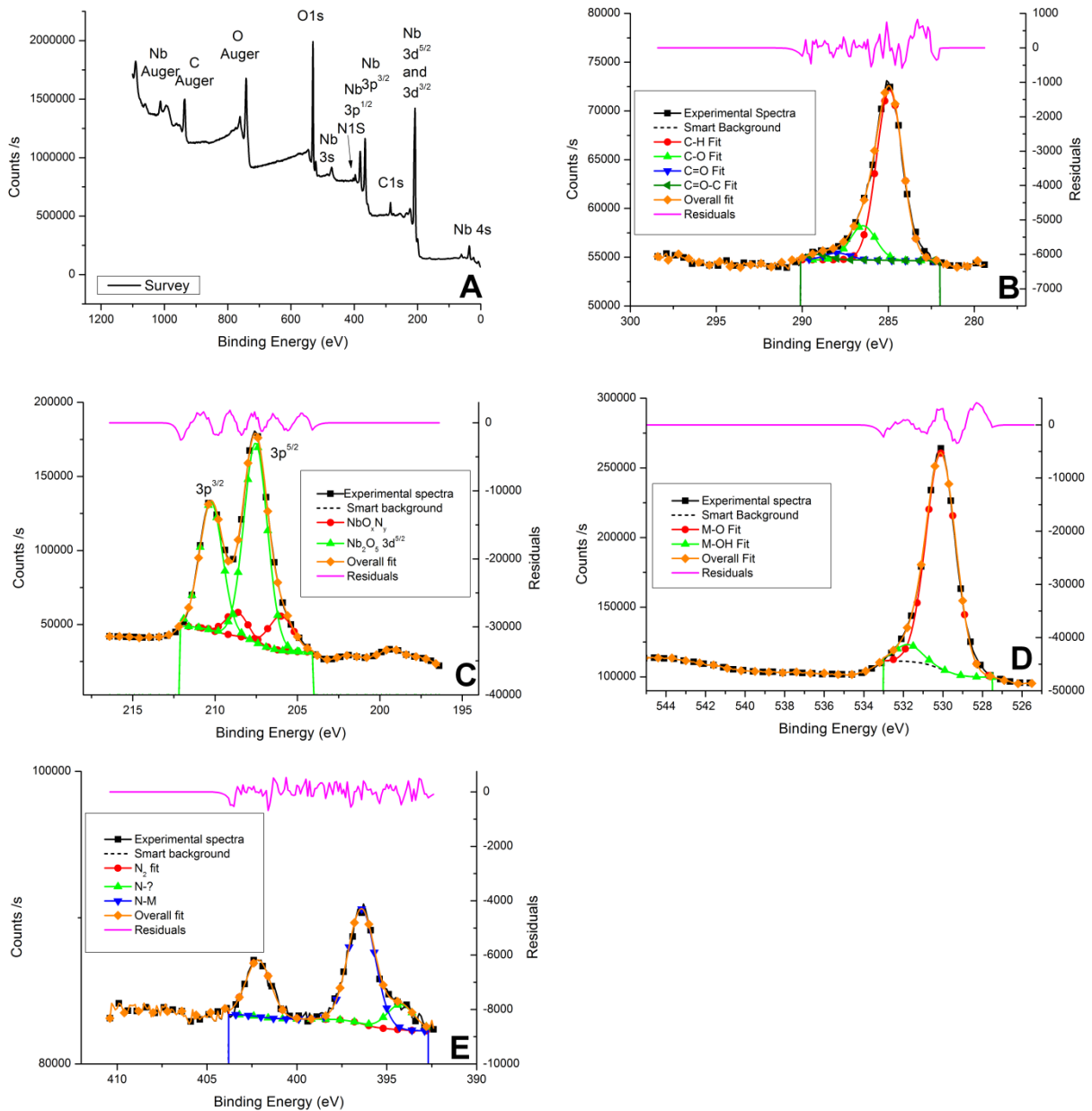


Figure V. 13: XPS surface analysis of Thermal ALD sample at 400°C, 5000 cycles. A- Survey, B- C1s, C- Nb3d5/2 and 3d3/2, D- O1s and E- N1s

The Survey (Figure V.13-A) for thermal-ALD sample presents the same features than for the PEALD recipe, except for the presence of greater amounts of nitrogen on the surface: Niobium, Oxygen and Nitrogen are detected along with contamination carbon [20]. The C1s spectra (Figure V.13-B) show the presence of C-H, C-O, C=O and C=O-C contributions, accounting for diverse contamination on the surface [24]. The niobium spectra (figure V.13-C) is very different from what is observed with the PEALD recipe, with a minor niobium contribution detected. Thus, the major surface compound is probably niobium pentoxide, with an energy peak situated at 207.5 eV on Nb^{5/2} [24–30]. The minor contribution has an energy located at 206.5 eV for Nb^{5/2} peak; this could be niobium dioxide (NbO₂)

[24] or niobium oxinitrides (the presence of a contribution between 206 and 207 eV is reported when niobium nitride is oxidized into niobium oxinitrides [31–34]). The observation of the others contributions (O1s and N1s), will give a better insight on the compound, which is responsible for the peak at 206.5 eV. The O1s peak (Figure V13-D) shows two contributions, in line with what is observed for the PEALD recipe; the first at 530.5 eV is accounted for metal oxides [24, 28, 31], and the second to surface hydroxides [24]. The N1s spectra (Figure V13-E), exhibit much larger intensity than for the sample elaborated by PEALD. This means that a larger concentration of nitrogen species is at stake. As for the PEALD, the contribution at 402 eV is due to N-N bound [24, 35] (thus adsorbed di-nitrogen from air). However, the second contribution (which is the larger one, at 396.4 eV), is accounted for nitrides [24, 32, 33]. This might indicate that the $\text{Nb3d}^{5/2}$ contribution located at 206.5 eV is due to oxinitrides, but it was explained in the literature that this contribution is observed around 399-400 eV [31–33] on the N1s spectra. A minor contribution was also detected around 394 eV and could not be explained. As more nitrogen was detected for the thermal ALD, versus PEALD, it was decided to conduct XPS analysis with erosion of the surface by ion sputtering [24] (depth analysis of the deposit). This experiment shall give better insight into what compound is responsible for the $\text{Nb3d}^{5/2}$ contribution, observed at 206.5 eV. The sample elaborated at 375°C was chosen, as it was the best of all deposit, conducted by thermal ALD. The surface analysis of this sample is presented on Figure V.14.

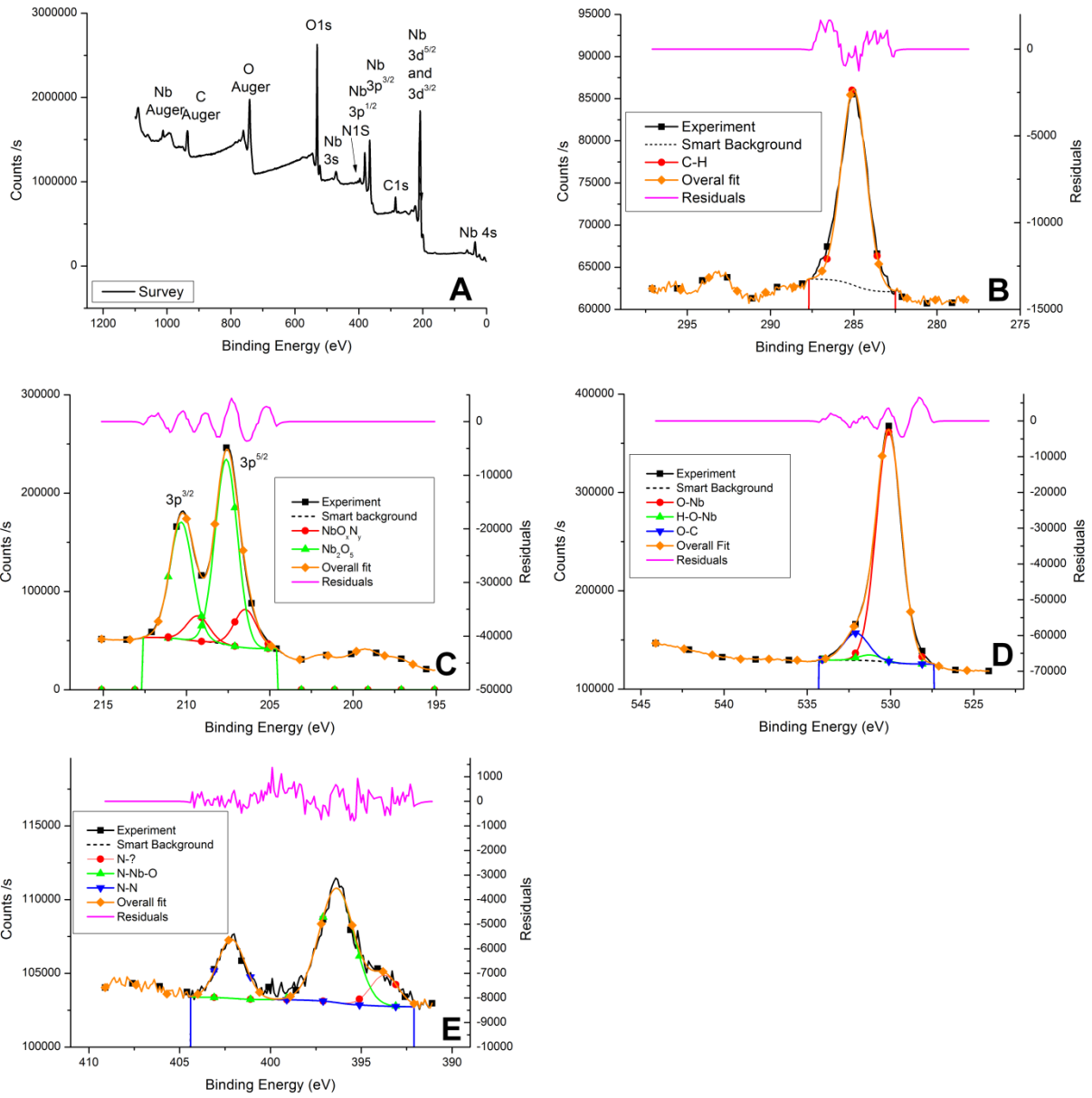


Figure V. 14: XPS surface analysis of thermal ALD sample at 375°C, 5000 cycles. A-Survey, B- C1s, C- Nb3d5/2 and 3d3/2, D- O1s and E- N1s

The features of the sample, elaborated at 375°C are very similar to what was observed at 400°C. As a consequence, the Survey (Figure V.14-A) is nearly identical: Niobium, Oxygen, Nitrogen and contamination carbon are detected. Concerning the contamination carbon (Figure 14-B), only the C-H contribution is detected this time, at 285 eV [24]. The niobium features are the same than for the sample elaborated at 400°C (Figure V.14-C): the contribution of niobium pentoxide [24–30] (Nb 3d^{5/2} peak situated at 207.5eV), which is the most important, and the one situated at 206.5 eV (which is not attributed yet). The O1s spectra (Figure V.14-D) is also very similar to what is observed for the sample elaborated at 400°C, with the M-O contribution located at 530.5 eV [24, 28, 31] and the M-

OH contribution located at 531.5 eV [24, 36–38]. Concerning the N1s spectra, the same features are observed: the N-N bound at 402 eV, the contribution at 396 eV (metal nitrides [24, 32, 33]), and the unexplained contribution at 394 eV. The erosion analyses were taken after 30, 60, 90 and 120 minutes of erosion; for better clarity, the same spectra will be presented on each figures. As the surface is etched, the carbon contribution is heavily extinguished, but it can still be used to correct the XPS shift. The Survey for the four erosion times are presented on Figure V.15.

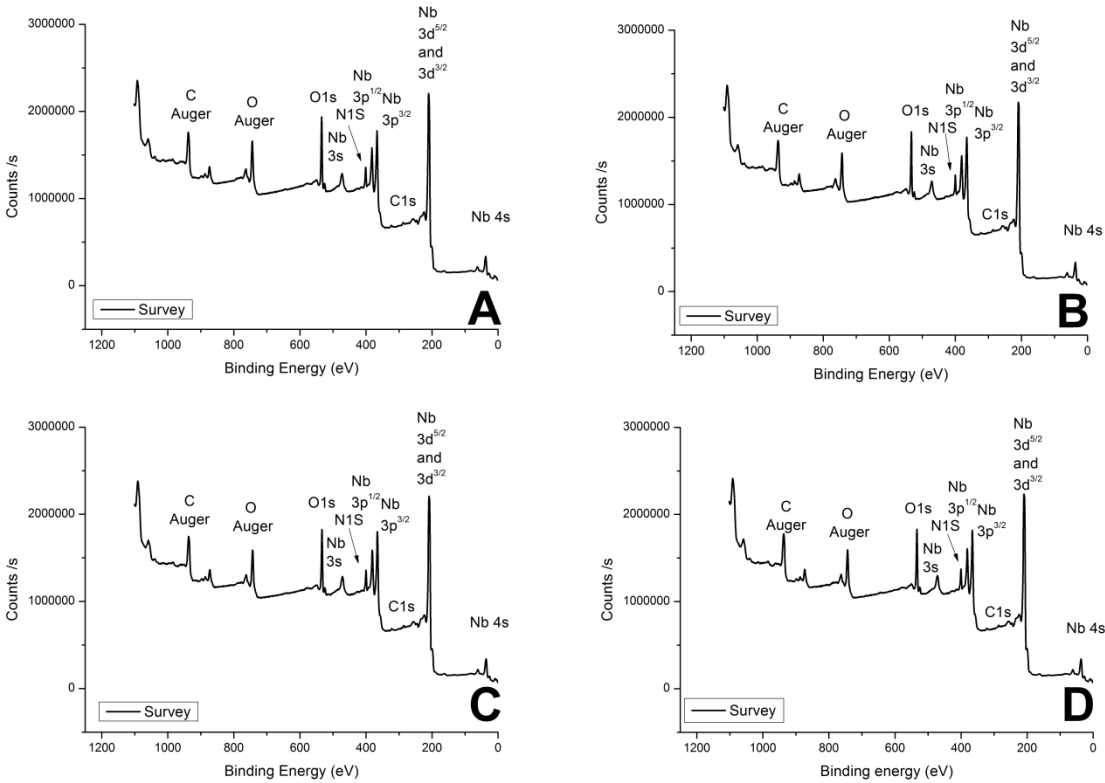


Figure V. 15: Full XPS spectra for different erosions times. A-30 minutes, B-60 minutes, C-90 minutes and D-120 minutes.

The first observation of the erosion experiments is that erosion did not go all the way through the deposit to the substrate (Silicon), as the most intense band of silicon (2p) is not visible on the Survey (Figure V.15) (occurrence around 100 eV for metallic silicon and around 104 eV for SiO₂). Secondly, the deposit seems relatively homogeneous within the depth, as the full spectra do not change (or very little). The comparison for different erosion time of the C1s peak is presented on Figure V.16.

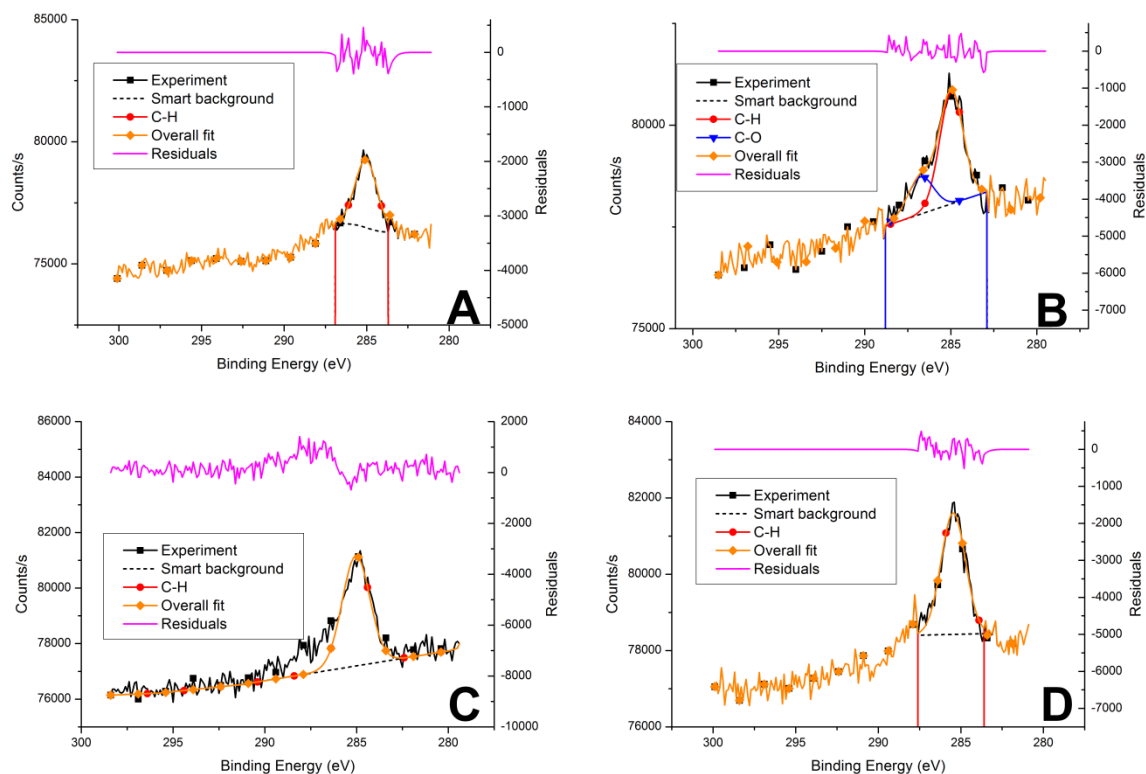


Figure V. 16: C 1s contributions for different erosion times. A-30 minutes, B-60 minutes. C-90 minutes. D-120 minutes.

The fit of the C1s spectra was not done in order to find a physical meaning of the spectra. As the sample is eroded, the carbon contamination content is greatly reduced. However, it was still detected as presented on the Figure V.16. Thanks to its detection, the other spectra were adjusted, as C-H bounds are detected at a very specific value of 285 eV [24]. The comparison for the 3d^{5/2} and 3d^{3/2} peaks of niobium for the different erosion time is presented on Figure V.17.

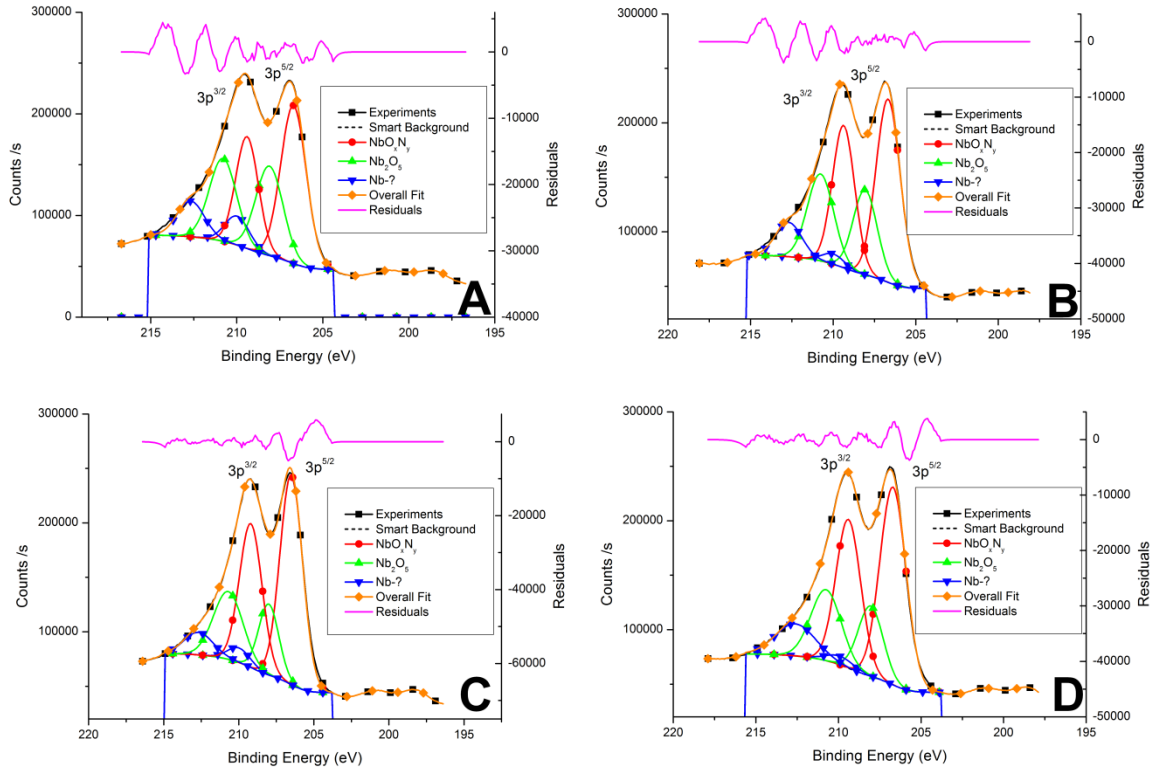


Figure V. 177: Nb $3d^{5/2}$ and Nb $3d^{3/2}$ contributions for different erosion times. A-30 minutes, B-60 minutes. C-90 minutes. D-120 minutes.

Concerning the positions of the Nb $3d^{5/2}$ and Nb $3d^{3/2}$ peaks, three contributions are detected in the depths of the deposit. In contradiction with what was observed on the surface, the most important contribution in the core of the deposit is the one located at 206.5 eV. As Niobium pentoxide is more stable than niobium dioxide, both at ambient temperature and at the temperature of the deposition (free energy of formation of the former at ambient temperature: -412 kcal/mol, the latter: -173 kcal/mol; at 400°C : the former: -376 kcal/mol, the latter: -158 kcal/mol [39]), the contribution at 206.6 eV is very unlikely due to niobium dioxide. In addition, the niobium precursor used for this deposition is in the +V state, and nothing can explain the formation of an oxide, at an inferior oxidation state than the precursor, in oxidizing atmosphere. It is thus postulated that the contribution observed at 206.6 eV is due to niobium oxinitrides (several examples in the literature illustrated its presence for the Nb $3d^{5/2}$ peak, between the one of niobium nitride (204 eV) and niobium pentoxide (207.5 eV) [31–34]). This explanation is satisfying as the second reactant used for this recipe is N_2O , which comprises both nitrogen and oxygen. The second most intense contribution for the Nb $3d^{5/2}$ peak is located around 208.1 eV. It is postulated that this contribution is due to niobium pentoxide, as supported by several example in the literature claiming its occurrence at higher energies [3, 40]. A third contribution of the Nb $3d^{5/2}$ peak was detected, around 210 eV. However, even after an extensive literature search, no explanations were found, as no niobium

compound were detected as such high energies, for $3d^{5/2}$. The comparison for different erosion time of the O1s peak is presented on Figure V.18.

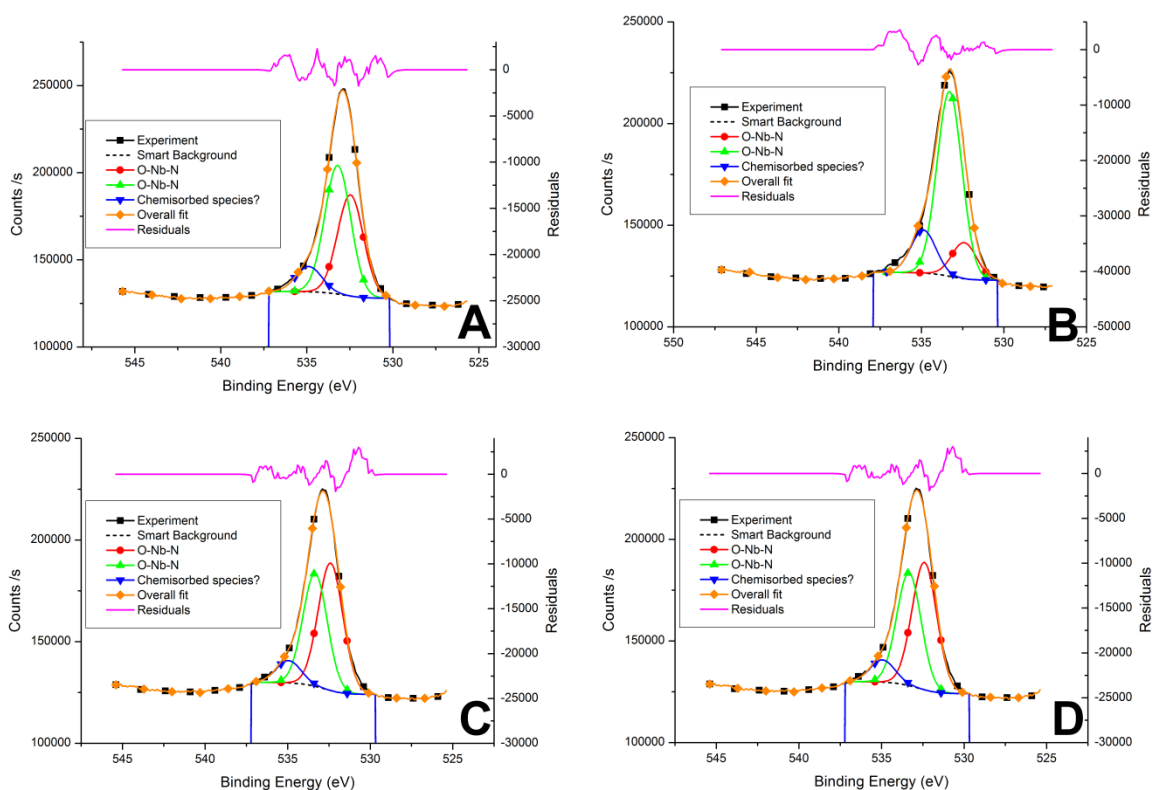


Figure V. 188: O1s contributions for different erosion times. A-30 minutes, B-60 minutes. C-90 minutes. D-120 minutes.

O1s peaks show the convolution of three contributions: two intense ones at 532.5 eV and 533 eV and a small one at 535 eV. At such high energies, it appears clear that the main contribution cannot be an oxide (as metal oxides are detected from 529 to 532 eV [24]). The reason why this contribution totally disappeared upon erosion remains unclear. It is postulated that the etching of the surface with the argon beam somehow changed the location of the peak. Only one example was found in the literature, where the etching of the ion beam shifted the position of the O1s band of a TiN coating from 530 eV to 533 eV [41]. However, cautiousness must be taken in regard to this hypothesis, as not many papers support this explanation in the literature. Concerning the peak at 532.5 eV, a possible explanation could be the presence of O-O bound in the oxinitrides [42], but as for the former explanation of the peak at 533 eV, it must be looked wisely. Concerning the contribution at 535 eV, it is probably the presence of chemisorbed species [24, 34, 43] (due to the decomposition of the deposit by the ion beam). The comparison for different erosion time of the N1s peak is presented on Figure V.19.

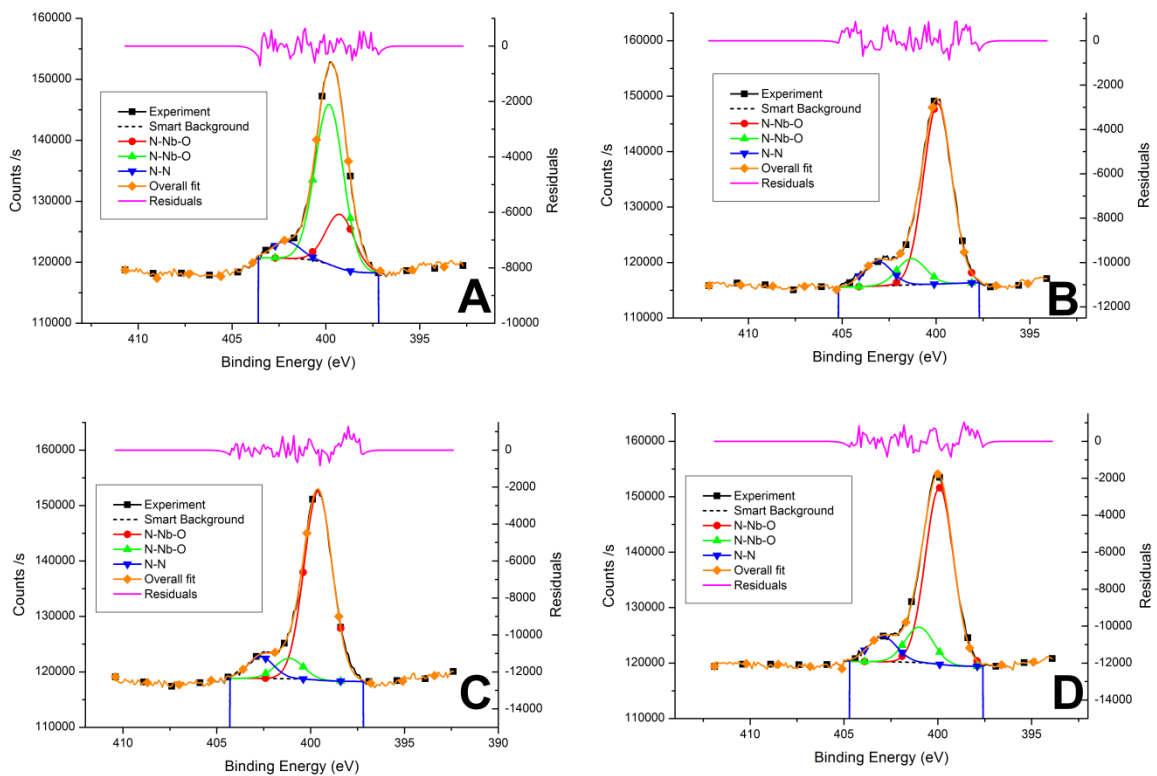


Figure V. 199: N1s contributions for different erosion times. A-30 minutes, B-60 minutes. C-90 minutes. D-120 minutes.

Concerning N1s, a very strong contribution can be observed around 399-400 eV. This contrast with what was observed on the surface (one strong peak at 396 eV and one at 402 eV). In the literature, a contribution can be observed for niobium oxinitrides species around 399 eV [32, 33], and other oxinitrides [24, 44, 45]. For the sample at 30 minutes of erosion (Figure V.19-A), two contributions arise at 399.2 eV and 399.8 eV. It is postulated that both contributions are due to oxinitrides, possibly of different chemistries. The peak at 402 eV is attributed to adsorbed N-N bounds[35]. For erosion times of 60, 90 and 120 minutes, a contribution at 401.5 eV can also be observed, which is often attributed to ammonium in the literature [24, 46]. The presence of such compound might originate either from decomposition products of the niobium precursor encapsulated in the deposit, or from ionization of nitrogen species on the surface of the sample, because of the erosion. However, it will not be further discussed here, as it is not a major contribution of the N1s spectra.

Computing the whole XPS data allows to draw a "composition profile", as the composition did not change in the depth of the sample, as presented on Figure V.20.

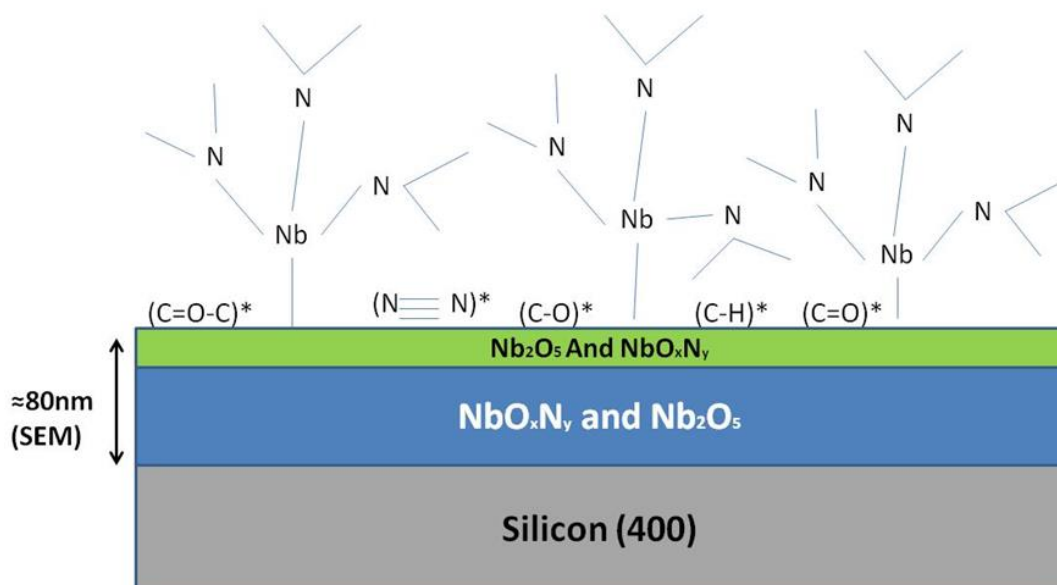


Figure V. 20: Possible composition of the deposit, conducted by thermal ALD. The first compound written is the one present in majority

On the one hand, these results prove that PEALD produces a deposit entirely composed of niobium pentoxide. On the other hand, thermal ALD seems to preferentially form a mix of niobium pentoxide and niobium oxinitride on its very surface (as niobium pentoxide is the most stable oxide/species formed [39]), but in the core of the material, it the dominant compound is the oxinitride, with niobium pentoxide in smaller proportions. It was also proven the presence of a metal nitride on the N1s spectra on the surface, contribution absent for the niobium spectra. This contribution probably arises from chemisorbed niobium precursor on the surface. However, the niobium nitride is not detected on the Nb spectra as the contribution of those chemisorbed species is probably hidden (the solid deposit is far more "concentrated" than those chemisorbed species).

A summary of the composition of the sample, for both recipes is presented on Table V.4

Table V. 4 : Summary of the composition analyses of the samples, elaborated on Silicon (400), for both recipes

Recipe	Adsorbates?	Surface Composition	Composition in the depth of the deposit
Thermal-ALD	Chemisorbed Niobium precursor	Mix of Nb ₂ O ₅ (predominant) and NbO _x N _y	Mix of NbO _x N _y (predominant) and Nb ₂ O ₅
PEALD	Chemisorbed Niobium precursor	Nb ₂ O ₅ alone	X

iv. Conformity of the deposit

In the required application, the ALD recipe must have the ability to make a conformal deposition on high-roughness samples. In order to decide which recipe is preferable versus the other, a deposition for both recipes was made in Silicon (400) wells, with a form factor of 6 (1 μm large, 6 μm deep), and analyzed by SEM. Those sample were then cleaved and the thickness of the deposit, and its conformity at the bottom of the well was observed. For the PEALD, 1570 cycles were realized at 200°C (GPC of about 0.3 \AA per cycle, giving a deposit of about 50 nm for 1570 cycles). For the Thermal ALD, 3000 cycles were realized at 400°C (GPC of about 0.11 \AA per cycle, giving a deposit of about 33 nm). In practice, both deposits showed a thickness of about 50 nm on the surface, when analyzed by SEM. The SEM image of the deposits at the top of the well are presented on Figure V.21.

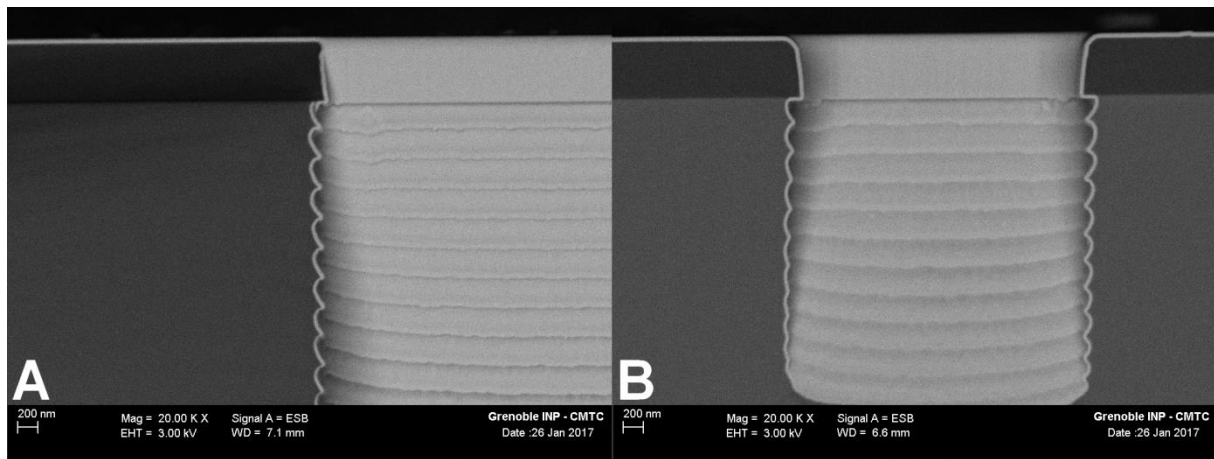


Figure V. 21: SEM images of the top of the wells, using the back-scattered electron detector, for a better appreciation of the deposit. Energy of the beam: 3kV, magnification 20.00 kX. A-PEALD recipe. B-Thermal ALD recipe.

Thanks to the ESB detector, the deposit appears brighter, allowing its better observation. Both recipes have the ability to form a conformal deposit, even inside the well close to the surface. The bottom of the well was then analyzed and the SEM images are presented on Figure V.22.

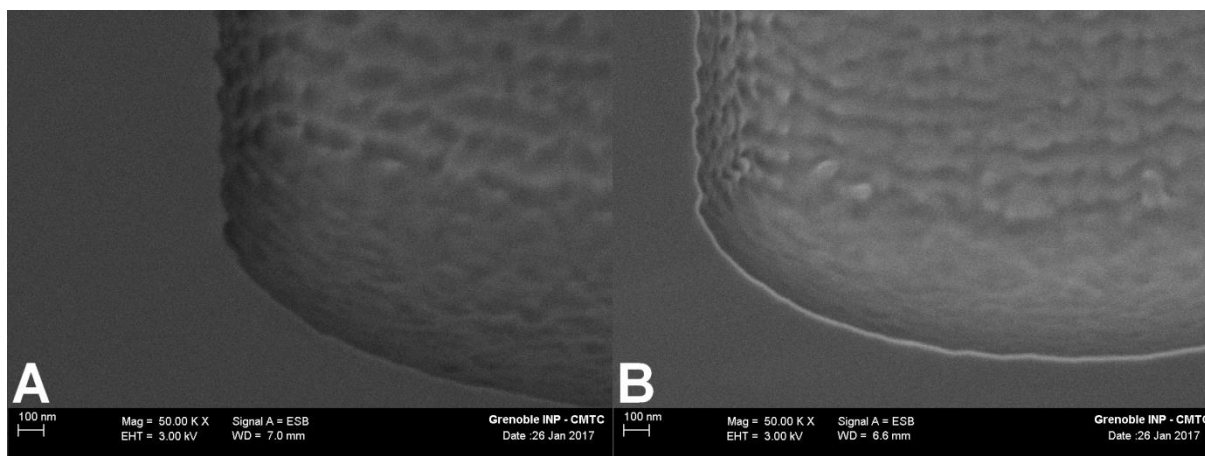


Figure V. 22: SEM images of the bottom of the wells, using the back-scattered electron detector, for a better appreciation of the deposit. Energy of the beam: 3kV, magnification 20.00 kX. A-PEALD recipe. B-Thermal ALD recipe.

As seen on Figure V.22, no deposit is observed for the PEALD recipe, at the bottom of the well, whereas some deposit is still observable for the thermal ALD recipe, as expected (the use of a plasma yields a more directive deposit [6, 47]). As the objective of this chapter is to make a conformal deposition at the surface of rough and 3-dimension substrates, the latter results led us to favor the thermal ALD process over the PEALD one. As such, depositing a thin protective layer onto Panex 30 carbon cathodes was performed using thermal ALD.

III. Cathode elaboration with Nb_2O_5 deposits

The carbon material used for the deposition of Nb_2O_5 was Zoltek Panex 30 (described in chapter three and four). This material was chosen thanks to its low price, high electronic conductivity, macroporosity and high corrosion resistance, properties that make of it a proper substrate material for the positive electrode in a Li- O_2 battery. However, the author acknowledges that this material is still a model compound for a practical cathode as it is of too low surface area compared to high surface area carbon powders. The reason why carbon powder was not chosen in this chapter is linked to the ALD reactor; powder materials would contaminate the whole equipment and compromise its use for other applications. Also, their surface have much higher roughness, which could hinder proper ALD. As explained in the previous section, the deposition was performed by thermal ALD, as it allows a more conformal deposition, even at the bottom of wells, and it is believed that this would enable the complete coverage of the Panex 30 carbon cloth. For each batch, eight samples of 8 mm diameter (hereafter denoted electrodes) were prepared and placed in the ALD reactor for the deposition. In order to prevent the movement of the carbon cloth in the reactor, a

sample holder in copper was machinated. For this study, the deposits were realized at 400°C, with different conditions, as presented in Table V.5.

Table V. 5 : Depositions conditions for the cathodes, prepared with thermal ALD, at 400°C

Sample name	TBTDEN injection time (s)	TBTDEN purge time (s)	N ₂ O injection time (s)	N ₂ O purge time (s)	Number of cycles
1500	1.1	2	4	4	1500
2000	1.1	2	4	4	2000
2500	1.1	2	4	4	2500
1500-Extended	1.6	2	8	4	1500

a. Composition of the deposit, non-uniformities of the deposits

Each deposit composition was analyzed by X-EDS and XPS, a reproducibility analysis being performed by X-EDS to spot any possible non-uniformity of the deposits from one electrode to the other. The X-EDS results are presented in Figure V.23.

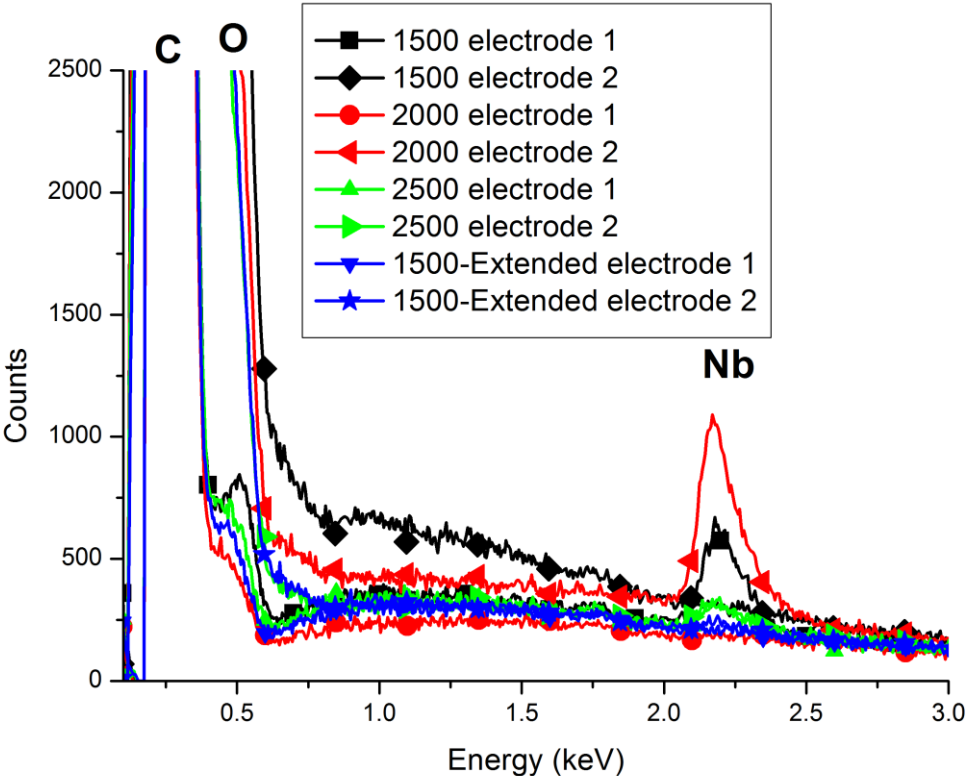


Figure V. 23: X-EDS spectra of the deposits, realized on Panex 30 carbon cloth coated by Nb₂O₅, taken at 8.00 kV

Figure V.23 reveals severe non-uniformities between two samples of the same recipe, that should have been identical. The two thicker deposits (leading to the largest signal of Nb at ca. 2.2 keV) were obtained for the electrode 2, elaborated at 2000 cycles and for the electrode 1, elaborated at 1500 cycles. The reason for these non-uniformities cannot be explained, as the temperature is supposedly uniform in the ALD-reactor. One can speculate that, as the samples were used bare and not prepared (for instance, washed with absolute ethanol, let for dry, etc.), the deposition rate could have been altered, locally. Still, deposition of Nb₂O₅ is possible on these carbon substrates, which is good news. However, the nitrogen signal disappeared from the X-EDS spectra, which indicates that the product obtained on carbon is different from the one obtained on silicon, with the same recipe (see previous section). XPS has been conducted on the electrode 2 of each sample, to complement the characterization. The full XPS survey for the four recipes is presented on Figure V.24.

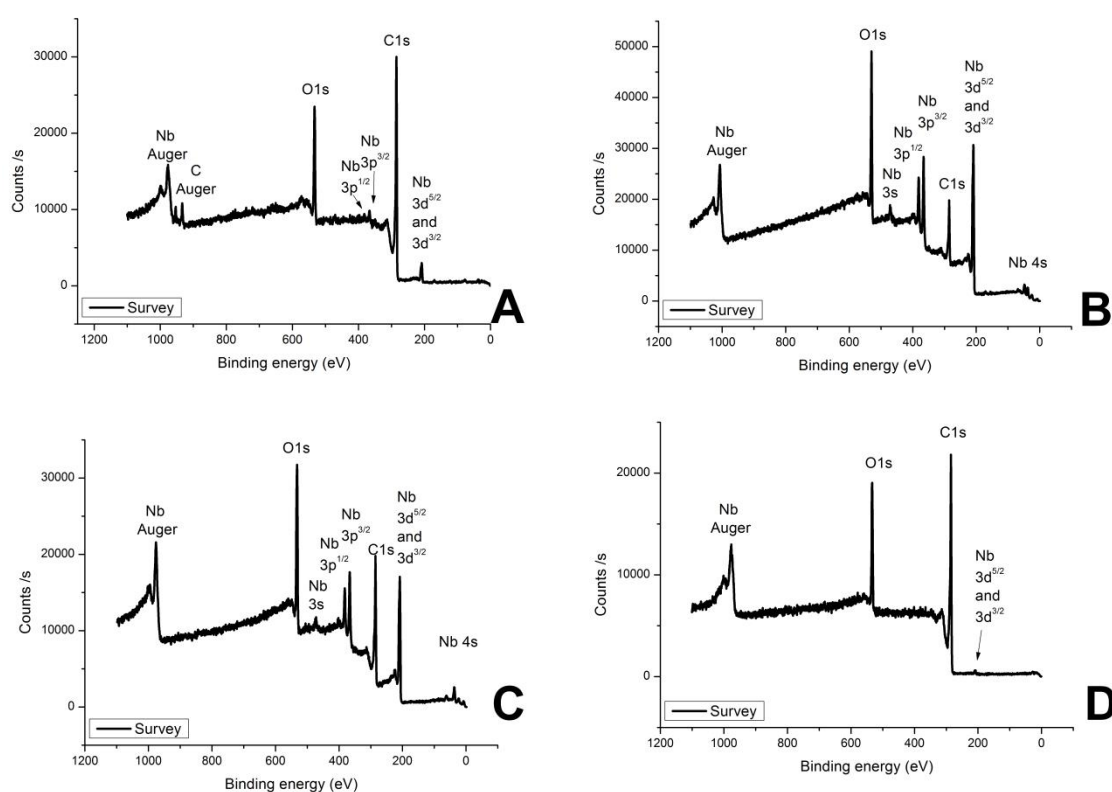


Figure V. 24: XPS full survey for electrodes A-1500, B-2000, C-2500 and D- 1500-Extended.

Figure V.24 supports the results obtained by X-EDS. For the sample elaborated at 1500 cycles (Figure V.24-A), niobium is detected, but in little proportions, as Nb3s and Nb4s features are not detected (only the most intense contribution Nb3d^{5/2} and Nb3d^{3/2}, with noisy peaks for the 3p^{1/2} and 3p^{3/2}

contributions, are observed). The samples elaborated with 2000 and 2500 cycles (Figure V.24-B and C) exhibit almost the same trace, with all the contribution of niobium (including minor contributions Nb₃s and Nb₄s). The sample elaborated at 1500 cycles extended (1500-Extended, Figure 24-D), shows almost no trace of niobium: a small contribution of the Nb₃d^{5/2} and Nb₃d^{3/2} peaks can be observed, probably indicating either chemisorbed species, or a very thin layer of deposit. For a more complete analysis, the carbon peaks are presented on Figure V.25.

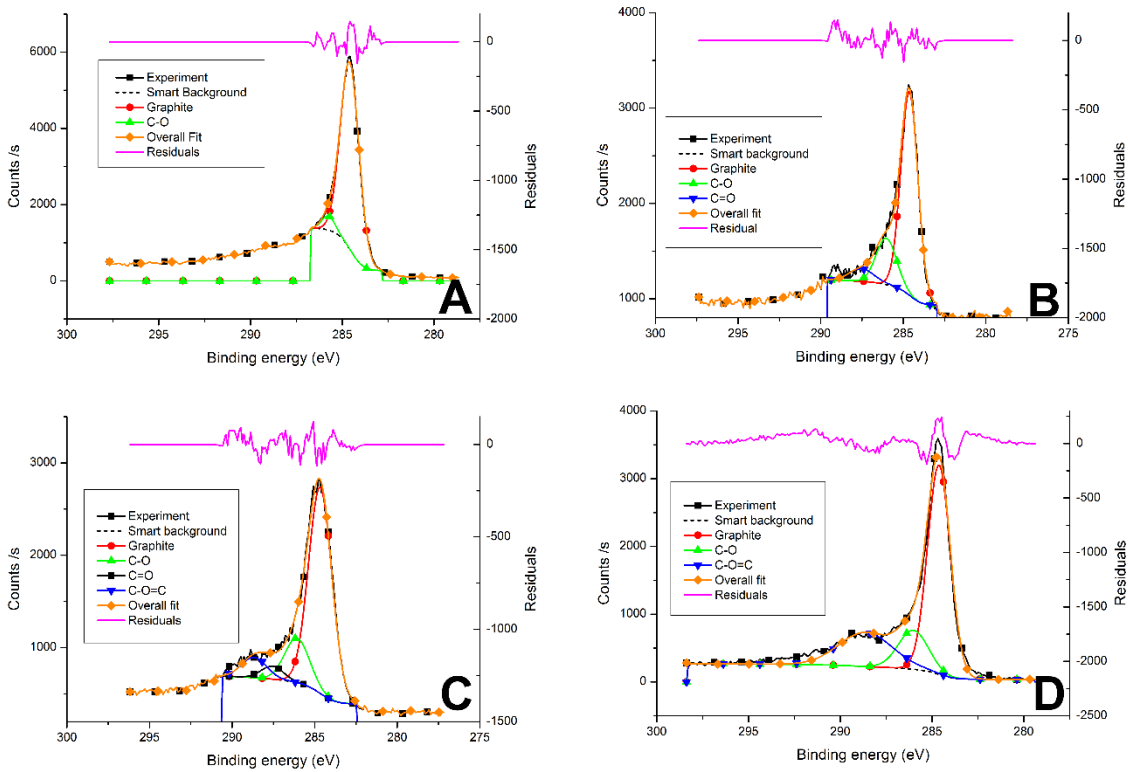


Figure V. 25 : C1s peaks for electrodes A-1500, B-2000, C-2500 and D-1500-Extended

As presented in the previous part, for the deposits made on silicon, the carbon peak is mainly used for setting the shift of energy at the correct position. It must be noted that normally, the graphite peak is located around 284.6 eV [24]. As presented in Chapter three, the Panex 30 cloth is made of graphitic fibers, with no amorphous zone (no amorphous carbon nor amorphous graphitized lattice), thus the most intense peak of the C1s was set at 284.6 eV. Consequently, the contributions of the graphitized carbon are set at 284.6 eV and other contributions such as C-O, C=O and C=O-C (of contamination carbon) can be observed at higher energies (respectively, at 286 eV, 287.5 eV and 289 eV). The Nb₃d^{5/2} and Nb₃d^{3/2} peaks are presented on Figure V.26.

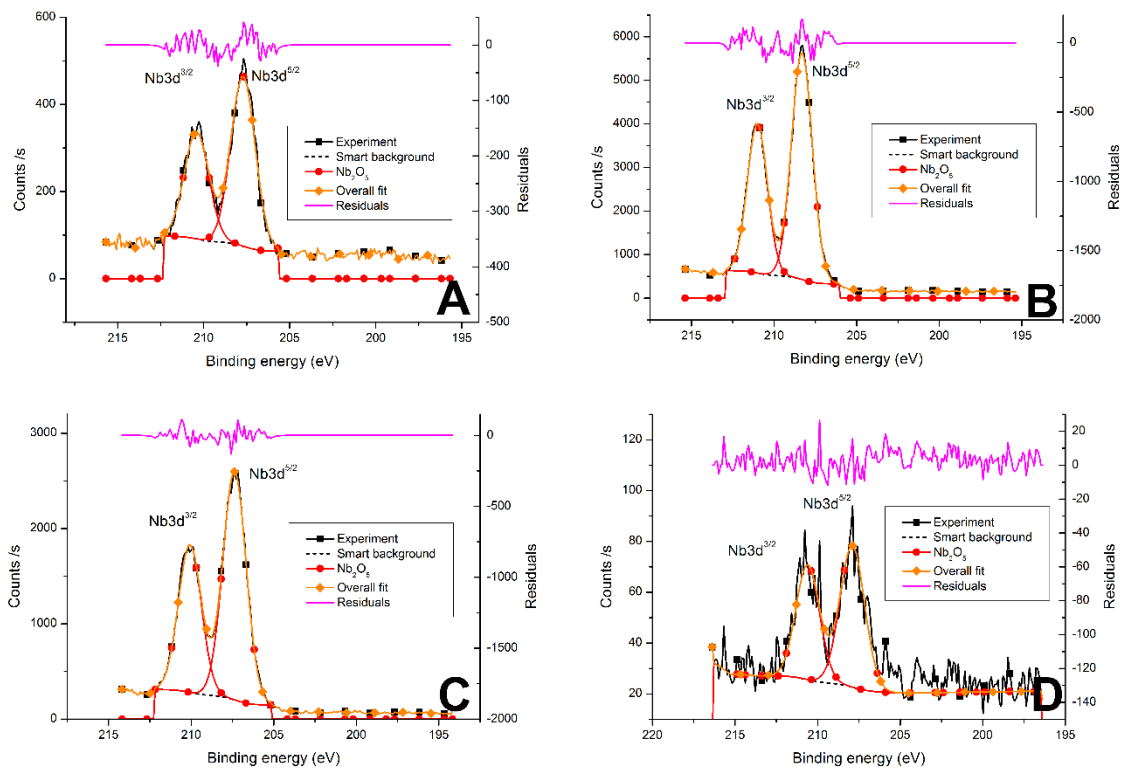


Figure V. 26: Nb3d^{5/2} and Nb3d^{3/2} peaks for electrodes A-1500, B-2000, C-2500 and D-1500-Extended

Even though the same reactants were used for the deposition on carbon, the deposits obtained here do not present a contribution around 206.5 eV, which contrasts with the results obtained on silicon. For those experiments, only one contribution is necessary to fit correctly the experimental data, indicating that only one form of niobium product is present on the surface. Concerning the Nb3d^{5/2} peak location, its position is at higher energies (207.8 ± 0.1 eV) for the thinner deposits (1500 and 1500-Extended). This corresponds to very thin Nb₂O₅ deposits, as presented by Okazaki *et al.* [40].

The Nb3d^{5/2} peak of the thicker deposits is located around 207.4 eV (for 2500) and around 208 eV (for 2000), which perfectly corresponds to niobium pentoxide (in the literature, its contribution is located around 207.6 ± 0.1 eV[24–30]). The reason for the shift from 207.5 eV to 208 eV for the thicker sample (Figure V26-B) remains unclear. A better refinement of this results can be obtained thanks to the O1s spectra, presented on Figure V.27.

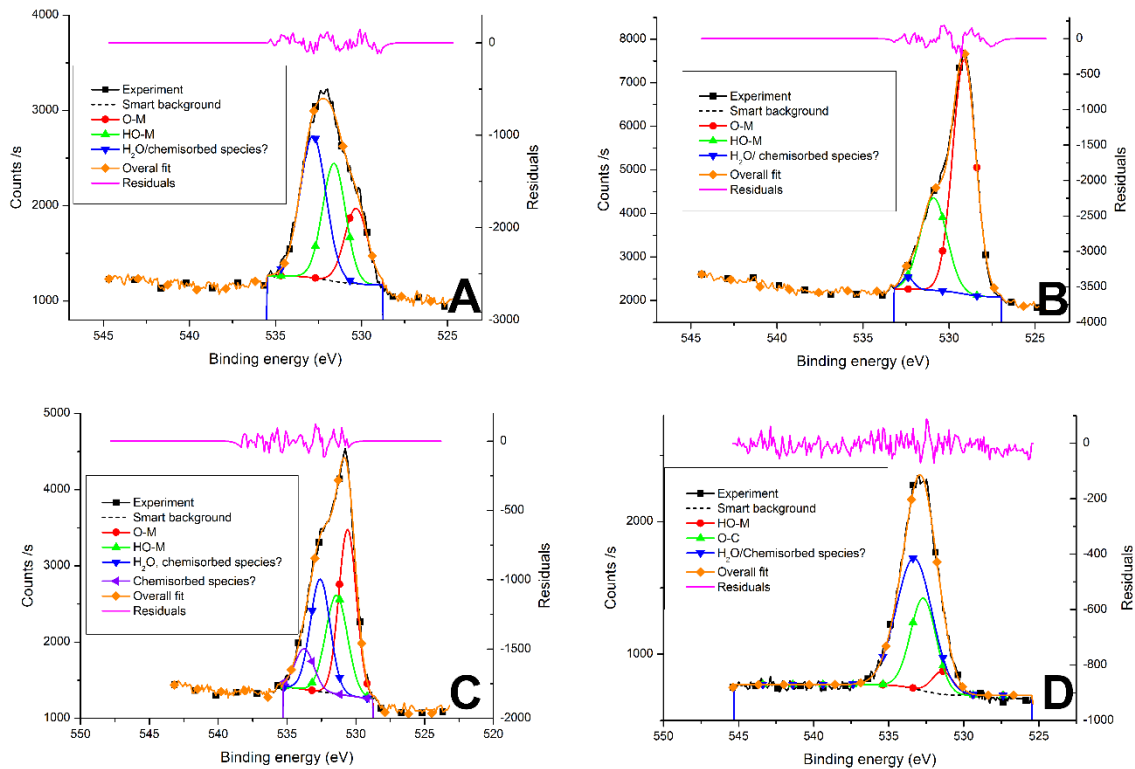


Figure V. 27 : O1s peaks for electrodes A-1500, B-2000, C-2500 and D-1500-Extended

Three/four contributions can be observed on the O1s spectra. Firstly, a contribution around 530.3 ± 0.2 eV, that is accounted to the metal oxides [24, 28, 31]. For the sample elaborated at 2000 cycles (the thicker), this contribution is detected at 529.1 eV, which is highly shifted, compared to the other samples. However, as presented in the Handbook of X-Ray Photoelectron Spectroscopy, the metal oxide contribution of O1s can be located in the region 528-531 eV [24], depending on the nature of the metal involved in the bound. It must be noted that below 530 eV, no other contributions than metal oxide can be held responsible on the O1s spectra [24, 36–38]. As no other metal were detected on the Survey (Figure V.24), it is the Nb-O bound that is held responsible for this bound. However, the reason for this shift remains unclear. Concerning the contribution observed at 531.5 ± 0.2 eV, it is attributed to metal hydroxides on the surface [24, 48–51]. The O1s contribution at higher energies (above 532 eV) is attributed either to water [24] or others chemisorbed species [34, 43, 52]. As such, for the thinner sample (1500-Extended, figure V.27-D), no M-O bound is detected, only a small contribution of M-OH is detected, indicating that a very thin layer of niobium pentoxide is present on the surface, and that this oxide is more likely an hydroxide. The reason for this is that probably a monolayer (or two) of niobium pentoxide was (were) formed during the ALD process on this sample, and upon contact with air, it (they) transformed into hydroxide. Concerning the second thinner

sample (1500, Figure V.27-A), the M-O bound is detected along with M-OH in greater proportion. This indicates that even though this deposit is very thin, it is thick enough not to be fully transformed from oxide into hydroxide. With no surprise, the largest contribution of the thicker deposit (2000, Figure V.27-B) is M-O, with still M-OH formed. The intermediate compound (2500, Figure V.27-C), has more or less the same amount of M-O and M-OH contribution on its surface.

To summarize, the niobium and O1s spectra confirm the X-EDS data in terms of thickness order of the samples analyzed (electrode 2): 2000 > 2500 > 1500 > 1500-Extended.

Computing the XPS results, it is highly probable that the deposits made onto the carbon cathodes are of the following composition: niobium pentoxide in the core of the deposit (when it is thick enough); then, niobium hydroxide (still in the +V oxidation state for niobium) on the very surface. As a consequence, it is confirmed that the deposition of niobium pentoxide is achievable onto graphitized carbon cloth, but as the deposit thickness (and therefore average composition) could not be strictly controlled from one electrode to another of the same batch, a stricter protocol should have been found to prepare the electrode surface prior ALD so to have comparable deposit thickness for all the electrodes of a same batch. Unfortunately, this protocol could not be developed for this present work, because of lack of time. However, the objective here was to elaborate cathodes with deposits and test the latter for the ORR/OER, so electrochemical tests (in three-electrode, DEMS and full cell) were nevertheless performed to determine if such deposits have an interest for practical Li-O₂ systems.

A summary of the deposits composition is presented on Table V.6.

Table V. 6 Deposit composition of the electrodes analyzed

Sample	Surface Composition	Order of thickness for deposit (1 > 2 > 3 > 4)
1500	Hydroxide of Niobium in +V state on surface (predominant) + Nb ₂ O ₅ + chemisorbed O species	3
2000	Nb ₂ O ₅ (predominant) + hydroxide on surface + chemisorbed O species	1
2500	Nb ₂ O ₅ (predominant)+ hydroxide on surface + chemisorbed O species	2
1500-Extended	Niobium hydroxide in +V state + chemisorbed O species	4

b. Protected Li-O₂ positive electrodes behavior

i. Three-electrode cell

In order to fully characterize the electrochemical behavior of the deposit itself, cyclic voltammeteries were realized in argon-purged electrolyte (Figure V.28). The DEMS setup was used for these experiments, performed moments before the DEMS recording. The scan-rate chosen was 2 mV s⁻¹, which is slow enough to observe the inherent electrochemical behavior of the deposit, without being disturbed by a strong double layer effect of the carbon cloth. The upper reverse scan was extended to 1 V vs. Ref, in order to see the oxidation of the carbon cathode.

Three materials were compared: pristine Panex 30, one electrode elaborated at 1500 cycles, and one electrode elaborated at 2000 cycles. As explained in the previous section, the deposits are of the same nature for the four batches (1500, 2000, 2500 and 1500-Extended), but the thickness of the electrodes are not reproducible within the same batch.

As such, it is of no use to test one electrode of each batch (as the thickness of the deposit on the electrodes is not dependent on the deposition parameters, and as the composition of the deposits are nearly the same for each batch), and two electrodes were tested. In order to avoid confusion and for better clarity, these electrodes will be presented as electrode 3.

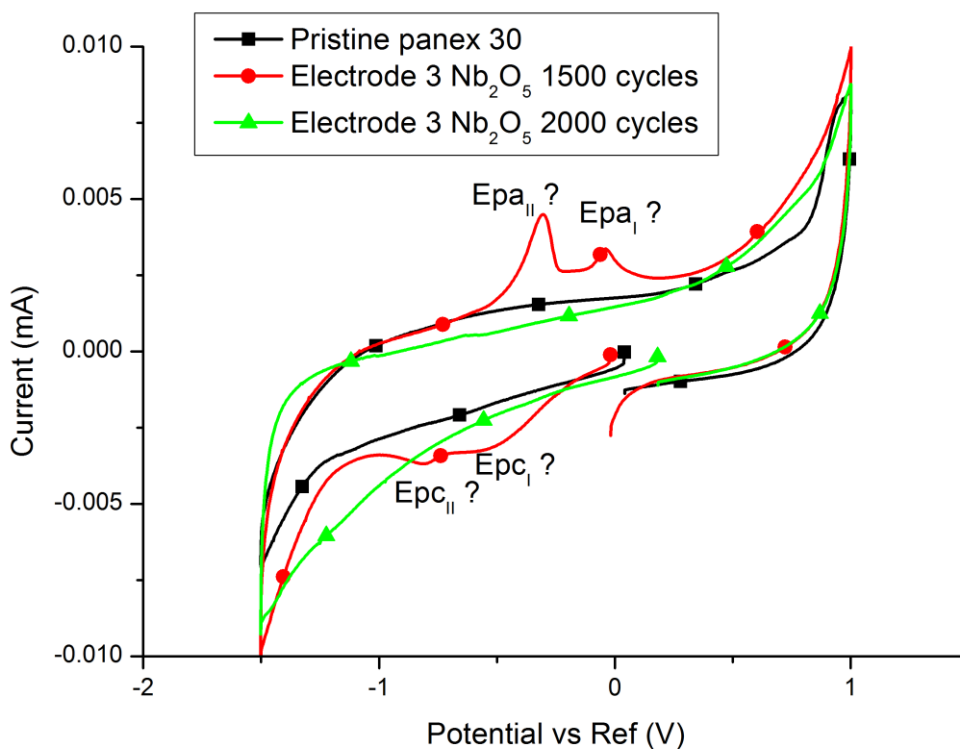


Figure V. 28: Cyclic voltammetry, recorded in 0.2 M LiClO₄ DMSO, Ar-purged, at 2 mV s⁻¹. Black line: pristine Panex 30, Red line: 1500 cycles and Green line: 2000 cycles.

As presented on Figure V.28, the electrode elaborated at 1500 cycles possess an electrochemical activity, which is absent for pristine Panex 30 and the sample elaborated at 2000 cycles. It is postulated that this electrochemical activity is linked to the activity of the deposit.

Concerning the sample elaborated at 2000 cycles, it may have either no deposit, or very thin deposit, that prevents major redox activity on the surface. The behavior of the same electrodes were then recorded in O₂-saturated electrolyte (by purging the electrolyte for at least 45 minutes, Figure V.29).

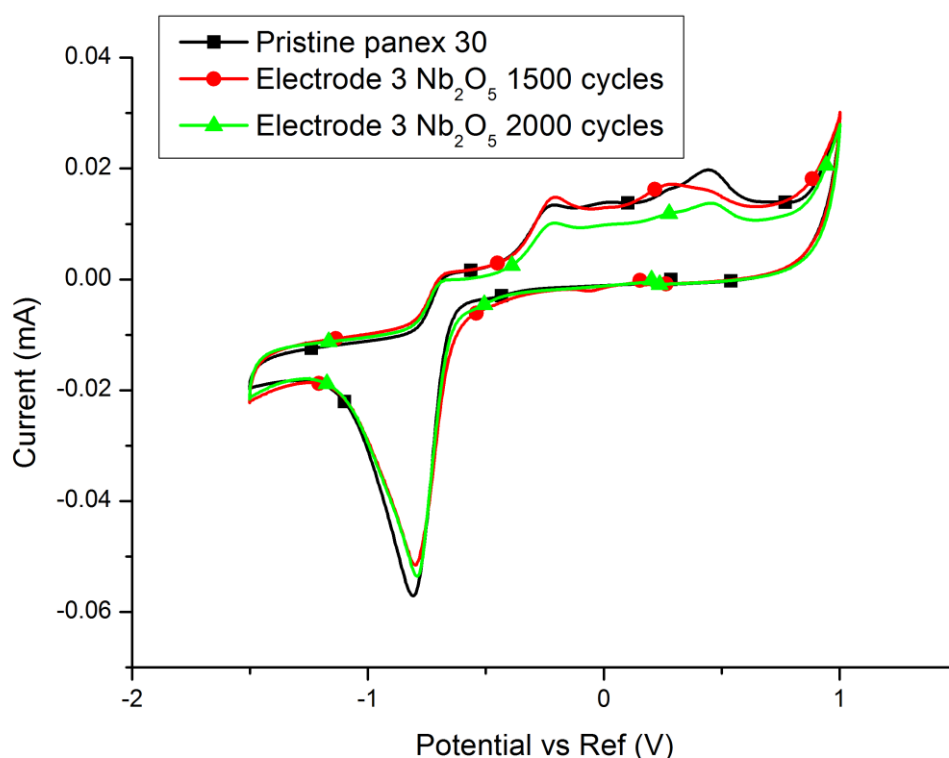


Figure V. 29: Cyclic voltammetry, recorded in 0.2 M LiClO₄ DMSO, O₂-saturated, at 2 mV s⁻¹. Black line: pristine Panex 30, Red line: 1500 cycles and Green line: 2000 cycles.

As depicted on Figure V.29, the presence of the deposit does neither impact the ORR nor the OER processes on the electrodes, as very similar features are observed for the three samples. This demonstrates that the presence of the Nb₂O₅ semi-conducting deposit on the surface of a conducting electrode does not affect the kinetics the reduction/oxidation of oxygen (at least on cyclic voltammetries). In order to better analyze the behavior of the deposits on a practical system, full cell experiments must be conducted on Nb₂O₅-protected Panex 30 and compared to the pristine material.

ii. Full cells

Full cells tests were conducted, in the same conditions of discharge and charge between the materials (see chapter two, experimental section). The comparison is made on the first cycle of the cell (for short term testing, not for long-term experiments, Figure V.30). Electrode 2 could not be used as cathode for this experiment, as the carbon duct-tape damaged the samples (and possibly contaminated them). Unused electrodes of each batch were selected as a consequence and for a better traceability, they will be labeled electrode 4.

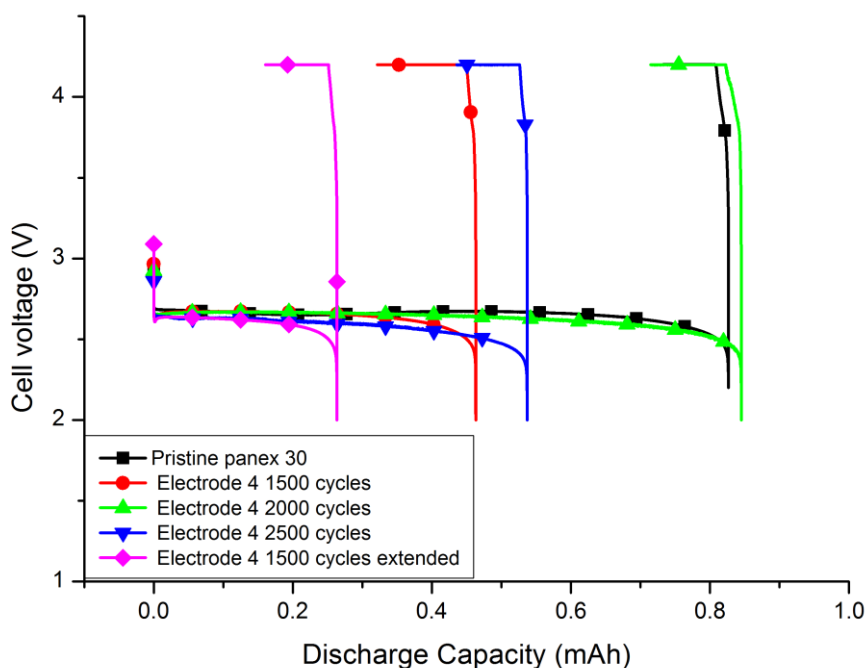


Figure V. 30: Full cell performances comparison between pristine Panex 30 and electrode 4 of each batch

As depicted on figure V.30 the electrochemical performances achieved are very different between each electrode. It is postulated that no deposit at all were formed on Electrode 4 2000 cycles, as it exhibits almost the same performances than pristine Panex 30.

As the performances of the other electrodes allow less discharge capacity than pristine Panex 30, it is postulated that the presence of the semiconducting deposit on the surface limits the capacity (as the transfer by tunneling effect is supposedly shut down quicker than without deposit), leading the sudden death of the cell [53]. As such, the thicknesses of the deposit order for the electrode 4 of each batch is supposed: 1500-Extended > 1500 > 2500 > 2000. This goes in line with the conclusions that the thickness are not uniform for each electrodes of the same batch. In addition, the presence of the deposit did not enhance the charging of the full cell, indicating that with such deposit in a practical full cell, the use of a redox shuttle is also (and may be all-the-more) mandatory. It is of high interest to compare the surface morphology of pristine electrodes (here electrode 2 of each batch), versus the discharged electrode (here electrodes 4 of each batch), by SEM. The images for the pristine electrodes are presented on Figure V.31.

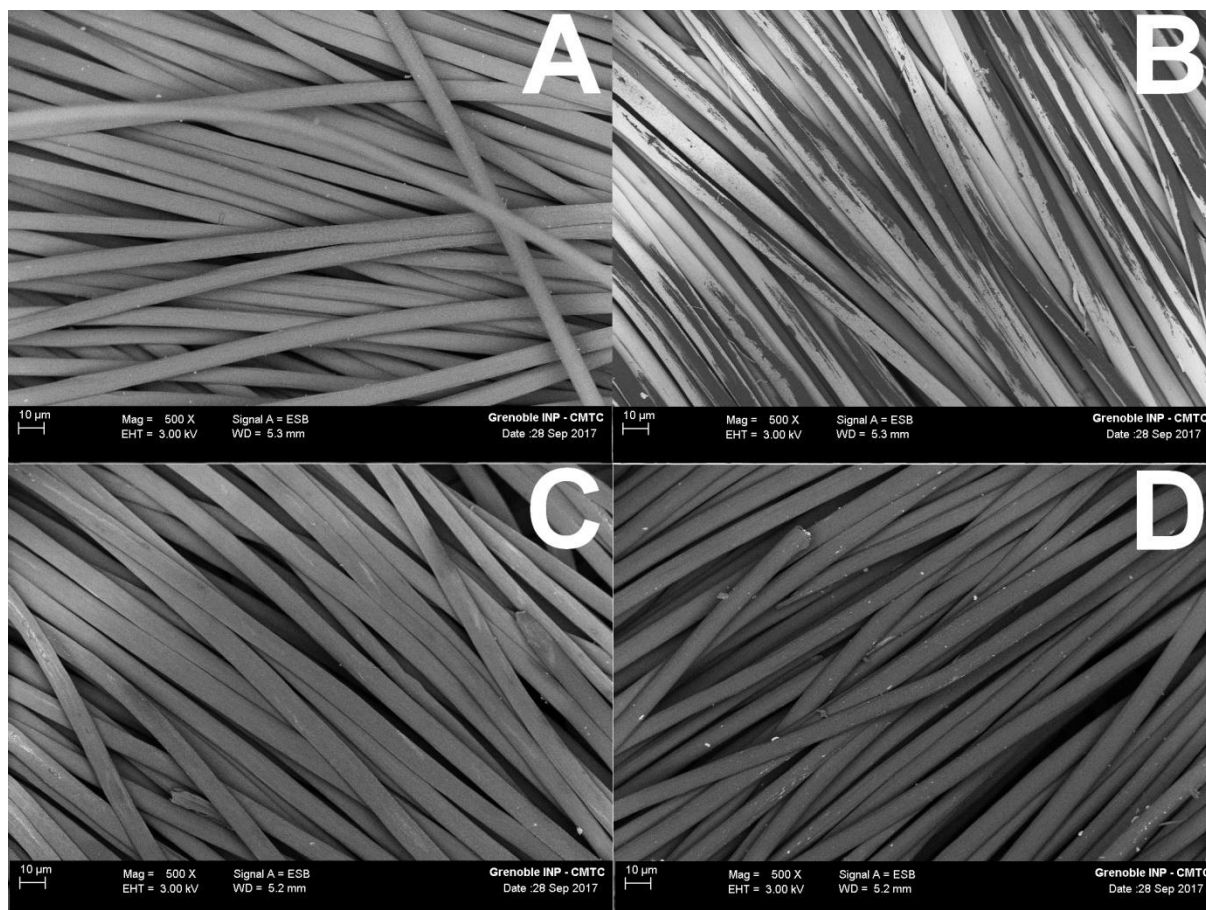


Figure V. 31: SEM images of Electrodes 2 of each batch, recorded with 3 kV energy and a magnification of 500X, using ESB detector. A-1500, B-2000, C-2500 and D-1500-Extended.

The ESB detector is of great use in our case, as heavier elements appear brighter on the images. In line with the X-EDS and XPS experiments, a thick (but damaged) deposit is observed for the electrode 2-2000. It is postulated that the deposit was damaged because of the manipulation of the electrode by the lab pliers, as the fibers, which are located beneath the surface seemed less damaged. The deposit on A and C on the other hand, are harder to spot, probably owing to the fact that they appeared thinner.

Post test SEM was also realized on electrodes 4 (electrodes used in the full cell tests), both with secondary electron (InLens detector), for the morphological analysis, and with back scattered electrons (ESB), in order to spot any chemical contrast. As a reminder, *post mortem* SEM pictures of Panex 30 (already presented in chapter three), are depicted on Figure V.32 to allow a better comparison between the pristine carbon cloth and the deposits. *Post test* SEM of electrodes 4 of each batch are also presented in Figures V.33-36.

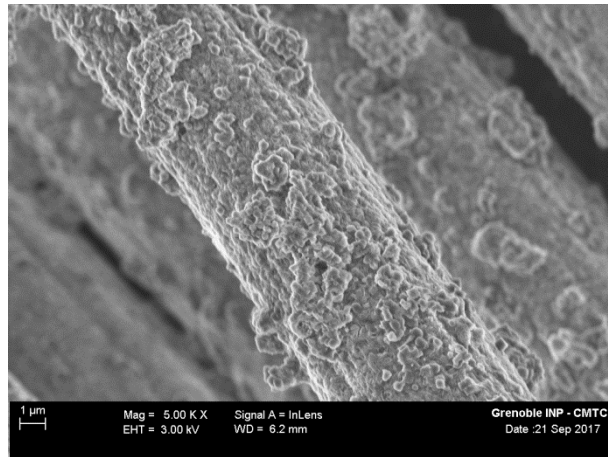


Figure V. 32: SEM image of a *post test* Panex 30 Electrode, taken with an energy of 3.0 kV and a magnification of 5.00 kX, Secondary Electrons detector.

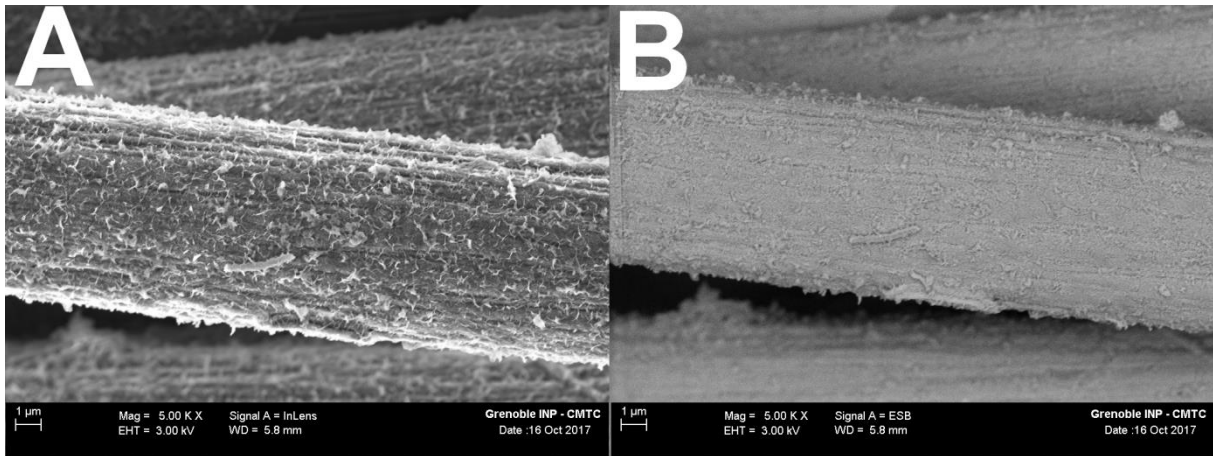


Figure V. 33: SEM image of *post test* Electrode 4-1500, taken with an energy of 3.0 kV and a magnification of 5.00 kX. A- Secondary Electrons detector. B- Back Scattered Electrons detector.

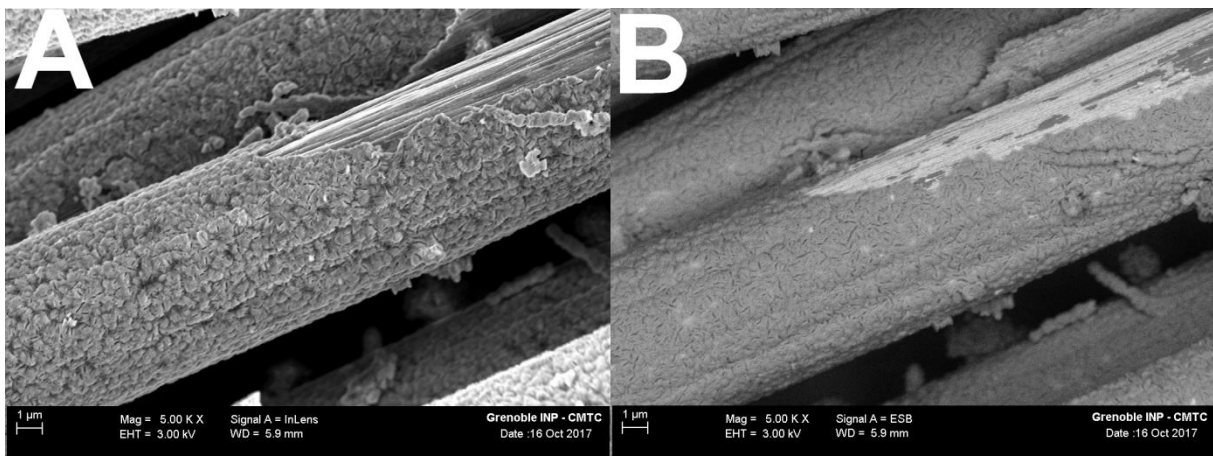


Figure V. 34: SEM image of *post test* Electrode 4-2000, taken with an energy of 3.0 kV and a magnification of 5.00 kX. A- Secondary Electrons detector. B- Back Scattered Electrons detector.

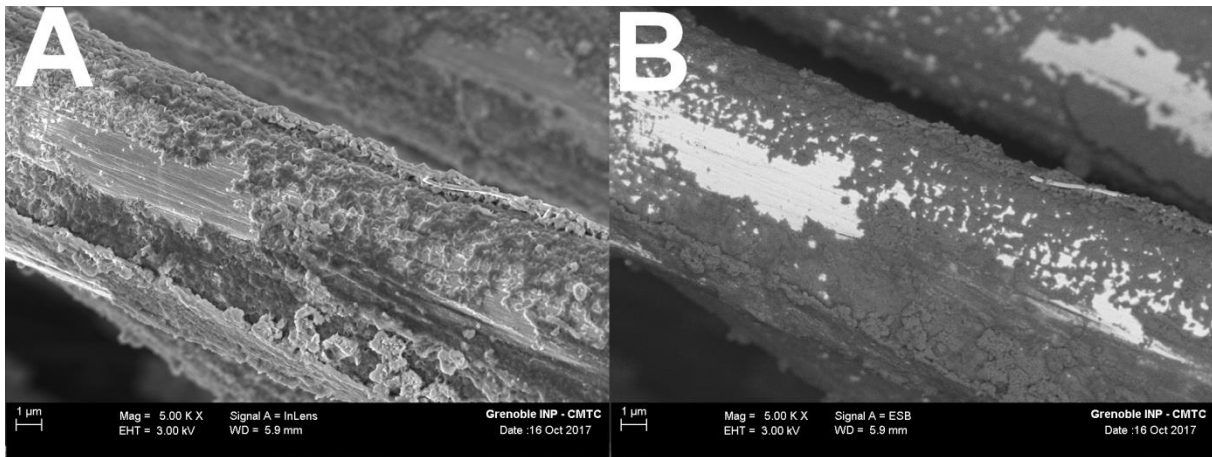


Figure V. 35: SEM image of *post test* Electrode 4-2500, taken with an energy of 3.0 kV and a magnification of 5.00 kX. A- Secondary Electrons detector. B- Back Scattered Electrons detector.

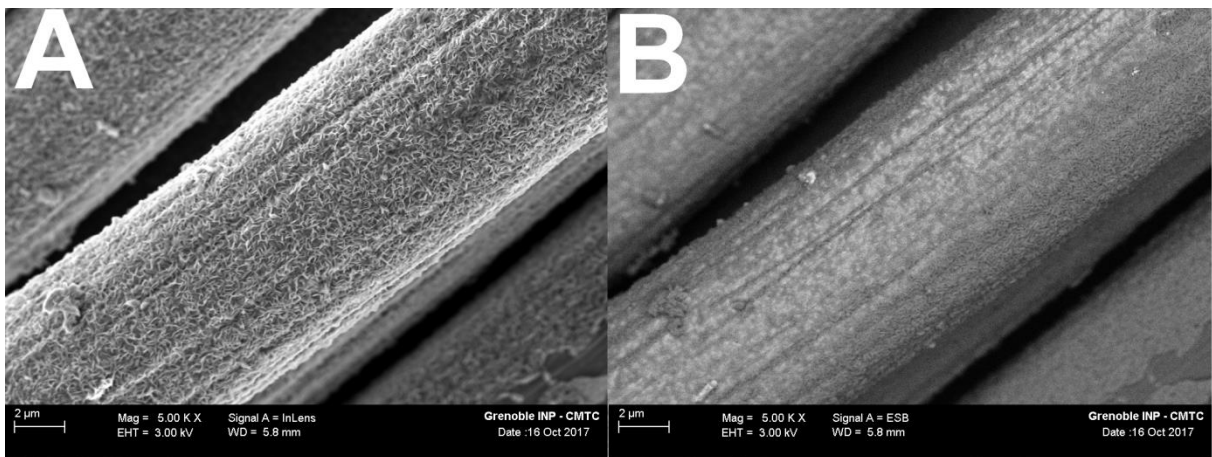


Figure V. 36: SEM image of *post test* Electrode 4-1500-Extended, taken with an energy of 3.0 kV and a magnification of 5.00kX. A- Secondary Electrons detector. B- Back Scattered Electrons detector

Figure V.33 confirms that no (or very little) niobium deposit is on the electrode 4-1500. However, for the other electrodes, important conclusions can be drawn. Firstly, the SEM pictures confirm the presence of a deposit for electrodes 4-2000, 4-2500 and 4-1500-Extended, as bright zones are observed with the ESB detector, which sign the presence of an heavier element (niobium). However, these results contrasts with the hypothesis that the electrode 4-2000 did not possess a niobium deposit (as it is observed in the SEM images). Secondly, the SEM images confirm that the formation of lithium peroxide is possible onto the surface of the Nb_2O_5 deposit, which is desired for the use of the latter in a practical system. Moreover, no Nb_2O_5 deposit is detected on the Electrode 4-1500 deposit, which exhibited a much lower discharge capacity than pristine Panex 30.

The X-EDS analysis of the post test electrodes was taken at the same time than the SEM images, and will give a better insight on the amount of deposit, for each batch (for Electrode 4!). This experiment is presented on Figure V.37.

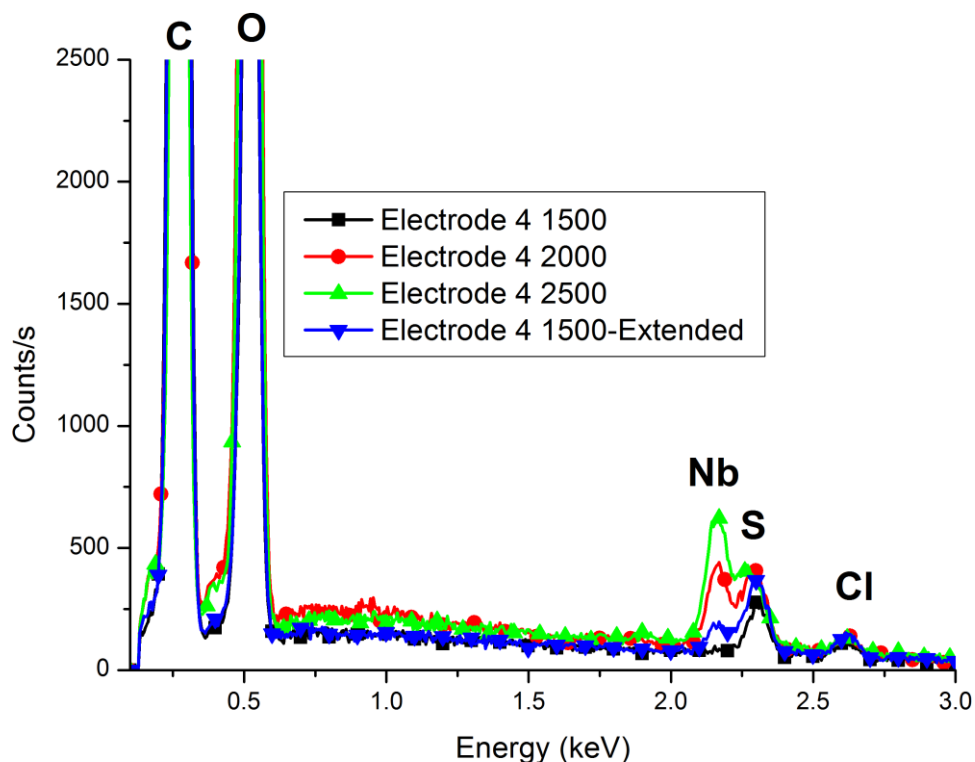


Figure V. 37: X-EDS spectra of the *post mortem* Electrodes 4. Black.-1500, Red-2000, Green-2500, Blue-1500-Extended, taken at 8.00 kV

X-EDS experiment shows a drastically different thickness order (than what was assumed from the full cell electrochemical behavior): 2500 > 2000 > 1500-Extended > 1500. As X-EDS is an elemental analysis, the latter scale is the correct one.

Consequently, no explanations can be proposed concerning the discharge capacity order (from the lowest to the highest: 1500-Extended > 1500 > 2500 > 2000), as it does not match the thicknesses of the deposits.

iii. DEMS experiments.

DEMS experiments were conducted on Electrodes 3 (the same than the for the three-electrode tests presented above). Linear scan voltammetries were conducted from the OCV to -1.5 V vs. Ref, followed by an OCV of five minutes (for signal stabilization). Then another linear scan voltammetry

was conducted from the OCV to 1 V vs. Ref. The DEMS signal was recorded in parallel of the current. The first experiment conducted is under argon purge, the O₂ DEMS signal being recorded (Figure V.38).

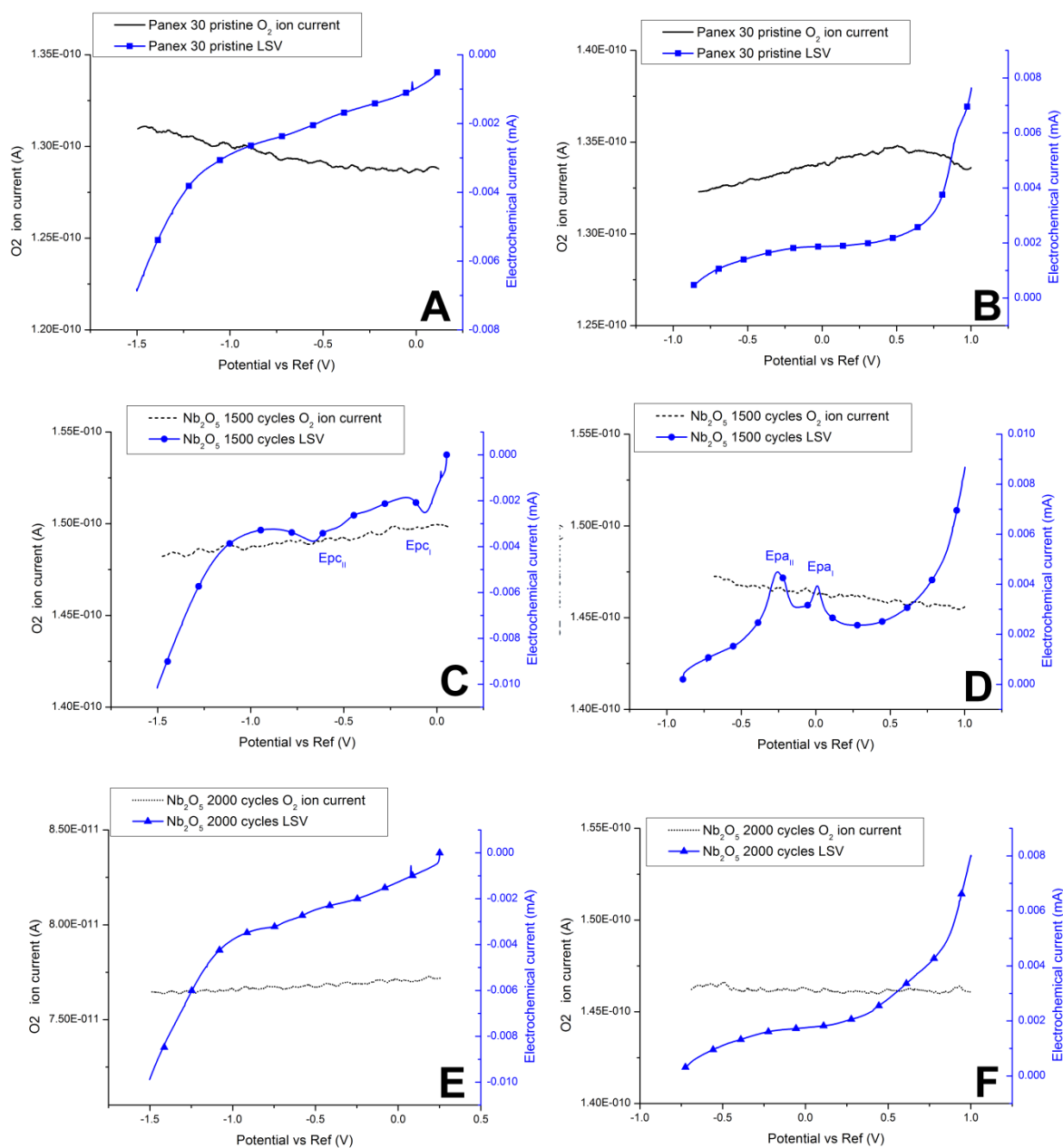


Figure V. 38: Y-primary axis: O₂ ion current (A). Y-Secondary axis: Electrochemical current (mA). Electrolyte 0.2 M LiClO₄ DMSO, Ar-purge. Scan rate 2 mV s⁻¹, for pristine Panex 30 (A and B). Electrode 4 1500 cycles (C and D). Electrode 4 2000 cycles (E and F).

The O₂ DEMS signal in Ar-purged electrolyte (Figure V.38) shows neither ORR nor OER for the three materials (Panex 30 pristine, Electrode 4-1500 and electrode 4-2000), as expected.

The redox activity of Electrode 4-1500, observed during the cyclic voltammtries (E_{pcI} and E_{pcII} ; E_{paI} and E_{paII}), is still observed on the electrochemical signal.

As the O_2 DEMS current is flat for both experiment, it is clear that those redox features are related to the activity of the deposit, and not to oxygen traces in the electrolyte.

In the same fashion, the CO_2 DEMS signal was recorded and is presented on Figure V.39.

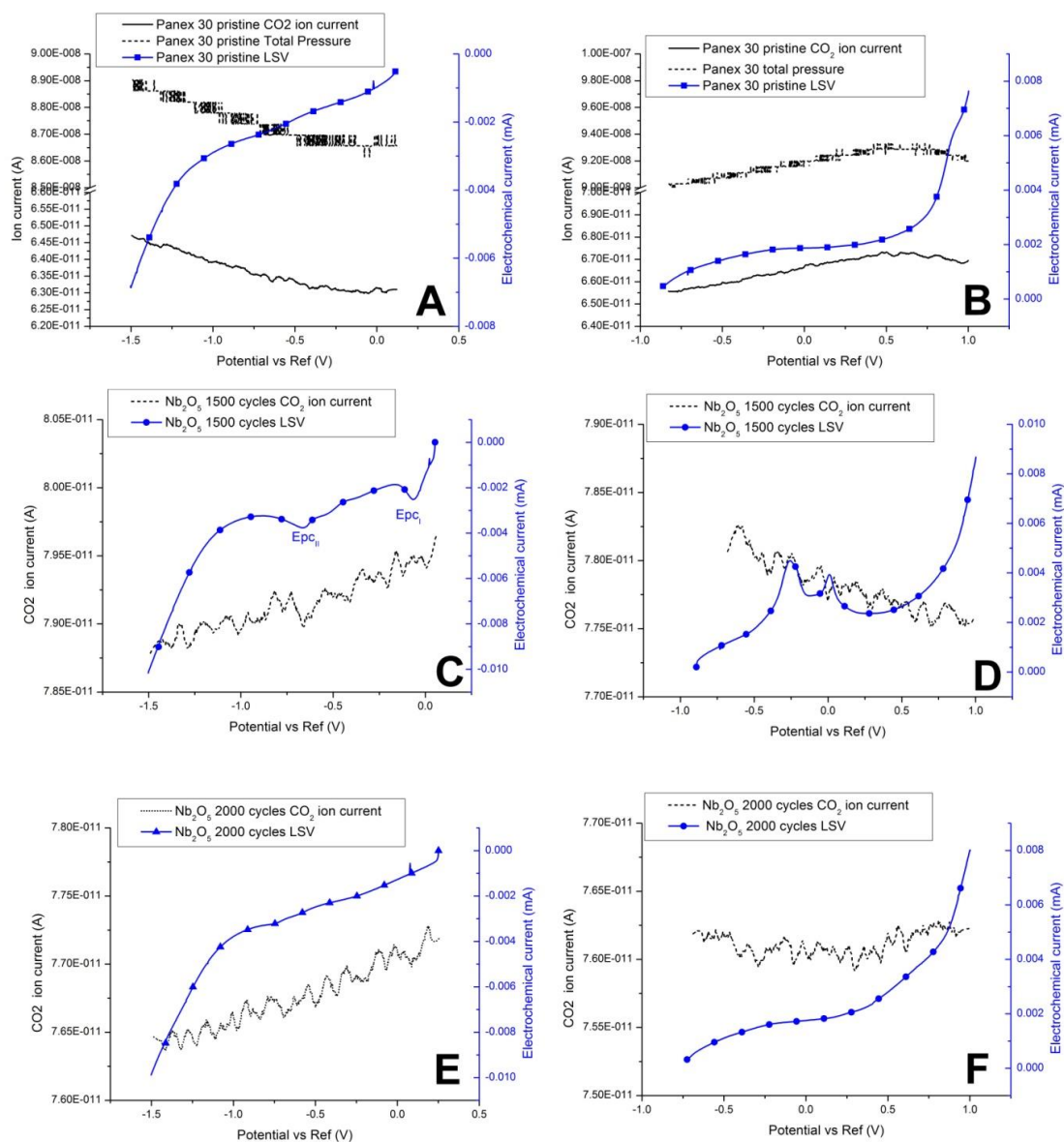


Figure V. 39: Y-primary axis: CO_2 ion current (A). Y-Secondary axis: Electrochemical current (mA). Electrolyte 0.2 M $LiClO_4$ DMSO, Ar-purge. Scan rate 2 mV s^{-1} , for pristine Panex 30 (A and B). Electrode 4 1500 cycles (C and D). Electrode 4 2000 cycles (E and F).

Concerning the CO₂ ion current, the signal obtained for the three materials is also flat, indicating no carbon corrosion in Ar-media. This results means that the presence of Nb₂O₅ does neither destabilize the carbon support, nor the electrolyte (at least in this potential domain).

One notes that the total pressure for the Panex 30 experiment (Figure V.39 A and B) varies like the CO₂ ion current (the same features are observed, but on Figure V.38 A and B), which means that this apparent variation of the CO₂ ion current is not linked to any detection of CO₂ but rather to variation of the baseline of the DEMS (variation of total pressure).

The DEMS experiment (O₂ ion current) in O₂-purged electrolyte is depicted on Figure V.40.

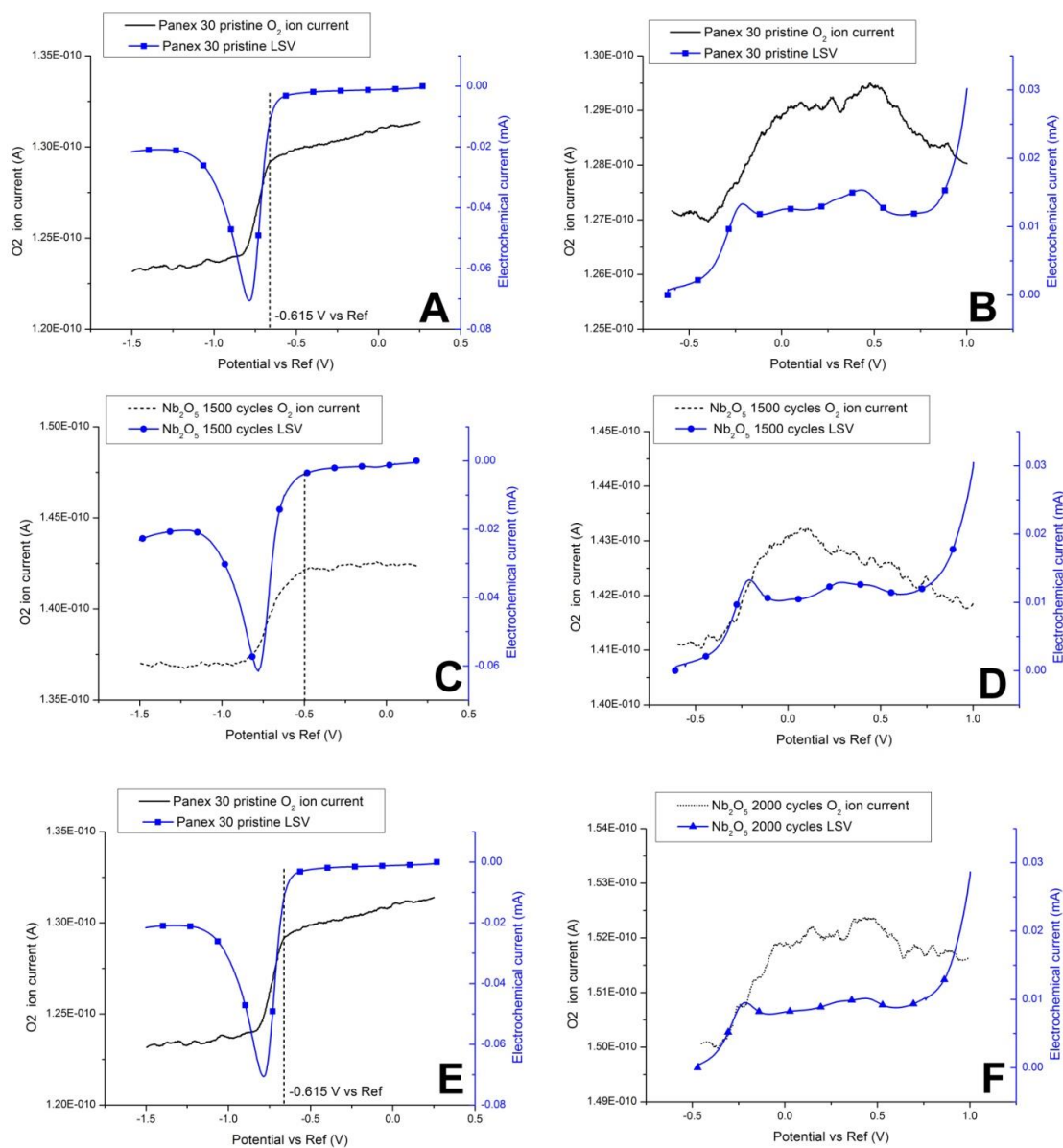


Figure V. 40: Y-primary axis: O₂ ion current (A). Y-Secondary axis: Electrochemical current (mA). Electrolyte 0.2 M LiClO₄ DMSO, O₂-purge. Scan rate 2 mV s⁻¹, for pristine Panex 30 (A and B). Electrode 4 1500 cycles (C and D). Electrode 4 2000 cycles (E and F).

The OER features of the three materials (Panex 30, Electrode 4-1500 and Electrode 4-2000) show almost the same behavior, both electrochemically and in terms of ion current. Once the onset of the OER (electrochemical) is reached, the O₂ current increases, which is the true sign of the oxidation of the lithium peroxide into oxygen [54, 55].

However, the behavior for the ORR is not the same for the three materials: the O₂ ion current decreases (O₂ consumption at the electrode), at -0.615 V vs. Ref for both Panex 30 and Electrode 4-2000, while it decreases around -0.5 V vs. Ref for the Electrode 4-1500.

This improvement is of 115 mV, which is non-negligible in a practical system. Interestingly, the electrochemical current occurs at the same time, for the three materials (-0.5 V vs. Ref), meaning that ORR current can be recorded for pristine Panex 30 and Electrode 4-1500, while no oxygen is consumed at the electrode.

These results contrast with what was observed at a reverse scan potential at lower values for Panex 30 (see chapter 3), where the ORR current was occurring exactly at the same potential than consumption of oxygen at the electrode.

Here, the only thing that was conducted before those LSV experiments under oxygen, was the full CV at 2 mV s⁻¹ (Figure V.29), but with a much higher reverse scan potential than in chapter three. An effect of the subsequent high potential might be responsible for the formation of oxygen adsorbates on the electrode surface, which prevent the formation of the latter at the onset potential.

Yet, this "explanation" is more an hypothesis, and the author acknowledges that this behavior is an "off" one. The same experiment, but this time with the recording of carbon dioxide is presented on Figure V.41.

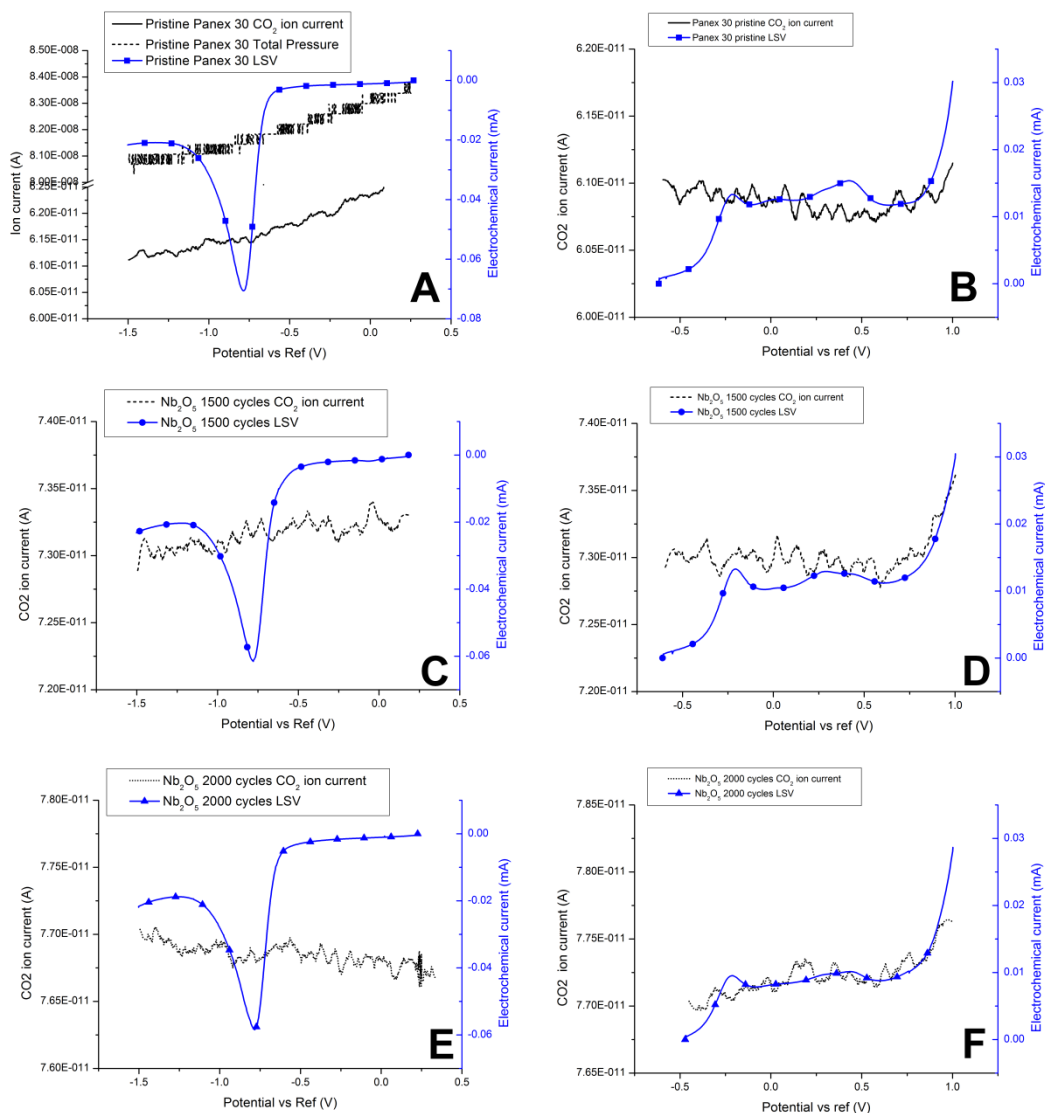


Figure V. 41: Y-primary axis: CO₂ ion current (A). Y-Secondary axis: Electrochemical current (mA). Electrolyte 0.2 M LiClO₄ DMSO, O₂-purge. Scan rate 2 mV s⁻¹, for pristine Panex 30 (A and B). Electrode 4 1500 cycles (C and D). Electrode 4 2000 cycles (E and F).

Important observations arise from Figure V.41. Firstly, even at very high potential (around 1 V vs. Ref), Panex 30 remains un-attacked, with no carbon dioxide evolution detected, which supports the results of chapter three. Sadly, carbon dioxide is detected, for an O₂-purged solution, for the samples Electrode 4-1500 and Electrode 4-2000, with an onset for the CO₂ evolution around 0.7 V vs. Ref. It can be seen that the thinner the Nb₂O₅ deposit, the lower the quantity of CO₂ evolution, which directly makes of the deposit the trigger of the CO₂ evolution. As niobium pentoxide does not comprise carbon in its structure, it is thus highly probable that it is the carbon fibers that get oxidized and consumed, the reaction being somewhat catalyzed by the Nb₂O₅ deposit. In particular, one may postulate that the niobium pentoxide catalyzes the reaction between the discharge product (Li₂O₂) and the carbon support, thus forming lithium carbonate (Li₂CO₃), the latter being oxidized at higher potential, and responsible for the CO₂ evolution [55].

Conclusion

Atomic Layer deposition of niobium pentoxide by two recipes (Plasma Enhanced Atomic Layer Deposition and Thermal Atomic Layer Deposition) were studied on silicon, with the aim to transfer this deposition for the protection of carbon cathodes. It was found that the product formed by Plasma Enhanced Atomic Layer Deposition was likely amorphous niobium pentoxide (Nb_2O_5), and that the product formed by Thermal Atomic Layer deposition was likely a mix between the latter product and niobium oxinitrides (NbO_xN_y). The deposition rate was much higher for plasma enhanced ALD than for thermal ALD. However, because the latter showed a much better conformal deposition on rough silicon substrates (silicon wells), it was used for the deposition on carbon cloth (Zoltek Panex 30), a 3D material. Firstly, the deposits made on the Panex 30 electrodes were not uniform in thickness, from one electrode to one other of the same batch, as measured from X-EDS. Secondly, in opposition with what was observed on silicon, the deposit onto the Panex 30 was only niobium pentoxide, showing a clear influence of the substrate on the nature (and thickness of the NbOx deposit). Finally, even though deposition was achievable and Nb_2O_5 covered Panex 30 could be tested in electrochemistry as positive electrodes for Li- O_2 systems, it was found that this deposit has a bad effect on the carbon cathode: in presence of Nb_2O_5 , the carbon cathode was highly unstable (although Panex 30 is very stable when used pristine). Lithium carbonate formation and carbon dioxide evolution (thus electrode consumption) were observed with the NbOx deposit, which probably catalyzes the decomposition of the carbon support, by the lithium peroxide. This, sadly is not something acceptable for a practical system, thus those deposits are not recommended for carbon protection. One can think that changing the chemistry of the deposit could still be a winning strategy.

So, the idea of using a deposit such as vanadium pentoxide [56, 57] might still be of interest, as those compound are known to intercalate lithium ions (in Li-ion positive electrodes), which will allow a better energy capacity than pristine carbon material, and their impact on the CO_2 evolution is not yet known. This material will be characterized in the next chapter for its use as positive electrode. Also, solutions will be proposed in the next chapter, for the use of Co-salen, in a real Li- O_2 full cell (with metallic lithium on the negative side).

References

1. Peng Z, Freunberger S a., Chen Y, Bruce PG (2012) A Reversible and Higher-Rate Li-O₂ Battery. *Science* (80-) 337:563–566. doi: 10.1126/science.1223985
2. Ottakam Thotiyil MM, Freunberger S a, Peng Z, et al (2013) A stable cathode for the aprotic Li-O₂ battery. *Nat Mater* 12:1050–6. doi: 10.1038/nmat3737
3. Weibin Z, Weidong W, Xueming W, et al (2013) The investigation of NbO₂ and Nb₂O₅ electronic structure by XPS, UPS and first principles methods. *Surf Interface Anal* 45:1206–1210. doi: 10.1002/sia.5253
4. Leskelä M, Ritala M (2003) Atomic Layer Deposition Chemistry: Recent Developments and Future Challenges. *Angew Chemie - Int Ed* 42:5548–5554. doi: 10.1002/anie.200301652
5. Johnson RW, Hultqvist A, Bent SF (2014) A brief review of atomic layer deposition: From fundamentals to applications. *Mater Today* 17:236–246. doi: 10.1016/j.mattod.2014.04.026
6. Sablier M, Bergmann E (2014) Depots sous vide par procedes plasma - Principes. *Tech. l'ingénieur* 33:
7. Suntola T (1992) Atomic layer epitaxy. *Thin Solid Films* 216:84–89. doi: 10.1016/0040-6090(92)90874-B
8. Schneider N, Deposition AL (2016) Atomic Layer Deposition (ALD) Atomic Layer Deposition (ALD) Principes généraux , matériaux. 33:
9. Knapas K, Rahtu A, Ritala M (2009) Etching of Nb₂O₅ thin films by NbCl₅. *Chem Vap Depos* 15:269–273. doi: 10.1002/cvde.200906795
10. Bechelany M, Bedjaoui M, Blanc-pelissier D, et al (2016) Evaluation thermodynamique des précurseurs ALD. *Principes Appl. la Tech. ALD*
11. Viet a Le, Reddy M V, Jose R, et al (2010) Nanostructured Nb₂O₅ Polymorphs by Electrospinning for Rechargeable Lithium Batteries. *J Phys Chem C* 114:664–671. doi: 10.1021/jp9088589
12. Blanquart T, Niinistö J, Heikkilä M, et al (2012) Evaluation and comparison of novel precursors for atomic layer deposition of Nb₂O₅ thin films. *Chem Mater* 24:975–980. doi:

10.1021/cm2026812

13. Kukli K, Ritala M, Leskelä M, Lappalainen R (1998) Niobium Oxide Thin Films Grown by Atomic Layer Epitaxy. *Chem Vap Depos* 4:29–34. doi: 10.1002/(SICI)1521-3862(199801)04:01<29::AID-CVDE29>3.3.CO;2-I
14. *Transactions ECS, Society TE* (2010) , Paola De Cecco. 33:101–110.
15. Knapas K, Rahtu A, Ritala M (2010) Reaction Mechanism Studies on Atomic Layer Deposition of Nb₂O₅ from Nb(OEt)₅ and Water. *Langmuir* 26:848–853. doi: 10.1021/la902289h
16. Anderson MD, Aitchison B, Johnson DC (2016) Corrosion Resistance of Atomic Layer Deposition-Generated Amorphous Thin Films. *ACS Appl Mater Interfaces* 8:30644–30648. doi: 10.1021/acsami.6b11231
17. Hoffeditz WL, Pellin MJ, Farha OK, Hupp JT (2017) Determining the Conduction Band-Edge Potential of Solar-Cell-Relevant Nb₂O₅ Fabricated by Atomic Layer Deposition. *Langmuir* acs.langmuir.7b00683. doi: 10.1021/acs.langmuir.7b00683
18. Jungsk G (1993) Possibilities and limitations of ellipsometry. *Thin Solid Films* 234:423–431.
19. Collins RW (2000) Ellipsometry in Analysis of Surfaces and Thin Films. *Encycl Anal Chem*. doi: 10.1002/9780470027318.a2507
20. Konuma H (1983) Rate of Carbon Contamination on Copper , Iron and Aluminum Targets in Gas Flows by an Electron Microprobe. 99–108.
21. Ferraz NP, Marcos FCF, Nogueira AE, et al (2017) Hexagonal-Nb₂O₅ /Anatase-TiO₂ mixtures and their applications in the removal of Methylene Blue dye under various conditions. *Mater Chem Phys* 198:331–340. doi: 10.1016/j.matchemphys.2017.06.029
22. Sahu KR, De U (2014) Role of Nb₂O₅ phase in the formation of piezoelectric PbNb₂O₆. *Thermochim Acta* 589:25–30. doi: 10.1016/j.tca.2014.05.008
23. Shao R, Cao Z, Xiao Y, et al (2014) Enhancing photocatalytic activity by tuning the ratio of hexagonal and orthorhombic phase Nb₂O₅ hollow fibers. *RSC Adv* 4:26447. doi: 10.1039/c4ra02038c
24. Moulder JF, Stickle WF, Sobol PE, Bomben KD (1992) *Handbook of X-ray Photoelectron Spectroscopy*. doi: 10.1002/sia.740030412

25. Mcguire GE, Schweitzer GK, Carlson TA (1973) Study of Core Electron Binding Energies in Some Group IIIa, Vb, and VIb Compounds. *Inorg Chem* 12:2450–2453. doi: 10.1021/ic50128a045
26. Pollak R a, Stolz HJ, Raider SI, Marks RF (1983) Chemical Composition and Interface Chemistry of Very Thin Nb₂O₅ Films Prepared by rf Plasma Oxidation. *J Vac Technol* 20:185–192. doi: 10.1007/BF00656840
27. Damyanova S, Dimitrov L, Petrov L, Grange P (2003) Effect of niobium on the surface properties of Nb₂O₅-SiO₂-supported Mo catalysts. *Appl Surf Sci* 214:68–74. doi: 10.1016/S0169-4332(03)00347-7
28. Romero R, Ramos-Barrado JR, Martin F, Leinen D (2004) Nb₂O₅ thin films obtained by chemical spray pyrolysis. *Surf Interface Anal* 36:888–891. doi: 10.1002/sia.1793
29. Yue Z, Chu D, Huang H, et al (2015) A novel heterogeneous hybrid by incorporation of Nb₂O₅ microspheres and reduced graphene oxide for photocatalytic H₂ evolution under visible light irradiation. *RSC Adv* 5:47117–47124. doi: 10.1039/C5RA05348J
30. Destro FB, Cilense M, Nascimento MP, et al (2016) Corrosion behaviour of polycrystalline Nb₂O₅ thin films and its size effects. *Prot Met Phys Chem Surfaces* 52:104–110. doi: 10.1134/S2070205116010081
31. Kościelska B, Winiarski A (2008) Structural investigations of nitrated Nb₂O₅ and Nb₂O₅-SiO₂ sol-gel derived films. *J Non Cryst Solids* 354:4349–4353. doi: 10.1016/j.jnoncrysol.2008.06.049
32. Alfonso JE, Buitrago J, Torres J, et al (2010) Influence of fabrication parameters on crystallization, microstructure, and surface composition of NbN thin films deposited by rf magnetron sputtering. *J Mater Sci* 45:5528–5533. doi: 10.1007/s10853-010-4612-3
33. Jouve G, Séverac C, Cantacuzène S (1996) XPS study of NbN and (NbTi)N superconducting coatings. *Thin Solid Films* 287:146–153. doi: 10.1016/S0040-6090(96)08776-7
34. Ermolieff A, Girard M, Raoul C, et al (1985) An XPS comparative study on thermal oxide barrier formation on Nb and NbN thin films. *Appl Surf Sci* 21:65–79. doi: 10.1016/0378-5963(85)90008-X
35. Martin P, Netterfield R, Kinder T, Bendavid a (1992) Optical properties and stress of ion-assisted aluminum nitride thin films. *Appl Opt* 31:6734–6740. doi: 10.1364/AO.31.006734

36. Galtayries A, Sporken R, Riga J, et al (1998) XPS comparative study of ceria/zirconia mixed oxides: powders and thin film characterisation. *J Electron Spectros Relat Phenomena* 88–91:951–956. doi: 10.1016/S0368-2048(97)00134-5
37. Beccaria AM, Poggi G, Castello G (1995) Influence of passive film composition and sea water pressure on resistance to localised corrosion of some stainless steels in sea water. *Br Corros J* 30:283–287. doi: 10.1179/000705995798113709
38. Peng H (2014) Composition chimique et nanostructure des films passifs formés sur acier inoxydable austénitique : effet du molybdène. Université Pierre et Marie Curie
39. Massih AR, Perez RJ (2006) Thermodynamic evaluation of Nb-O system. *Quantum Technol AB* 31. doi: PM 05-002 v2
40. Okazaki Y, Tateishi T, Ito Y (1997) Corrosion Resistance of Implant Alloys in Pseudo Physiological Solution and Role of Alloying Elements in Passive Films. *Mater Trans* 38:78–84.
41. Jouan PY, Peignon MC, Cardinaud C, Lemperiere G (1993) Characterisation of TiN coatings and of the TiN/Si interface by X-ray photoelectron spectroscopy and Auger electron spectroscopy. *Appl Surf Sci* 68:595–603. doi: 10.1016/0169-4332(93)90241-3
42. Estrade-szwarckopf H, Rousseau B, Herlod C, Lagrange P (1998) Sodium - Oxygen Graphite Intercalation Compound: XPS, UPS and STM Study. *Mol Cryst Liq Cryst Sci Technol Sect A Mol Cryst Liq Cryst* 310:231–236. doi: 10.1080/10587259808045341
43. Gardner SD, Singamsetty CSK, Booth GL, et al (1995) Surface characterization of carbon fibers using angle-resolved XPS and ISS. *Carbon N Y* 33:587–595. doi: 10.1016/0008-6223(94)00144-O
44. Liao HM (1993) Surface composition of AlN powders studied by x-ray photoelectron spectroscopy and bremsstrahlung-excited Auger electron spectroscopy. *J Vac Sci Technol A Vacuum, Surfaces, Film* 11:2681. doi: 10.1116/1.578626
45. Goldberg MJ, Clabes JG, Kovac CA (1988) Metal-polymer chemistry. II. Chromium-polyimide interface reactions and related organometallic chemistry. *J Vac Sci Technol A Vacuum, Surfaces, Film* 6:991–996. doi: 10.1116/1.575006
46. Sadough Vanini A, Audouard J-P, Marcus P (1994) The role of nitrogen in the passivity of austenitic stainless steels. *Corros Sci* 36:1825–1834. doi: 10.1016/0010-938X(94)90021-3

47. Profijt HB, Potts SE, van de Sanden MCM, Kessels WMM (2011) Plasma-Assisted Atomic Layer Deposition: Basics, Opportunities, and Challenges. *J Vac Sci Technol A Vacuum, Surfaces, Film* 29:50801. doi: 10.1116/1.3609974
48. Jin S, Atrens A (1987) ESCA-studies of the structure and composition of the passive film formed on stainless steels by various immersion times in 0.1 M NaCl solution. *Appl Phys A Solids Surfaces* 42:149–165. doi: 10.1007/BF00616726
49. Moulder JF, Hammond JS, Smith KL (1986) Using angle resolved ESCA to characterize Winchester disks. *Appl Surf Sci* 25:446–454. doi: 10.1016/0169-4332(86)90087-5
50. Brion D (1980) Etude par spectroscopie de photoelectrons de la degradation superficielle de FeS₂, CuFeS₂, ZnS et PbS a l'air et dans l'eau. *Appl Surf Sci* 5:133–152. doi: 10.1016/0378-5963(80)90148-8
51. Barr TL (1978) An ESCA study of the termination of the passivation of elemental metals. *J Phys Chem* 82:1801–1810. doi: 10.1021/j100505a006
52. Kim KS, Davis RE (1972) Electron spectroscopy of the nickel-oxygen system. *J Electron Spectros Relat Phenomena* 1:251–258. doi: 10.1016/0368-2048(72)85014-X
53. Viswanathan V, Thygesen KS, Hummelshj JS, et al (2011) Electrical conductivity in Li₂O₂ and its role in determining capacity limitations in non-aqueous Li-O₂ batteries. *J Chem Phys* 135:0–10. doi: 10.1063/1.3663385
54. Luntz AC, Mccloskey BD (2014) Nonaqueous Li – Air Batteries : A Status Report. *Chem Rev* 114:11721–11750. doi: 10.1021/cr500054y
55. McCloskey BD, Speidel A, Scheffler R, et al (2012) Twin problems of interfacial carbonate formation in nonaqueous Li-O₂ batteries. *J Phys Chem Lett* 3:997–1001. doi: 10.1021/jz300243r
56. Aravindan V, Gnanaraj J, Lee YS, Madhavi S (2014) Insertion-type electrodes for nonaqueous Li-ion capacitors. *Chem Rev* 114:11619–11635. doi: 10.1021/cr5000915
57. Fu R, Ma Z, Zheng JP, et al (2003) High-Resolution ⁷Li Solid-State NMR Study of Li_xV₂O₅ Cathode Electrodes for Li-Rechargeable Batteries. *J Phys Chem B* 5:9730–9735. doi: 10.1021/jp0305077

Chapter VI:

Perspectives for a stable Li-O₂ positive electrode, with high recharge ability

Somewhere, something incredible is waiting to be known

- Carl Sagan

The previous chapters of this work unraveled important issues linked with the positive electrode of Li-O₂ batteries, owing mainly to both the reactivity and electrically-insulating properties of the (ORR) discharge product, lithium peroxide. We nevertheless managed to address the latter aspect by selecting an appropriate redox shuttle, which enables to enhance both the Oxygen Reduction Reaction (ORR) and the Oxygen Evolution Reaction (OER). As such, the problem of the rechargeability of the thick deposit shall be mitigated, for a practical system. Concerning the former aspect however, the previous chapter showed that protecting carbon by Niobium Pentoxide (Nb₂O₅) was insufficient; even worse, CO₂ evolved in the presence of the deposit (which implies reactivity between the carbon support, and the discharge product) whereas no carbon dioxide was evolved without deposit. As such, it is probable that Nb₂O₅ catalyzes the formation of lithium carbonate, which urges the need to find another candidate for carbon protection. A deposition of Vanadium Pentoxide (V₂O₅) on carbon was thus realized, and tested, in association with the redox shuttle in full cell setup.

I. Replacement of Nb₂O₅ by V₂O₅

Vanadium pentoxide was deposited in an lab-made Atomic Layer Deposition Reactor, with heating, supplied by hot-walls (equipment described in the literature [1–4]). This reactor was used instead of the previous one used for Nb₂O₅, because no Vanadium line was available on the Picosun™ R200-Advanced. The deposit was conducted directly onto a $\varnothing = 50$ mm Panex 30 carbon cloth, using vanadium(V)-tri-*i*-propoxy oxide as the precursor (Strem Chemicals). The ALD cycle differed a bit from the recipe used for the deposition of Nb₂O₅ (see chapter five), as an exposure time of 10 seconds was applied both after the pulse of the precursor and after the pulse of the oxidant (to leave sufficient time for both species to diffuse in and on the sample and to react properly). As such, the pulse of the vanadium precursor was set on four seconds, and the pulse of the oxidant (N₂O) was set on five seconds. The purge time for both reactants was set on twenty seconds. Lastly, the temperature of the deposition was set at 175°C, and 1500 ALD cycles were conducted. After the deposition, the deposit appeared very thick as colors could be spotted onto the substrate. In order to possess an electrode of the same diameter than the ones used in the rest of the present work, 8 mm disk electrodes were cut out of the V₂O₅-coated Panex 30 carbon cloth.

a. Morphology/ thickness

SEM image an electrode, taken at center of the sample and “cleaved” for the observation of the deposit thickness is presented on Figure VI.1.

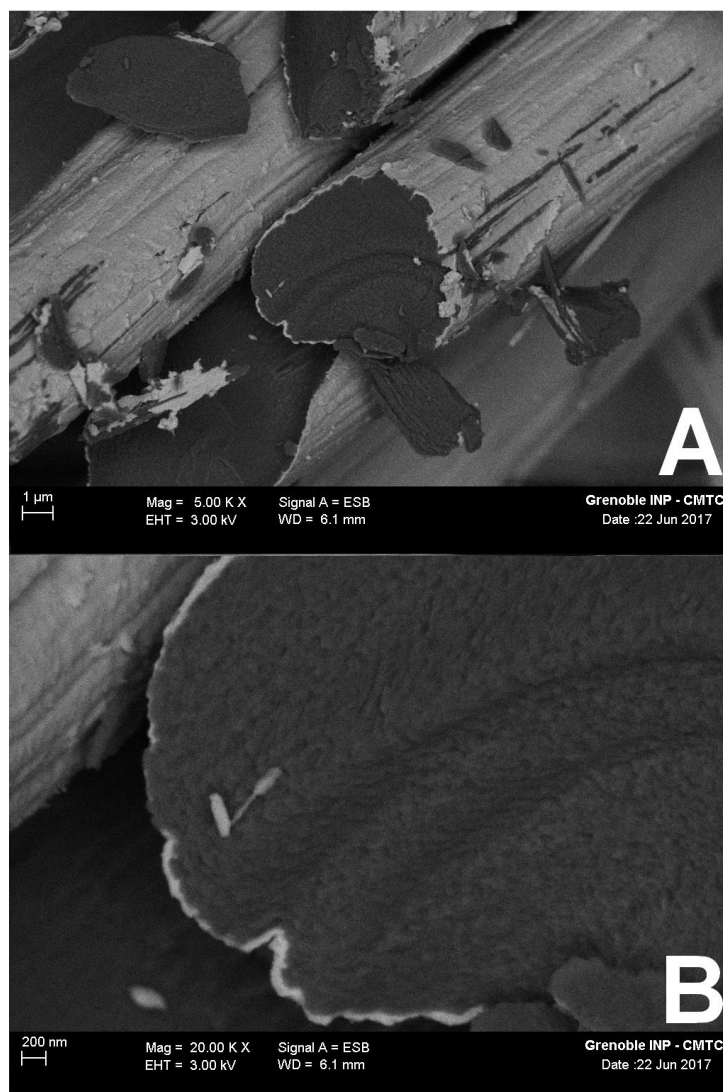


Figure VI. 1: SEM image of the deposit, taken at an energy of 3.00 kV, using a back-scattered electron detector and a magnification of 5.00 kX (A) and 20.00 KX (B).

The SEM image of Figure VI.1 clearly shows the V_2O_5 deposit, as a white layer is observed onto the carbon (heavier elements appear brighter on the ESB images). Also, as expected, the deposit is very thick (with thickness in the range of 100 nm observed), and even though the latter seems to cover entirely the fibers, the thickness does not appear to be of the same value on different zones of the fibers (Figure VI.1-B). The same amount of cycles were performed than for Nb_2O_5 , but apparently, the deposition processes of V_2O_5 are easier on carbon than for Nb_2O_5 . In order to have an insight into the chemistry composition of the vanadium deposit, XPS was realized.

b. Composition

Figure VI.2 presents the XPS characterizations of the sample.

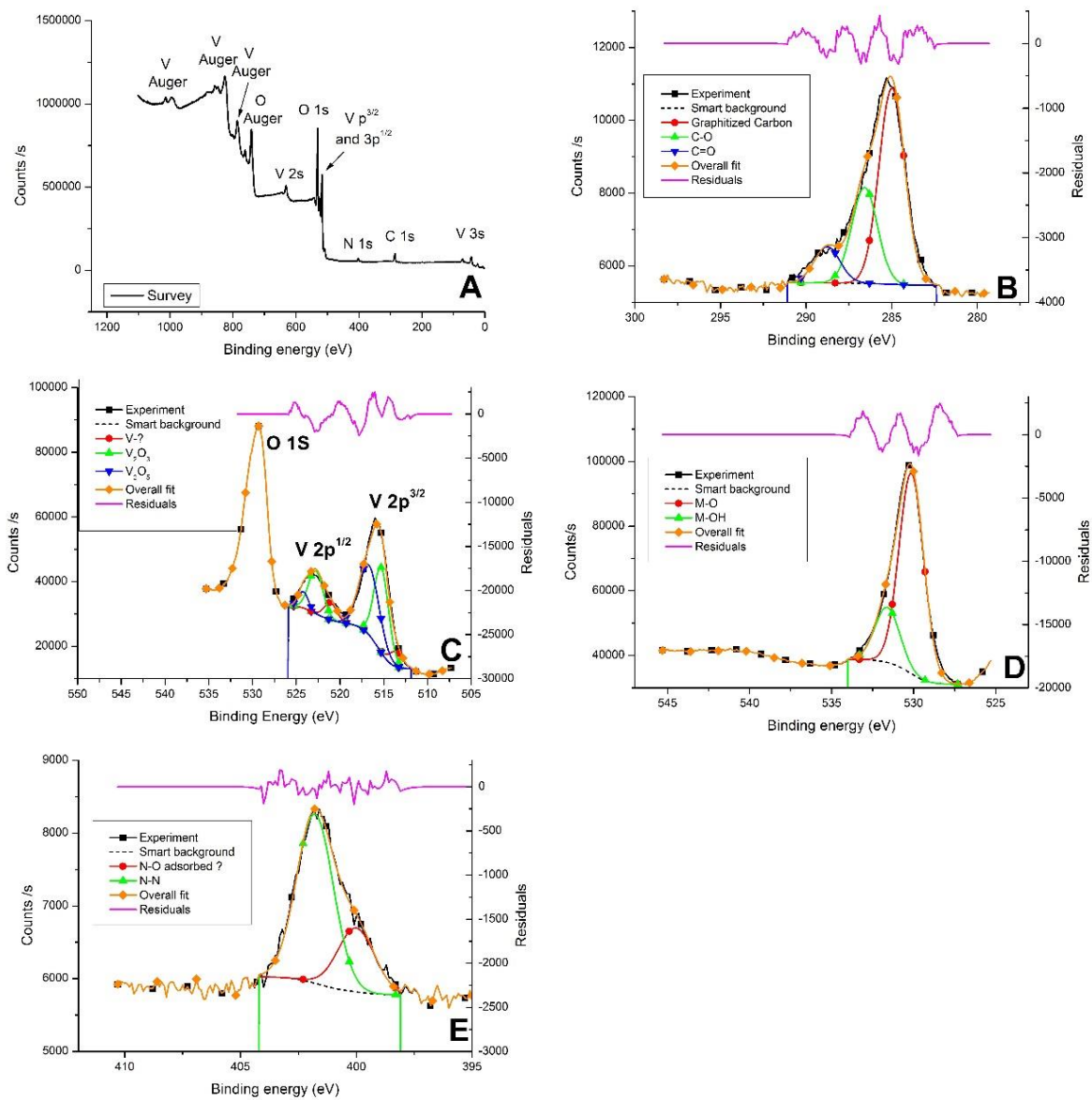


Figure VI. 2: XPS characterization of the V_2O_5 deposit. (A) global spectrum, and contributions of (B) C1s, (C) O1s and V2p, (D) O1s and (E) N1s.

Figure VI.2-A clearly shows that vanadium is detected, along with oxygen, carbon and nitrogen. As for the niobium-based samples, the C1s peak (un-convoluted) is centered at 285 eV (Figure VI.2-B). Surprisingly, this time, the graphite component of the Panex 30 carbon cloth is detected at the correct binding energy (284.6 eV) [5, 6].

No C-H contribution (or maybe comprised in the C1s graphitized peak) are detected. However, the C-O and C=O contributions of contamination-carbon are indeed detected at respectively 286.4 a 289 eV [5].

The Vanadium $2p^{3/2}$ and $2p^{1/2}$ peaks (Figure VI.3) are composed of three contributions, indicating possibly three different phases in the deposit. As the $2p^{3/2}$ and $2p^{1/2}$ are distant from 2.7 eV [5], the determination of the nature of each contribution can be conducted on the $2p^{3/2}$ peak only. The First contribution (513.5 eV) could not be identified, as at this energy shift, it could be either metallic vanadium, VB_2 or a vanadium metallocene [5], vanadium nitrides being normally observed at higher energies (514.1 eV).

As the precursor of vanadium used was in (+V) state, and as no boron is comprised in the process, no reasonable explanation could explain the presence of a contribution for the presence of VB_2 , which is therefore ruled out. The same applies to vanadium nitrides, because the shift of binding energy between the experiment and the expected shift cannot be explained. The second contribution, however is observable at 515.4 eV and could be the contribution of V_2O_3 (energy shift located at 515.5 ± 0.3 eV) [7–10].

The third contribution, located at 516.5 eV, is probably accounted for vanadium pentoxide (V_2O_5), with an energy shift measured at 516.5 eV [10–12].

Considering the O1s peak (figure VI.2-D), two contributions are observed. The first contribution is linked to the metal-oxide bonding and is located at 529.7 eV, and is coherent with the binding between the oxygen and vanadium (literature: 529.7 ± 0.1 eV) [5, 10, 12]. The second contribution, is measured at 531.5 eV and is perfectly matching the value of hydroxides [5, 13–16].

Concerning the N1s peak, two contributions are detected (figure VI.2-E). The first at 400 eV could be similar to what was observed for the niobium pentoxide deposition on silicon (broad peak corresponding to oxynitrides located in the 399-400 eV region) [17–20]. The second contribution (402 eV) is linked to adsorbed nitrogen species on the sample surface [5]. Thus, the small contribution that was observed on the V $p^{3/2}$ peak at 513.5 eV is probably linked with oxynitrides.

These data are compatible with a deposit composition consisting of a mix of different species, V_2O_3 and V_2O_5 being the most dominant chemistries of the deposit (with as small proportion of what appear to be vanadium oxynitrides).

The presence of V_2O_3 in the deposit is hardly explained, as the vanadium is introduced in the reactor in the (+V) state, and placed in contact with an oxidant (not a reducer).

The authors cannot rule out that the Panex 30 carbon itself has acted as a reducer in the conditions of the deposit, but more work would be needed in order to assert so.

In order to confirm the chemical composition of the deposit, other techniques of identifications must be used in parallel (for instance U-V Photoelectron Spectroscopy). The latter analysis is pointless in our case, as the aim is rather to have a deposit with the good electrochemical performances (and an idea of the nature of the deposit), than a precise identification of the compound deposited. These deposits were then tested in terms of electrochemical activity.

c. *Electrochemical behavior*

The electrochemical behavior of the deposit was evaluated by DEMS, associated with cyclic voltammetry, conducted at 5 mV s^{-1} .

The electrochemical response of the deposit was first compared in argon-purged medium, oxygen-purged medium and in oxygen-purged medium in presence of 1.75 mM of Co salen (Figure VI.3).

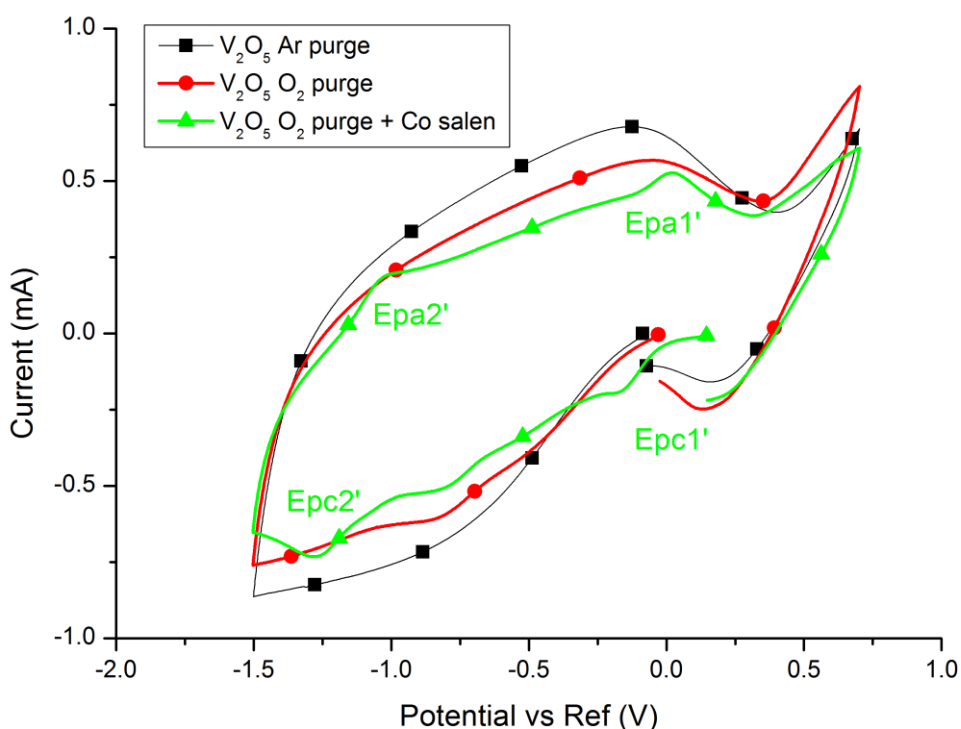


Figure VI. 3: Electrochemical behavior of the V_2O_5 deposit, scan rate 5 mV s^{-1} , in Ar-purged (black), O_2 -purged (red), and O_2 -purged + Co salen (green) electrolyte.

As depicted on Figure VI.3, the electrochemical response is almost the same in Ar-purged and O_2 -purged media. This might be linked with the important thickness of the V_2O_5 deposit, that generates a high double layer current that essentially masks the electrochemical features of the faradaic ORR and OER. However, the impact of the Co-salen can be observed, when added in the electrolyte (the $E_{pa1'}/E_{pc1'}$ and $E_{pa2'}/E_{pc2'}$ features are observed). In order to ensure that the contribution seen on the voltamperometric traces is (or not) linked only to the double layer effect, the DEMS signal of oxygen has also been monitored in the three cases (the oxygen DMES signal being expected flat if only double layer current is involved). In order to detect any decomposition of the deposit (in a similar fashion than Nb_2O_5), the carbon dioxide DEMS signal is also monitored (Figure VI.4).

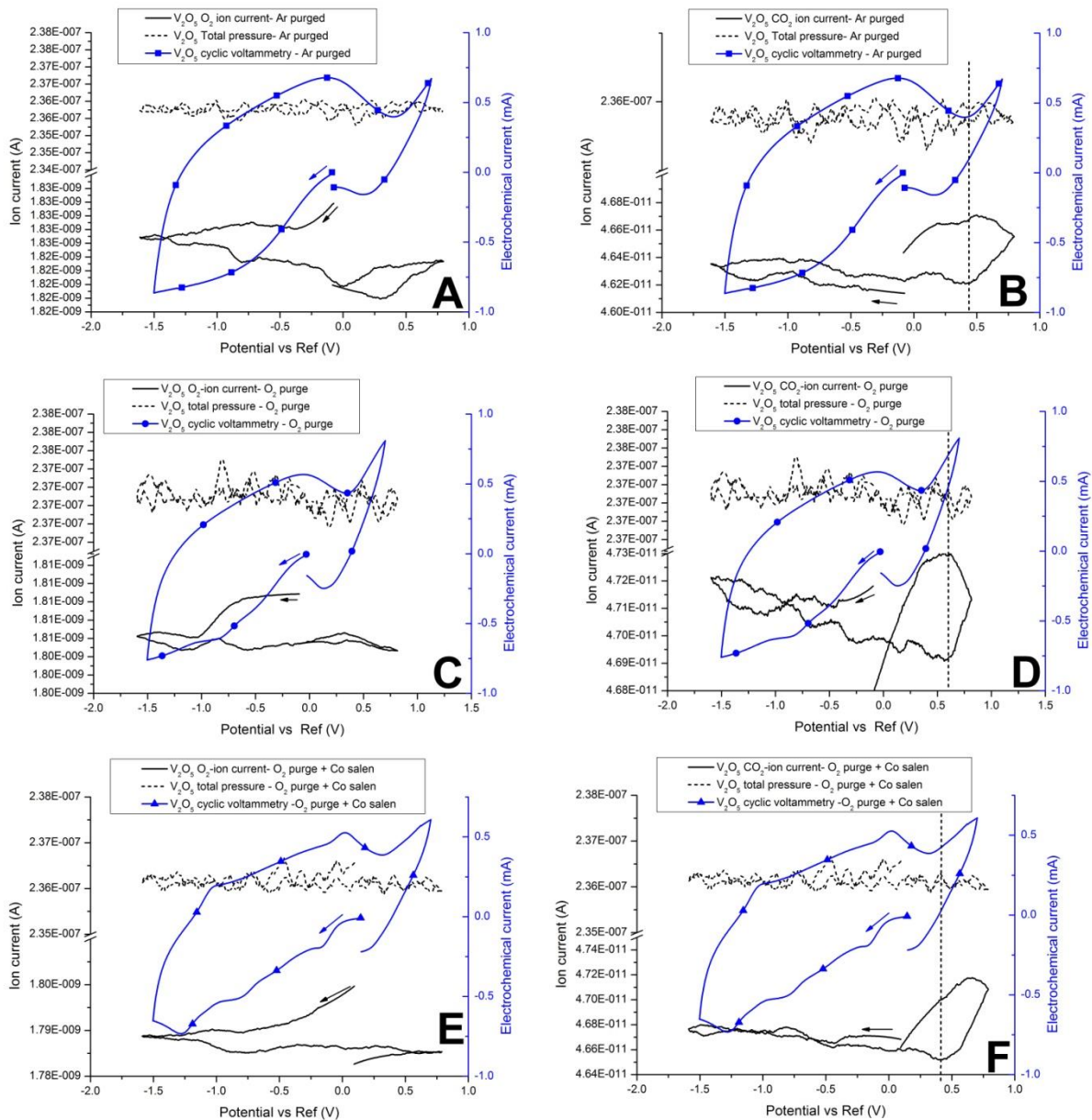


Figure VI. 4: O₂ DEMS signal for A, C and E; CO₂ DEMS signal for B,D and F. Primary Y-Axis: Ion current. Secondary Y-Axis: electrochemical current. Ar-purged (A & B). O₂-purged (C&D). O₂-purged + 1.75 mM Co salen (E&F). Scan rate 5 mV s⁻¹.

The total pressure signal was added for this experiment, as the m/z signals of interest were very noisy. It is found that the signals of interest (here O₂ or CO₂) are not similar to the one of the total pressure; this mean that their variation are not due to variation of the baseline of the DEMS signal.

This being ensured, the O₂ signal shows an absence of O₂ consumption under argon (Figure VI.4-A), which is as expected. Also, a consumption of O₂ is detected around -0.5 V vs. Ref, in O₂-purged electrolyte (Figure VI.4-C), which is consistent with what was observed on pristine carbon (see chapter two). This might indicate the ORR is still proceeding on the surface of V₂O₅, even though it is

not clearly seen on the electrochemical signal, because of the huge double layer contribution of the electrode.

When Co-salen is included (Figure VI.4-E), the O₂ signal is less clear but it appears that O₂ is still consumed, at higher potential (which is consistent with the positive impact of the Co-salen on the ORR, as explained in chapter four).

Sadly, carbon dioxide evolution is still detected, at potentials inferior than for niobium pentoxide, for the three cases (Ar-purge, O₂-purge and O₂-purge in the presence of Co-salen). This puts even more discredit on the use of this compound as a protective layer, than for the niobium pentoxide.

As such, it was decided to use pristine Panex 30 for the full cell tests (two-electrode setup, with metallic lithium on the negative side, with Co-salen additive in the electrolyte), as it is the most stable positive electrode material tested here (see chapter three).

II. Toward the use of Co-salen in a Li-O₂ full cell

The interest of Co-salen as an additive that can enhance both the ORR and OER was demonstrated in chapter four. However, its use as is in the actual setup of Li-O₂ full cell (lithium on the negative side, separated by Celgard from the carbon cathode on the positive side) is not feasible.

To be more specific, in such geometry, nothing prevents the redox shuttle to cross from the positive side to the negative side, which will necessarily lead to an increased consumption of lithium (thus discharge capacity loss), possible degradation of the mediator on the metallic lithium, and an infinite recharge loop (at least, as long there is still some metallic lithium available).

A very simplified scheme of the capacity losses, that will occur in such Li-O₂ system is depicted on Figure IV.5.

a. Scheme of a solution

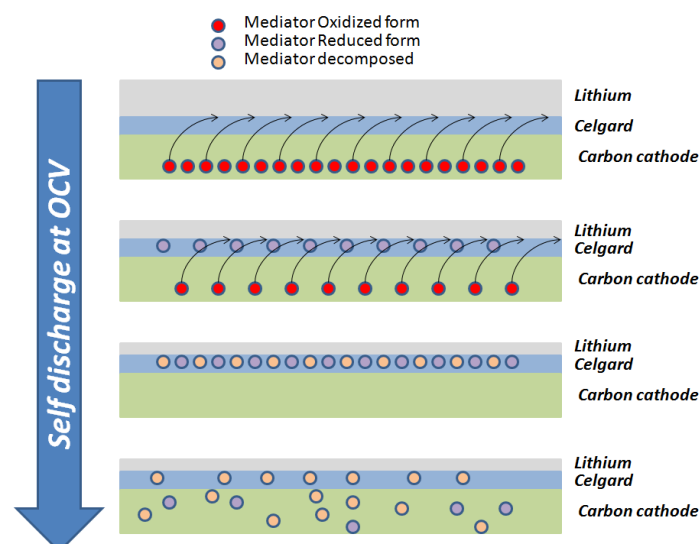


Figure VI. 5: Scheme of self-discharge in a Li-O₂ system, without the use of a solution to prevent the crossing of the mediator to the negative side and its reaction with metallic lithium.

Figure VI.5 is very alarming: if the mediator was “just” reduced on the lithium side, a solution to recover the redox shuttle in the required form, will be “simply” to overcharge the system for the mediator to operate (it must be noted that in this case, the infinite loop for the recharge will not be prevented, as the oxidized form of the mediator could still cross the separator, being reduced on lithium, consuming the latter).

However, it is well-known that owing to its very low potential, metallic lithium often decomposes compounds on its surface (as explained by Peled for the formation of the Solid Electrolyte Interface [21, 22]).

If the redox shuttle was irreversibly decomposed (and not only reduced), the overcharging of the system would be very detrimental, as the mediator would not have the ability to play its role anymore.

However, it came to our attention that this issue could be prevented, with the formation of a sufficient and protective SEI on the lithium, prior to being in contact with the redox shuttle, as explained on the simplified scheme on Figure VI.6. This concept was introduced by Matsumoto *et al.* [23], but was aimed to pre-form SEI on Li-ion graphite anodes.

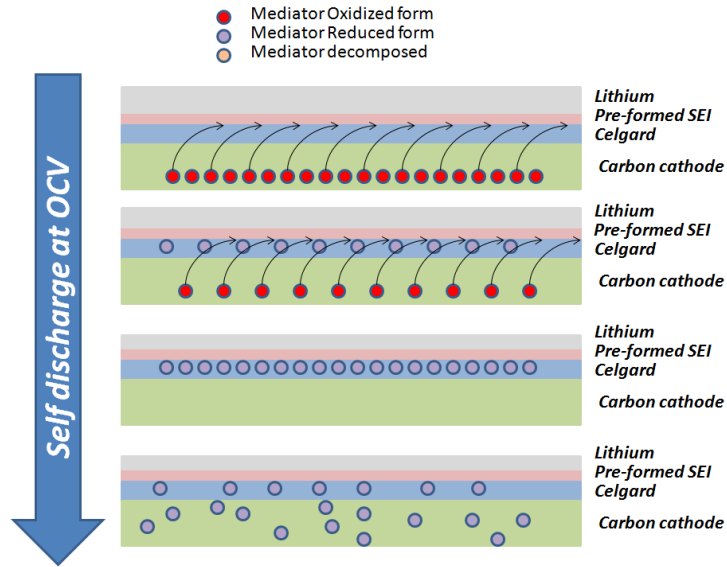


Figure VI. 6: Scheme of self-discharge in a Li-O₂ system, with the pre-forming of an SEI to prevent the decomposition of the Mediator to the negative side

As depicted on Figure VI.6, in the present case, with a sufficient SEI, the mediator would not see metallic lithium and would thus not be irreversibly decomposed. This solution is very appealing, even though it does not enable to solve the issue of the infinite charging loop.

One could also dream of an ideal SEI, pre-forming, where the SEI will be both resistive to electrons and ion-conducting, enabling to transport Li⁺ cation with $t^+ = 1$; this would allow to prevent the mediator reduction, even on the negative side (thus preventing self-discharge), as depicted on Figure VI.7.

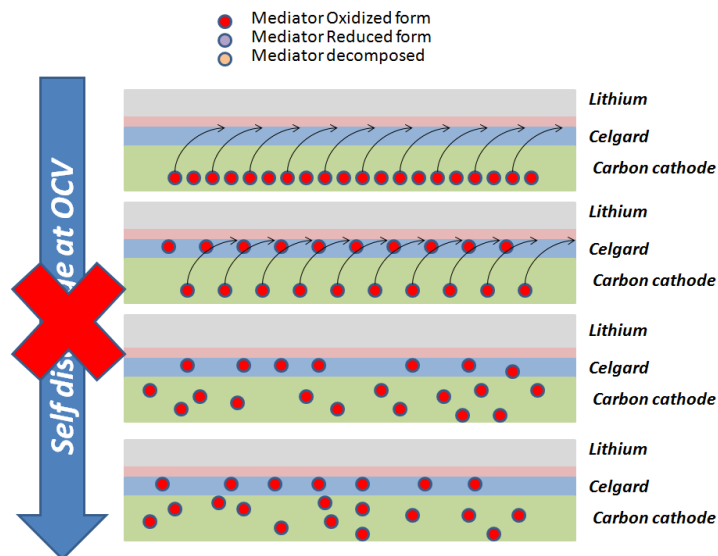


Figure VI. 7: Ideal case for a Li-O₂ full cell, where the self-discharge is suppressed thanks to a fully optimized, pre-formed Solid Electrolyte Interface

The latter case, presented on Figure VI.7 is possible, as it was proven that the SEI structure is composed of the superposition of a dense layer of crystalline product, and an amorphous and porous layer [24–30]. The nature of the compound that composes those inner and outer layers depends on the chemicals that were put in contact with the lithium electrode.

For instance, concerning the inner crystalline layer, it can be composed of crystalline Li_2CO_3 [24, 26–28, 30] (when put in contact with alkyl carbonates solvents), LiF (for the decomposition of LiBF_4 salt [24, 26–28, 30], LiCl (for the decomposition of LiClO_4 salt) [24, 28], but also Li_2O , *etc.*

In addition, the amorphous and porous layer consisted mainly of alkyl carbonates, and others organic decomposition products [24–30]. The thickness of the inner layer was found in the nanometer range (2-20 nm) [21, 27, 30], while the outer layer is in the range of the hundred nanometers [26, 27].

Later studies pointed out that the conduction through the inner layer was ensured thanks to the diffusion of excess interstitial Li^+ [30] through the crystalline planes of Li_2CO_3 (to be more specific, through the [010] channels [29]). Those studies confirm that in the dense inner layer, the charge transport was ensured only by lithium cations, with thus $t^+ \approx 1$, *i.e.* the desired scenario.

b. SEI-pre-forming experience

It was thus decided to test such scenario, to verify that the pre-forming of an SEI could be the solution to prevent (or at least limit) the undesired redox shuttle effect of the crossover of the mediator between the positive and the negative electrode.

Firstly, two disk of lithium foil of $\varnothing 18$ mm were cut and placed in a 20 mm diameter flask. The lithium was firmly pushed to the bottom of the flask to ensure a good adhesion. Then, in the first flask, 1 mL of anhydrous dimethyl sulfoxide (Ar-purged) was added, and in the second one, a blend of ethylene carbonate and propylene carbonate (Ar-purged and anhydrous) was introduced (carbonates solvents and especially ethylene carbonates are known to form very good SEI, and the two-layer SEI formation, with lithium carbonate, as described in the literature was aimed [24–30]).

The two flasks are presented, as mounted on Figure VI.8.

Li
+
DMSO

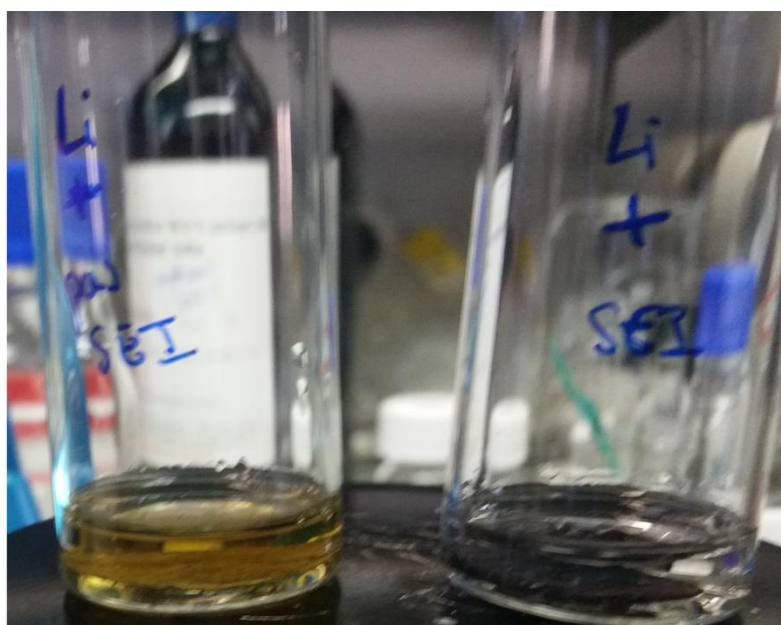


Li
+
EC/PC

Figure VI. 8: Pictures of the samples right after their preparation. Left side: metallic lithium and DMSO. Right-Side: metallic lithium and EC:PC blend

When prepared as mounted, (Figure VI.8), no differences can be spotted readily. The two flasks were left for the SEI to form for four days. Then, a new picture was taken (Figure VI.9).

Li
+
DMSO



Li
+
EC/PC

Figure VI. 9: Pictures of the samples after four day of SEI formation. Left side: metallic lithium and DMSO. Right-Side: metallic lithium and EC:PC blend

On the one hand, Figure VI.9, the DMSO solution, in which the lithium is placed, turned from colorless to yellow, after four days. This indicates, probably, that decomposition products of DMSO have been formed; as the solution is colored, those are likely soluble (which is something non-desirable for the formation of an SEI).

On the other hand, the EC:PC solution in which the second lithium foil was placed, remained colorless, and the lithium surface appeared darker (sign of the formation of products on the surface).

The two solutions were then removed, and both flask were rinsed with 2 mL DMSO, five consecutive times, in order to remove any trace of the previous solvent used for the SEI formation (for the EC:PC case).

Then, 300 μ L (which corresponds to the amount of electrolyte that is used in the present full cell experiments) of 1 M LiClO₄, containing 0.51 mM of Co-salen (a low concentration was used in order to spot easily differences in color - Co-salen is orange in this electrolyte solution [31]) was added in each flask, and left for one day.

As a following, another picture was taken of each samples (Figure VI.10).

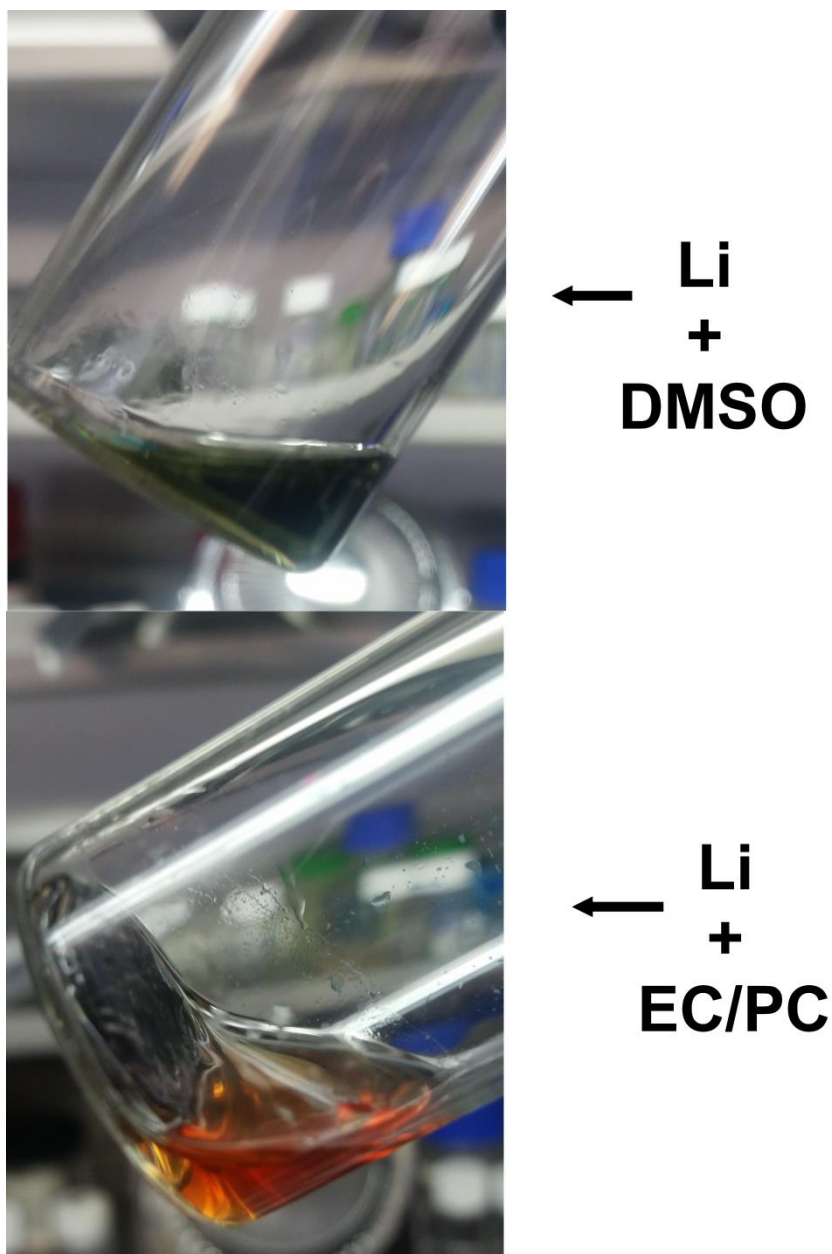


Figure VI. 10: Results of the contact between Lithium and Co-salen electrolyte, after the pre-formation step of the SEI. Top picture: pre-forming with DMSO. Bottom picture: pre-forming with EC:DEC

For the pre-forming of the SEI in DMSO, the solution changed from orange to blue (which is the color of Cobalt in +II state in anhydrous electrolyte [32]), while no changes in color were spotted for the sample with the SEI pre-forming in EC:PC electrolyte.

Those observation clearly show that the Co-salen has been decomposed in the case where the SEI was pre-formed in DMSO, while no decomposition (at least nothing visually observable) occurred for the lithium protected with a SEI pre-formed in EC:PC. This further indicates that, when the SEI is pre-formed in DMSO, only the case depicted on Figure VI.5 can occur (most of the additive is

decomposed); on the contrary, when the SEI is pre-formed in EC:PC, it is either the case depicted on figure VI.6 or on Figure VI.7 that are happening (this experiment is not sufficient to determine which case is truly happening here).

c. A protected Li-O₂ full cell with Co-salen

As this test was highly encouraging, a full cell was mounted, with an SEI pre-formed in EC:PC (four days) to protect the lithium negative electrode. Also, carbonate solvents are known to reacts readily with ORR products [33–37], thus the cell was carefully washed with 3 mL DMSO, five times to eliminate as much as possible the traces of carbonates from the cell.

The electrolyte was 1 M LiClO₄ + 1.15 mM of Co-salen (400 μL); the positive electrode was pristine Panex 30 carbon cloth. It must be noted that, even though the SEI pre-formation is encouraging and was conducted for the full cell experiment, the setup used was not ideal, as the copper wires could not be isolated from the electrolyte (the mediator can be reduced onto the copper). Whatever this bias, electrochemical tests in full cell conditions were performed (Figure VI.11).

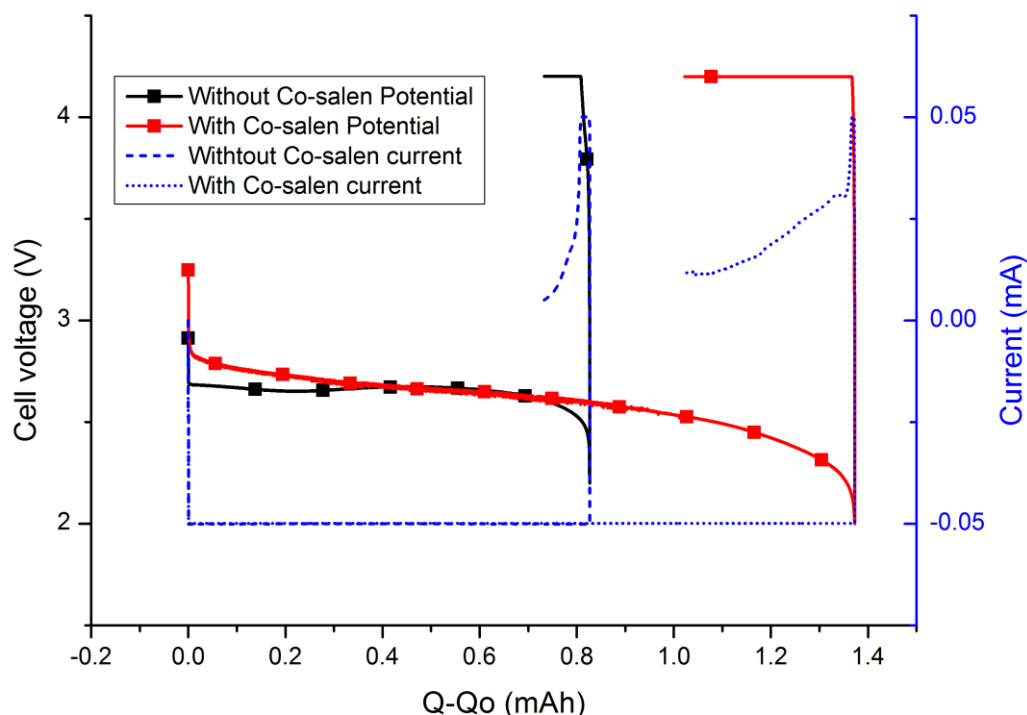


Figure VI. 11: Full cell performances, with a pre-formed SEI when Co-salen is (or not) comprised in the electrolyte. Primary Y-axis: Cell voltage. Secondary Y-Axis: Cell current.

Firstly, the very encouraging result is that indeed, the cell voltage was increased in OCV and in discharge, when Co-salen additive was used (this is due to the fact that Co-salen enhances the ORR, see chapter four).

Also, for an equivalent charging procedure, the Co-salen enables to recharge more capacity and to retain a better charging current than when no Co-salen is added in the electrolyte. Sadly, even with these positive effects, the overall capacity could not be retrieved, and this is probably due to a too-high current set for the charging process. In order to prove this point, a three-electrode setup experiment in which 1.7 mM Co-salen is used, with a low scan rate (thus closest to a stationary experiment) and with the same electrode (pristine Panex 30 with 8 mm diameter) is presented on Figure VI.12.

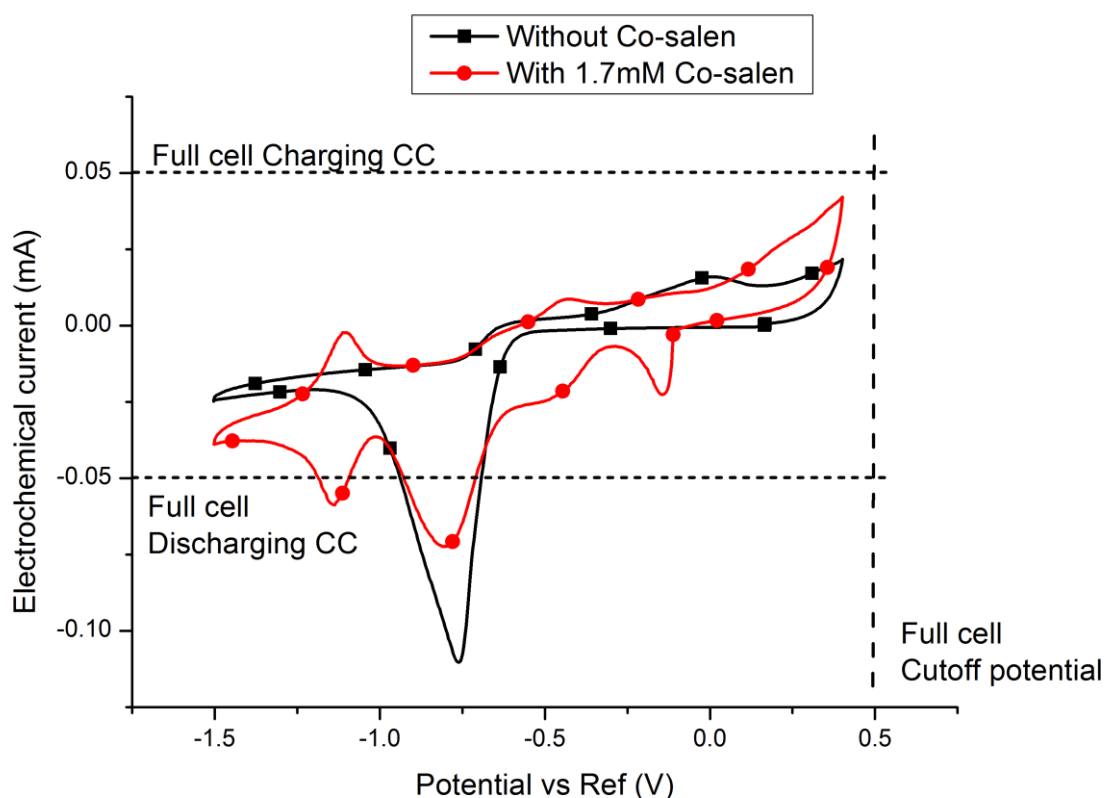


Figure VI. 12: CV operated at 2 mV s^{-1} with drawing of the full cell settings. Black without Co-salen, Red, with Co-salen

The conditions of Figure VI.12 are not exactly the same than the one of the full cell (as the Co-salen concentration used was of 1.15 mM, versus 1.7 mM for this three-electrode experiment).

However, the discharge current can be easily supported in both case as the peak current measured for the case without Co-salen was of -0.1 mA and of -0.075 mA in presence of the Co- salen. This

experiment also explains why not so much differences are spotted on the discharge plateau, for the experiment without Co-salen, versus the experiment with Co-salen, as this current is supported at nearly the same potential (-0.95 V vs. Ref in both case, which corresponds to a potential near 2.7 V vs. Li/Li⁺).

The second crossing point was selected for this calculation (not the first point at -0.7 V vs. Ref), as it corresponds to the case when the experiment is limited by diffusion (which is the case in full cell setup). In both cases, the "stationary" curve never crosses the CC current set at 0.05 mA, which explains well why almost no capacity is recharged during this step, for both cases (with and without Co-salen). As such, if one really wants to spot the differences, between the case with the Co-salen and the one without, other boundary conditions for the cell testing must be set.

Consequently, this experiment needs to be repeated, with a discharge current of -0.025 mA and with a charging current of 0.01 mA. Yet, another effect might also explain the rather sluggish performances in this case: when the cell was un-mounted, it was sadly found dry. Pictures (Figure VI.13) were taken of the lithium and of the color of the remaining liquid in the cell.

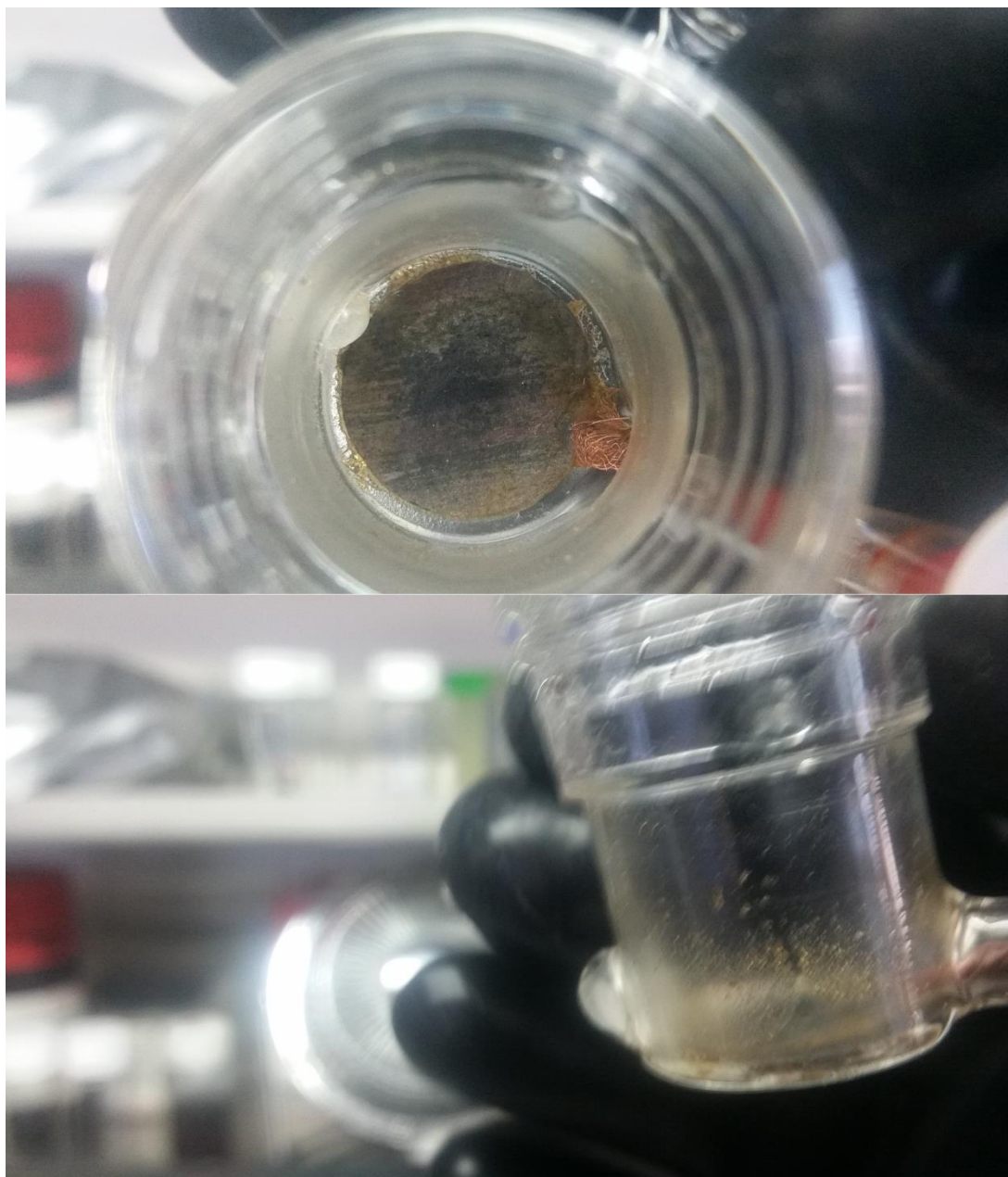


Figure VI. 13: Images of the unmounted SEI pre-formed + Co-salen cell, in the glovebox

Despite the poor quality of these images (the focus of the camera was difficult, as the picture was taken from the outside of the glovebox), they show the orange color of the Co-salen on the side of the cell (bottom image), but also directly onto the lithium (close to the copper wires).

This goes in line with the experiment conducted in the flasks as it appears that the Co-salen remained pristine (as no blue solid is spotted in the cell), even though the electrolyte had evaporated, confirming that the issue was not linked to any reactivity of the Co-salen with lithium (which had been appropriately protected by its carbonate-based SEI). At the time where this manuscript was written, these failed experiments could not be reproduced in due time, unfortunately.

Conclusion

Several paths of improvements of the cyclability of Li-O₂ batteries were tested in this chapter. Unfortunately, it was proven that the new compound tested (V₂O₅) behaves in a similar fashion than Nb₂O₅: it triggers carbon dioxide evolution, *i.e.* instead of protecting the Panex 30 carbon cloth, it promotes (or at least facilitates) its oxidation/decomposition. Sadly, this puts an end to the use of those compounds in practical systems. Another solution (that was not investigated in this chapter), could be to engineer high surface area materials, self-supported (thus no PVDF), with no amorphous graphitic phase nor amorphous carbon phase in their composition (as it was proven in chapter two that those phases are likely the ones responsible for the destruction of the carbon electrodes, by reacting with lithium peroxide).

A solution was also proposed to prevent the detrimental effects of the crossover of the redox shuttle in a full cell, which would lead both to the decomposition of the additive onto lithium (if no SEI is formed), or to its reduction onto lithium (which will consume lithium thus trigger capacity losses). As carbonate solvents are the best for a good SEI formation, but must be prohibited for a practical Li-O₂ system (as they react with lithium peroxide and triggers irreversible loss at each cycles), a SEI on lithium was pre-formed using carbonate solvents and such SEI-protected lithium was then tested in full cells using DMSO-based electrolytes. Similar benchmark tests were performed by attempting to form an SEI in DMSO. It was proven that either no SEI (or a non-protective one) was formed on lithium in contact with DMSO. On the contrary, the pre-forming of a carbonate electrolyte-based SEI on lithium during four days, followed by a careful washing of the cell and the addition of the redox shuttle in the electrolyte gave very encouraging results: no decomposition of the Co-salen was observed. A full cell was mounted in these same conditions, in presence of the Co-salen, and no evidence of the redox shuttle decomposition was confirmed. However, an improvement of the full cell setup and experimental conditions is required as for this experiment, both the discharge and charge current were of too important values, for a true characterization of the performance enhancement, allowed by the Co-salen. This final demonstration is yet to come.

References

1. Salaün AL, Mantoux A, Blanquet E, Djurado E (2009) ESD and ALD depositions of Ta₂O₅ thin films investigated as barriers to copper diffusion for advanced metallization. *J Electrochem Soc* 156:H311–H315. doi: 10.1149/1.3086781
2. Lintanf-Salaün A, Mantoux A, Djurado E, Blanquet E (2010) Atomic layer deposition of tantalum oxide thin films for their use as diffusion barriers in microelectronic devices. *Microelectron Eng* 87:373–378. doi: 10.1016/j.mee.2009.06.015
3. Blanquet E, Nuta I, Brizé V, et al (2010) Developments of ALD Processes: Experiments and Thermodynamic Evaluations. *ECS Trans* 33:321–332.
4. George SM (2010) Atomic layer deposition: An overview. *Chem Rev* 110:111–131. doi: 10.1021/cr900056b
5. Moulder JF, Stickle WF, Sobol PE, Bomben KD (1992) *Handbook of X-ray Photoelectron Spectroscopy*. doi: 10.1002/sia.740030412
6. Mcguire GE, Schweitzer GK, Carlson TA (1973) Study of Core Electron Binding Energies in Some Group IIIa, Vb, and VIb Compounds. *Inorg Chem* 12:2450–2453. doi: 10.1021/ic50128a045
7. Mendialdua J, Casanova R, Barbaux Y (1995) XPS studies of V₂O₅, V₆O₁₃, VO₂ and V₂O₃. *J Electron Spectros Relat Phenomena* 71:249–261. doi: 10.1016/0368-2048(94)02291-7
8. Sawatsky GA, Post D (1979) X-Ray photoelectron and Auger spectroscopy of some vanadium oxides. *Phys revix B*. doi: 10.1103/PhysRevB.20.1546
9. Demeter M, Neumann M, Reichelt W (2000) Mixed-valence vanadium oxides studied by XPS. *Surf Sci* 454:41–44. doi: 10.1016/S0039-6028(00)00111-4
10. Silversmit G, Depla D, Poelman H, et al (2004) Determination of the V2p XPS binding energies for different vanadium oxidation states (V⁵⁺ to V⁰⁺). *J Electron Spectros Relat Phenomena* 135:167–175. doi: 10.1016/j.elspec.2004.03.004
11. Senthil Kumar N, Chandrasekaran J, Mariappan R, et al (2014) V₂O₅ nano-rods using low temperature chemical pyrophoric reaction technique: The effect of post annealing treatments on the structural, morphological, optical and electrical properties. *Superlattices Microstruct*

- 65:353–364. doi: 10.1016/j.spmi.2013.09.035
12. Hopfengartner G, Borgmann D, Rademacher I, et al (1993) XPS studies of oxidic model catalysts: Internal standards and oxidation numbers. *J Electron Spectros Relat Phenomena* 63:91–116. doi: 10.1016/0368-2048(93)80042-K
 13. Jin S, Atrens A (1987) ESCA-studies of the structure and composition of the passive film formed on stainless steels by various immersion times in 0.1 M NaCl solution. *Appl Phys A Solids Surfaces* 42:149–165. doi: 10.1007/BF00616726
 14. Moulder JF, Hammond JS, Smith KL (1986) Using angle resolved ESCA to characterize Winchester disks. *Appl Surf Sci* 25:446–454. doi: 10.1016/0169-4332(86)90087-5
 15. Brion D (1980) Etude par spectroscopie de photoelectrons de la degradation superficielle de FeS₂, CuFeS₂, ZnS et PbS a l'air et dans l'eau. *Appl Surf Sci* 5:133–152. doi: 10.1016/0378-5963(80)90148-8
 16. Barr TL (1978) An ESCA study of the termination of the passivation of elemental metals. *J Phys Chem* 82:1801–1810. doi: 10.1021/j100505a006
 17. Alfonso JE, Buitrago J, Torres J, et al (2010) Influence of fabrication parameters on crystallization, microstructure, and surface composition of NbN thin films deposited by rf magnetron sputtering. *J Mater Sci* 45:5528–5533. doi: 10.1007/s10853-010-4612-3
 18. Jouve G, Séverac C, Cantacuzène S (1996) XPS study of NbN and (NbTi)N superconducting coatings. *Thin Solid Films* 287:146–153. doi: 10.1016/S0040-6090(96)08776-7
 19. Liao HM (1993) Surface composition of AlN powders studied by x-ray photoelectron spectroscopy and bremsstrahlung-excited Auger electron spectroscopy. *J Vac Sci Technol A Vacuum, Surfaces, Film* 11:2681. doi: 10.1116/1.578626
 20. Goldberg MJ, Clabes JG, Kovac CA (1988) Metal-polymer chemistry. II. Chromium-polyimide interface reactions and related organometallic chemistry. *J Vac Sci Technol A Vacuum, Surfaces, Film* 6:991–996. doi: 10.1116/1.575006
 21. Peled E (1979) The Electrochemical Behavior of Alkali and Alkaline Earth Metals in Nonaqueous Battery Systems—The Solid Electrolyte Interphase Model. *J Electrochem Soc* 126:2047. doi: 10.1149/1.2128859
 22. Peled E (1997) Advanced Model for Solid Electrolyte Interphase Electrodes in Liquid and

- Polymer Electrolytes. *J Electrochem Soc* 144:L208. doi: 10.1149/1.1837858
23. Matsumoto K, Nakahara K, Inoue K, et al (2014) Performance Improvement of Li Ion Battery with Non-Flammable TMP Mixed Electrolyte by Optimization of Lithium Salt Concentration and SEI Preformation Technique on Graphite Anode. *J Electrochem Soc* 161:A831–A834. doi: 10.1149/2.091405jes
 24. Aurbach D (1994) The Surface Chemistry of Lithium Electrodes in Alkyl Carbonate Solutions. *J Electrochem Soc* 141:L1. doi: 10.1149/1.2054718
 25. Bar-Tow D (1999) A Study of Highly Oriented Pyrolytic Graphite as a Model for the Graphite Anode in Li-Ion Batteries. *J Electrochem Soc* 146:824. doi: 10.1149/1.1391688
 26. Jeong S-K, Inaba M, Abe T, Ogumi Z (2001) Surface Film Formation on Graphite Negative Electrode in Lithium-Ion Batteries: AFM Study in an Ethylene Carbonate-Based Solution. *J Electrochem Soc* 148:A989. doi: 10.1149/1.1387981
 27. Andersson AM, Henningson A, Siegbahn H, et al (2003) Electrochemically lithiated graphite characterised by photoelectron spectroscopy. *J Power Sources* 119–121:522–527. doi: 10.1016/S0378-7753(03)00277-5
 28. Christensen J, Newman J (2004) A Mathematical Model for the Lithium-Ion Negative Electrode Solid Electrolyte Interphase. *J Electrochem Soc* 151:A1977. doi: 10.1149/1.1804812
 29. Iddir H, Curtiss LA (2010) Li Ion Diffusion Mechanisms in Bulk Monoclinic Li_2CO_3 Crystals from Density Functional. 20903–20906.
 30. Shi S, Lu P, Liu Z, et al (2012) Direct calculation of Li-ion transport in the solid electrolyte interphase. *J Am Chem Soc* 134:15476–15487. doi: 10.1021/ja305366r
 31. Aldrich S (2017) Material Safety Data Sheet of N,N'-Bis(salicylidene)ethylenediaminocobalt(II). <http://www.sigmaaldrich.com/MSDS/MSDS/PleaseWaitMSDSPage.do?language=&country=FR&brand=ALDRICH&productNumber=274712&PageToGoToURL=http%3A%2F%2Fwww.sigmaaldrich.com%2Fcatalog%2Fsearch%3Fterm%3DCo%2Bsalen%26interface%3DAll%26N%3D0%26mode%3Dmatch%2520partial>. Accessed 1 Jan 2017
 32. Aldrich S (2017) Material Safety Data Sheet of CoCl_2 . <http://www.sigmaaldrich.com/MSDS/MSDS/DisplayMSDSPage.do?country=FR&language=fr&productNumber=409332&brand=ALDRICH&PageToGoToURL=http%3A%2F%2Fwww.sigmaaldrich.com%2Fcatalog%2Fsearch%3Fterm%3DCobalt%2528II%2529%26bchloride%26interface%3>

DProduct%2520Name%26N. Accessed 1 Jan 2017

33. McCloskey BD, Speidel A, Scheffler R, et al (2012) Twin problems of interfacial carbonate formation in nonaqueous Li-O₂ batteries. *J Phys Chem Lett* 3:997–1001. doi: 10.1021/jz300243r
34. Luntz AC, Mccloskey BD (2014) Nonaqueous Li – Air Batteries : A Status Report. *Chem Rev* 114:11721–11750. doi: 10.1021/cr500054y
35. Bryantsev VS, Blanco M (2011) Computational study of the mechanisms of superoxide-induced decomposition of organic carbonate-based electrolytes. *J Phys Chem Lett* 2:379–383. doi: 10.1021/jz1016526
36. Viswanathan V, Thygesen KS, Hummelshj JS, et al (2011) Electrical conductivity in Li₂O₂ and its role in determining capacity limitations in non-aqueous Li-O₂ batteries. *J Chem Phys* 135:0–10. doi: 10.1063/1.3663385
37. McCloskey BD, Bethune DS, Shelby RM, et al (2012) Limitations in Rechargeability of Li-O₂ Batteries and Possible Origins. *J Phys Chem Lett* 3:3043–3047. doi: 10.1021/jz301359t

General Conclusion

Non-aqueous Li-O₂ batteries are potential (very) high energy density batteries, owing to the remarkable properties of the Li negative electrodes and of the positive electrode, the energy-density of which is virtually infinite, if the oxygen is not stored in the system. Yet, this system suffers from major issues, linked to the usage of Li metal at the negative electrode, but also to the positive electrode; indeed, the product formed during the discharge (Li₂O₂) is extremely reactive towards the binder (PVDF), the solvent and salts, but also the material used at the positive electrode (carbon); in addition, Li₂O₂ is rather electronic-insulating, and overall, the recharge and cycling-ability of non-aqueous Li-O₂ batteries are really not granted. In this work, these issues have been tackled, and solutions looked for with regards to the electrolyte and positive electrode materials.

In the former case, high-surface-area (partially- graphitized or not) carbon based-materials were tested and analyzed for the non-aqueous ORR and OER in conditions relevant to the Li-O₂ battery. The decomposition of their amorphous-graphitic phase was highlighted by Raman spectroscopy and CO₂ evolution (destruction of the material) was clearly observed by Differential Electrochemical Mass Spectrometry (DEMS). The carbon cloth used as primary current collector and support for the ink deposition of those materials (Zoltek Panex 30), a highly graphitized material (neither amorphous graphitic phase nor amorphous carbon was detected on its Raman spectra), suffered no decomposition in the same conditions, indicating that this material is resilient to usage in Li-O₂ batteries. Comparing the fate of all these carbon-based materials, it is concluded that the carbon phases which are the most reactive (and therefore degraded) toward Li₂O₂ are probably the amorphous ones (amorphous carbon and amorphous-graphitic phase). However, even though this material is of very high interest for a practical system, a second undesirable effect induced by lithium peroxide is still at stake.

This effect is induced by the morphology of the latter, which is known to form large crystallites, with high resistivity (the band gap of Li₂O₂ is of 5 eV). Consequently, those crystallites are nearly impossible to re-oxidize during the charging process, triggering a strong irreversible loss, impacting the cell performance. It is well known that, in order to operate, a charging process needs a triple interface between the electrolyte, the electrode and the product (Li₂O₂), and this reason explains well why the charging step is very difficult for the positive electrode. Redox shuttle additives may delocalize the electron transfer from the electrode to the solution, therefore enabling to “prolong” the triple interface in the electrolyte phase: in theory, even detached Li₂O₂ particles from the electrode could be efficiently re-oxidized. In the present work, two new redox shuttles were tested in three-electrode setup and proved efficient to assist the recharge of Li-O₂ positive electrodes: 5,10,15,20-Tetrakis(4-methoxyphenyl)-21H,23H-porphine cobalt(II) and N,N'-Bis(salicylidene)ethylene diaminocobalt(II). The former was not as interesting as the latter, as its

solubility in the solvent used (dimethyl sulfoxide), was limited. Also, the latter compound demonstrated a very interesting beneficial effect (characterized by three-electrodes experiments and DEMS) on the oxygen reduction (ORR): the ORR onset potential increased by 230 mV, thanks to the formation of a complex between the cobalt(II) core, and molecular oxygen, producing a superoxide-like specie. The formation of the latter complex was already studied in the literature, but evidence of its formation (and reversibility) was studied thanks to UV-Visible spectrophotometry. This effect, which is a sign of homogeneous catalysis, is of very high interest, as it could improve greatly the discharge potential of a practical Li-O₂ system (and thus its practical energy density). Now, whatever the successes of the redox shuttle compounds, they do not impede the possible degradation of the positive electrode material by (electro)chemical reaction with Li₂O₂. Addressing this issue was the third objective of this thesis.

The protection of a model carbon material, the Zoltek Panex 30, was studied by Atomic-Layer Deposition of Nb-oxides, this material being chosen as a representative benchmark of the potential carbon materials to be used in the positive electrode of Li-O₂ batteries. To that goal, ALD thin layers were realized, firstly on Silicon (400), in order to characterize the Atomic-Layer-Deposition (ALD) processes. Two methodologies were studied: Plasma-Enhanced Atomic Layer Deposition (PEALD) and (classical) thermal ALD. On the one hand, the former is known to lead to larger deposition rate and to decrease the temperature of the deposition, but can induce a more "directive" deposit (depending on the orientation of the substrate, the deposit thickness could be different). On the other hand, thermal ALD processes proceed at greater temperature, with lower deposition rates, but are usually more conformal, with a better thickness homogeneity in three dimensions. The composition of the deposits formed by these two recipes were analyzed thanks to X-Ray Energy Dispersive Spectroscopy (X-EDS) and X-Ray Photoelectron Spectroscopy (XPS). The composition of the thermal ALD layers was mainly niobium oxides (Nb₂O₅, predominant) and oxynitrides (NbO_xN_y) on the surface. The composition in the depth of the deposit was analyzed thanks to *in situ* erosion and XPS, and the same components were detected but this time, the oxynitrides appeared predominant. The surface-composition of the PEALD sample showed only Nb₂O₅. For both recipes, the deposit morphology was analyzed by Scanning Electron Microscopy (SEM) and appeared very flat (except with a little surface roughening for the Thermal ALD recipe). The conformity of the deposit was then analyzed by conducting a deposition on a Si (400) wells (with a form factor of 6). The SEM back-scattered images of the cleaved samples showed that only the thermal ALD recipe allows to have a deposit at the bottom of the wells. Consequently, the thermal ALD recipe was chosen for the deposition onto the Zoltek panex 30 carbon electrodes. Four batch were realized (eight electrodes of Panex 30 in each batch), at different numbers of ALD cycles: 1500, 2000, 2500 and 1500-extended. The latter was

realized, with an increased pulse-time for each reactant (to allow a better diffusion). As for the silicon samples, the composition was analyzed by X-EDS and SEM, and the product detected was Nb_2O_5 , which contrasted with the experiment on silicon. Also, strong differences could be spotted in the amount of deposit from one electrode to the other within the same batch. As a consequence, the impact of the number of cycles could not be highlighted in a clear manner. The electrochemical behavior of such NbOx-protected Panex 30 electrodes was studied by DEMS; surprisingly, the presence of the deposit triggered CO_2 evolution (thus decomposition of the carbon of the electrode), while the pristine material was highly resilient. Therefore, it was concluded that this deposit was harmful to the electrode and behaved at the exact opposite of the expected behavior. Another deposit (V_2O_5) was (shortly) tested, but its behavior was exactly the same than for Nb_2O_5 (it triggered carbon decomposition).

Finally, full cell experiments were performed using Zoltek Panex 30 at the positive electrode, metallic lithium at the negative and a Celgard® separator impregnated with a DMSO-based electrolyte comprising the redox shuttle. As this separator alone cannot prevent the cross-over of the efficient redox shuttle (N,N'-Bis(salicylidene)ethylene diaminecobalt(II)) from the positive side of the cell to the negative side, we tested the pre-forming of a Solid Electrolyte Interface (SEI) onto the lithium thanks to a mixture of Ethylene Carbonate (EC) and Propylene Carbonate (PC). For comparison, one lithium sample was prepared by pre-forming a SEI in DMSO. Evidence of the decomposition of the latter was spotted for the lithium, pre-formed in DMSO, while nothing occurred for the lithium pre-formed in EC:PC. This latter solution demonstrated promising behavior in a not-fully-optimized full-cell Li-O₂ battery: increased performance were monitored versus a full cell without the redox shuttle.

The performances can be improved in a fully optimized full cell setup, with a SEI formed in the ideal mixture of carbonates solvents. Still, many issues are needs to be addressed for a truly efficient Li-O₂ system. As such, three axes of research are proposed, in the perspective of an efficient Li-O₂ positive electrode. The first will be to find a solvent and salt, both stable toward Li_2O_2 , which is mandatory for a practical system. The second will be to find a way to synthesize a high surface area carbon material, in which no amorphous carbon nor amorphous graphitic phase are comprised, and to test it as a positive electrode. If the behavior of the latter is the same than Zoltek Panex 30 (no reactivity between the material and Li_2O_2), this material could be used in a practical system, directly as the positive electrode (as it will be stable). If not, others deposit chemistries (for instance nitrides) must be studied for the deposition of a protective layer on the positive electrode. Finally, an extensive research for the negative electrode must be conducted, especially for the pre-formation of a stable SEI, which showed promising results.

Annexes

Annexes 1: Raman Fit of pristine carbon materials in LabSpec

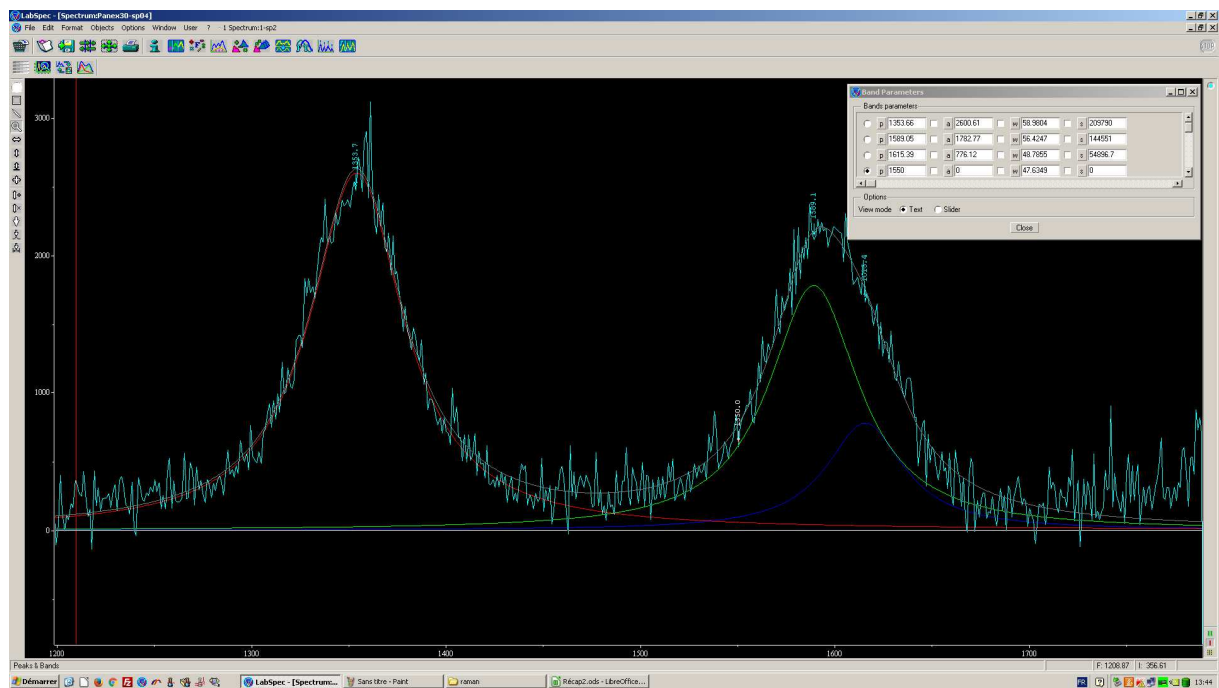


Figure Annexe. 1 : Fit of a Raman spectra of Panex 30

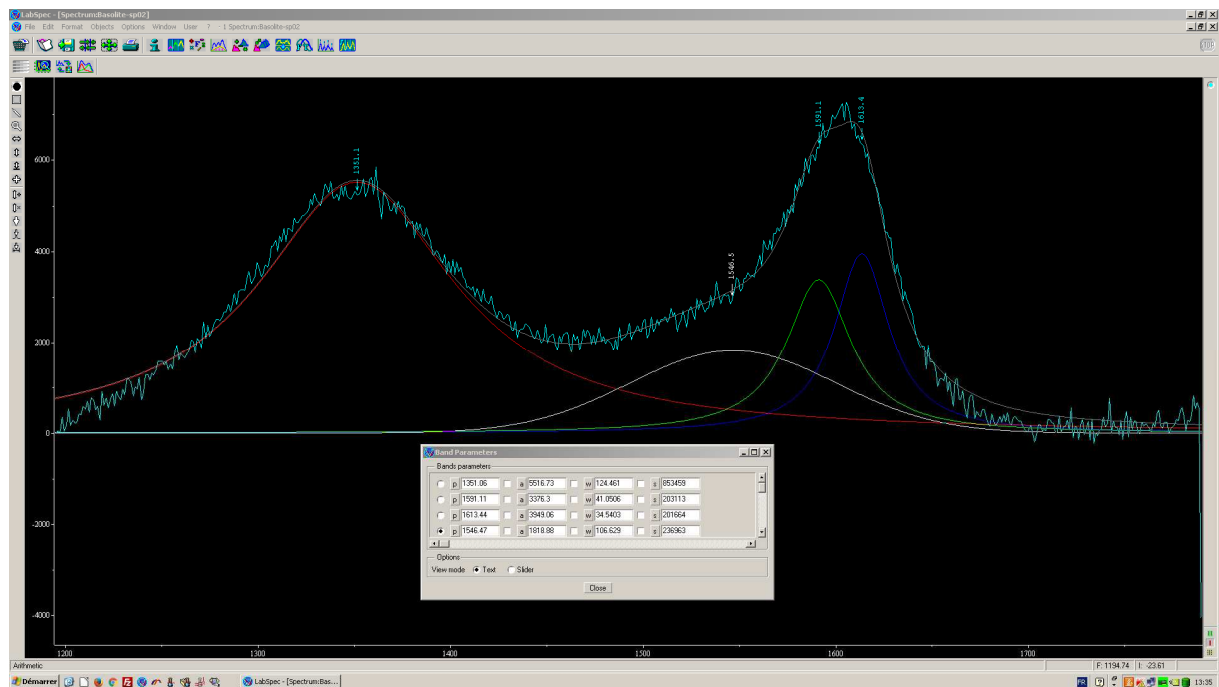


Figure Annexe. 2 : Fit of a Raman spectra of Basolite

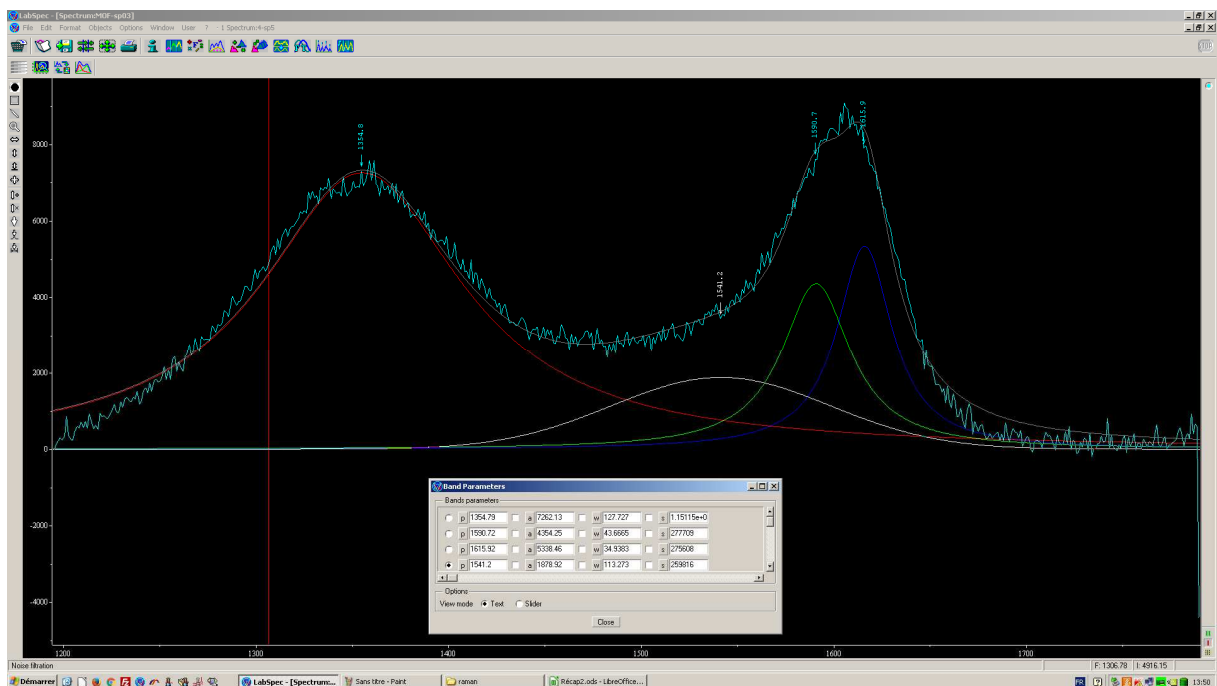


Figure Annexe. 3 : Fit of a Raman spectra of MOF

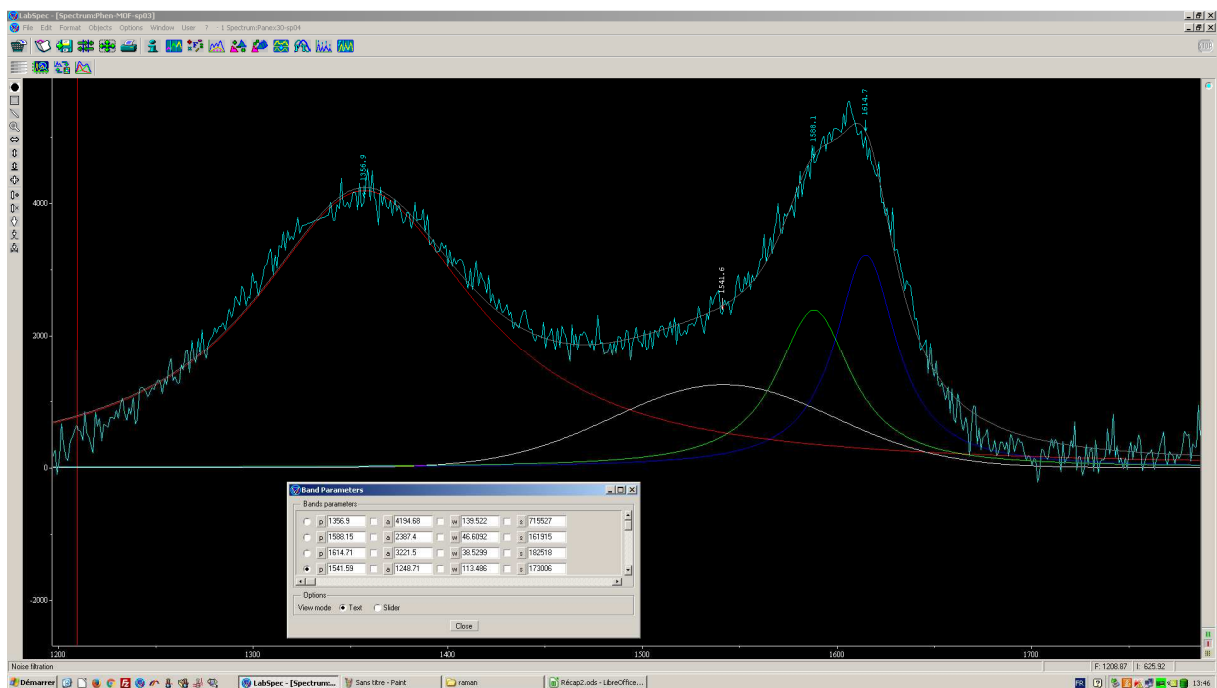


Figure Annexe. 4 : Fit of a Raman spectra of PhenMOF

Annexes 2 : Raman Fit of discharged carbon materials in Labspec

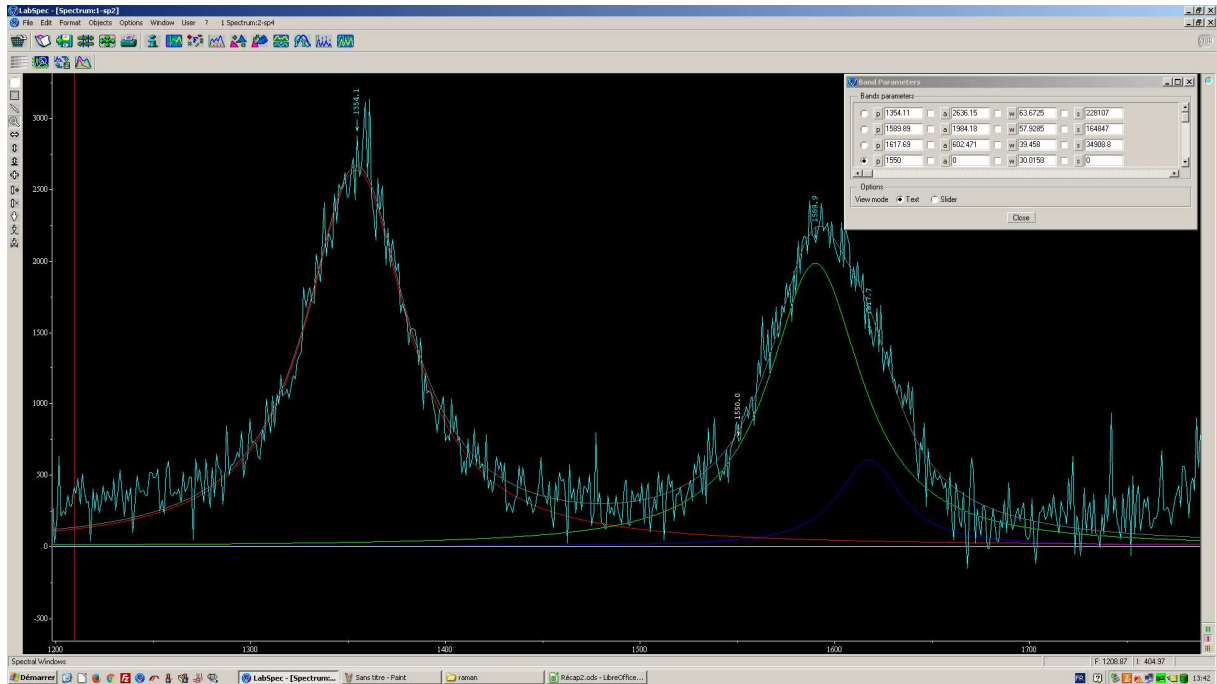


Figure Annexe. 5 :Fit of a Raman spectra of Panex 30

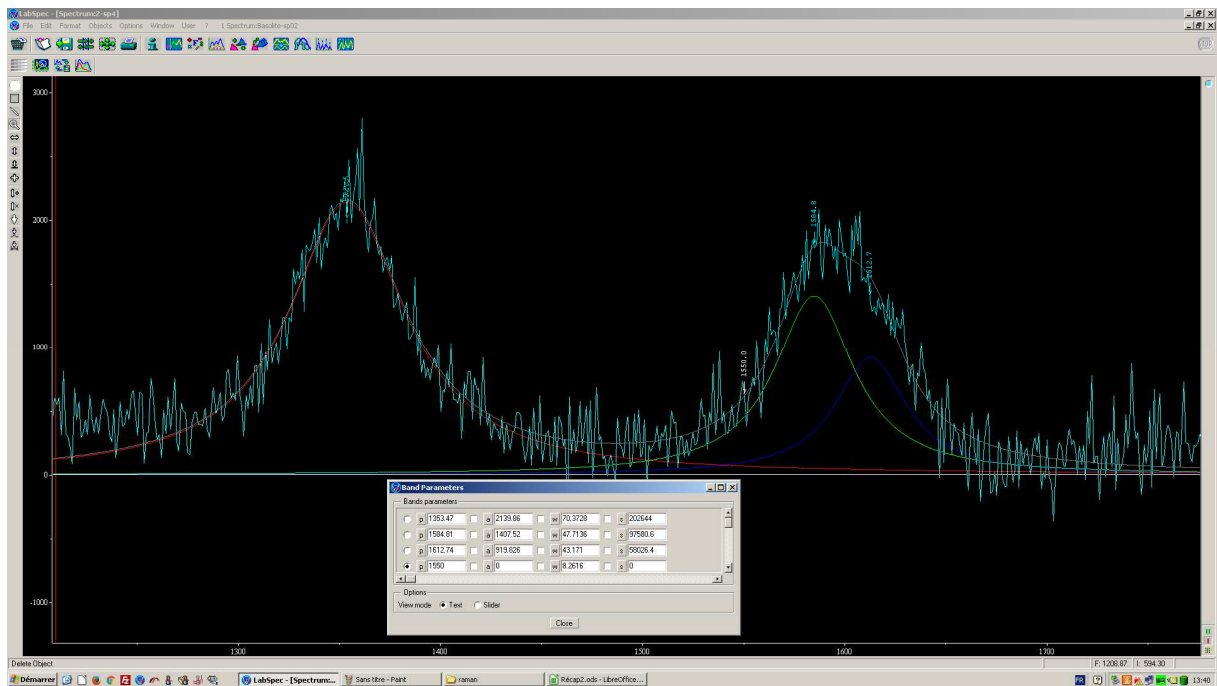


Figure Annexe. 6 : Fit of a Raman spectra of Basolite

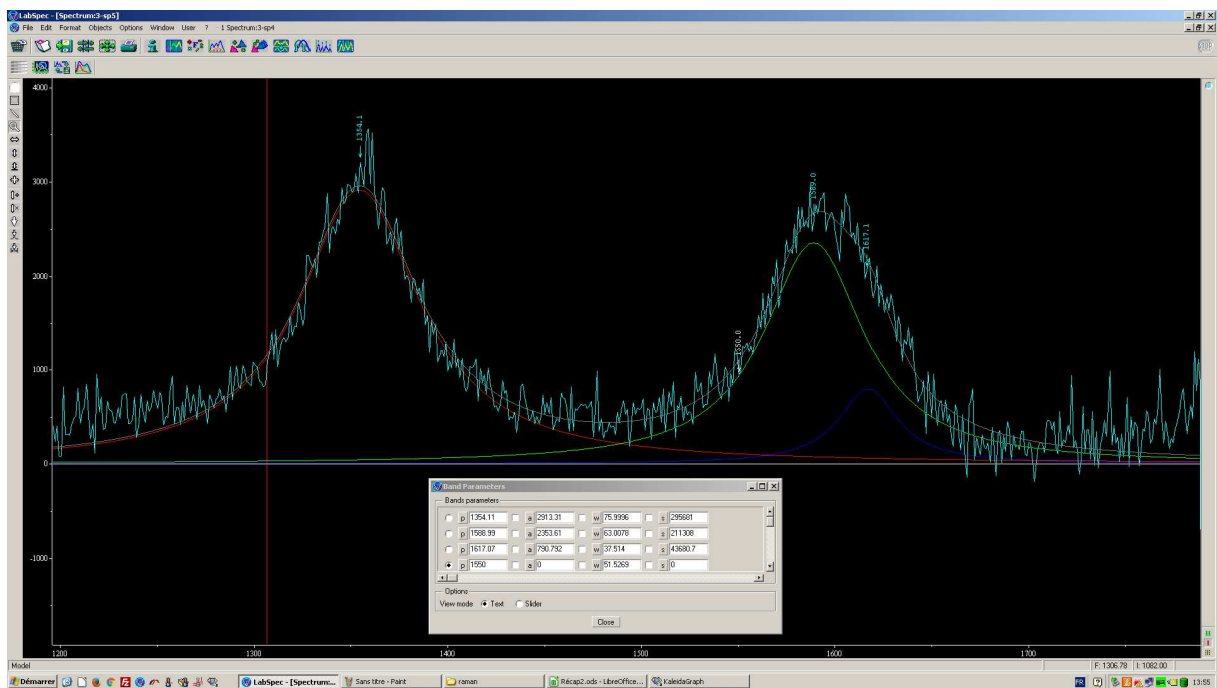


Figure Annexe. 7 : Fit of a Raman spectra of MOF

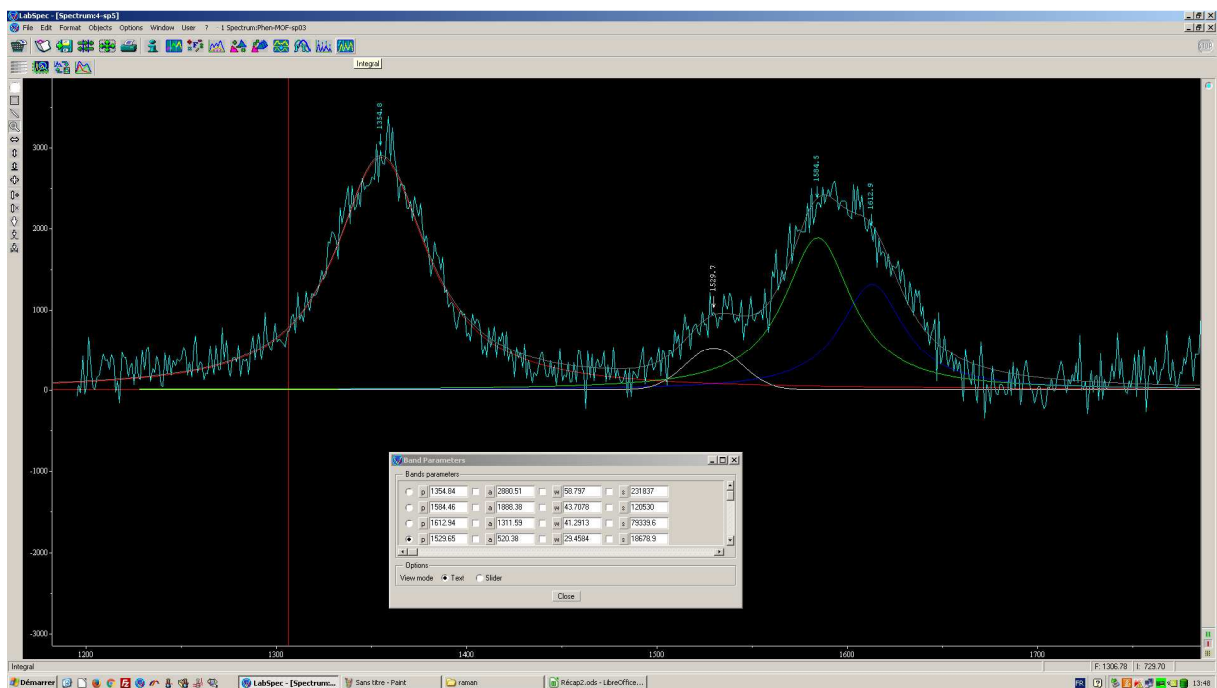


Figure Annexe. 8 : Fit of a Raman spectra of PhenMOF

Conferences & Publications

Conferences:

-ISE Providence 2017: Presentation in Symposia 12: “Electrochemical Technology for solving 21st Century Challenges”. Title: Homogeneous catalysis and redox shuttle for non-aqueous Li-O₂ cathode.

Publications:

- Blanchard R, Martin V, Mantoux A, Chatenet M (2017) Cobalt porphyrin and Salcomine as novel redox shuttle species to enhance the oxygen evolution reaction in Li-O₂ batteries. (Electrochim Acta) 261:384–393. doi: 10.1016/j.electacta.2017.12.129

Abstract (English version)

The present PhD work focuses on solving two major issues of the Li-O₂ positive electrodes, both being linked with the nature of the discharge product formed during the Oxygen Reduction Reaction, in Lithium cation electrolyte: Lithium peroxide (Li₂O₂). The first issue is related to the Discharge mechanism (consecutive Electrochemical nucleation and chemical disproportionation of an intermediate, lithium superoxide), which lead to the formation of large particles of lithium peroxide on the electrode surface. Owing to their size and resistivity (bandgap of lithium peroxide : 5 eV), it is nearly impossible to re-charge efficiently the electrode. This issue can be solved, thanks to the dissolution of an additive in solution, that promote the transport of electrons, and allow the oxidation of large discharge particles (in theory, even the ones disconnected from the electrode). A very good compound was found to efficiently work as a redox shuttle (enhanced Oxygen Evolution reaction), with also a highly beneficial effect for the ORR, with a catalysis effect that allowed to increase the onset of the ORR of 230 mV. However, this solution require a engineering of the practical system as this additive could cross from the positive electrode to the negative side (lithium) and trigger capacity loss and infinite charging loop. The second issue is linked to its reactivity. As a matter of fact, it is an hard base (according to HSAB theory), which reacts readily with a large panel of electrodes component (reactivity toward the PVDF binder, solvent, salts, but also with the carbon material, used as the positive electrode). As such, it is necessary to find a way to protect the latter, and a solution proposed in this work was to use Atomic Layer deposition of Niobium pentoxide (Nb₂O₅), in order to form a very thin deposit, which was supposed to prevent any contact between the discharge product, and the carbon support (consumption of Carbon, with formation of a large bandgap compound : Lithium carbonate). The deposition was conducted onto a graphitized carbon cloth (Zoltek Panex 30), which surprisingly proved to be highly resistant toward lithium peroxide. Sadly, the presence of the deposit did not protect the electrode but rather made it weaker, with tracers of the formation lithium carbonate. This compound was thus not considered anymore, and others deposits are yet needed to be tested in future studies.

Résumé (Français)

Les travaux de cette thèse focalisent sur la résolution de deux problèmes majeurs des électrodes positives de systèmes Li-O₂, dus à la nature du produit de décharge formé pendant la réaction de réduction de l'oxygène, en milieu Li⁺ : Lithium peroxyde (Li₂O₂). Le premier problème est lié au processus de formation de ce dernier (étapes successives de nucléation électrochimiques et de dismutation chimique d'un intermédiaire : le superoxyde de lithium), qui conduit à la formation de très grosses particules de peroxyde lithium à la surface de l'électrode. Du fait de leurs taille et de leur résistivité (le gap du peroxyde de lithium est de 5 eV), il est impossible de recharger de manière efficace et à 100% ce dernier. Cependant, ce problème peut être résolu, grâce à l'ajout d'un additif, qui permet le transport d'électron en solution, et qui peut (en théorie), recharger les particules de Li₂O₂, détachées de l'électrode. Un très bon candidat a été trouvé dans cette étude, qui a prouvé de très bonne performances pour l'amélioration du processus de recharge, et un effet bénéfique supplémentaire a été caractérisé sur le potentiel de décharge, grâce à un effet catalytique (augmentation du potentiel de réduction de 230 mV). Cependant, cette solution demande de repenser totalement le design actuel des systèmes Li-O₂, car ce composé (soluble) peut facilement traverser le séparateur, vers l'électrode de lithium (et causer une autodécharge importante ainsi qu'une boucle de recharge infinie). Le second problème est lié à une autre caractéristique du peroxyde de lithium : sa réactivité. De fait, c'est un base forte au sens de Lewis (en accord avec la théorie HSAB), et réagit de manière importante avec les constituants de l'électrodes (réactivité avec le liant PVDF, mais aussi avec les solvant, le sel et le support carboné de l'électrode). Il est donc nécessaire de trouver un moyen de protéger ce dernier, et une solution proposé dans ce manuscrit a été de réaliser la déposition d'une couche nanométrique de Nb₂O₅, qui a pour but d'éviter tout contact direct entre le carbone, et le peroxyde de lithium (réaction entre ces deux derniers, qui conduit à la formation d'un composé avec un gap de 7 eV : le carbonate de lithium). Le dépôt fut étudié sur un carbone graphitisé (Zoltek panex 30) qui, de manière surprenante, a été très résistant versus le peroxyde de lithium. Malheureusement, la présence du dépôt à la surface du tissu n'a pas protégé l'électrode, mais a plutôt eu l'effet inverse, car des traceurs de la formation de carbonate de lithium ont pu être observé (alors qu'aucun traceur n'était détecté sur le tissu nu). Le Nb₂O₅ a donc été écarté, et d'autres composés doivent être testés dans de futures études, pour cette application.

